Theoretical study on the mechanism of the reaction catalyzed by protein kinase A

Ayax Pérez Gallegos

Universitat Autònoma de Barcelona

Theoretical study on the mechanism of the reaction catalyzed by protein kinase A

Ayax Pérez Gallegos

PhD Thesis

Doctoral Studies in Chemistry

PhD Supervisors:
Àngels González Lafont
Mireia Garcia Viloca

Chemistry Department
Faculty of Science

2016

Universitat Autònoma de Barcelona

Dissertation submitted to aspire to the PhD degree by:

_____

Ayax Pérez Gallegos

PhD supervisors' approval:

_____ _____

Àngels González Lafont **Mireia Garcia Viloca**

Bellaterra (Cerdanyola del Vallès), April 26, 2016

A Margarita, Alejandra y Erik

The author acknowledges “Consejo Nacional de Ciencia y Tecnología” (CONACYT, México) Supporting Grant 213582.

I am really grateful to my PhD supervisors, Prof. Àngels González Lafont and Prof. Mireia Garcia Viloca, as well as to Prof. Josep M. Lluch, for the possibility of forming part of their research group.

Some of the results presented in this PhD dissertation have been published in scientific journals:

SP20 phosphorylation reaction catalyzed by Protein Kinase A: QM/MM calculations based on recently determined crystallographic structures
Ayax Pérez-Gallegos, Mireia Garcia-Viloca, Àngels González-Lafont, and José M. Lluch
ACS Catalysis **2015** *5* (8), 4897-4912
DOI: 10.1021/acscatal.5b01064

A QM/MM study of Kemptide phosphorylation catalyzed by protein kinase A. The role of Asp166 as a general acid/base catalyst
Ayax Pérez-Gallegos, Mireia Garcia-Viloca, Àngels González-Lafont, and José M. Lluch
Physical Chemistry Chemical Physics **2015** *17*, 3497-3511
DOI: 10.1039/c4cp03579h

A QM/MM study of the associative mechanism for the phosphorylation reaction catalyzed by protein kinase A and its D166A mutant
Ayax Pérez-Gallegos, Mireia Garcia-Viloca, Àngels González-Lafont, and José M. Lluch
Journal of Computer-Aided Molecular Design **2014** *28* (11), 1077-1091
DOI: 10.1007/s10822-014-9786-3

Contents

Todd's Hypothesis: "Where there is life, there is phosphorous"

1. Introduction.

Protein phosphorylation was first described as a regulatory mechanism in 1958 through the pioneering studies of Krebs and Fischer.[1-2] They showed for the first time that the activity of an enzyme was activated by the covalent addition of a phosphate moiety. Nowadays it is difficult to find a biochemical event that is not related directly or indirectly to reversible protein phosphorylation processes, which rank among the most important posttranslational modifications in the living cell,[3-5] and is said to be the central regulation mechanism of basic cell processes and protein functions.[6] That is, the simple addition of a phosphate on a specific protein site,[7] represents a universal mechanism for cellular signaling networks of control and adaptation.[8-10] Protein phosphorylation serves to modulate the activation or deactivation of a wide variety of enzymes, the recruitment of proteins, as well as the control of specific protein-protein interactions related with changes in cellular localization.[11-14] For that reason, the class of enzymes that catalyze phosphorylation of proteins, protein kinases,[15-18] are now considered a cornerstone of the signal transduction field in both eukaryotes and prokaryotes.[19-20]

In eukaryotes, protein kinases are divided in two large classes based on their ability to phosphorylate serine/threonine side chains, or tyrosine side chains. There is a class of protein kinases that can phosphorylate serine, threonine, and tyrosine side chains, termed dual-specific protein kinases, but it is a small number and it is not well characterized from a mechanistic standpoint.[21] There are even protein kinases that catalyze the phosphorylation of histidine residues, as well as other amino acids, but they are really uncommon.[22]

Regarding their activity, protein kinases are rapidly turned on and turned off in response to intracellular and extracellular cues, typically initiated by an extracellular signal such as a hormone, a neurotransmitter, nutrient deprivation, or some other kind of stress.[23] Thus, when chemically active protein kinases function by catalyzing the γ-phosphoryl group transfer from an ATP cofactor (or another nucleotide triphosphate, in some cases) to the hydroxyl group of a serine, threonine, or tyrosine side chain of the target substrate protein or peptide, to produce a phosphomonoester and ADP products.[21]

The biological importance of phosphoryl-transfer chemistry is clearly attested by the fact that approximately 1.7% of the human genome sequence translates for the 518 known human protein kinases (and, approximately, 20 lipid kinases), encompassing the largest superfamily of enzymes: the human kinome.[6] A number of 478 protein kinases present a eukaryotic protein kinase domain, which contains the cofactor and substrate binding sites, so they are further classified into seven major subfamilies based on sequence similarity within this domain (see

Figure 1.1).[24] Although the remaining 40 kinases lack sequence similarity to eukaryotic protein kinase domain, they are known to have kinase activity, and for that reason they are referred to as atypical protein kinases.[6] It is estimated that protein kinases can collectively phosphorylate up to one-third of intracellular proteins in mammalian cells, generating up to 20,000 distinct phosphoprotein states just in humans.[25]

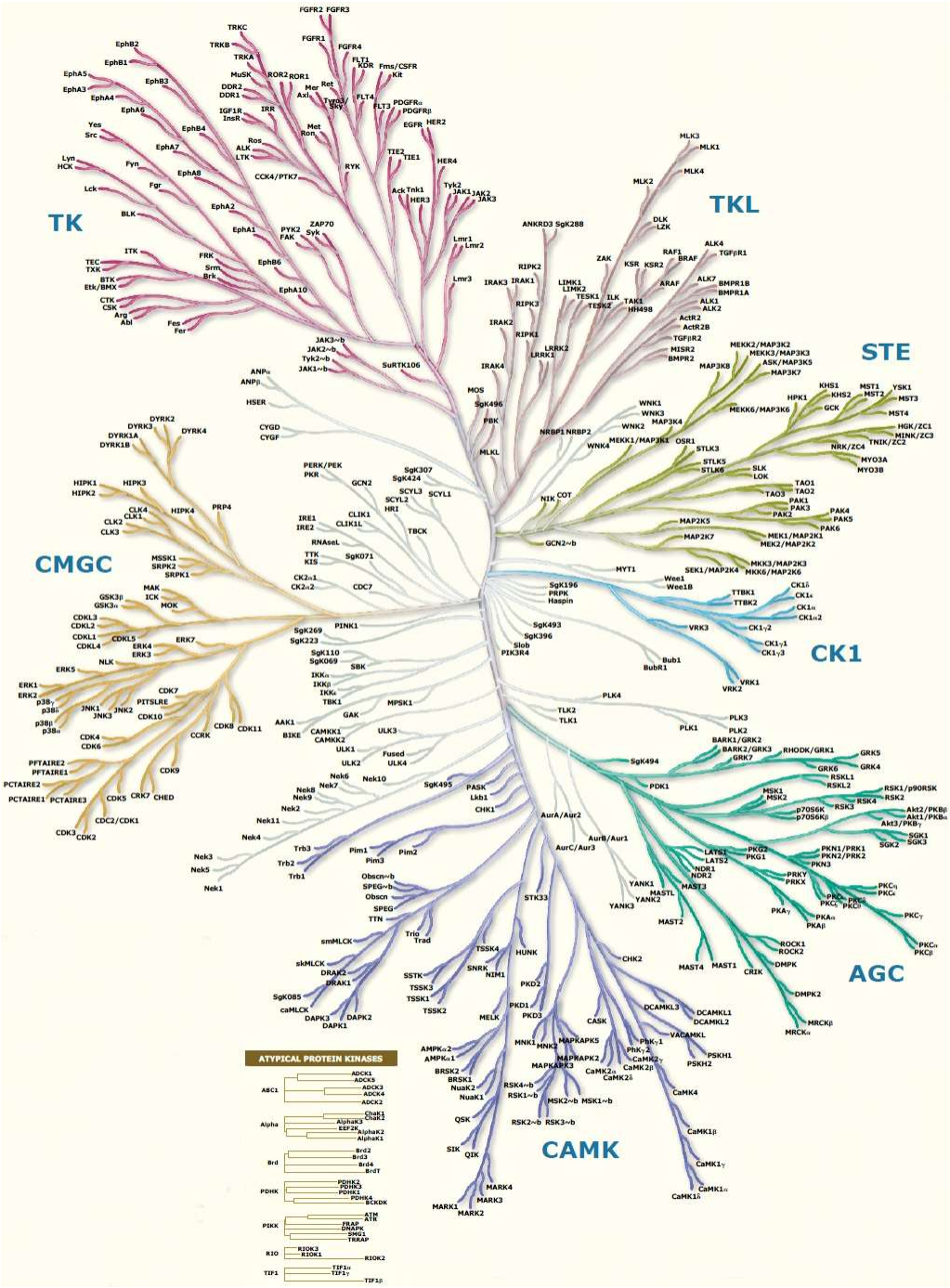

Figure 1.1. The human kinome. As kinases are so important, not only for biochemistry, but also for disease phenotypes and molecular biology, many kinase structures have now been solved by academia, industry, and structural genomics consortia in different conformations, and bound to different ligands and proteins (illustration from 2010, Cell Signaling Technology, Inc; www.cellsignal.com).

In Figure 1.1, the subfamilies abbreviations stand for: TK, tyrosine kinases; TKL, tyrosine kinase-like; STE, homologous to yeast Sterile kinases; CK1, casein kinase 1 group; AGC, protein kinase A, G and C related kinases; CAMK, Ca^{2+}/calmodulin-dependent kinases; CMGC, containing CDK, MAPK, GSK, and CDK-like kinases. In addition, ten percent of the eukaryotic protein kinases contain evolutionarily conserved alterations in otherwise highly invariant motifs critical for phosphate transfer that are thought to render them catalytically inactive, prompting them to be designated "pseudokinases" and grouped as receptor guanylyl cyclases (RGC; meaning that all of these enzymes convert GTP to GMP).[6,26]

As noted above, by modification of substrate activity protein kinases represent one of the fundamental components in many critical signaling and regulation pathways in eukaryotic cell processes,[7,21,27] including cell cycle progression and intracellular communication during development, DNA transcription, replication and repair, angiogenesis, organelle trafficking, carbohydrate and lipid metabolism, cell differentiation and growth, neurotransmitter biosynthesis, motility and smooth muscle contraction, in physiological responses and homeostasis, in the functioning of the nervous system, and apoptosis.[6,28-32] Thus, protein kinases dysfunction or deregulation of its activity, normally due to activating mutations,[33] has been linked to over 400 diseases and with the malfunction of the signaling networks that control the immune system,[7,28-29] and many naturally occurring toxins and pathogens exert their effects by altering the phosphorylation state of proteins,[7] then becoming important targets for rational drug design.[34-39] Actually, for the pharmaceutical industry, protein kinases have become the most relevant drug targets for cancer therapy in the last fifteen years and the growing interest in targeting kinases has also now been extended to the area of inflammatory and autoimmune diseases (as diabetes).[40-42]

1.1. Protein kinases: allosteric macromolecular switches.

Protein kinases belong to a group of very dynamic and typically oscillating macromolecular complexes.[23] Their structures have been studied extensively, so our most comprehensive understanding of protein kinases at the molecular level has come from crystal structures, but advances in NMR spectroscopy has enable the revelation and exploration of residue-specific dynamics, synchronous motions of structural elements, and dynamically committed, uncommitted and quenched states of a protein in solution (among other dynamic properties).[43-45] Furthermore, due to the development of theoretical methods and computational techniques that explore the relation between dynamics,[46-48] reactivity,[49-50] and the principles of enzymatic catalysis,[51-53] we can now analyze in a far more comprehensive way how proteins work and behave in solution.[54-60] In this manner, we now appreciate that whereas

the metabolic enzymes have evolved to be efficient catalysts that turn over large amounts of small molecule substrates, protein kinases have specifically evolved to be highly regulated molecular switches working on proteins, that initiate a cascade of downstream signaling events involved in the regulation of cellular processes by catalyzing phosphorylation of proteins.[61] Moreover, while simple allosteric regulation is important in all cells and allows many proteins to be sensitive to their immediate environment, protein phosphorylation allows cells to be responsive to their external environment. That is, the signal transduction pathways that allow a cell to respond to external stimuli, whether it is a hormone, a grow factor, a photon or osmotic shock, are all regulated at critical switch points by protein phosphorylation.[62] In addition, the identification and study of protein kinases and their functioning has led to the outcome and consolidation of two fundamental concepts in biochemistry. First, the idea of the power of signal amplification within the cell considering that there are many elaborate kinase cascades that lead from a single event at the plasma membrane to the eventual mediation of gene expression in the nucleus. Second, the recognition of the "second messenger" concept, since the binding of a molecule at the surface of a cell can led to the generation of a second molecule within the cell that mediates a biological response. In this sense, the three most prominent intracellular protein kinase second messengers, cAMP, Ca^{2+} and phospholipids, all mediate their primary responses by contributing to the activation of specific protein kinases.[61-62]

To achieve such complex behavior, protein kinases have developed a set of conserved motifs that span the entire kinase core. Those motifs that are essential for catalysis were hijacked from the eukaryotic-like kinases, but other motifs were recruited to integrate regulation as a key feature.[12] All motifs were first recognize by Hanks and Hunter when only a handful of kinase sequences were known;[63] their careful designation of 11 subdomains based on these conserved sequence motifs has remained as a good way to assess the elements of kinases' secondary structure, and after the first protein kinase structures were solved these subdomains were mapped onto its fold generating a template for align and compare the entire kinome, and now is even possible to correlate any motif with disease phenotypes in the ProKinO data base.[64-65] Furthermore, now it is possible to appreciate the functional importance of these motifs not only for structure and function but also for activation,[61] and we are learning how these motifs are integrated in a correlated way to create a dynamic allosteric network.

The complexity of such regulatory machinery not only distinguishes the eukaryotic protein kinases from the eukaryotic-like kinases, but also from most metabolic enzymes, and points to the fact that eukaryotic protein kinases have evolved not to efficiently turn over lots of product, but rather to be transiently activated, thus representing a unique, highly dynamic, and precisely regulates set of switches that control most biological events in eukaryotic cells.[16] In this sense,

the eukaryotic protein kinases all share a conserved kinase core and are regulated in some way by auto- or heterologous kinase phosphorylation.[66-68] That is, besides the potential of the covalent addition of a phosphate as a ubiquitous regulatory mechanism of protein functions and, in particular, to mediate the equilibrium between active and inactive conformations, phosphorylation can regulate the kinases themselves too. Some of the phosphorylation sites lie in the so named activation loop,[69] while other sites are located in highly dynamic flanking regions (tail and linker segments that are frequently an integral part of the active kinase) which may differ in each kinase.[70]

Taylor and coworkers have pointed out, since long, the necessity and sufficiency of the various phosphorylation and binding sites across the kinases' structures,[26,69] but its implication on the phosphoryl-transfer mechanism was not compared until very recently, when it has been demonstrated that the activity of protein kinases can be altered by mutations and binding events distant from the active site, and structural and function community analysis have provide a conceptual framework for long-distance allosteric communication between different sites on protein kinases.[71]

1.2. Molecular features of protein kinases.

The protein kinase family of enzymes is large and structurally diverse although all the members are characterized by a conserved catalytic core with a bilobal structure (see Figure 1.2), which suggests a common phosphoryl-transfer mechanism. Unlike other enzymes, the protein kinases are unique as, in general, they do not have a single active and inactive conformation. The active state of the enzyme is highly dynamic with the core toggling between different conformations, while the inactive state has traditionally been divide into general groups defined by positioning of structurally conserved motifs.[72]

The protein kinase are approximately 350 amino acids in length, from which the conserved kinase core is represented by residues 40-300 (for convenience, the Protein Kinase A motifs and numbering of individual conserved residues is used).[73-74] The conserved core consists of two major subdomains, the N-terminal (residues 40-119) and C-terminal lobes (residues 128-300).[75] Such lobes, made up of helical and beta subdomains, and connected by a short loop termed the hinge region or linker (residues 120-127), are structurally and functionally distinct and contribute in unique ways to both catalysis and regulation.[16] In general terms, the N-terminal lobe provides the major binding sites for the ATP molecule, while the C-terminal lobe has the major binding sites for the peptide/protein substrate.

The smaller N-terminal lobe (N-lobe, see Figure 1.2 and Figure 1.3) is an essential part of the ATP-binding mechanism. Structurally, is dominated by a five-stranded antiparallel β-sheet

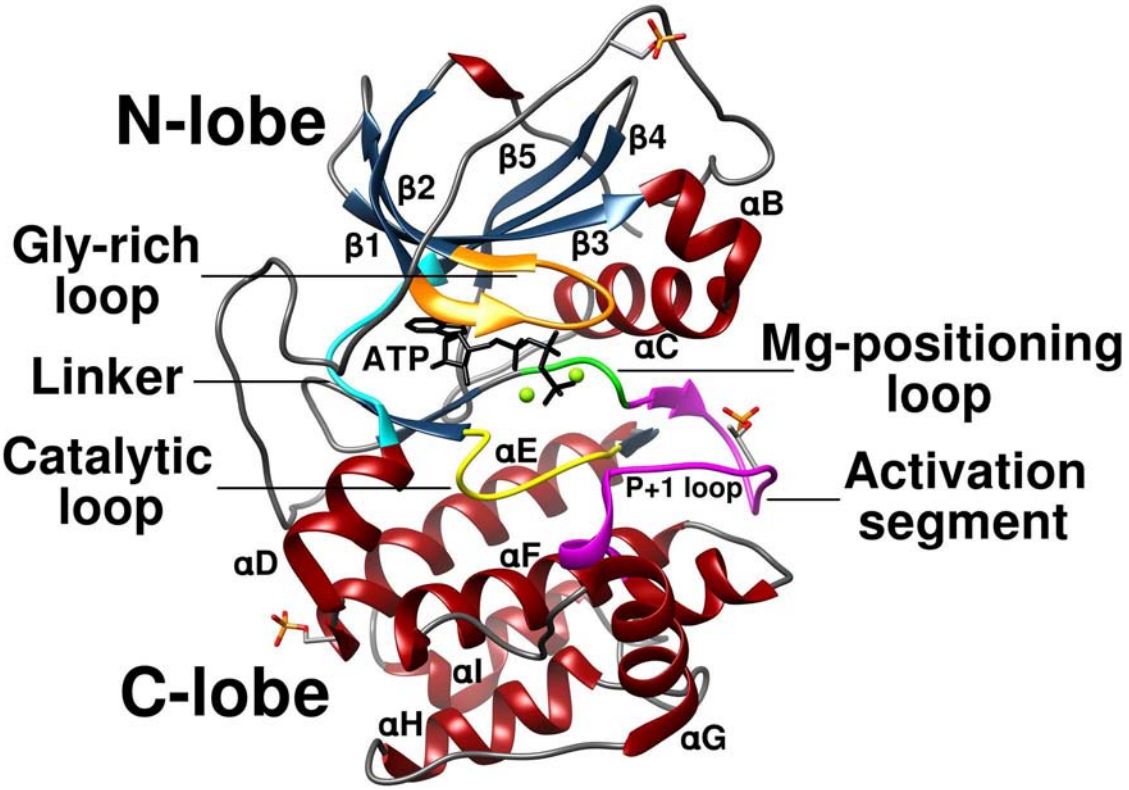

Figure 1.2. Structure of the conserved protein kinase catalytic core with its characteristic bilobal fold. The N-terminal lobe (N-lobe) contains five β strands (1 through 5) and a universally conserved αC-helix. The C-terminal lobe (C-lobe) is mostly helical. An ATP molecule is bound to a deep solvent-hidden cleft between the lobes. Major structurally and catalytically important loops and motifs are highlighted with specific colors. Three phosphorylated residues in template model (PDB code 4IAC[76]) are also shown.

coupled to a universally conserved αC-helix.[27] This helical subdomain, located between the β3 and β4 strands, is an essential regulatory and very dynamic feature of every protein kinase molecule. Moreover, the extended chain that links a variant motif to the first structural element of the N-lobe, the strand β1, anchors firmly the C-terminus.[77] The first two strands, β1 and β2, are joined by the characteristic Gly-rich loop, a hairpin structure that spans nine residues and comprises three glycine residues in a Leu49-Gly50-Thr51-Gly52-Ser53-Phe54-Gly55-Arg56-val57 sequence.[78] This loop folds over the nucleoside moiety of ATP, harboring its adenine ring with the two β-strands it connects, and is thought to help positioning the γ-phosphate for catalysis when its backbone tip is fully closed.[79] However, being the most flexible part of the N-lobe, it has been observed in recent crystallographic structures of reactive kinase ternary complexes that it does not always anchors the transferring γ-phosphate of ATP.[76,80] The Gly-rich loop end with a highly conserved Val57 that makes a hydrophobic contact to the base of ATP.[16] Regarding the β3-strand (residues 67-75), it contains the essential Lys72 residue that interacts with the α- and β- phosphate groups of ATP and couples to the conserved Glu91 residue in the αC-helix. This Lys72-Glu91 salt bridge is highly conserved through the entire protein kinase family, and is often considered as a hallmark of the activated state.[81] It can be established that the β1-β3 motif

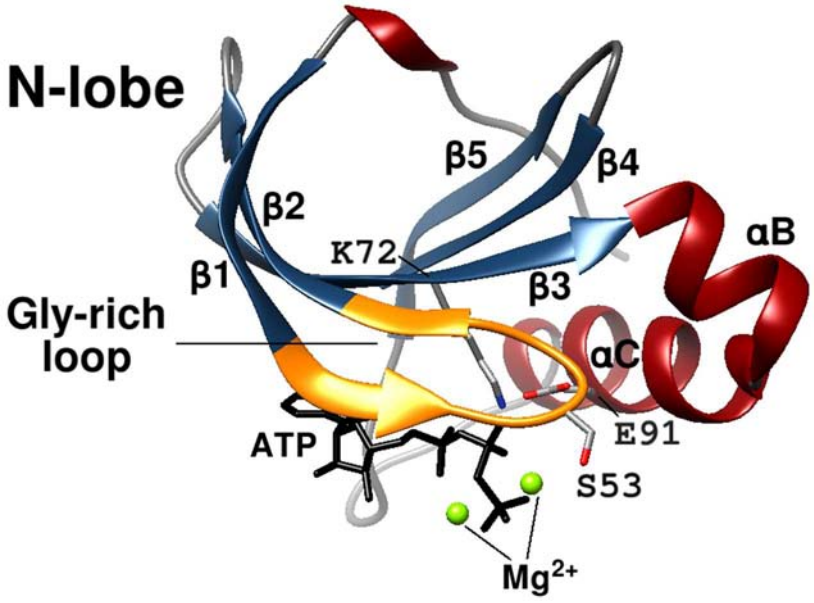

Figure 1.3. Structure of the N-terminal lobe (N-lobe). The Gly-rich loop covers the phosphorylated tale of ATP. Lys72 from β3 couples through hydrogen bonds the α- and β-phosphate groups from ATP, and Glu91 from the αC-helix.

or segment functions as a highly conserved nucleotide-positioning motif, which is then connected to the helical segment in the N-lobe containing αB- and αC-helices.

As mentioned above, in terms of sequence the αC-helix (residues 85 – 95) belongs to the N-lobe, however it actually occupies a strategically important position between the two lobes. It connects and holds together different segments of the enzyme, widely separated in the amino acid sequence, in a folded, active conformation, thus serving as a "signal integration motif".[26] Positioning the N-terminus of the αC-helix for efficient catalysis is one of the critical steps that must be achieved for the activation of a kinase, and the distance between the N-terminus of the αC-helix and the activation loop is a gauge that defines the so called open and closed conformations that are essential for catalysis.[12]

Strands β4 and β5 form another β hairpin, where the loop is variable. The two β hairpins and the middle strand β3 form an antiparallel twisted β sheet. Strand β5 is followed by the linker region which contains two highly conserved glycine residues and is the only main chain entry point into the C-terminal lobe in the conserved core. Except for the αB-helix, the secondary structure elements of the N-lobe are conserved in all threonine/serine and tyrosine protein kinase structures.[3,22,82-83]

The larger C-terminal lobe (C-lobe) is mostly helical (see Figure 1.2 and Figure 1.4). In particular, it is composed of eight α helices and four short β strands (6-9).[17] The helical subdomain, which is extremely stable, forms the core of the kinase and also serves as a tethering surface for protein/peptide substrates. That is, it contributes significantly to substrate binding,

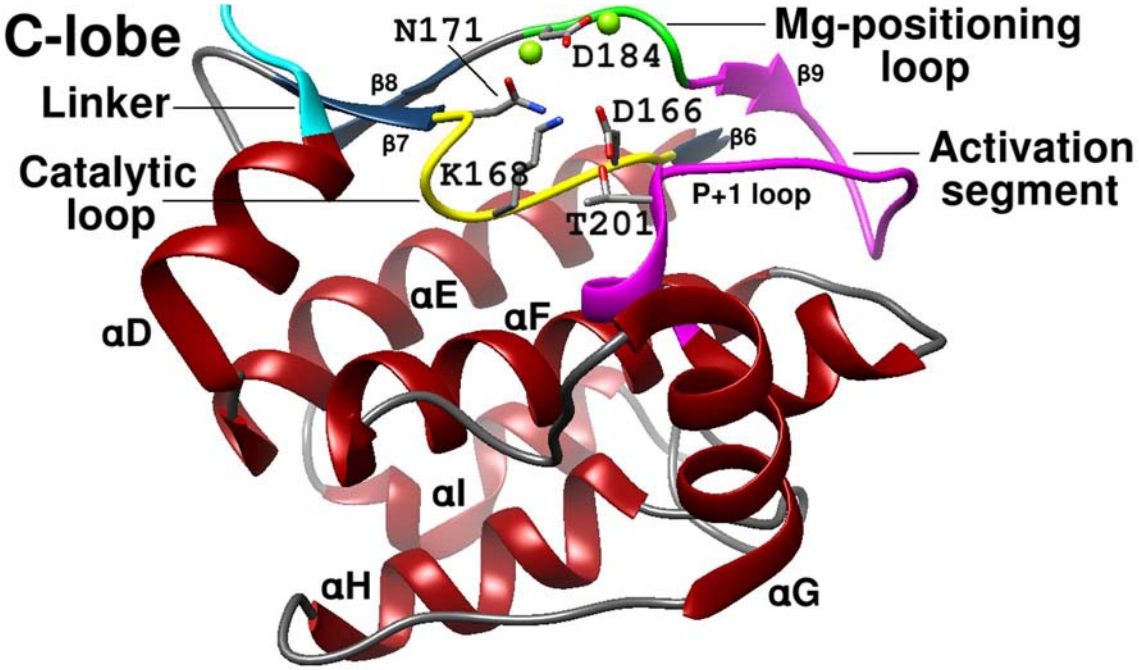

Figure 1.4. Structure of the C-terminal lobe (C-lobe). Catalytic and regulatory machinery is bound to the rigid helical core of the C-lobe. The P+1 loop accommodates the P+1 residue of the peptide substrate that is docked to the peptide-binding groove.

so, in general, the backbone of the core helices (D, E, F, and H) are well shielded from solvent, the exception being the αG-helix.[84] Resting on the helical core, to which is anchored through hydrophobic residues, is the four-stranded β sheet. These short β strands contain several structural elements essential for all protein kinases, particularly, much of the catalytic machinery associated with γ-phosphate transfer from ATP to the protein substrate, and form the bottom surface of the active site. In particular, between β-strands 6 and 7 lies the catalytic loop (residues 166 – 171), which contains a set of catalytically important conserved residues: Asp166 and Lys168, directly involved in the phosphoryl-transfer reaction, and Asn171, involved in one Mg^{2+} ion binding site. Between β-strands 8 and 9, referred to as the magnesium-positioning loop (residues 184 – 187), is the Asp-Phe-Gly (DFG) motif, where the conserved Asp184 is critical for recognizing the ATP-bound Mg^{2+} ions.[12,85] Finally, the activation segment extends from the DFG motif to the beginning of the αF-helix (residues 188 – 205). Its length and sequence are the most variable part of the kinase core, and this segment is responsible for precisely turning the eukaryotic protein kinases on and off, mainly through the phosphorylation state of a Ser/Thr residue.[16]

As it can be inferred from the preceding structural description (and from the examination of Figure 1.2), the active site of protein kinases is located at the interface between the small N-lobe and large C-lobe, forming a deep cleft where the adenine ring of ATP is bound and shaping a ledge for protein/peptide substrate docking.[16] Regarding the latter, to ensure the essential

integrity of signal transduction, kinases must be very precise and sufficiently specific to act only on a defined subset of cellular targets. To achieve such precision of specificity, the side chains of the bound protein/peptide substrate are located in specific pockets, or subsites, which are shared between the two lobes, so the chemistry of the residue side chains in each pocket provides the molecular basis of the specificity of a protein kinase.[86] That is, protein kinases poorly phosphorylate free amino acids because they rely partly on local residues for high affinity, phosphorylating peptide regions based on the residues immediately flanking the phosphorylation site (P-site).[21] Accordingly, the local residues define a consensus sequence, which have been determined for most protein kinases using peptide variants in either a manual screening[87-89] or a random peptide library approach.[90-92] In general, amino acids that are approximately four residues or less from the P-site in either the N- (P-) or C-terminal (P+) directions are the most significant for directing phosphoryl-transfer. Interestingly, although the consensus sequence varies depending on the phylogeny, the class and the cellular location of the protein kinase, all protein kinases bind the protein/peptide substrate in an analogous manner: in an extended conformation and with the same orientation of the substrate protein/peptide chain relative to the protein kinase catalytic domain.[93]

One of the most intriguing aspects of protein kinases has to do with the structural features that regulate the assembly of an active protein kinase core. Very recently, the search for spatially conserved residues (by means of a method referred to as local spatial pattern alignment) when comparing many protein kinase structures, has revealed an internal architecture that enables distal parts of the enzyme to be linked by non-consecutive conserved hydrophobic residues.[94] They cannot be identified from sequence alone so they are thought of as hydrophobic "spines" that are assembled only in the active conformation of the kinase.[95] In particular, two hydrophobic spines going across and connecting both structural lobes, one regulatory (R-spine) and one catalytic (C-spine), and a single hydrophobic helix that spans the large C-lobe (αF-helix), define the active protein kinase conformation and enable protein kinases to bind efficiently to cofactors and substrates (in Figure 1.5, see internal architecture of the catalytically active subunit of a model protein kinase and the residues that constitute the hydrophobic R- and C-spines).[18,70]

The R-spine comprises two residues from the N-lobe: Leu106 at the beginning of the β4 strand and Leu91 at the C-terminus of the αC-helix; and two from the C-lobe: Phe185 from the DGF motif of the activation loop and Tyr164 from the catalytic loop, with the backbone of the latter anchored to the αF-helix through a conserved Asp220, which then serves as the base of the R-spine.[12] That is, the assembled R-spine brings together all of the functional motifs that are essential for transferring the γ-phosphate group from ATP to a tethered protein substrate. This

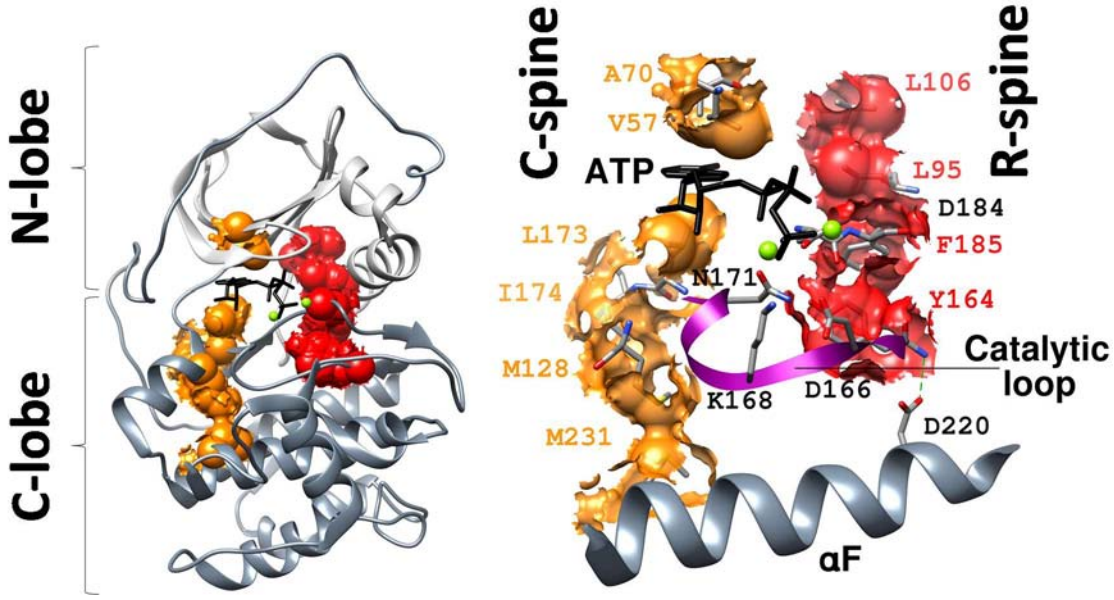

Figure 1.5. The comparison of many X-ray crystallographic structures has allowed the definition of the core hydrophobic spine architecture that is shared by all eukaryotic protein kinases. Thus, two hydrophobic spines (one catalytic, C, and one regulatory, R) define the active protein kinase conformation. The C-spine is completed by the adenine ring of bound ATP whereas the R-spine is typically dynamically assembled following phosphorylation of the activation loop. Both spines are anchored to the unusual hydrophobic αF-helix located in the middle of the C-lobe. They span the N- and C-lobes of the kinase core, providing a firm but flexible connection between them. The C-spine and R-spine residues are shown as orange and red surfaces, respectively.

includes the G-loop (which anchors the ATP cofactor), the catalytic loop, the DFG motif fused to the activation loop (in addition, assembly of the R-spine is typically facilitated by phosphorylation of the activation loop), and the αC-helix.[61] However, because the middle part of this hydrophobic motif, the αC-helix and the activation loop, can be very mobile,[26,72] it can be dynamically assembled or disassembled, thereby regulating the protein kinase activity and thus designated as a regulatory spine.[16]

Regarding the C-spine, what distinguishes it from the R-spine is that it is completed by the adenine ring of ATP. That is, ATP binding positions the C- and N-lobes so that the catalytic residues are aligned optimally for catalysis, and this hydrophobic spine was thus termed catalytic.[16] Specifically, there are two C-spine residues from the N-lobe, Val57 in β2 and Ala70 from β3, that are docked directly onto the adenine ring of ATP, whereas in the C-lobe it is Leu173 that docks directly onto the adenine ring. Leu173 lies in the middle of β7 and is always flanked by two hydrophobic residues, Leu172 and Leu174. These two residues interact with a hydrophobic residue from the αD-helix, Met128, which, in turn, is bound to the αF-helix trough Leu227 and Met231.[12] Furthermore, correlation analysis of multiple-microsecond duration molecular dynamics (MD) simulations have identified dynamic communities, structurally contiguous regions of active protein kinases that exhibit backbone correlated motions and

complements the identification of the hydrophobic C- and R-spines.[71] Most of the communities (40-60 residues) were associated with a particular protein kinase function or a regulatory mechanism, and also were sensitive to the presence of different ligands. Additionally, well-known motifs based on sequence and secondary structure were often split into different communities, which allowed the interpretation of long-distance allosteric coupling between different sites on protein kinases.[12]

On the other hand, protein kinases are metalloenzymes that were thought to require one or two divalent metal ions to bind in the active site for activity, particularly for nucleotide binding.[96] Although several divalent alkali earth and transition metals have proved to be effective in supporting phosphotransferase activity,[76,97] at physiological settings ATP exists as a complex with one Mg^{2+} ion (highest binding constant considering the most common metal ions in a prototype cell). The Mg^{2+} ion is the most abundant and available divalent metal ion in living cells, so $MgATP^{2-}$ (hereinafter abbreviated as MgATP) is considered the actual cofactor of most protein kinases.[98-99] No ordered Mg^{2+} ions had been identified in protein kinase crystal structures in the absence of bound ATP (*e.g.* Protein Kinase A binds Mn^{2+} weakly, $K_D > 1$ mM, in the absence of a nucleotide).[99] The Mg^{2+} ions were considered critical for the binding of anionic nucleotide phosphates because the active site region that surrounds the ATP phosphates is also strongly negatively charged. Thus, Mg^{2+} ions could neutralize the electrostatic repulsion by forming bridging contacts between the phosphorylated tail of ATP and the electronegative and negatively charged protein functional groups within the active site.[96] There are additional effects owing to magnesium ions that are not fully understood. Some kinases have been erroneously described as possessing both essential and inhibitory divalent metal binding sites,[100] or thought to be unable to catalyze phosphoryl-transfer with a single or even zero magnesium or divalent ions.[21] However, as will be discussed further below in more detail, the understanding regarding the role of metal ions in the general catalytic cycle and in the phosphoryl-transfer chemical step of protein kinases has been revised recently by means of several X-ray crystallographic studies of diverse protein kinases.[76,101-105]

1.3. The cAMP-dependent protein kinase paradigm.

Among over 2000 unique eukaryotic protein kinases, cyclic-adenosine monophosphate (cAMP)-dependent protein kinase (PKA), that phosphorylates the side chain of serine/threonine residues, has taken a main role. PKA was the first protein kinase to be analyzed[106] and its crystallographic structure the first to be solved.[93,107] Now, besides the simplicity of its mechanism of activation,[108-109] there is the consensus that PKA is the best characterized member,[109] and, therefore, is considered as a frame of reference for every protein kinase and a

prototype for the catalytic core of the whole family.[26,62,95,100,109-112]

Regarding its role, PKA is ubiquitous in every mammalian cell (it is also conserved in fungi and even in single-cell pathogens, although is absent in the plan phyla) and functions both in the cytoplasm and in the nucleus to regulate a plethora of cell physiology events, including memory, differentiation, proliferation, and metabolism.[23] However, this kinase do not usually function in isolation; instead, it is part of larger signaling systems. In mammals, such "PKA signaling system" comprises four genes that encode functionally non-redundant regulatory subunits and three genes that encode catalytic subunit, and being a regulatory enzyme, PKA is highly regulated itself. The inactive PKA holoenzyme is a heterotetramer (R_2C_2), composed of a regulatory homodimeric (R_2) and two catalytic (C) monomeric subunits (see Figure 1.6A). The two main subfamilies of PKA are determined by the R subunit type. The type RI subunits (α and β) are not autophosphorylated by C and have an absolute requirement for MgATP to form a tight complex with the C subunit. The type RII subunits (α and β), in contrast, are autophosphorylated and do not require MgATP to form a holoenzyme complex.[108-109,112]

Before describing the activation mechanism of PKA, it should be mentioned that about the same time as the discovery of protein phosphorylation, Sutherland discovered that cAMP was a second messenger for hormone action in mammalian cells.[113] In the subsequent years, G protein-coupled receptors (GPCRs) were discovered as a mechanism for transducing the information from the hormone receptor to adenylyl cyclases.[114] The characterization of PKA,[106] and later the discovery of its regulatory subunits and the concomitant elucidation of the mechanism for its regulation by cAMP,[115-117] which is produced by adenylyl cyclase, brought together these two major signaling mechanisms. Accordingly, it is now recognized that like protein kinases, GPCRs are widespread biological switches that regulate several events in eukaryotic cells.[23]

Regarding the inactive PKA holoenzymes, these are localized to specific sites in the cell by scaffold proteins, the best known being the A kinase anchoring proteins (AKAPs, see 1.6A).[118] These proteins constitute a diverse PKA signaling system that exists in every mammalian cell, provide a mechanism for specificity (the system is defined by what GPCRs, PKAs and AKAPs are expressed in each cell). Therefore, in response to a variety of stimuli -among which stands out the adrenergic stimulation- and almost independently on the cell type (*i.e.* the morphology and phenotype), cAMP is generated in response to the activation of GPCRs through the activation of Gαs, the activating G-protein subunit that stimulates adenylyl cyclase (see Figure 1.6B).[119] Being the R subunits of PKA the primary receptors for cAMP in eukaryotic cells (each of the regulatory subunits contains two contiguous cyclic nucleotide-binding domains),[62] when four cAMP molecules bind cooperatively to R_2, a five order of magnitude decrease in the affinity of R for C

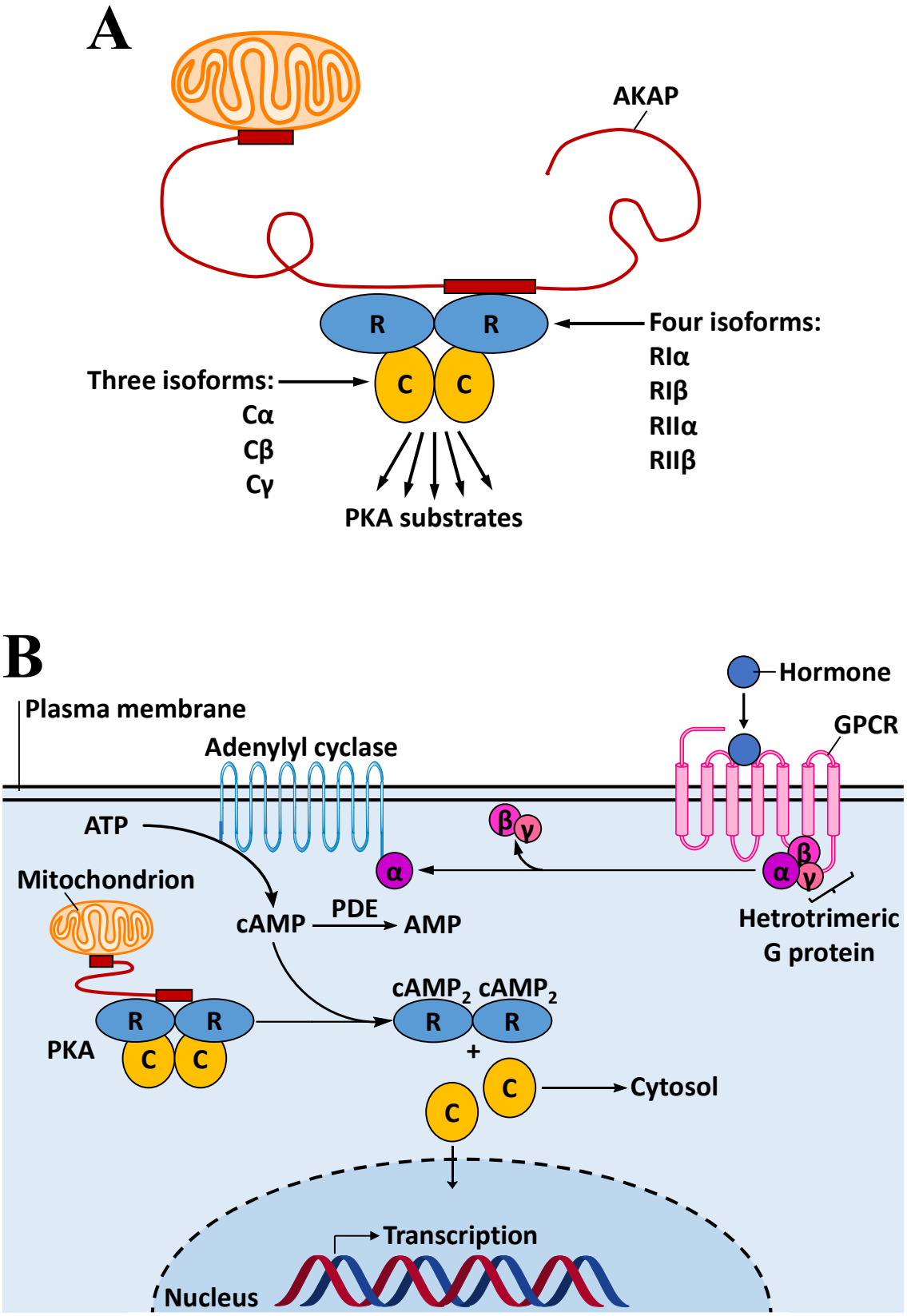

Figure 1.6. (**A**) The PKA signaling system includes the regulatory (R) and catalytic (C) subunits, PKA substrates and targeting proteins, such as A kinase anchoring proteins (AKAPs); the hallmark motif in AKAPs is an amphipathic helix that docks with high affinity to a PKA regulatory subunit,[120] targeting PKA to specific sites in the cell in close proximity to dedicated substrates. **(B)** Schematic representation for the role of G protein-coupled receptors (GPCRs) and adenylyl cyclase in the generation of cAMP as a hormone second messenger in eukaryotic cells, and for the activation mechanism of PKA under control of cAMP.

is promoted due a change of the domain tertiary structure.[121] Thus, under physiological conditions, an increase in cAMP concentration and its consequent binding to the regulatory subunit dimer, leads to the dissociation of the tetramer into a $R_2(cAMP)_4$ dimer and two active C subuints.[122-123] Accordingly, the regulatory R subunit defines the mechanism whereby the second messenger cAMP translates an extracellular signal into an intracellular biological response. Once the two catalytic subunits become dissociated they work independently, and are refered to individually as PKAc, which represents the catalytically active subunit best characterized, structurally and kinetically (both *in vitro* and *in vivo*), among protein kinases.[124]

The *apo* form, the catalytically competent form of PKAc without ATP or substrate bound, constitutes one domain approximately 350 amino acids long within the characteristic bilobal structure of the kinase. The highly conserved kinase core in the bean-shaped fold for PKAc encompasses residues 40-300.[26,112,125] The small N-lobe involves residues 40-126, and the large C-lobe residues 127-300.[126]

As a glimpse regarding the active site of PKAc (a more detailed description is given further below), it should be mentioned that PKAc recognizes and phosphorylates the consensus recognition peptide R-R-X-S/T-Z, which is present in hundreds of cellular protein substrates and physiological inhibitors (in the latter case, generally with A, or Alanine, instead of S/T).[87,89] Specifically, S/T, or serine/threonine, is the phosphorylation (P) site, the P-2 and P-3 positions are occupied by two arginines (R, a positively charged residue), X stands for any residue since there are few constraints for the P-1 site, and Z (P+1) is a large hydrophobic residue.[73] This consensus site peptide is sufficient to convey low affinity binding in the μM range and substitution of either the P-2 or P-3 arginine with uncharged residues leads to poor substrates. Actually, a standard peptide substrate for PKAc, based on this consensus sequence, is Kemptide (sequence LRRASLG).[127] It was designed in 1977 showing kinetic constants comparable to those of native protein substrates.[128-130] Very recently, the Kemptide substrate has been used again to prove by MD simulations its cooperative binding with ATP to PKAc,[131] and also in single molecule experiments to prove the conformational variability of the PKAc-Mg_2ATP-Kemptide complex.[132]

It is worth mentioning that the regulatory subunits, R, have a substrate-like motif that resembles the consensus site peptide and binds to the active site cleft, so they are competitive inhibitors of protein substrates. In addition, there is another class of physiological inhibitors of PKAc, the heat stable protein kinase inhibitors (PKIs), which were discovered almost simultaneously with PKA because they were copurified as a contaminate.[106] Like the R subunits, the PKIs bind with high affinity (< 1 nM) to free PKAc, and they also share an inhibitor site that resembles a PKA substrate (PKIs and the RI subunits have a pseudosubstrate inhibitor site, while the RII subunits have a true phosphorylation site).[133] That is, PKI is a potent endogenous inhibitor

of PKA.[62] PKI also contains near its carboxyl-terminus a leucine rich region that has been shown to function as a nuclear export signal when PKI is bound to PKA.[134] Consequently, PKI is capable of freely entering the nucleus and actively shuttling the catalytic subunit of PKA back to the cytoplasm, where PKA regulatory subunits are located. By facilitating nuclear export of PKA, PKI is thought to affect the kinetics and/or extent of PKA activity in the nucleus. PKI may, for example, terminate the transcriptional regulation by PKA of specific genes and rapidly reset the PKA system for subsequent gene induction responses.[135-136]

1.3.1. The PKAc catalytic cycle.

Over the past two decades, extensive efforts have been conducted to understand the catalytic cycle of PKAc using several experimental and theoretical approaches. So far, the sequence of events and the kinetics of each individual step comprising the overall phosphorylation process have been established, making the PKAc one of the best understood kinases. Generally speaking, the catalytic cycle of an active kinase is a multistep process involving significant structural fluctuations that take place towards catalysis and product release.[127,137-139] It comprises nucleotide binding, substrate recognition and positioning, the chemical step of phosphoryl-transfer, and finally product release (ADP and phosphorylated substrate).[140]

The study of the molecular and dynamic features related with the catalytic cycle has attracted a great deal of attention over the years, with crystallographic studies providing a wealth of information on how the protein kinases function.[26,43,95] Specifically, many crystal structures[120-121,134] have defined the wide range of conformations adopted by PKAc, while NMR data[44] has demonstrated that the dynamic structural changes involve in going from one conformation to another contribute to the regulation of the activity of PKAc.[123-124,141] In this regard, a number of crystallographic structures of the *apo* form, of complexes of PKAc with nucleotide or substrate analogs (binary form), and of nucleotide-substrate/inhibitor-bound PKAc complexes (ternary form) have been reported.[77,101,142-144] The ternary structures are experimental snapshots of the phosphoryl-transfer process, and a comparison of those structures with binary complexes and *apo* crystals has revealed the major conformational states of PKAc along the catalytic cycle. Such states differ in the relative orientation of the N- and C-lobes and ultimately involve the narrowing or closing of the active site cleft, therefore they are termed “open”, “intermediate”, and “closed”.[12,95]

In particular, the open conformation adopts the largest distance between the N- and C-lobe and was observed with the *apo* form of PKAc.[143-144] Upon nucleotide or substrate binding, PKAc transitions to an intermediate, partially closed, state. Both steady-state kinetics and isotope partitioning experiments demonstrated that PKAc binds ATP and peptide substrates

randomly, although initial binding of ATP is preferred.[145] A representative intermediate conformation was observed when PKAc was crystallized with adenosine;[77] however, there is clearly an ensemble of intermediate conformations.[146] Finally, the closed conformation displays tight packing between the N- and the C-lobe, which causes a closing of the active site cleft and the exclusion of water; this conformation is typically seen when all components for the reaction are in place.[26,110,147] Dynamic analyses based on recent NMR measurements and MD simulations have shown that during turnover PKAc interconverts between these conformational states with the nucleotide acting as a dynamic and allosteric activator; that is, the nucleotide acts to dynamically couple the C-lobe and the N-lobe making it "committed" to catalysis, thereby establishing a relationship between the PKAc conformational fluctuations and its turnover rate.[44-45,72,148-149]

Three specific distances have been used to distinguish the conformational states of PKAc: the Glu170-Tyr330 distance measures the distance of the C-terminal tail to the front of the active site; the interaction distance between His87 and phospho-Thr197 at the edge of the active site measures the position of the αC-helix relative to the large lobe; and the Ser53-Gly186 distance measures the opening and closing of the Gly-rich loop at the top of the active site.[77,81,150] In accordance with experimental observations, MD trajectories[151] initiated with closed PKAc-Mg_2ATP-PKI (inhibitor) conformation, have simulated the opening of the active site cleft of PKAc when both ligands are removed, regardless of the kinase phosphorylation state. Those simulations also show that the most stable state is the closed ternary complex, whereas all the other systems with one or two ligands removed visit different conformations along the MD trajectory.

Moreover, NMR measurements together with thermodynamic data and Principal Components Analysis carried out on MD simulations of PKAc in water using the apo, binary, and ternary complexes (in this case, containing the native substrate PLN_{1-20} or the inhibitor PKI) have shown that PKAc has an intrinsic dynamic nature behaving as a regulated molecular switch.[43-45] Those studies have been used to characterize the conformational dynamic states of PKAc along its catalytic cycle, describing the free-energy landscape for PKAc in which the *apo* form would correspond to the so-called dynamically uncommitted state, where motion are present but not on a time scale relevant for turnover. In contrast, the nucleotide-bound or the Michaelis complex with the substrate, would correspond to dynamically committed states, where motions are synchronous with the rate-limiting state of enzyme turnover. Although these motions are slower than the chemical step (*i.e.* the phosphoryl-transfer), they help to position the substrate for catalysis giving access to those enzyme conformations that facilitate turnover. Finally, the inhibited complexes have been characterized as dynamically quenched states where the enzyme

dynamics are hindered. This result may explain, according to the authors, why most crystal structures of protein kinases have been more accessible in their inhibited forms while substrate bound forms have been elusive to such analysis.

Undoubtedly, the chemical step happens only in the fully closed conformation of PKAc after the protein or peptide substrate binds to produce a ternary complex, and the release of products is concurrent with the enzyme returning to the open conformation.[44,152] However, single molecule electronic measurements of PKAc catalysis indicate that not every open-close conformational cycle results in the phosphorylation reaction and/or product release, which can partially explain the relatively low catalytic efficiency of the enzyme and the assigned role of allosteric macromolecular switch.[132] That is, the bulk kinetic values, such as the k_{cat}, should not be correlated with the time it takes each individual molecule to go through a particular conformational change or a chemical reaction.

The kinetics of the phosphoryl-transfer reaction catalyzed by protein kinases are also well characterized, which has improved our understanding of the progression of the catalytic cycle progression. Pre-steady-state and steady-state kinetics of PKAc showed that phosphoryl-transfer of the γ-phosphate of ATP onto the substrate is a very rapid event, being other processes which govern the rate of the reaction.[21] Specifically, the PKAc phosphoryl-transfer step is fast, >500 s^{-1}, while the product turnover rate is at least an order of magnitude slower; k_{cat} is ≈20 s^{-1}.[130] Additionally, solvent viscosity effect studies of the fully activated states of many protein kinases have also shown that product release is rate-limiting.[21,84,129,153-155] These data also suggested that one of the two Mg^{2+} ions reversibly binds and that its release is coupled to conformational changes that facilitate release of the product. Therefore, ADP release is one of the most important steps in the PKA catalytic cycle and the reaction turnover is highly influenced by the magnesium ions. Besides, although the magnesium ions charge neutralization and stabilization is an efficient mechanism for activating the catalyzed phosphoryl-transfer, the two divalent metals together unavoidably limit or suppress the rate of ADP release, then showing a different behavior at different steps of the catalytic cycle.[103-104,146]

1.3.2. The role of divalent metal ions.

There are two metal binding sites in PKAc, the final coordination of which depends on the bound nucleotide.[156] In general, the rate-limiting steps are strongly regulated by magnesium ions, considered the predominant protein kinase cofactor under physiological conditions.[96] From the first crystallographic structures with ATP, one metal-binding site was considered activity-sufficient when occupied by a high affinity Mg^{2+} ion, then termed Mg1 and activating. Mg1 is coordinated by the β-and γ-phosphates of ATP, the side chain of the invariant residue Asp184 in

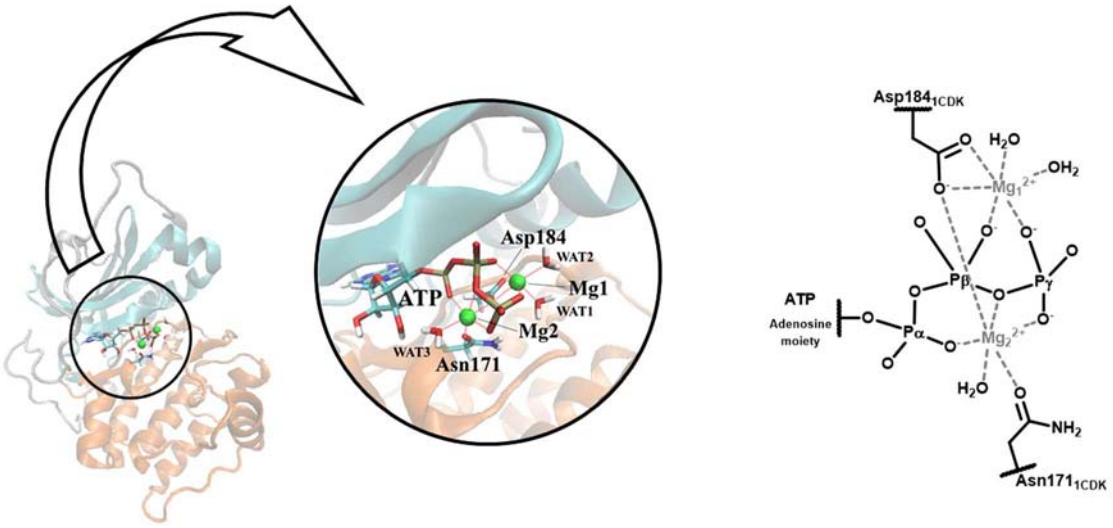

Figure 1.7. Schematic representation of the binary PKAc-Mg_2ATP complex. The black circle highlights the position of the solvent-hidden nucleotide and metal binding sites. The inset shows, in atomistic rendering and licorice style, a close view of the coordination sphere of the magnesium ions with the phosphorylated tale of the nucleotide, Asp184 from the DFG-motif, Asn171 in the catalytic loop, and water molecules within the active site cleft. A scheme of the octahedral coordination of both magnesium ions is also shown.

bidentate manner, and two water molecules to fulfill an octahedral coordination state (see Figure 1.7). The other metal binding site, when occupied by a second Mg^{2+} ion and initially termed Mg2 and inhibiting, is octahedrically coordinated also by the α- and γ-phosphates of ATP, the side chains of Asn171, one oxygen atom of Asp184, and one water molecule.[96,156] The active site water molecules that help to coordinate the magnesium ions were shown to be highly conserved among many protein kinases likely due to conservation of key active site residues.[150]

In some PKAc crystal structures only one metal ion is present, but the γ-phosphate in these structures does not seem to be ideally oriented for phosphoryl-transfer.[157] In other kinases, two metal ions are bound, and recently a comprehensive analysis of cyclin dependent kinase 2 (CDK2) showed that two metal ions are required for the phosphoryl-transfer reaction.[103-104] Given the highly conserved nature of the active site residues of protein kinases, it is predicted that all kinases will likely utilize two metal ions, but the details of catalysis and product release may be regulated differently in different kinases.[102] In this regard, the multiple and complex roles of the magnesium ions provide an explanation of why some of protein kinases have been observed to be stimulated[158-159] or suppressed[96,103-104] by increases in magnesium concentration, while others show no effect in the presence of a magnesium excess.[21]

The nomenclature Mg1 and Mg2, and the activating/inhibiting terminology used to describe the magnesium ions arose from two experimental observations. First, an older low-resolution crystal structure reported electron density for mostly one magnesium ion and very little for the other when PKAc was crystallized with a low concentration of magnesium;[142] the

ion that showed more electron density was thus termed Mg1 because it was thought to bind first or more strongly with ATP, and then to be the most important ion for phosphoryl-transfer. Accordingly, the other ion was termed Mg2. Second, the fact that low concentrations of magnesium (0.5 mM) yield higher k_{cat} (or turnover rate) values than high magnesium concentrations (10 mM), suggested and inhibitory effect attributed to the second magnesium ion to bind; namely, Mg2.[66,92] However, as Adams and coworkers demonstrated later for different PKAc + substrate models,[21,140,160] both, the MgATP binding and the MgADP release are the two potentially catalytic rate-limiting steps. They observed that the higher magnesium concentration increases the affinity to both nucleotide species involved, that is, ATP (lower K_{ATP}), and ADP (lower $k_{ADP\text{-}release}$), but apparently had no effect on the rate of the chemical step. That is, the magnesium ion terminology is misleading because binding two magnesium ions does not actually influence the rate of phosphoryl-transfer but, instead, affects the rate of ADP release which is the rate-limiting step at high magnesium concentrations. Summarizing, the two magnesium ions were thought to bind with equal affinity to ADP but at the low magnesium concentration the turnover rate is governed partially by ADP release and partially by conformational changes that occur before and after phosphoryl-transfer,[140,161-162] while at high magnesium ion concentrations the PKAc reaction rate is strictly governed by ADP release and the conformational changes that are associated with it.[96,128,163]

Recent studies suggest that the designation of magnesium ion most likely does not correlate with the order in which they bind. Specifically, a crystal structure of PKAc obtained under low magnesium concentration showed electron density for only the magnesium ion binding site corresponding to Mg2.[164] Furthermore, other protein kinases such as CDK2 often crystallize with just one magnesium ion, and the ion observed is analogous to Mg2.[104] That is, under that particular conditions, at most a single divalent ion bounds with ATP occupying the site labeled Mg2. These studies also revealed that the open conformation of the *apo* form of the protein kinase closes just partially in response to the formation of the binary PKAc-MgATP complex, thereby shaping an active site primed for substrate binding in the intermediate conformation (the proposed catalytic cycle of kinases is schematized in Figure 1.8). This, in turn, indicates that the intermediate conformation evolves to the closed conformation essential for chemical catalysis with substrate (or inhibitor) binding.[26,83]

Also recently, a transition state structure of CDK2 crystallized at high magnesium concentrations showed a second Mg^{2+} ion bound at the site labeled Mg1.[103] The active site with the ATP and two Mg^{2+} ions bound revealed to be conformationally distinct from that with only Mg2ATP bound. Specifically, besides confirming that Mg2 binds along with ATP first, the comparison of these structures showed that the subsequent binding of Mg1 helps to positioning

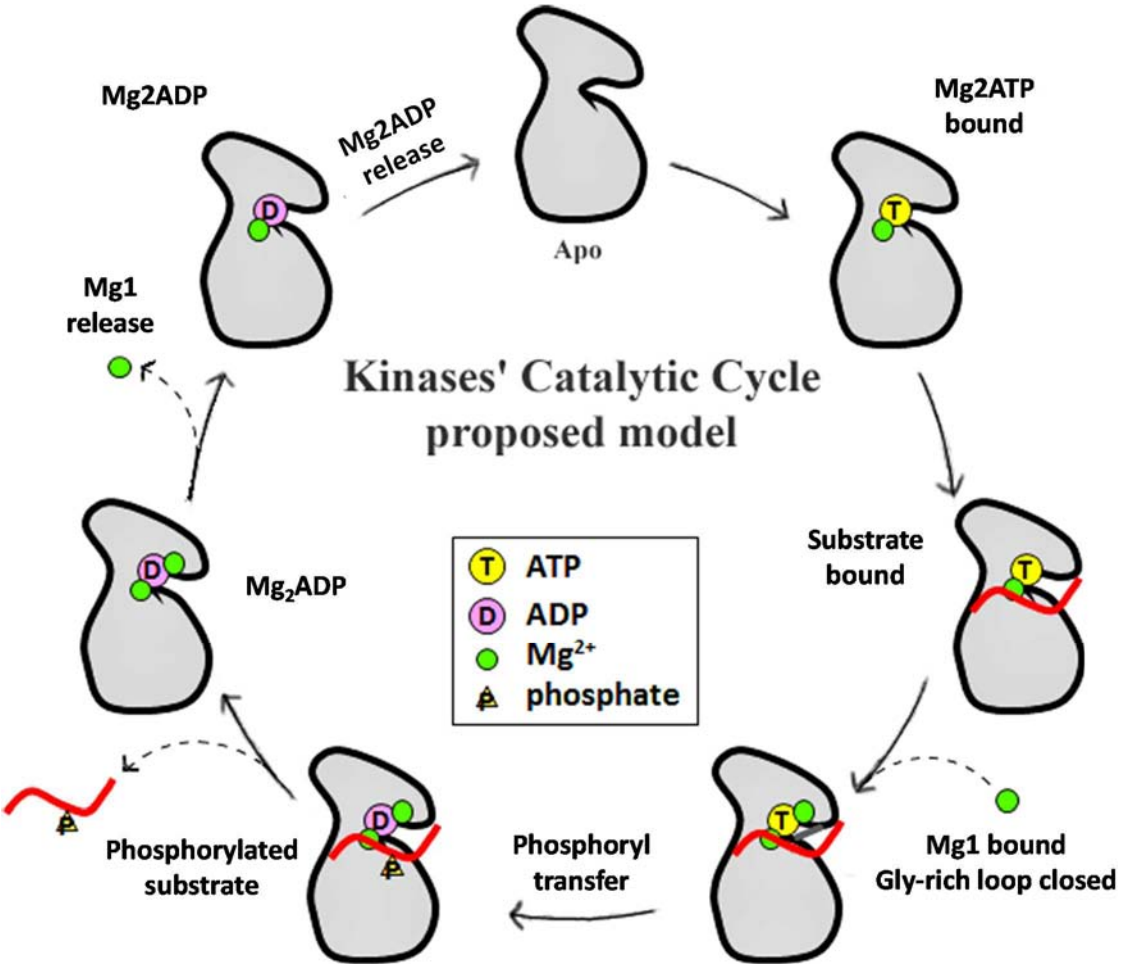

Figure 1.8. The sequence of events in the proposed or classic model for the catalytic cycle of protein kinases at roughly physiological conditions are: first, Mg2ATP and protein substrates bind; then Mg1 binds, closing the Gly-rich loop (Michaelis complex) and promoting phosphoryl-transfer (transition state); next, with physiological substrates, the phosphorylated protein is released and the Gly-rich loop opens, resulting in the ADP2Mg state, after which Mg1 is released; finally, after Mg2ADP release, the *apo* protein kinase can bind Mg2ATP and protein substrate to star the catalytic cycle again.

the γ-phosphate group of ATP for transfer and facilitates the closing of the Gly-rich loop. That is, to achieve optimal catalysis of the phosphoryl-transfer step both magnesium ions should be simultaneously bound. Furthermore, although in some kinases the second magnesium ion may only bind transiently during the complete catalytic cycle, in general both magnesium ions are present in the active site immediately following the bond-forming and cleavage due the phosphoryl-transfer step, coordinating the ADP and the phosphorylated-protein product.[76,103,164] Computational studies also support greater involvement of Mg2 in chemical catalysis than Mg1.[165-167]

In particular, Kovalevsky and coworkers have recently solved two new X-ray crystallographic structures of ternary PKAc-Mg_2AMPPNP-SP20 complexes (where AMPPNP is adenosine-5'-(β,γ-imido)triphosphate, which is a generally nonhydrolyzable analog of ATP where the oxygen atom bridging the β- and γ-phosphates is replaced with a nitrogen;[168] and

SP20 corresponds to the 20 amino acid peptide substrate whose sequence (TTYADFIASGRTGRRASIHD) is based on the heat-stable endogenous protein kinase inhibitor PKI (5−24, sequence TTYADFIASGRTGRRNAIHD)[169-170] with two mutations that convert it from an inhibitor to a substrate (N20A, A21S)[73]) showing partial and total phosphoryl-transfer, respectively.[102] Those structures seem to indicate, according to the authors, that one of the magnesium ions could probably be expelled first from the active site after the completion of the phosphoryl-transfer step and the release of the phosphorylated substrate, but preceding ADP release. Accordingly, the second magnesium ion would remain bound with ADP, then expelled as an important part of the rate-limiting ADP release.[83,102] Khavrutskii *et al.*,[163] Kovalevsky *et al*.,[164] and Jacobsen *et al.*,[103] in separate studies of reaction progression by PKAc and CDK2, besides showing that release of ADP from the kinase catalytic core with two Mg^{2+} ions bound is so strongly unfavorable as to be nearly impossible, they identify Mg2 as the ion that likely remains in the active site following phosphoryl-transfer. That is, they suggested that the energetically preferred reaction pathway for product turnover corresponds to Mg1 being lost prior to the release of Mg2ADP (see Figure 1.8).

More recently, Bastidas *et al*.[146] have reported the MgADP bound structure of the myristylated PKAc, where the ADP binds the active site with only one magnesium ion corresponding to Mg2. This structure, besides demonstrating that Mg2 may be the more stably bound ion, allowed the authors to highlight the conformational changes by means of which the Mg2ADP release likely proceeds. Interestingly, the ADP bound structure is reported to adopt a conformation that does not conform the previously characterized open, intermediate, or closed states. That is because the C-terminal tail (C-terminus) and the Gly-rich loop are more closed than in the open state adopted in the *apo* structure but are also much more open than the intermediate or closed conformations. This structure then provides evidence of how the reaction may proceed in PKAc and kinases in general. Thus, after the phosphoryl-transfer step, the phosphorylated substrate and Mg1 are released, and its departure may be an important step that precedes ADP release due the destabilization of ADP binding and the opening of the active site cleft trough rising of the Gly-rich loop and disengagement of the C-terminal tail. This uncoupling of the C-terminus from the Gly-rich loop and its coordinated motions away from the active site destabilizes in turn the ADP binding, facilitating its release. That is, the ADP bound structure provides evidence about the progression of the phosphoryl-transfer reaction and turnover in PKAc and kinases in general, and is consistent with the forementioned reports suggesting a general pathway in which Mg1 is released following the phosphoryl-transfer step but before the Mg2ADP release. Given that the binding of a second Mg^{2+} ion increases the protein kinase binding affinity to both ATP and ADP, but only a single Mg^{2+} ion is required for

ADP to remain bound, this sequence of events may explain the slower turnover rate at high magnesium concentrations due to continued occupancy of both metal binding sites following phosphoryl-transfer. Finally, whether the phosphorylated substrate is released before the Mg1 or whether the Mg1 leaves the active site first, seems to depend on the nature of the substrate: with high affinity peptides, it is the Mg1 that is released first; in contrast, with physiological substrates, it is likely that the phosphorylated protein will leave first.

Interestingly, an X-ray crystallographic study by Kovalevsky and coworkers has provided evidence that PKAc is active in the presence of other divalent metal cations, rather than just with the previously assumed physiological Mg^{2+} cofactor. They observed that almost all divalent alkali earth metals support the phosphoryl-transfer catalyzed by PKAc in complexes with SP20. Specifically, they found, in their corresponding crystal structure, Mg^{2+}, Ca^{2+}, Sr^{2+}, and Ba^{2+} bound in the active site along with trapped products of the phosphoryl-transfer chemical reaction, ADP and the SP20 peptide phosphorylated at Ser21. It is worth noting that the ability to trap the products was attributed to the unique binding properties of the high-affinity SP20 peptide substrate used. These results contradicted early kinetic measurements showing no PKAc activity in the presence of Ca^{2+} or Sr^{2+} using Kemptide peptide substrate, and no nucleotide binding when Ba^{2+} was present.[97] The Kovalevsky and coworkers results challenge the conventional views about the roles metals play in the chemistry of protein kinase and raise the important possibility that Ca^{2+} may also be a physiological cofactor. From a computational chemistry standpoint, these results point to the need to theoretically study the phosphoryl-transfer catalyzed by PKAc with different divalent alkali earth metal cations.

Kovalevsky and coworkers have also reported single-turnover enzyme activity measurements with [γ-^{32}P]ATP which proved that PKAc can bind ATP and transfer the γ-phosphoryl group to Ser21 of SP20 in the absence of divalent ions.[101] Thus, their results conclusively demonstrate that catalyzed phosphoryl-transfer can take place without divalent metals. As noted by the authors, SP20 phosphorylation catalyzed by PKAc with no metal ions bound was not detected in steady-state kinetics experiments since the incubation times they used were longer than the required, and as a result the measurements did not provide a reaction rate constant. Also notable from that study is the fact that alkaline metal ions had no effects on the kinase activity with SP20, because the amount of phosphorylated peptide quantitatively measured by Kovalevsky and coworkers was similar in the reactions with no metal, with Na^+ or with K^+. This results raised the possibility that such cations may not be present when the phosphotransfer takes place. In contrast, they did not detect any kinase activity with Kemptide as a peptide substrate in a metal-free environment or in the presence of Na^+ or K^+. In this sense, the same group was able to obtain also the crystal structure of the PKAc-SP20 binary complex

(in the absence of the ATP nucleotide and without metal ions), which showed a stable intermediate, partially closed, conformation that can coordinate ATP to form the catalytically active ternary complex. Because of that, the ability of PKAc to phosphorylate SP20, but not Kemptide, in a metal-free environment was related to the extremely high binding affinity (≈100 nM) of SP20,[170] and it was proposed that, under that particular conditions, the SP20 binds first to prime the enzyme for subsequent ATP binding.[101] All together, these results indicate that divalent cations do not constrain the active site geometrically to promote the reaction and are not engaged in the chemical transformation, but provide a favorable electrostatic environment for the reaction thereby lowering the transition state energy.

1.3.3. The PKAc active site.

As has been already mentioned, several X-ray crystallographic studies of PKAc (and other protein kinases) in complexes with substrate/inhibitory peptides and various nucleotides and metal ions have been recently deposited in the Protein Data Bank (PDB) repository. As described just above, such crystal structures have been used to elucidate some of the molecular details of the product release step, as well as to provide more information of the role that magnesium ions have at different stages of the reaction pathway. However, the pooled analysis of all these structures have also turned out to be very useful to shed some light over the chemical step of the phosphorylation process, along with to reveal new aspects about the interactions between the enzyme, the cofactors, and the substrates within and around the active site.[76,102,147,153,164]

The active site cleft is located between the N- and C-lobes. As depicted in the Figure 1.9, the slender edge is near the linker region (residues 120 – 127), which is seen as the base of the cleft. The outer thicker edge is positioned towards the residues Lys83 in the N-lobe and Leu198 in the C-lobe, and can be described as the mouth of the cleft. In the conventional view of PKAc, the upper and the lower surfaces of the active site cleft are lined by the residues from the N-lobe and C-lobe, respectively. One side of the cleft is masked by the αC-helix, which then forms the "back" side of the cleft, while the outer edge of the cleft is the binding site for the substrate provided mainly by the C-lobe.[73,171] That is, in the closed conformation of the ternary enzymatic state (PKAc-Mg_2ATP-substrate complex) ready to phosphorylation of the target substrate, the adenine ring of the nucleoside moiety of ATP is completely buried at the base of the cleft, the triphosphate arm of ATP and the divalent metal ions are located at the entrance of the cleft, with the substrate docked to the surface of the large C-lobe where the hydroxyl group of the P-site Ser/Thr residue is poised for a direct in-line transfer of the γ-phosphate of ATP.[142-143] In addition, the two segments that flank the core also contribute to function. The C-terminus tail that spans both lobes is quite solvent exposed and malleable in the free PKAc in contrast to the

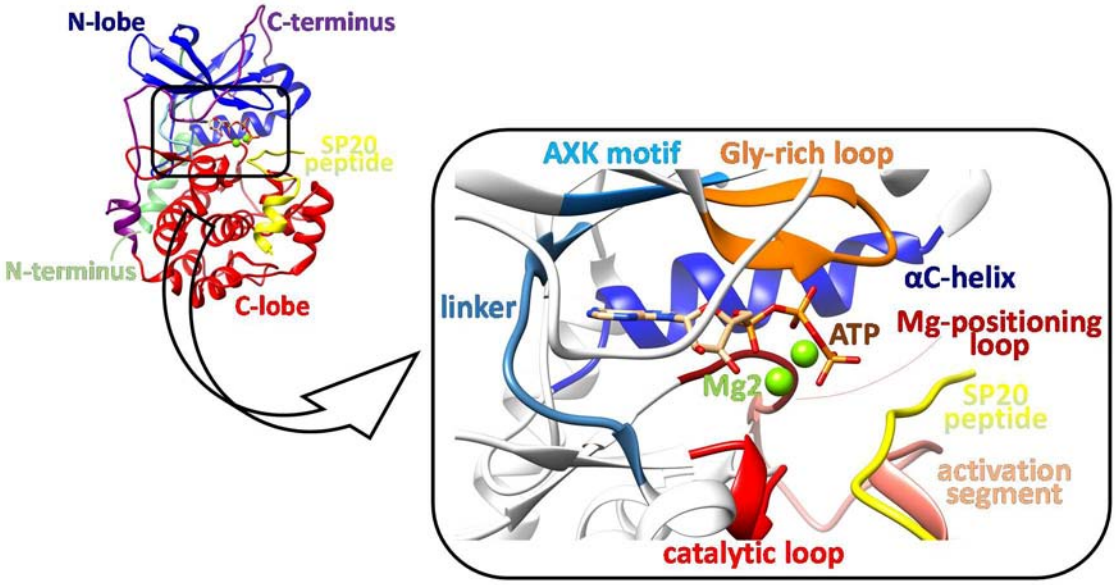

Figure 1.9. The depicted model of the catalytic subunit of PKA (PKAc) was derived from the pseudo-Michaelis complex structure with the PDB code 4IAC[76]. The small (N) and large (C) lobes of the conserved catalytic core are shown using cartoon representation in blue and red, respectively. PKAc-specific N-terminal and C-terminal tails are depicted in lime and purple, with the hollow segment showing disordered residues. The substrate peptide SP20 is depicted in yellow. The inlet shows a close up of key structural and catalytic motifs conserved throughout the entire protein kinase family. The linker, the αC-helix, the Gly-rich loop, and the Mg-positioning loop, colored in light blue, blue, orange and dark red, respectively, shape the active site for ATP, Mg^{2+} ions (depicted as green balls) and substrate binding. The activation segment and the catalytic loop are colored in pink and red, respectively.

ternary complex.[172] Tyr330 flanked by a string of acidic residues interacts with the 2'OH of ATP, and positions a highly conserved water molecule that bridges the N-lobe, the linker, the C-lobe, ATP, and the peptide.[150] The N-terminus helix that also bridges both lobes contributes, in turn, to stability and helps to anchor the αC-helix.[173] In general, three specific components largely contribute to the closing of the cleft: rotation and twisting of the N-lobe relative to the C-lobe, movement of the C-terminus tail, and closing of the Gly-rich loop.[77]

From the analysis of the aforementioned crystal structures, it has been possible to establish that several conserved residues, although widely disbursed in the linear sequence of the protein core of the kinase family, cluster around the active site cleft, playing different and important substrate affinity, binding (of ATP, metal ions, and substrate), and catalytic functions.[174] Most of these residues are localized specifically in three structural motifs: the Gly-rich loop, the Mg-positioning loop, and the catalytic loop (see Figures 1.3 and 1.4, and inlet in Figure 1.9); although other motifs are also involved. Furthermore, the X-ray crystallographic structures provide considerable insights into the conformational flexibility of these loops also. Based on temperature factors for the various structures, it is apparent that the tip of the Gly-rich loop is only stable in the fully closed conformation containing ATP/inhibitor peptide or an ATP analog/substrate peptid. The conformation of the catalytic loop and the Mg-positioning

loop, in contrast, are remarkably stable, with low temperature factors and conformations unchanged even when no peptide is bound.[77]

The Gly-rich loop in the N-lobe (see Figures 1.3 and 1.9) is one of the most prominent motifs in the highly conserved protein kinase catalytic core.[78,172] With ATP in the active site, the Gly-rich loop with its characteristic extended "U" shape, usually makes contact with all three parts of the spatially aligned ATP: the adenosine ring, the ribose ring, and the triphosphate moiety;[78] then constituting a nucleotide-positioning motif and forming the ceiling of the wedge-shaped nucleotide binding pocket.[27,142] In this sense, being the most flexible and mobile motif in PKAc, the Gly-rich loop experiments a displacement up to 6.5 Å when going from the open to the closed conformation to tightly enfolding the nucleotide by means of both stable hydrogen bond and hydrophobic interactions, then functioning as a lid on top of the ATP and serving as a sensor for what is occupying the active site cleft also.[151,172] Specifically, the highly conserved Val57 and Gly50 lay above the ribose ring while the glycines at the tip of the loop appear to be important for positioning the phosphates of ATP, and markedly the γ-phosphate, for the subsequent phosphoryl-transfer step.[26] Thus, the α- and β-phosphates of ATP are stabilized via interactions with the backbone amides of residues Phe54 and Gly55 while the γ-phosphate interacts with the backbone amide of residue Ser53.[62,142,175] The importance of the residues found in the nucleotide-positioning loop were examined previously by Lee *et al*.[176] and showed that mutation of residues other than the first two conserved glycines or Val33 (equivalent to Val58 in PKAc) in phosphorylase kinase had little effect on the phosphorylation by this enzyme. Mutagenesis experiments have also been used to analyze the role of this loop in the catalytic activity of PKAc.[153,177-178] In this respect, although Gly52 does not contact either ATP or the peptide substrate directly, mutations of this residue had more kinetic consequences than the replacements of either Gly50 or Gly51.[177] Substitution of Gly52 by Ala/Ser led to changes in the k_{cat} and the K_m for both peptide substrate and ATP, although the effect on the k_{cat} was no larger than 6-fold.[178] Moreover, the replacement of Ser53 with Thr, Gly, or Pro did not affect k_{cat}, showing that the interaction between the backbone amide of Ser53 with the γ-phosphate of ATP in the closed conformation of the wild type enzyme, is relevant for the nucleotide binding process, whereas the hydroxyl group of Ser53 side chain is not required at all for the phosphorylation of a peptide substrate whatever interaction it may established with the γ-phosphate group (although it does seems to take part on the P-site specificity).[153] All these results together negate the hypothesis that the loop may play a stabilizing role along the phosphoryl-transfer chemical step. On the other hand, the structural studies of the PKAc-Mg_2AMPPNP-SP20 ternary complex and the related products captured in a crystal lattice, showed that the Gly-rich loop is perturbed depending on the substrate bound[179] and following

complete phosphoryl-transfer.[102] Even more, while the Gly-rich loop must be in a closed conformation for optimal phosphoryl-transfer, the open conformation of the Gly-rich loop is related to the ATP loading and, as explained before, to the release of ADP product and the divalent metal ions. The later makes clear that the Gly-rich loop senses and responds to what is present at the P-site.[146,180] It should be noted that in the PKAc-Mg_2ATP-IP20 and PKAc-Mg_2AMPPCP-SP20 pseudo-Michaelis complexes (where IP2o is an inhibitor and AMPPCP is adenosine-5'-(β,γ-methylene)triphosphate, a nonhydrolyzable analog of ATP with the carbon atom of a methylene group instead of the oxygen atom bridging the β- and γ-phosphates), recently obtained by Kovalevsky and coworkers, the main chain of the Gly-rich loop adopts a different position related by a more than 2 Å sliding shift, thereby losing some of the interaction with ATP.[76,164] This structural feature was attributed to the strong steric effects of the CH_2 group in the ATP analog. The authors observed a similar shift of the Gly-rich loop in their product structures with different divalent alkali earth metal ions, and in those cases such behavior was ascribed to the different ionic radii of the metals. Nevertheless, in all cases the change in the relative position of the Gly-rich loop does not affect its closed conformation, so it seems that there are some inconsistencies between the results from mutagenesis experiments and the structural studies. Thus, it is not clear yet which degree of openness is sufficient to allow the phosphoryl-transfer reaction and t products release.

Besides the Gly-rich loop, most of the essential features for binding of ATP are contained within the linker strand and the αC-helix. The adenine ring of ATP is bolstered directly against the linker via two hydrogen bonds (N_6-Glu121 backbone carbonyl, and N_1-Val123 backbone amide).[81] There are no water molecules in this pocket when the adenine ring is present, but in the absence of nucleotide, however, two structured water molecules are present and they form the just mentioned hydrogen bonds with the residues of the linker.[150,172] The αC-helix, an important indicator of the activation state of any kinase too, spans the entire wedge-shaped ATP binding pocket so position the entire ATP molecule for catalysis through multiple interactions. In this regard, the αC-helix houses an essential motif in the N-lobe, the Glu91 residue (unless otherwise indicated, Figure 1.10 accompanies the description of the active site residues that is carried out hereinafter). At the back of the active site cleft, the Glu91 together with Lys72 and Asp184 forms an strictly conserved triad that electrostatically links the β sheet and the αC-helix with the Mg-positioning loop.[163] In the PKAc active conformation, this triad reorganizes itself to bind the nucleotide with the Mg^{2+} ions by breaking the Lys72-Asp184 salt bridge. This change allows the αC-helix to be oriented such that the Glu91 is directed toward the Lys72 forming an ion pair.[125,142] Structural information from many inactive kinases indicates that the orientation of the αC-helix is typically altered, disrupting many of its active conformation interactions.[181-183]

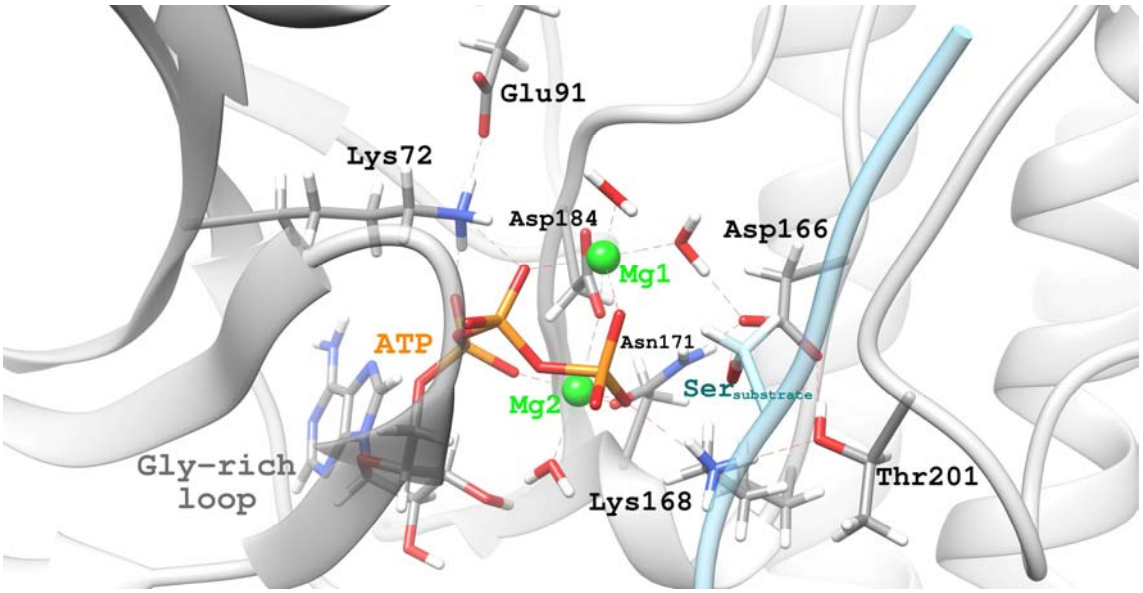

Figure 1.10. Schematic representation of the active site cleft of PKAc (in cartoon representation and transparent gray color) in a ternary reactant state ensemble. Conserved residues that cluster around the active site are depicted in licorice representation and colored by atom type. They exhibit the average conformation, relative orientation and key interactions (depicted with dashed bonds) between them and with the ATP cofactor, the side chain of P-site serine (substrate in cyan color), the two Mg^{2+} ions (shown in green balls), and three conserved waters coordinating the divalent metal ions.

That is, in the optimal ternary complex for catalysis, Glu91 does not interact directly with the nucleotide but rather gets Lys72 poised to interact directly with the α- and β-phosphates of ATP, then positioning ATP for phosphoryl-transfer. Thus, Lys72 and Glu91 residues linked by electrostatic contact are truly important for maintaining the essential catalytically active conformation of the N-lobe. Mutation of Lys72 leads to a dead kinase even though this mutation does not abolish ATP binding. Specifically, an 800-fold loss in catalytic activity for K72A mutant, although the results for Arg, His and Met mutations –that conserved charge or approximate size– where no distinct for the alanine mutant.[137,155] It was suggested that, after autophosphorylation on Thr197, the mutant residues at the 72 position are not capable of competing Glu91 away from Arg165 (a common interaction observed in the PKAc inactive forms).[154-155] Arg165, in turn, interacts strongly with phosphorylated Thr197 in the PKAc active form. As expected, the replacement of Glu91 with Ala has severe consequences too.[137] Concerning Asp184, this residue belongs to the so-called "DFG" motif, within the Mg-positioning loop. It is strategically positioned on the floor of the active site cleft where it can shuttle between the N- and C-lobes. In this regard, MD simulations indicate that Asp184 tracks with the N-lobe rather than the C-lobe when correlated motions and rigid body movements are compared.[184] Specifically, Asp184 contributes to catalysis by binding the magnesium ions that bridge the phosphorylated tale of ATP. Thus, summing up, the Lys72-Glu91-Asp184 triad, together with the hydrophobic pocket that binds the adenine ring, provide a docking site for Mg_2ATP and,

particularly, anchor the phosphates of ATP directly and through the Mg^{2+} ions. In this way, the terminal γ-phosphate is better positioned and oriented for direct transfer while its charge is masked, thus limiting electrostatic repulsion for the incoming substrate Ser/Thr hydroxyl nucleophile.[26] In general, the position of the Mg-positioning loop is stabilized by interaction with Arg165 which binds to the backbone carbonyl of Phe187, another highly conserved residue the latter that also helps to exclude water from the site of phosphoryl-transfer.

The catalytic loop (Asp-Leu-Lys-Pro-Glu-Asn, residues 166 – 171; Figures 1.4 and 1.9) contains several highly conserved residues. The amide group of Glu170 side chain points away from the active site cleft and is part of the binding pocket for the P-2 Arg in the peptide substrate or inhibitor. Regarding Asn171, it is strictly conserved throughout the protein kinase family. It binds to the Mg2 ion that bridges the α- and γ-phosphates of ATP and also interacts with the Mg1 ion that bridges the β- and γ-phosphates. Furthermore, Asn171 also hydrogen bonds through its side chain amide to the α-carbonyl of Asp166, thereby stabilizing the loop.[26]

Asp166 is a residue from the catalytic loop completely conserved in the active site of all protein kinases. In the first PKAc X-ray crystallographic structures, the carboxylate group of Asp166 was found near the hydroxyl proton of the substrate Ser, residing in a position likely to form a hydrogen bond and then thought to position it for phosphoryl-transfer.[73,142-143,175] Mutagenesis experiments performed at high magnesium concentrations showed a severe 370-fold reduction in k_{cat} of yeast D210A mutant and a negligible activity in D149A and D149N mutants of protein kinase PhK (Asp149 corresponds to Asp166 in mammalian PKAc), without greatly affecting the K_m for either ATP or the substrate peptide.[85,137] The null or reduced capability of Ala and Asn, respectively, to behave as basic residues or even for positioning the serine nucleophile in the case of the Ala residue, confirmed that the conserved aspartate is clearly important for efficient catalysis, and were used as evidence to support that Asp166 could act as a general-base catalysis via proton-transfer. That is, Asp166 could accept the proton from the substrate hydroxyl thus enhancing the nucleophilic reactivity of the P-site Ser. That suggestion was consistent with the early pH dependence studies,[185] which indicate that there is a catalytic base existing in the active site. However, later kinetic studies by Zhou *et al*.,[186] in which the burst phase in PKAc activity was monitored with rapid quench flow techniques showed that the rate constant for this phase is independent of pH between pH 6 and 9. The same authors, considering the basicities of aspartate (pK_a of less than 5) and serine (pK_a of 14) in the aqueous solvent, suggested that Asp166 may not be an effective general base, and the catalytic role of Asp166 could either be to correctly orient the reactants or to accept the proton late in the reaction process. Computational studies on the phosphorylation reaction catalyzed by PKAc from Cheng *et al*.[166] and Valiev *et al*.[187] with different initial structures and different QM/MM

partitions of the system, confirmed a concerted catalytic base assignment for Asp166. Furthermore, their observations were consistent with a late proton-transfer result from several experimental studies,[79] rather than a structural anchor to maintain the substrate serine active site configuration. Recently, Montenegro *et al*.[188] have reported a comprehensive molecular dynamics study on the PKAc Michaelis complexes containing Kemptide or SP20 as the substrate. They found that the OH group of Ser17 of Kemptide is rotated toward Asp166, forming hydrogen bonds with this aspartate and Lys168. Conversely, the OH group of Ser21 of SP20 is rotated away from Asp166, forming a hydrogen bond with a γ-phosphate oxygen of ATP instead. The later conformation is very similar to that observed in the pseudo-Michaelis complex PKAc-Mg_2AMPPCP-SP20 obtained by Kovalevsky and coworkers.[76] In that crystal structure, the hydroxyl group of Ser21 in SP20 is rotated towards the bulk solvent, lacking a hydrogen bond to Asp166 and lying at a hydrogen bond distance of the γ-phosphoryl group of ATP. Very recently, Kovalevsky and coworkers, acknowledged that all previous crystal structures of the Michaelis complex mimics of the PKAc were obtained with either peptide inhibitors or ATP analogs. For that, they utilized Ca^{2+} ions (which support the phosphoryl-transfer catalyzed by PKAc), sulfur in place of the nucleophilic oxygen in a 20-residue pseudo-substrate peptide (CP20), and ATP to produce the PKAc-Ca_2ATP-CP20 crystal structure, a close mimic of the Michaelis complex.[80] Interestingly, in their resulting ternary reactant complex the thiol group of Cys21 of the peptide has a near-attack conformation facing and interacting in close proximity with the Asp166 carboxyl group, and the sulfur atom is positioned for an in-line phosphoryl-transfer.

Lys168 is another important residue from the catalytic loop in the entrance to the active site of PKAc.[125,174] Lys168 is highly conserved in all Ser/Thr kinases and replaced by Arg in tyrosine kinases, indicating that catalytic machinery of kinases employs its flexible, positively charged side chain.[63] In yeast PKAc with Kemptide, replacement of this lysine with alanine led to a 30-fold elevated K_M for the substrate peptide and a 50-fold reduced k_{cat},[137] and more recent mutagenesis studies showed the complete loss of catalytic activity for the K168A mutant of IP_3-3 kinase.[189] In various PKAc crystal structures, Lys168 is the catalytic loop residue that is located in a close proximity of hydroxyl group of substrate serine and interacts directly with one of the γ-phosphate oxygens of ATP before and after the phosphoryl-transfer,[62,73,76,79] but this interactions are not fully conserved throughout the protein kinase family. In some of the crystallographic structures,[79,142,175] interactions between the ammonium group of Lys168 side chain with the backbone carbonyl group of the P-2 Arg of the substrate peptide, and with the hydroxyl group of Thr201 side chain have also been observed. Furthermore, different computational studies on the phosphoryl-transfer mechanism of PKAc, besides the already mentioned interactions,[166-167] have also reported a salt bridge formation of Lys168 with

Asp166,[148,165,190] and even with Asn171.[163] Although, in general, Lys168 is considered a major source of destabilization along the critical points of the phosphoryl-transfer step,[165-167] the conclusions expressed in those works regarding the function of Lys168 are differing. In this respect, Cheng *et al*.,[166] based on 12 ns MD simulations on both wild type and K168A mutant, proposed that Lys168 serves to keep ATP and the substrate peptide in the near-attack reactive conformation; the same role was defined by Montenegro *et al*.[148] from a QM/MM study. Valiev *et al.*,[167,187] in contrast, from first principles MD simulations and a QM/MM implementation of the nudged elastic bond (NEB) method, suggested a rapid proton exchange from the Lys168 to the γ-phosphoryl group in the product state, then aiding in the phosphoryl-transfer reaction. Finally, Szarek *et al*.[165] postulated that Lys168 eases the nucleophilic attack by neutralization of the negative charge developing in the course of catalysis. That is, although Lys168 is recognized to be important, its role in the catalytic mechanism, whether structural, neutralizing, or directly participating in the reaction, is not clear.

Thr201, a residue that forms part of the P+1 substrate hydrophobic residue recognition and binding region of the C-lobe, besides anchoring the side chain of Lys168 via a hydrogen bond, also interacts, in some cases very strongly, with Asp166. Based on such a location of Thr201 it has been suggested its involvement in a proton shuttle between Asp166 and Lys168.[26] Experimentally, however, its replacement with alanine impaired the ability of PKAc to autophosphorylate Thr197 and abolished activity due to steric factors. This points to a structural role in which Thr201 regulates the active site conformation through its interaction with Lys168 and, mainly, with Asp166. This latter residue interacts strongly with substrate serine and it is directly connected to Arg165.[191-192] Surprisingly, although it is considered that together Asp166-Lys168-Thr201 form a versatile functional triad,[163] the possibility that Thr201 participates in the catalytically competent conformation of the active site, facilitates the near attack orientation of the Asp166 with respect to the substrate serine hydroxyl group, and correctly positions Lys168 has not been confirmed yet.

Regarding the activation loop of the C-lobe (see Figures 1.3 and 1.9), it is an essential part of the active site, and the conformation of this loop is typically dependent on a phosphorylation site that serves a critical role in arranging its active conformation. The essential phosphorylation site in PKAc is Thr197 which is always autophosphorylated (pThr197; p stands for phosphorylated) for full activity. In a variety of crystal structures, it is 8 – 10 Å away from the catalytic site, right at the edge of the cleft, establishing several key contacts with charged residues from the N- and C-lobes.[26] The salt-bridge between the essential phosphate on Thr197 and the His87 in the N-terminal portion of the αC-helix is proposed to contribute to the closure of the active site,[193] distancing from each other more than 7 Å in the most open PKAc

conformations.[143] This contact forms the outermost edge of the active site cleft and it is one of the few direct ionic interactions between the N- and C-lobes.[81] Through its stable phosphate, pThr197 also forms a bivalent hydrogen bond with the residue Arg165. Specifically, Arg165 is highly conserved in most protein kinases, precedes the catalytic loop (is directly bonded to Asp166) and also interacts with the backbone carbonyl of Phe187 that ends the Mg-positioning loop, so it is considered another important bridging residue. Summarizing, pThr197 forms a critical contact between the activation loop and the αC-helix in the N-lobe, and initiates a major hydrogen bonds network within the C-lobe. The removal of the activation loop phosphorylation site by a T197A mutation reduces the phosphoryl-transfer rate by 100-fold from over 500 s^{-1} to 3.6 s^{-1}, while it increases the K_m for ATP by two orders of magnitude (from 10 μM to 1.4 mM).[130,194] In this regard, Cheng *et al*.[195] have provided theoretical understanding about how the activation loop phosphorylation modulates the catalytic activity in PKAc. Through the comparison of MD simulations and principal component analysis of the wild type and the T197A-mutated PKAc, they concluded that pThr197 not only facilitates the phosphoryl-transfer reaction by stabilizing electrostatic interactions but also strongly affects the essential PKAc dynamics as well as its active site conformation. In particular, the authors concluded that pThr197 regulates the rotameric state for the first dihedral angle χ_1 of the substrate P-site serine side chain, favoring the hydrogen bond interaction of such residue with Asp166 in the wild type (a G^+ rotameric state). Instead, the P-site Ser forms a hydrogen bond with an Oγ of ATP in the T197A mutant (G^- rotameric state). Moreover, they observed that the most significant motion of the wild type PKAc in the context of a ternary complex is a "breathing" mode with the N- and C-lobes moving in opposition, rotating and twisting around the linker region, with the active site opening and closing as the protein kinase breathes. In contrast, the collective motions in the T197A mutant don't include interdomain twisting, indicating that the replacement of Thr197 not only directly disrupts part of the hydrogen-bonding network in the C-lobe and between the N- and C-lobes but also affects the internal motion, which plays an important role in regulating the active site conformations. Recently, Meharena *et al*.,[83] using site-directed mutagenesis and various *in vitro* biochemical assays, have demonstrated that phosphorylation of the activation loop is involved in stabilizing the assembled R-spine. Specifically, the authors define the salt-bridge between pThr197 a His87 as the required intramolecular interaction that prevents the movement of the N- and C-lobes away from each other.

It should be mentioned that the catalytic subunit of PKA has other phosphorylation sites depending on its phenotype. In *E. coli* the PKAc is autophosphorylated at four sites, Ser10, Ser139, Thr197 and Ser338.[66] In the mammalian enzyme Thr197 and Ser338 are very stable phosphorylation sites and are very resistant to removal by phosphatases.[196] Based on

mutagenesis analysis, the phosphate on Ser338 is thought to contribute to stability but, in contrast to the phosphate on Thr197, does not influence the kinetic properties of the enzyme. Recently, Montenegro *et al*.[188] theoretically studied the complex between PKAc and substrate Kemptide by MD simulations. In particular, they focused their attention on two crystallographic models with different phosphorylation state for PKAc: with just pThr197 (PDB code 1CDK), and with pThr197 and pSer338 (PDB code 1ATP). Besides confirming that pThr197 is essential for maximum activity and the correct configuration of residues at the active site cleft, the authors concluded that the difference between the two models is most likely due to the different degree of rigidity, so the higher flexibility of 1CDK may in fact allow the reactants to move rather freely in the active site, thus permitting them to rearrange more suitably along the reaction path.

The minimum peptide recognition site can be defined as the region at the active site cleft where the consensus site peptide docks. In PKAc, this region, also known as the peptide-positioning loop, is sufficient to convey low affinity binding typical of most physiological substrates.[26] Specifically, the arginines at the P-3 and the P-2 positions are key determinants for peptide recognition of the consensus sequence by PKAc, with each site for recognition of these arginines comprised of several acidic residues.[62] The P-2 Arg interacts with two carboxylates, Glu230 and Glu170, the latter being located in the middle of the catalytic loop. The replacement of Glu230 with Gly causes an increase of K_m (from 6.9 μM to approximately 1.4 mM) and a reduction of the phosphoryl-transfer rate (from over 500 s^{-1} to 20 s^{-1}), clearly showing the important role of this residue for catalytic efficiency. The adjacent P-3 Arg interacts directly with Glu127 in the linkers segment –a residue that also interacts with the 2' and 3'-hydroxyl of ATP ribose– and it also does so with Tyr330 in the carboxyl terminal tail which coordinates the highly ordered water molecule that was described before. On the other hand, the P+1 residue is hydrophobic,[127] and its binding pocket is provided by the side chains of Leu198, Pro202, and Leu205, although, as already mentioned, Thr201 also contributes.[26] This region, known as the P+1 loop, follows pThr197 and because of all the residues involved, it communicates with many parts of the protein. Within such loop, Gly200 hydrogen bonds to the backbone amide of the P-site residue resting directly under it, and Glu203 provides a recognition and docking site for the P-6 Arg. Finally, Tyr204 hydrogen bonds to Glu230, a primary determinant of the P-2 Arg recognition site.[62]

1.3.4. The catalyzed phosphoryl-transfer reaction: experimental and theoretical approaches.

Several crystal structures of PKAc in complexes with substrate or inhibitory peptides and various nucleotides and metal ions, have turned out to be very useful to reveal the interactions between the enzyme and the substrates at different stages along the catalytic reaction pathway,

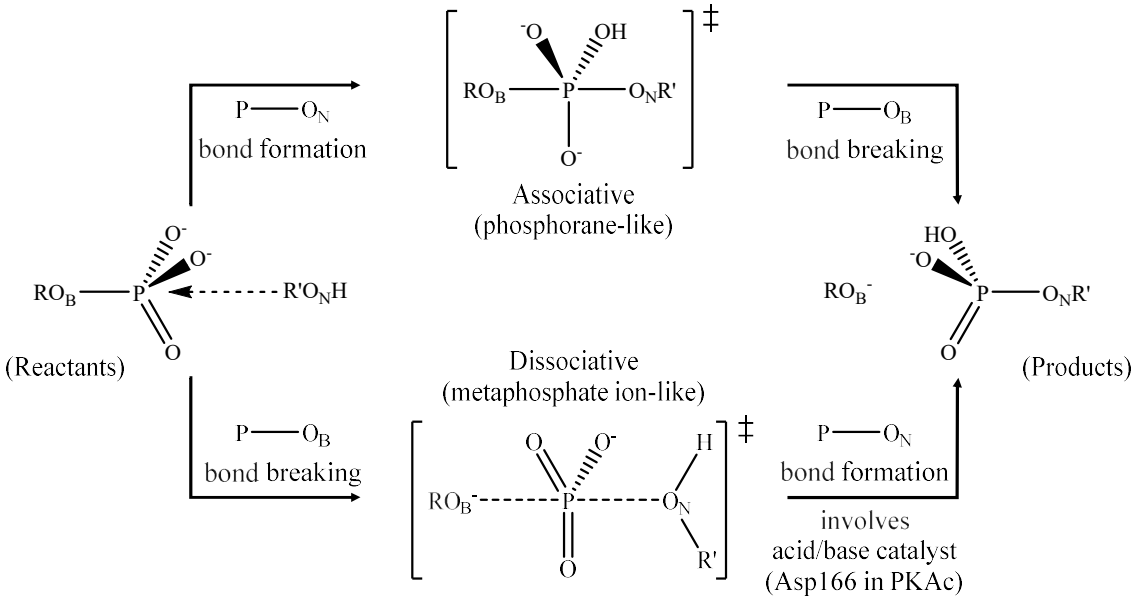

Figure 1.11. The general mechanism of phosphoryl-transfer catalyzed by protein kinases may be either "associative" or "dissociative", proceeding via pentacoordinated phosphorane-like or metaphosphate ion-like transition states, respectively. In the associative path the hydroxyl group of the substrate nucleophile transfers its proton directly to one of the oxygen atoms of the incoming γ-phosphoryl group. The dissociative path involves acid/base catalysis in which a basic residue first deprotonates the nucleophile (then acting as a general base catalyst) in an almost concomitant step to the phosphoryl-transfer, and then, in a second proton-transfer, donates the proton (then acting as a general acid catalyst) to one of the peripheral oxygens of the phosphate group of the newly formed phosphoserine. R and R' stand for the ADP and serine moieties, respectively, whereas B and N subscripts on oxygen atoms account for β,γ-bridging and nucleophile, respectively.

as already mentioned. This structural information has been recently complemented by dynamic analysis based on NMR experiments and MD simulations.[43-45,149] These studies provided very interesting insights into the dynamic fluctuations of the protein needed for turnover and for the regulation mechanism in which protein kinases behave as signal switches. However, various crystallographic structures of PKAc ternary complexes before and after the phosphoryl-transfer reaction and recently deposited in the PDB repository, have also been used to elucidate molecular details of the chemical step. Moreover, these structural studies have also provided more information on the role of magnesium ions along with new aspects of the product release step.[76,80,101-102,146-147,164]

The transition states of the transfer of a phosphoryl group from ATP to a substrate Ser/Thr or Tyr residue have been traditionally classified as associative or dissociative since the putative mechanism was once suggested to vary individually for each kinase between these two limiting cases resembling to a S_N2-like and a S_N1-type mechanism, respectively (see Figure 1.11).[197] Recently, the same definition was given by Warshel and coworkers for the reaction paths related the phosphate monoester hydrolysis in aqueous solution.[198-199] According to the IUPAC nomenclature, the associative and dissociative mechanisms are both concerted mechanisms

(A_ND_N) that proceed through a trigonal bipyramidal pentacoordinated transition state, in which the fission of the bond of the leaving ADP group and formation of a bond to the hydroxyl groupof the nucleophile both occur at the same time. This transition state can be tight or loose depending on the distances from the central phosphorous atom to the apical positions in the trigonal bipyramid and on how synchronous the nucleophilic attack and leaving group departure are.[11,76] For reasons of merely simplicity, the associative and dissociative terms will be used in this work. In the associative mechanism the bond formation with the nucleophilic hydroxyl group of substrate serine/threonine or tyrosine residue begins when the ADP and the γ-phosphate leaving group are still quite closely connected. That is, along the reaction path a pentacoordinated phosphorane-like transition state is formed in which the transition vector related to the $P_{\gamma\ ATP}$–$O_{\gamma\ Ser/Thr\ or\ Tyr}$ bond formation takes place before the bond between β- and γ-phosphates is completely broken. Evidently, the nucleophile and the ADP moiety may be bonded to differing extents to the γ-phosphorous. The phosphorous atom is, in turn, apically coordinated by the donor β,γ-bridging oxygen of ATP and the nucleophilic oxygen of the acceptor residue. Conversely, the dissociative mechanism implies a complete breakage of the bond between the ADP and γ-phosphoryl leaving group yielding a metaphosphate ion-like group that is attacked by an incoming nucleophilic hydroxyl group of serine/threonine or tyrosine residue to form the new P-O bond.[148,166,187] Another important difference between this two possible mechanistic scenarios arise from the path followed by the proton of the nucleophilic hydroxyl group of the substrate along the phosphoryl-transfer step. The OH group of the substrate Ser/Thr either transfers directly its proton to one of the oxygen atoms of the incoming γ-phosphoryl group in the transition state of the associative mechanism. It may also donate the proton to the adjacent conserved Asp166 residue, whose carboxylate moiety lies within hydrogen bond distance,[73,175] facilitating general base catalysis in the dissociative mechanism. Interestingly, despite extensive structural and kinetic characterization of PKAc, the detailed chemical mechanism for the phosphoryl-transfer step remains elusive. In particular, it is still not clear whether the phosphoryl-transfer proceeds as direct attack by the hydroxyl group of the substrate residue on the γ-phosphorous atom of ATP via a phosphorane-like transition state defining an associative mechanism, or through a metaphosphate ion-like transition state characterizing a dissociative mechanism.

According to stereochemical NMR analysis performed at high magnesium concentration, the phosphoryl-transfer reaction proceeds with inversion of configuration at the γ-phosphoryl group and a pentacoordinated phosphorous in the transition state, which is consistent with a direct in-line nucleophilic displacement.[200] Regarding kinetic measurements, the pH dependence of the apparent second-order rate constant ($k_{cat}/K_{Kemptide}$) for Kemptide

phosphorylation is bell-shaped with limiting pK_a values of approximately 6.2 and 8.5.[185] Initially, the lowest pK_a value was attributed to a hypothetical base catalyst that would activate the nucleophilic hydroxyl group during the phosphoryl-transfer reaction. This hypothesis was supported by the already mentioned X-ray structure of PKAc complexed with ADP and a peptide substrate in which the hydroxyl group of the nucleophilic serine and the strictly conserved Asp166 establish a hydrogen bond interaction,[73] and by the 370-fold reduction in the k_{cat} of the D166A mutant enzyme.[137] In addition, early NMR measurements of the enzyme-substrate distances in the active site supported this mechanistic scheme too.[201] However, according to kinetic analysis performed with PKAc and four peptide substrates, the lowest pK_a value corresponds to the ionization of an enzyme residue interacting with the P-2 Arg of the peptide substrate,[202] not to deprotonation of the invariant Asp166. Therefore, the pK_a of Asp166 seems to be lower than 6, and so it is no basic enough to accept a proton from the serine side chain in the ground state at physiological pH.[203] Some other experimental data do not support Asp166 being the catalytic base as well,[186] and the first computational studies gave results that support the associative mechanism, without any major role of Asp166.[204-205] In those studies, the catalytic impact of Asp166 observed in the mutagenesis experiments, was explained by proposing that this residue helps positioning the nucleophilic hydroxyl group toward the γ-phosphoryl of ATP through the hydrogen bond contact observed in the crystallographic structure.[186] In fact, the main chain torsion angles ϕ and ψ of Asp166 (and also of Asp184 coordinating one metal ion) are distorted from their Ramachandran favorable values in PKAc structures in order to position the side chain close to the substrate. More recent computational studies concluded that Asp166 might act as the catalytic base or 'proton trap' late in the reaction process, then pointing to the dissociative mechanism.[148,166,187]

More recently, the molecular information obtained from two different X-ray crystallographic studies[76,102] has been used, together with the 1L3R transition state AlF_3 mimic structure (which is considered the most detailed model for the phosphoryl-transfer transition state conformation of a protein kinase),[79] to reveal new insights on the reaction mechanism of the phosphoryl-transfer process catalyzed by PKAc. Particularly relevant are the X-ray crystallographic structures with PDB code 4IAC, in which the 20-residue long SP20 substrate has been successfully co-crystalized within PKAc with AMPPCP and two Mg^{2+} ions in a pseudo-Michaelis complex conformation,[76] and those with PDB codes 4IAF, 4HPU,[102] and 4HPT,[102] in which both ADP and the phosphorylated SP20 (pSP20) products have been trapped. In addition, the role of metals in the chemical step as well as in the rate-limiting step of ADP release has been revised for PKAc and other kinases also by means of recently determined crystallographic structures.[76,101,103-104,146]

Specifically, Bastidas *et al.*,[102] taking advantage of the slow phosphoryl-transfer that occurs in the PKAc-Mg_2AMPPNP-SP20 crystals, were able to capture and characterize the related products in crystal lattice at a midpoint (4HPU) and end point (4HPT) in the phosphoryl-transfer reaction. That is, these structures, besides giving direct insight of the complex regulatory roles that magnesium ions display on the reaction progression and turnover in PKAc and protein kinases in general (see above, section 1.3.1), give structural evidence of a partial and total phosphoryl-transfer reaction. In this sense, the orientation of the serine substrate residue in both structures is flipped away from Asp166. In contrast, in the 1L3R transition state mimic structure, with a dissociative character and assisted by the Asp166 residue as a catalytic base, the OH group of the substrate serine is facing Asp166 at the hydrogen bond distance of its carboxylate group.

With respect to the molecular features and details of the catalyzed phosphoryl-transfer reaction, Kovalevsky and coworkers[76] interpret the structural data from their crystallographic structures as snapshots of the PKAc active at different stages of the phosphoryl-transfer reaction mechanism. Comparison of the 4IAC[76] and 4DH3[164] pseudo-Michaelis complexes reveals that they are similar, especially in the way that the metal ions coordinate to AMPPCP and ATP, respectively. The importance of the similarity of these two structures, according to the authors, is that it tells that the conformations of ATP, SP20, and PKAc in the two different structures, when combined, are representative of the actual Michaelis complex. Surprisingly, at the 4IAC pseudo-Michaelis complex, the hydroxyl group of the substrate serine is hydrogen-bonded to the γ-phosphate and located away from the Asp166. Moreover, after the phosphoryl-transfer reaction, in the configuration represented by 4IAF structure, the phosphate group on pSer21 of substrate SP20 is too far (4 Å or more according to the authors) to form hydrogen bonds with Asp166 and Lys168. However, it is hydrogen-bonded with the OH group of Ser53 in the Gly-rich loop. That is, the Cβ-Oγ bond of pSer21 is rotated away from the metal and Asp166, thus directed toward the bulk solvent. The authors validate the orientation of the hydroxyl side chain of Ser21 in SP20 at the 4IAC crystallographic structure by indicating that it had been found before in MD simulations of the PKAc-Mg_2ATP-SP20 Michaelis complex initiated from the PDB code 1CDK crystallographic structure.[188] Moreover, a physiological relevance is given to that particular orientation of the pSer21 phosphate group because it has also been observed at the crystallographic structure of the tetrameric PKA RIIβ holoenzyme-product complex.[124]

The analysis of those structures can be placed in context with previous structural reports of PKAc complexes before, along and after the phosphoryl-transfer reaction,[73,79] in which the nucleophilic OH group of substrate serine and the transferring γ-phosphoryl group are rotated toward metals, with and Oγ-Cβ-Cα-N torsion angle of –65°, forming hydrogen bonds with

Asp166 and Lys168. Therefore, assuming that the 4IAC and 4IAF structures represent stable intermediates before and after the phospohoryl-transfer reaction with SP20, and that the structure with AlF_3 truly mimics the transition state, the OH group of substrate Ser21, with a potential hydrogen bond to one oxygen atom of the γ-phosphoryl group in 4IAC structure, should rotate ~110° from its initial position in 4IAC to reach the conformation found in the 1L3R transition state mimic, *i.e.* facing and hydrogen-bonded to Asp166. Then, once the phosphate is transferred, the phosphate group at the phosphorylated substrate serine should rotate back, that is, moving away again from Asp166, ~110° to assume its position represented by the 4IAF structure, and then even more toward the bulk solvent so that the product can be released from the active site cleft. Consequently, according to the authors, the initial conformational change of the flexible Ser21 side chain may initiate the chemistry and play the role of what the authors denominated as the "driving force of the reaction", and might prepare the phosphorylated product for release. However, this proposed mechanistic pathway does not agree with the previous experimental and theoretical studies for SP20 and other substrate ligands,[148,206 and references therein] which had put forward the active role of Asp166 as a general base catalyst. In any case, the authors clearly indicate that those conclusions about the chemical mechanism might depend on the substrate, and they claim that theoretical calculations could confirm that those crystallographic structures along with the transition state mimic structure do really represent sequential conformations along the reaction pathway of the phosphoryl-transfer catalyzed by PKAc, with the requirement that a suitable location of the hydrogen atoms before and after the chemical step is used in the starting computational models.

In fact, as it has already been asserted, a number of theoretical studies have been published on the catalytic mechanism of PKAc. Several groups have investigated the phosphoryl-transfer catalyzed by PKAc using semiempirical[204,207] or *ab initio* and/or DFT quantum mechanical (QM) methods with cluster models,[187,190] or by carrying out semiempirical or DFT quantum mechanical/molecular mechanics (QM/MM) calculations as well as molecular dynamics (MD) simulations using more complete models of the solvated ternary PKAc complex.[148,166-167,190,195,205,208] In some of those studies the 1ATP X-ray structure[100] corresponding to a ground state analogue (PKAc-MnATP-PKI(5-24))[166-167,187] or the transition state mimic structure 1L3R were used as the initial coordinates.[166,195] Díaz and Field[190] used the 1CDK X-ray structure[175] (PKAc-Mn_2AMPPNP-PKI(5-24)) and Montenegro *et al*.[148] have compared the phosphoryl-transfer mechanism with 1ATP and 1CDK crystallographic structures. The substrates chosen in those studies are substrate model ($HOCH_2CH_3$),[187] Kemptide,[148,208] a 20-residue peptide substrate with the sequence TTYADFIASGRTGRRNSIHD (obtained from the PKI(5-24) inhibitor by mutating Ala by Ser)[190] and the SP20 molecule.[166-167,195]

In particular, the early semiempirical QM (AM1, PM3) calculations on cluster models and semiempirical QM/MM calculations on complete models of the phosphorylation reaction catalyzed by the PKAc-Mg_2ATP-substrate complex, gave results that suggested very high energy barriers and supported that the proton in the substrate hydroxyl directly transfers to an O atom of the γ-phosphoryl group of ATP with or even without the aid of Asp166.[204-205] However, the inadequacy of semiempirical methods that lack *d*-orbitals to properly describe the active site of protein kinases was demonstrated.[207] Then, the exploration of the potential energy surface for the phosphoryl-transfer reactions was carried out by other authors with higher QM levels of theory on cluster or complete models of the biological system.[167,187,190,195] Most of those theoretical studies are consistent with a reaction pathway in which the nucleophilicity of the substrate Ser residue is assisted by a late proton-transfer to residue Asp166 that participates as catalytic base. Specifically, Valiev *et al*.[187] carried out B3LYP calculations on a cluster including all of the essential conserved residues and a molecule of ethanol to represent the serine substrate. Díaz and Field[190] performed B3LYP calculations on a cluster model including the 20-residue peptide model substrate based on the PKI(5-24). In turn, in two studies by Cheng *et al*.,[166,195] a B3LYP/MM potential energy surface was explored for a complete enzyme-Mg-ATP-substrate complex starting from the 1L3R and 1ATP crystallographic structures; the peptide substrate SP20 was used in both studies. Finally, Valiev *et al*.[167] carried out free energy calculations by combining a B3LYP/MM reaction path with appropriate MD simulations along the reaction path on the complete system; the starting structure for their calculations was taken from the 1ATP crystallographic structure and the peptide substrate SP20 was used. Only in the work by Díaz and Field using a cluster model the associative mechanism was analyzed and in that case it was discarded in front of the dissociative pathway. The calculated potential energy barriers for the dissociative phosphoryl-transfer in the cluster models go from 11.0 to 17.2 kcal/mol,[187,190] and in the more complete model those values are in the range of 11.6 to 18.3 kcal/mol,[166,195] with a free energy barrier of 15 kcal/mol.[167] Those energy barriers compare reasonably or quite well with the phosphoryl-transfer rate constant of 500 to 154 s^{-1},[130,160,186] measured for the burst phase of the reaction with different substrates, as the experimental phenomenological free energy barrier would be 14 – 15 kcal/mol according to conventional transition state theory.

On the other hand, a mechanistic aspect that clearly differentiates the energy profiles of the theoretical studies mentioned above is related with the product state of the phosphoryl-transfer mechanism. In some studies the energy profile for the dissociative pathway turns out to be endoergic (potential energy values in the range of 10.1 to 16.7 kcal/mol have been reported)[166,190] whereas in others it is exoergic with a reaction potential energy of 9 kcal/mol,[187]

or exoergonic with a reaction free energy of 3 kcal/mol.[167] Moreover, only in the study by Díaz and Field[190] the reaction pathway corresponding to the proton-transfer from Asp166 to one of the oxygen atoms of the phosphorylated serine is analyzed. That reaction pathway connects the product structure of the dissociative phosphoryl-transfer step (in which the proton of the hydroxyl group of substrate serine has been completely transferred to the carboxylate group of Asp166) with a structure of the product complex with a protonated phosphoserine and an unprotonated Asp166 residue. According to the authors this last structure could facilitate the release of the phosphorylated product (with one negative net charge) because of the electrostatic repulsion with the negatively charged carboxylate group of Asp166. In this way, Asp166 would in fact participate in the mechanism as an acid/base catalyst promoting the proton shuttle from the serine residue of the peptide substrate to the phosphoryl group of the phosphorylated peptide product. In contrast, Valiev *et al*.[187] stated that the protonation of the phosphoryl group at the product structure is unlikely because of its interactions with the Mg^{2+} ions.

Recently, the theoretical study of the γ-phosphoryl group transfer of ATP to Ser17 of the model substrate Kemptide in PKAc was carried out by Montenegro *et al*.[148,208] They employed two different crystallographic structures used in previous theoretical studies: 1CDK and 1ATP, the first one being phosphorylated only in residue Thr197 whereas the second structure also has the Ser338 residue modified into a phosphoserine. The higher flexibility of 1CDK observed in their MD simulations showed that the phosphorylation state of the enzyme can modify the dynamical behavior of the active biological system and the potential energy profile for the associative and dissociative mechanisms.[148] Thus, whereas the dissociative mechanism was found roughly equally fast for both structures at the B3LYP/6-31G(d)//AM1/d-PhoT/MM level, only in 1CDK the associative mechanism was found viable. In a later work,[188] the authors analyzed by means of MD simulations of the D166A mutant of the 1CDK structure, the effect of the presence and absence of Asp166. The results clearly showed that the aspartate to alanine mutation led to the opposite effect that the one obtained when modeling a deactivated form (without any phosphorylated residue) of 1CDK. In fact, in the mutated enzyme the interaction between ATP and Ser17 becomes stronger than in the deactivated enzyme, with the general disposition of the catalytic center resembling the associative mechanism prereactive state. Thus, as observed experimentally, the mutation does not completely deactivate the enzyme and the residual activity of the D166A mutant (0.4% of the wild type activity)[137] can only be explained by the viability of the associative mechanism.[82,209]

In summary, although the most common conclusion has been to favor the dissociative mechanism, previous work has also found examples fitting an associative mechanism scheme,

thus a general conclusion has not been reached. In addition, other kinases and protein systems have been experimentally and theoretically proposed to clearly function either by a dissociative[210-212] or an associative mechanism,[213-216] while very recently the role of the associative mechanism in phosphate hydrolysis has been highlighted and proposed to be also relevant for proteins.[198] These findings suggest that the mechanism of each individual reaction may be dependent on the specific reactants as well as the surrounding environment. Moreover, the possibility that the phosphoryl-transfer follows an associative path cannot be ruled out without the observation of a stable metaphosphate intermediate, so both mechanisms must be considered and studied in detail for every protein kinase.

1.4. Objectives.

Despite extensive experimental and computational studies about the structure and function of PKAc, or kinases in general, exact details regarding the complex structural changes and the mechanistic details of individual stages involved in the catalyzed phosphoryl-transfer mechanism remain uncertain. Specifically, mainly due to experimental challenges in defining the reaction mechanism as associative or dissociative at the bond-breaking/formation scale of chemical catalysis, there are still many old and new intriguing questions concerning the respective catalytic roles of specific residues, metal ions, and structural motifs. These questions, without a complete satisfying answer, have recently been analyzed and are still being widely debated in the literature,[76,80,95,101-103,146,152,188] and include: (1) how does the transition state character of the catalytic mechanism depend on the structure of the enzyme and on the substrate?[76,102,188] (2) What is the origin of the phosphoryl-transfer transition state stabilization?[139,217] (3) What is the exact role of metal ions and some particular residues in the catalytic mechanism?[76,101-103] (4) Which are the conformational fluctuations of PKAc linked with enzymatic turnover? (5) Which are the key conformational states along the catalytic cycle?[43-44] (6) What are the driving forces for the release of the phosphorylated product and ADP?[163] Considering the biological significance of the phosphorylation reaction catalyzed by protein kinases and the uncertainties of the experimental studies, such questions have motivated an intense revival of the interest for the catalytic mechanism of PKAc from the theoretical and computational chemists, while extending the discussion to the functioning of other kinases.[148,206,218-220] In principle, computational studies can provide detailed information and insights to complement experimental studies, but this goal can only be attained when the appropriate computational approaches are employed and the theoretical model used is a good mimic of the biological system.

Having in mind all the above mentioned issues, the objectives of this Thesis are:

1. The QM/MM approach at the DFT/MM level of theory will be used to locate the most relevant stationary points on the potential energy surface of the phosphoryl-transfer mechanism. Interestingly, besides employing more complete model systems and higher levels of QM/MM theory than the ones employed in previous works for the optimization of stationary points, the accuracy of the reaction path calculations will be improved by using flexible reaction coordinates and single-point energy corrections will be carried out at the MP2 level of theory.

2. Taking into account that its viability was raised in previous works, another aim of the present Thesis is to thoroughly analyze the possible catalytic role of the associative mechanism in the phosphoryl-transfer reaction in the mammalian PKAc enzyme and its D166A mutant. For this, a complete solvated model of the full PKAc-Mg_2ATP-Kemptide system will be built from structures generated during previous molecular dynamics simulations with 1CDK crystallographic structure (monophosphorylated at Thr197) as starting point. In addition, an analysis of the associative transition states from the charge balance hypothesis perspective will be carried out theoretically with the purpose of comparing the results with recent experimental conclusions concerning transition state stabilization for this reaction path in a key protein kinase.

3. Using the previous model, another objective of this Thesis is to examine minutely the entire dissociative phosphoryl-transfer mechanism, which involves two consecutive steps: phosphoryl-transfer and back-protonation of the phosphorylated substrate. In previous studies the proton-transfer from Asp166 to the phosphorylated substrate serine was not studied at all or, just in the case of Díaz and Field,[190] it was not comprehensively analyzed due the use of a non-solvated cluster model of the reaction core of PKAc. Here, special attention will be devoted to the proton-transfer step that follows the phosphoryl-transfer, and to the analysis of the protonation state of the product complex and its relevance in the reaction energetics and in the release of the phosphorylated peptide product. In addition, the integral reaction paths for the two possible mechanisms will be also studied with Kemptide as substrate peptide but using the corresponding molecular dynamics snapshots with 1ATP X-ray crystallographic structure (diphosphorylated at Thr197 and Ser338) as the initial model template of the enzyme.

4. In light of the fact that the phosphoryl-transfer mechanism can depend on the crystal structure, the recently determined X-ray crystallographic structures of Gerlits *et al*.[76] (research group of Prof. Kovalevsky) in which the SP20 substrate peptide is trapped in the PKAc ternary complex, before and after the phosphoryl-transfer, have provided very valuable structural information which is not biased by any inhibitor molecule. However, the experimental

mechanistic conclusions extracted from that crystallographic data urge for new theoretical calculations that could examine the mechanistic proposal by means of an accurate phosphoryl-transfer simulation at the molecular level. Hence, in this Thesis, from a complete solvated model of the PKAc-Mg_2ATP-SP20 ternary complex built from the 4IAC crystal structure (triphosphorylated at Thr197, and Ser338), both the associative and the dissociative mechanism will be exhaustively studied. From this results, a detailed comparison with the experimental structural data will be given in an effort to accommodate the enzyme-substrate, the earlier transition state mimic, and the enzyme-product crystallographic structures, as Kovalevsky and coworkers themselves suggest, on the proper molecular reaction pathway. Moreover, to delve into how the phosphoryl-transfer mechanism depends on the substrate peptide, the 4IAC ternary complex structure with Kemptide instead of SP20 as peptide substrate will be used to explore both the associative and dissociative reaction paths.

5. Finally, to provide functional insight on how alkali earth divalent metal cations other than Mg^{2+} ions can bind and facilitate the phosphoryl-transfer chemical reaction in the active site of PKAc, the PKAc-Ca_2ATP-SP20/Kemptide and PKAc-Sr_2ATP-SP20/Kemptide ternary complexes will be built from its corresponding 4IAC starting model defined just above, and the catalytic mechanism will be investigated. The results will be interpreted in view of the X-ray crystallographic studies from Kovalevsky and coworkers[76,80,101] which recently have challenged the conventional views about the role of metal ions in the catalytic cycle of protein kinases.

From what has been exposed so far, the whole objective of this Thesis is to apply a consistent and reliable multiscale methodology to a complex molecular system such as the PKAc protein kinase, in order to provide an accurate comparison of X-ray and theoretically determined structures that represent the evolution of the enzymatic system along the phosphoryl-transfer catalytic process. That is, through the comparison of such structures in this Thesis, it is sought to reveal conformational, coordination, and hydrogen bond changes that might occur during the chemical reaction and shed more light on the mechanism of the phosphoryl-transfer chemical step. In particular, the specific roles of: the invariant residues Asp166, Lys168, and Thr201, the conserved Gly-rich loop, the metal ions; and the conformation and protonation state of substrate residue side chain and transferred phosphate along the chemical reaction.

2. Methodology.

2.1. The QM/MM method and ChemShell.

In terms of the Quantum Mechanics theory, the stationary states and related energies of a particular system, can be described by the eigenfunctions ψ_n and eigenvalues E_n of the time independent Schrödinger equation ($\mathbf{H}\psi_n = \psi_n E_n$; where **H** is the Hamiltonian operator including kinetic plus time independent potential energy operators). The exact solution of $\mathbf{H}\psi_n = \psi_n E_n$ is not viable, so then approximations are needed. Within the Born-Oppenheimer approximation, electronic and nuclei movements can be separated. As the nuclei are much heavier than electrons and their movement is slower, they are taken as fixed when solving the so-called electronic Schrödinger equation that gives the electronic wave function. That is, the electronic Hamiltonian does depend on the positions (as parameters) of nuclei but not on their momenta, and the total wave function can be divided in an electronic and a nuclear wave function that can be calculated separately. Within both the Born-Oppenheimer and the adiabatic approximation, the electronic Schrödinger equation is solved first for an enough number of nuclear configurations in such a way that the Potential Energy hypersurface (PES) can be built. Next, the nuclei dynamics over the PES can be incorporated.

Since enzymes –or biomolecules in general– and the complex molecular mechanisms in which they are involved may contain thousands of atoms, to represent them all in terms of wave functions is not possible, no matter the expected accuracy of the calculations. Therefore, their comprehensive study from the standpoint of theoretical chemistry calls for the development first and then the implementation of multiscale methods for describing the PES. In that way, heavily accurate and demanding techniques, like the inclusion of the environment and its steric, electrostatic and dynamical effects, can be applied at affordable levels of calculation to study a broad array of chemical phenomena which are the base of fundamental biological processes.[221]

Nowadays, one of the most important multiscale models is the Quantum Mechanical/Molecular Mechanics (QM/MM) method, which uses both classical and quantum mechanical theory to evaluate the energy of such complex chemical systems and reactions.[221-223] The hybrid QM/MM approach is a method to calculate electronic energies by means of combining a numerical method (variational, perturbative or a combination of both) to solve –integrate- the Schrödinger equation along with a classical potential energy characterized by a force field (a set of functions depending on parameters that provide the energy of the system from a given nuclear configuration: distances, angles, torsions, Coulomb charges, Lennard-Jones van der Waals interactions, …).[224] It has been proven that the combination of both methodologies is required for those systems in which a group of atoms, usually the reacting part or the most relevant for the studied phenomenon, needs to be accurately treated by QM but

the rest of the environment must be also included and represented as a configuration of atoms that contribute to the total energy in a less rigorous but computationally affordable procedure as MM calculations, (*i.e.* according to the force field).[225-227] In other words, using a QM/MM approach, the computational effort can be concentrated where it is needed, that is, for the portion of the system that is subject to strong electronic rearrangements, and the rest of the system is treated in a more economical way. In this way, QM/MM methods are increasingly applied to model large systems.

Geometry optimizations, however, need more energy and gradient evaluations the larger the system becomes. Since one QM calculation is in principle required for any of such evaluations, the computational effort of QM/MM structure optimizations increases steeply with system size and remarkably with the accuracy of the QM method chosen. Evidently, how to divide the system is one of the cornerstones of the QM/MM approach to get a significant reduction on the computer resources (time, memory, and disk) that are needed for the calculations, while retaining a remarkable accuracy. In this regard, the degree of electronic delocalization in the system often dictates the minimum size of the QM part.

Once the whole system S is divided into QM and MM regions, there are two possible schemes to calculate the QM/MM energy: subtractive or additive. Subtractive QM/MM schemes consist of calculating the MM energy of the entire system (depending on the coordinates of all atoms), calculating the QM energy of the QM region, and finally calculating the MM energy of the QM region. This last term is then subtracted to the sum of the first two to avoid double counting:

$$\mathrm{E}^{\mathrm{sub}}_{\mathrm{QM/MM}}(\mathrm{S}) = \mathrm{E}_{\mathrm{MM}}(\mathrm{S}) + \mathrm{E}_{\mathrm{QM}}(\mathrm{QM}) - \mathrm{E}_{\mathrm{MM}}(\mathrm{QM}) \tag{2.1}$$

When following the additive scheme, the MM energy is calculated just in the MM region. This energy and the energy of the QM region are summed. To this sum, a QM/MM interaction term –thought as a correction term– has to be added:

$$\mathrm{E}^{\mathrm{add}}_{\mathrm{QM/MM}}(\mathrm{S}) = \mathrm{E}_{\mathrm{MM}}(\mathrm{MM}) + \mathrm{E}_{\mathrm{QM}}(\mathrm{QM}) + \mathrm{E}_{\mathrm{QM/MM}}(\mathrm{QM},\mathrm{MM}) \tag{2.2}$$

that is, with the E_{MM} depending on the coordinates of the MM atoms and E_{QM} depending on the coordinates of the QM atoms. The term $E_{QM/MM}$ includes all energy contributions coupling the QM and the MM parts:

$$\mathrm{E}_{\mathrm{QM/MM}} = \mathrm{E}_{\mathrm{Q}} + \mathrm{E}_{\mathrm{vdW}} + \mathrm{E}_{\mathrm{FF}} \tag{2.3}$$

that is, the electrostatic QM/MM interaction E_Q, the van der Waals interaction E_{vdW}, and the force field term E_{FF} at the boundary. The latter stem from covalent bonds between QM and MM atoms. Each particular way to calculate this interaction term defines a particular QM/MM method, and, remarkably, most QM/MM methods are additive.

Thus, in general, the QM/MM methodology allows for different approaches to assemble QM and MM regions. In this Thesis, in order to combine the QM and MM calculations, the ChemShell computational chemistry environment has been used.[228] ChemShell is able to interface to a variety of QM (Gaussian, Turbomole, GAMESS-UK, MNDO...) and MM (CHARMM, GROMOS, DL_POLY…) codes, and although it supports standard quantum chemical or force field calculations, its main strength lies in hybrid QM/MM coupling schemes, for which it leaves the time-consuming energy evaluation to the referred external specialized codes, while takes over the communication and data handling. Furthermore, from specific inputs ChemShell allows the use of a range of geometry optimizers that support a wide variety of optimization methods for finding minima and transition states, and all of them can make use of a linear-scaling delocalized coordinate algorithm used to convert Cartesian coordinates into hybrid delocalized internal coordinates (HDLCs), which is particularly important, in terms of CPU requirements, for large systems.

In this Thesis, we apply an additive QM/MM scheme with link atoms within an electrostatic embedding. Thus, the QM code calculates E_{QM} and E_Q (from equation 2.2 and 2.3, respectively), while the MM code computes the remaining terms E_{MM} (from equation 2.2), and E_{vdW} + E_{FF} (from equation 2.3). The HDLCOpt[229] driver module was used to control geometry optimizations, transition state search, and reaction profile calculations, whereas to treat the QM/MM coupling the *hybrid* scheme was used. In such scheme, the total energy of the system is essentially the sum of the QM and the MM energies obtained from the corresponding modules, but ChemShell calculates the coupling between both regions using link atoms, and with the MM energy designed to exclude the internal energy of the MM part. Link atoms are fictional hydrogen atoms that are placed between each pair of bonded QM and MM atoms. They are not taken into account by the QM or MM modules since they are not part of the molecule definition, but the fact that their positions are determined by the QM and MM atom positions allows the analytic derivative of the QM/MM energy to be corrected for forces acting on the link atoms. In this manner, angle terms that involve one MM atom and two QM atoms are not considered in the MM energy expression since a change in the position of the link atom already changes the QM energy. The electrostatic coupling includes the MM centers as point charges in the QM code with the so-called charge-shift scheme or correction,[228] in which the electrostatic interactions are handled by the QM code with QM polarization. The charge of the MM atom of the link is redistributed onto the MM atoms bonded to it so the overall charge is conserved (*i.e.* the charge of MM atoms bonded to QM atoms and close to the link atoms is shifted away). To conserve also the dipole moment, pairs of point charges of opposite sign are added to these neighboring MM atoms. That is, point dipoles are added on the recipient atom of the charge

shift to compensate. In contrast, the polarization of the MM region due the QM atoms has not been taken into account.

Finally, within any particular optimizer module, ChemShell allows to apply geometry dependent energy terms additional to the specific energy/gradient calculation (either a QM/MM scheme, QM or MM), which can be used in turn for constrained optimization. In this Thesis, to calculate the complex reaction profiles of the phosphoryl-transfer catalyzed by the PKAc, harmonic restraints have been applied to the appropriate linear combination of the bonds formed and broken along each particular type of mechanism.

2.2. The HDLCOpt optimization module.

2.2.1. Optimization methods for large molecular systems.

One fundamental problem in computational science is the optimization of a target function of many degrees of freedom. In computational chemistry different optimization algorithms are used for finding stationary points on potential surfaces, depending its performance on many factors: the shape of the target function, the number of degrees of freedom, the required accuracy, and the cost of evaluating the target function and its derivatives. For example, a large system whose atoms are tractable by simple classical force fields requires an optimizer which scales linearly with system size even at the cost of large number of cycles to convergence and the accuracy of the final geometry. On the other hand, the geometry optimization on quantum-chemical potential surfaces must not waste expensive energy and gradient calculations cycles for converge to an accurate final geometry, although this implies moderate system sizes.

Two types of optimizers are frequently employed on atomistic simulations. First-order methods like steepest descent or conjugate gradient methods take only the gradient of the total energy with respect to the nuclear coordinates into account. The computational time for evaluating the search direction is small and generally scales linearly with the number of degrees of freedom to be optimized. However, in general, many energy and gradient evaluations are required to achieve convergence. First-order methods are suited for large systems if the energy and gradient evaluations are very fast. For that reason, steepest descent and conjugate gradient methods using Cartesian coordinates are common choice in molecular-mechanical approaches. By contrast, second-order methods (*e.g.* Newton-Raphson or the Broyden-Fletcher-Goldfarb-Shanno (BFGS) algorithm) make use of the Hessian. Therefore, they require fewer steps until convergence, but the time to evaluate each step scales cubically with the number of degrees of freedom to be optimized. Second order methods are normally applied for geometry optimization in quantum chemistry.[229 (and references therein)] However, the development of linear

scaling quantum-chemical methods[230-231 (reviews)] and combined QM/MM approaches[222-223,226-228,232-233] have extended the applicability of QM treatments to much larger systems.

2.2.2. The coordinate system.

The coordinate system has a fundamental role in the efficiency of a linear scaling optimizer. Cartesian coordinates and Z-matrix internal coordinates are widely used.[234] Both span configurational space non-redundantly but are normally strongly coupled (particularly Cartesian coordinates). So, in the absence of accurate second derivative information (Hessian), the use of a less coupled coordinate representation, as natural internal coordinates,[235] facilitates the task of optimization. Natural internal coordinates consist of individual bond terms and linear combinations of angular terms around an atomic center or in a ring. To minimize complications related to detection of special topologies in their automatic generation, it has been proposed to perform the geometry optimization in natural internal coordinates with some remaining redundancy.[236] In this way, by means of the diagonalization of a matrix equivalent to the spectroscopic ***G*** matrix, every optimization cycle is calculated by projecting the redundant coordinates into a non-redundant space. Other approaches of geometry optimization in redundant internal coordinates make use of "*primitive internal coordinates* involving bond terms as well as individual angles (rather than a linear combination of angles". The use of this coordinates involves dealing with a much larger number of redundant coordinates but, computationally, it simplifies the code by discarding local symmetry.

Other use of the diagonalization of the ***G*** matrix is the transformation of a redundant set of primitive internal coordinates into a non-redundant set of *delocalized internal coordinates*.[237] Just one ***G*** matrix diagonalization at the beginning of the optimization cycle is needed to define fixed delocalized coordinates which are uncoupled enough to allow for an efficient iterative optimization. Nevertheless, with just one diagonalization the computational effort scales cubically with the number of redundant coordinates, limiting the size of the systems to be optimized. Through iterative solutions of linear equations, the computational procedures of delocalized internal coordinates definition and coordinate and gradient transformations have been reformulated, achieving up to an efficient quadratically scaling optimization algorithm for large molecules.[237-239]

2.2.3. The divide-and-conquer approach for the generation of hybrid delocalized internal coordinates (HDLC).

In ChemShell, within the optimization module HDLCOpt, an alternative divide-and-conquer approach is employed to achieve linear scaling in the search of stationary point for large

molecular systems. Hence, the macromolecular system is partitioned into user-defined fragments and the redundant internal coordinates are generated and delocalized exclusively within these fragments. The latter automatically ensures linear scaling of the computational effort for coordinate manipulations and associated gradient transformations.[229]

The automatic generation of redundant sets of internal coordinates and non-redundant sets of hybrid delocalized internal coordinates from Cartesian coordinates can be summarized as follows (the related theory can be found in reference 229 and references therein). For a given Cartesian input geometry, the connectivity between the atoms is determined first. A connection is made whenever the square of the interatomic distance is less than 1.25 times the square of the sum of the corresponding covalent atomic radii. To avoid insulated fragments the missing connections are inserted from the shortest-distance branched path and added to the connectivity list. Once the connectivity is determined, the angles between all adjacent bonds are calculated to create bending angles. Special measures are taken for the treatment of almost linear bends (greater than 175° or less than 5°) and planar systems (the scalar product between the normal vectors of two bends involving a common central atom is greater than 0.95). Finally, dihedrals are defined between all pairs of adjacent bends except in three membered rings. This procedure generates a set of coordinates that is usually highly redundant and is called *primitive internal coordinates*, which are less coupled than Cartesians and less biased than the Z-matrix coordinates. It does not require any knowledge of the user about the system to be optimized, nor is it biased by a prejudice. Importantly, it is generated automatically without any user intervention, but there is the option to force individual primitive coordinates to be included, for example, to impose constraints. A *total connection scheme* can also be chosen to generate a redundant set of internal coordinates in which every atom is connected to every other atom and no angles are defined. In general, this produces an even more redundant set of internal coordinates which is not biased toward any configuration. Figure 2.1 illustrates the difference between primitive internals and the total connection scheme for a simple molecule.

Being redundant, the primitive internal coordinates can describe trial moves without any physical equivalent, and therefore they can be rather inefficient for geometry optimization. To obtain a set of non-redundant highly decoupled internal coordinates, the primitives are linearly combined such that an equivalent of the spectroscopic ***G*** matrix becomes diagonal. Unfortunately, as mentioned above, the diagonalization of the ***G*** matrix becomes unfeasible for large systems. However, due to the sparsity and locality of the ***G*** matrix, the delocalized internal coordinates normally do not extend over large distances. Therefore, in order to generate realistic coordinates for geometry optimization, the system can be divided into user-defined fragments over which the primitive internal coordinates are delocalized (all atoms that are not

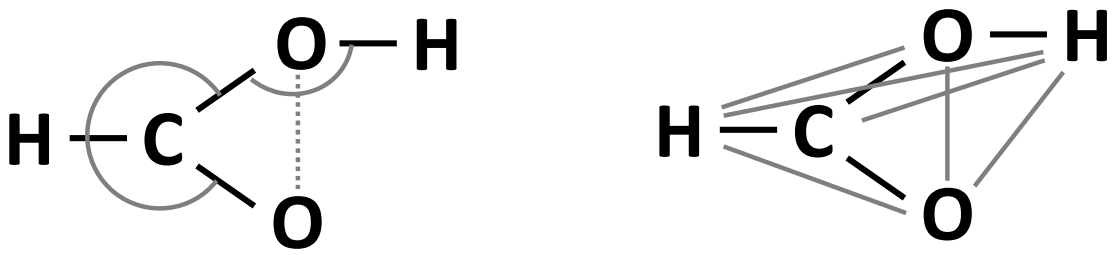

Figure 2.1. Formic acid as an example for primitive internal coordinates (left side) and the total connection scheme (right side). The dashed line is a part of an improper dihedral. The dihedrals are not drawn in order to simplify the scheme. Based on the Figure 1 of reference 229.

specified to be part of a fragment are automatically represented by Cartesian coordinates). In this Thesis, the PDB entries of the molecular entities used in the system models provided a good fragmentation for the purpose of the HDLC optimizer. In addition, ChemShell can import the PDB fragmentation automatically, and the fragmentation can be easily manipulated using set operations. Finally, external coordinates are needed to specify the position and relative orientation of the fragments. As implemented in ChemShell, Cartesian coordinates of all atoms of the fragment are added to the set of primitive coordinates to be delocalized (such Cartesian coordinates may be scaled by an appropriate weighting factor, the default being 0.5 in HDLCOpt). This redundant set of primitive coordinates is then delocalized to yield a non-redundant set that is called *hybrid delocalized internal coordinates*, or HDLC.

2.2.4. Geometry optimization and microiterative transition state search.

The HDLC approach is combined with linear scaling geometry optimization. Specifically, the HDLCOpt optimizer employs the limited-memory BFGS algorithm (L-BFGS)[240] for large-scale energy minimizations. The L-BFGS variant is a limited-memory quasi-Newton-Raphson method that approximates the BFGS algorithm using a limited amount of computer memory. It utilizes the Hessian information accumulated from the gradients over the history of the optimization and thus scales linearly with the number of degrees of freedom in both CPU time and memory requirements.

Specifically, Hessian-based optimization methods employ the inverse Hessian matrix and the gradient to steer its search through variable space (Newton-Raphson step). In The BFGS algorithm, when the explicit Hessian matrix is not available (initially it can be set equal to the identity operator) or its computation is not affordable at every cycle of the optimization, the inverse Hessian matrix can be approximated through the past updates of the positions and gradients, making the algorithm scale as the number of degrees of freedom squared. The L-BFGS variant rather uses a limited number of geometry steps and differences of the gradient to approximate the inverse Hessian matrix on the fly, and therefore it scales linearly with the

system size times the number of remembered steps, often less than 10 but which can be chosen to be any integer between 1 and the number of degrees of freedom (so the L-BFGS inverse Hessian approaches the BFGS inverse Hessian when the number of remembered steps approaches the number of degrees of freedom). The L-BFGS algorithm works better with delocalized internal coordinates than with Cartesian coordinates, and shows comparable convergence to other second-order optimizers.[229]

Figure 2.2 shows a flow chart of the overall algorithm for linear scaling geometry optimization in hybrid delocalized internal coordinates. In summary, the input of the optimizer consists of the initial Cartesian geometry, the fragmentation of the system, the choice of the working coordinate system, and any constraints to be imposed in Cartesian and/or internal coordinates. The optimizer requires an external function that provides the energy and gradient at a given Cartesian geometry.

On the other hand, for macromolecular systems the search for transition states is computationally even more demanding due the necessity of calculation and diagonalization of the Hessian to find the eigenmode to be followed.[241-242] In the HDLCOpt module, for linear scaling transition state searches in large molecular systems by Hessian-based algorithms, a microiterative scheme is employed. Accordingly, the system is divided into a reaction core (or

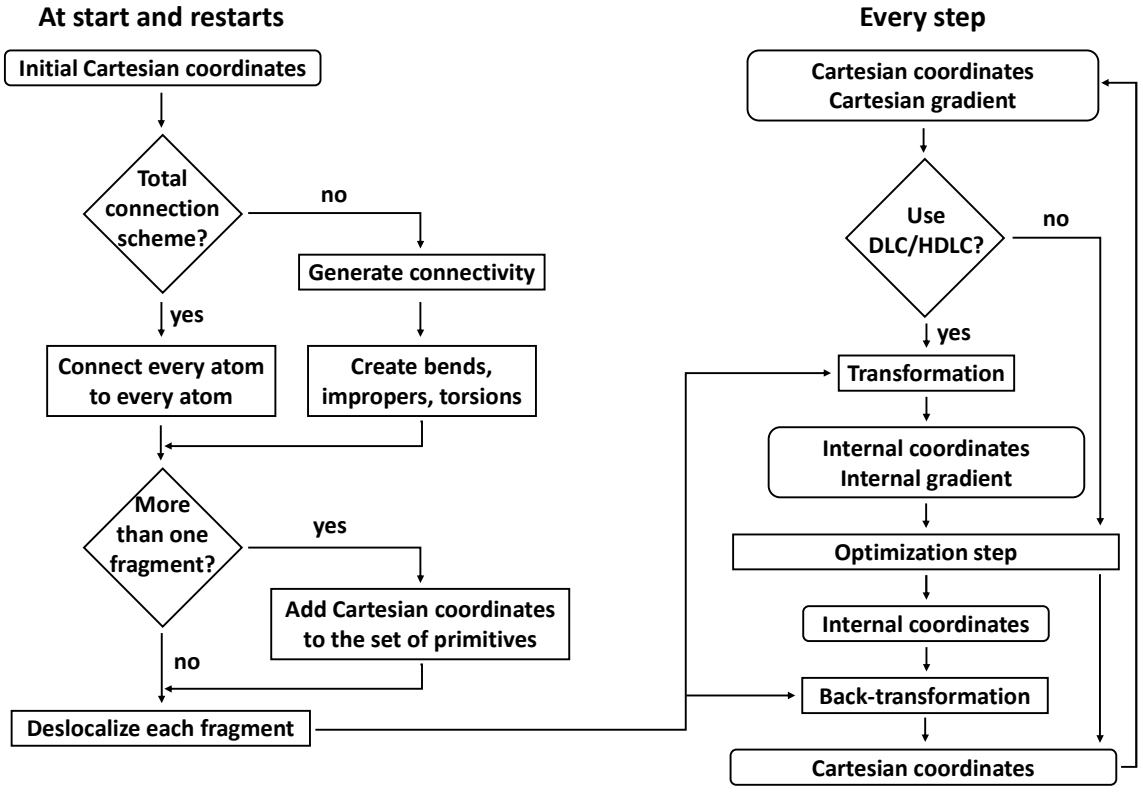

Figure 2.2. Outline of the algorithm for linear scaling geometry optimization in hybrid delocalized internal coordinates. Based on the Figure 2 of reference 229.

inner region including, but not limited to, the QM region), which is best defined as one single fragment and for which the P-RFO (partitioned rational function optimizer) algorithm is used, and its environment (or outer region covering the rest of the system), for which the L-BFGS algorithm is implemented,[243] such that the Hessian is only diagonalized within the reaction core. Computation time is thus saved because the number of costly optimization steps in the inner region (macroiterations) is reduced, at the expense of the number of optimization steps in the outer region (microiterations). In microiterative schemes the regions are optimized separately. It is possible either to use an adiabatic scheme in which the outer region is fully optimized after each optimization step of the inner region, or use an alternating scheme, in which the each region is completely optimized with the other one frozen. Both schemes are iterated until both regions are converged. This work uses the adiabatic scheme to minimize the number of required QM calculation, with the inner region including exclusively the QM region. The initial Hessian matrix is either obtained from a finite-difference scheme or from an analytic second derivative matrix. In the latter case, the derivatives are normally evaluated in Cartesian and thus need to be transformed to HDLC. During the P-RFO optimization the Hessian is updated after each step employing The Powell update formula to preserve the symmetry of the Hessian while the eigenvalue structure may change.

2.3. PKAc models.

The initial structures for the reactive system had been built employing different approaches and different PKAc crystallographic structures. It is important to note that at the beginning of the work the available PKAc structures close to a reactive conformation were scarce and had already been quite studied through different theoretical methodologies, although entailing small substrates and size-restricted molecular systems. Among these studies, the one conducted by the working group that coordinates this Thesis pointed out the importance of the substrates nature and the phosphorylated state of PKAc through MD simulations that also yield several snapshots with different molecular configurations. For this Thesis some of those calculated structures were considered propitious to model the phosphoryl-transfer process significantly increasing the size of the model and the level of theory from previous works. In circumstantial benefit of this work, however, the research groups of Prof. Taylor and Prof. Kovalevsky revealed very recently X-ray crystallographic structures that are close mimics of the enzyme-substrate complex structure at the reactants and products stages of the phosphorylation of SP20 (and SP20-derived molecules). In addition these recent crystallographic studies, span the alkali earth metal family as the divalent metal ion present. Thus, these crystal structures, besides allowing the definition of specific initial models, are references to compare

with the structures defined along the complex reaction coordinate simulations following both the associative and the dissociative mechanisms.

2.3.1. PKAc(1CDK)-Mg_2ATP-Kemptide and PKAc(1ATP)-Mg_2ATP-Kemptide models.

This initial structures had been built from the structures generated during previous MD simulations of the ternary Michaelis complex of the kinase with Mg_2ATP and the synthetic heptapeptide Kemptide as substrate;[188,208] specifically, to build the former biological models, the starting coordinates of PKAc were taken, respectively, from: a) the crystallographic structure with PDB code 1CDK,[175] which corresponds to the closed active conformation of the enzyme and has the residue Thr197 modified into a phosphothreonine (pThr197); and, b) from the crystallographic structure with PDB code 1ATP,[100] which also exhibits a closed active conformation of the enzyme but is di-phosphorylated because, in addition to the same pThr197, it has also the residue Ser338 modified into a phosphoserine (pSer338).

Whether a frame along the referred MD simulations[188,208] was geometrically appropriate to initiate the study of the associative and the dissociative mechanisms or not, was evaluated taking into account the PγATP-OγSer17 distance and the position of the HγSer17 relative to the carboxylate group of Asp166 residue. In addition, to take into account in this study the strong Asp166-Thr201 interaction observed in substrate-bound complexes of PKAc, such distance was used for defining the starting structures. Then: (1) values of 3.5 ± 0.2 Å for the PγATP-OγSer17 distance together with an OγSer17-HγSer17-Oδ2Asp166 angle not higher than 150° (so that the HγSer17 atom does not remain completely directed towards any of the two Oδ*i*Asp166 atoms, distinctive feature of the dissociative mechanism), were considered propitious to set up the initial structures in the simulations; and (2) from such set of selected structures, three initial Oδ*i*Asp166-OγThr201 distance values (3.0 ± 0.2, 3.7 ± 0.2, and 4.5 ± 0.2 Å) were considered representative to study the role of Thr201, and also the role of the Asp166-Lys168-Thr201 triad, in the geometry and energetics of the active site at the stationary points of the phosphoryl-transfer reaction mechanisms. All those structures, neither favoring nor excluding the associative or the dissociative mechanisms, kept the $Ser17_{Kemptide}$ side chain and the γ-phosphoryl group moieties close enough of each other so that it was possible to start modeling both of them: that is, the nucleophilic attack and its concomitant and defining proton-transfer path between moieties here involved.

For the PKAc(1CDK)-Mg_2ATP-Kemptide model, within the reported free 6 ns MD simulation (structural data was recorded for subsequent analysis every 0.05 ns),[208] the geometrical requirements indicated in the previous paragraph were fulfilled on frames, so named, eq21 (MD-snapshot at 1.05 ns; 3.0 ± 0.2 Å or short Oδ*i*Asp166-OγThr201 interaction),

eq55 (MD-snapshot at 2.75 ns; 3.7 ± 0.2 Å or intermediate Oδ*i*Asp166-OγThr201 interaction), and eq91 (MD-snapshot at 4.55 ns; 4.5 ± 0.2 Å or long Oδ*i*Asp166-OγThr201 interaction), which clearly correspond, respectively, to the initial, middle and final part of the MD simulation. In addition, a PKAc(1CDK)-Mg_2ATP-Kemptide Michaelis complex geometry defined in a previous work of our research group[148] was also used. Such geometry presented a suitable -almost specific- configuration for the associative mechanism (2.7 Å for the PγATP-OγSer17 distance and the HγSer17 directed towards the influence area of γ-phosphoryl oxygen atoms, resulting in a small OγSer17-HγSer17-Oδ*i*Asp166 angle of 66°). In this case, the system has a long Oδ*i*Asp166-OγThr201 distance (4.8 Å), but the Thr201 residue side chain remains close to both the Ser17 and Lys168 residue side chains involved in the reaction core (being OγSer17-OγThr201 and NζLys168-OγThr201 distances 3.2 and 3.4 Å, respectively). Henceforth, the M1 label is used to refer to this model geometry.

Regarding the PKAc(1ATP)-Mg_2ATP-Kemptide model, the geometrical requirements described above were fulfilled on frames, so named, eq4 (MD-snapshot at 0.02 ns; 2.6 ± 0.2 Å or short Oδ*i*Asp166-OγThr201 interaction; also, short 2.7 ± 0.2 Å and 3.1 ± 0.2 Å NζLys168-Oδ*i*Asp166 and NζLys168-OγThr201 interactions, respectively), eq49 (MD-snapshot at 2.45 ns; 2.9 ± 0.2 Å or short Oδ*i*Asp166-OγThr201 interaction; also, long 4.0 ± 0.2 Å NζLys168-Oδ*i*Asp166 and short 2.9 ± 0.2 Å NζLys168-OγThr201 interactions), and eq190 (MD-snapshot at 9.5 ns; 4.6 ± 0.2 Å or long Oδ*i*Asp166-OγThr201 interaction; also, intermediate 3.6 ± 0.2 Å NζLys168-Oδ*i*Asp166 and long 4.6 ± 0.2 Å NζLys168-OγThr201 interactions). Since the total length of the reported free MD simulation was approximately 11 ns and structural data was saved every 0.05 ns of the simulation,[188] these frames correspond -as for the PKAc(1CDK)-Mg_2ATP-Kemptide model- to the initial, middle and final part of the MD simulation.

2.3.2. D166A PKAc(1CDK)-Mg_2ATP-Kemptide mutant model.

We have also used as starting point a MD-generated structure from a previously built model based on the 1CDK crystallographic structure and the Kemptide substrate, in which the residue Asp166 was modified to an alanine, *i.e.* the D166A model. In this case, since only the associative mechanism is feasible and there is no Oδ*i*Asp166–OγThr201 distance, the other geometric parameter (besides the PγATP-OγSer17 distance) to consider when defining the MD-frame that could serve as starting point for the QM/MM calculations was the HγSer17-O*i*γATP distance. Therefore, just one MD-frame for this system was selected, namely D166A-eq71 (with 5069 and 3599 free and fixed atoms, respectively). As the M1 geometry for the PKAc(1CDK)-Mg_2ATP-Kemptide model, this selected geometry entailed Thr201 residue side chain close to the reaction core, interacting mainly with Lys168 ε-amino group.

2.3.3. PKAc-M_2ATP-SP20 and PKAc(4IAC)-M_2ATP-Kemptide: alkali earth metal models.

Coordinates from the X-ray crystallographic structure with PDB code 4IAC[76] were used to start modeling the Michaelis complex of PKAc with its ligands at the beginning of the phosphoryl-transfer chemical step. Specifically, this 2.15 Å resolution crystallographic structure contains the enzyme catalytic subunit, the AMPPCP nonhydrolyzable ATP analogue, the 20-residue SP20 substrate, the two Mg^{2+} ions and 339 crystallographic water molecules. That is, the reactive complex in the 4IAC structure represents a pseudo-Michaelis complex since it lacks the actual ATP cofactor.[76] Therefore, the ATP nucleotide was modeled by substituting the β,γ-bridging carbon atom in AMPPCP by an oxygen atom. The triphosphorylated state (pSer139, pThr197 and pSer338) of PKAc in the 4IAC structure was kept to build up the model of the Michaelis complex given that it represents an active configuration of the catalytic subunit of the enzyme.

Since the PKAc-catalyzed phosphoryl-transfer reaction happens at physiological pH, all tritable residues were set to their normal ionization state at pH 7. As a result, all Lys and Arg side chains are in the ammonium or guanidinium forms, respectively, and all Asp and Glu side chains are in the carboxylate form. Regarding the protonation state of the histidine residues of the kinase and peptide substrate, the choice was based on the work of Díaz and Field.[190] Thus, for PKAc, the residues His68, His142, His158 and His260 were protonated at Nδ, the residues His62, His131 and His294 were protonated at Nε, and the residue His87 was doubly protonated. The histidine present in the P+2 position of the SP20 peptide substrate was protonated at its Nε.

The coordinates of the hydrogen atoms added to the crystallographic heavy atoms were calculated making use of the HBUILD facility[244] implemented in the CHARMM program.[245-246] The origin of the system was then adjusted to the geometric center of the Oδ2Asp166, PγATP, and OγSer21 group of atoms. To solvate the structure, a water sphere of 24 Å radius centered at the origin was superimposed on the kinase ternary complex (PKAc, ATP, SP20, and Mg^{2+} ions) along with its crystallographic water molecules. Upon insertion, all solvent molecules overlapping or within 2.5 Å of any crystallographic atom were removed, and this was repeated three times with randomly rotated water spheres. Then, to relax energetically unfavorable contacts, a MD simulation (5 ps) of the solvent molecules was carried out. The 3-fold cycle of superposition, deletion, and rotation was then repeated to fill in additional cavities generated from the equilibration calculations. Finally, a second MD solvent equilibration process (5 ps) was performed. Briefly, the MD simulations, for which CHARMM22[247-248] force field was used, were performed at a temperature of 298 K with a leapfrog Verlet algorithm and a time step of 1 fs; also, a nonbonded cutoff of 12 Å was applied, and the bond length and bond angles of all water molecules were constrained by the SHAKE algorithm. The resulting system (8709 atoms) includes the PKAc monomer (336 aminoacids), one ATP molecule, the SP20 substrate (20

aminoacids), two Mg^{2+} ions and a water sphere with 938 crystallographic and solvent water molecules.

Regarding the 4IAC-Kemptide model, the substrate peptide was constructed using the SP20 X-ray coordinates as a template, and the model setup was carried out following the same protocol from the hydrogen addition step to the short solvent relaxation step. In this case, the size of the system is 8652 atoms, with Kemptide (7 aminoacids) and 981 total water molecules besides the PKAc, the ATP molecule, and divalent ions.

In addition, replacing the Mg^{2+} ions by Ca^{2+} or Sr^{2+} at the beginning of the setup procedure with SP20 or Kemptide as peptide substrate, furnished this study with the possibility of comparing its theoretical results with experimental snapshots[76,80] of the phosphoryl-transfer catalyzed by PKAc in presence of Ca^{2+} and Sr^{2+} in the active center.

From all these solvated enzyme-ATP-substrate models, an initial QM/MM optimization was carried out to avoid any distortions and to eliminate any artifact related with the manipulation and building up of the molecular systems. The resulting structures, named i_{SP20}, i_{Kemp}, i_{SP20Ca}, i_{KempCa}, i_{SP20Sr}, i_{KempSr} were taken as the starting points for the data presented in this work in regards to the 4IC-SP20 and 4IAC-Kemptide models with Mg^{2+}, Ca^{2+} or Sr^{2+} ions.

2.4. Potential energy surface.

For all the QM(DFT)/MM calculations the QM/MM partition was defined as follows. From the selected geometries all non-ternary complex residues (basically, solvation –or TIP3– water molecules) outside a 24 Å radius sphere, centered on the geometric center of the Oδ2Asp166, PγATP, and $O\gamma Ser_{Substrate}$ group of atoms (all within the active core of the enzyme), were deleted. All residues and water molecules within 20 Å of the geometric center defined above were included in the optimization process as the active –or allowed to move freely– region, while the remainder were kept fixed in their positions along the subsequent optimizations and simulations.

The size of the QM region varies depending on the nature of the divalent metal ions present in the model because the coordination scheme for the M1 binding site at the beginning of the simulations varies from one alkali earth metal ion to another, increasing the coordination number from 6 with Mg^{2+} ions, to 7 with Ca^{2+} ions and finally 8 with Sr^{2+} ions. As the protein residues cannot provide additional coordination to the metals, the extra ligands are water molecules. Thus, the Mg^{2+} bound to M1 has two crystallographic water molecules in its coordination sphere, Ca^{2+} has three, and Sr^{2+} coordinates to four. The M2 binding site coordination sphere remains constant regardless of the nature of the divalent metal ion, with only one crystallographic water molecule in its octahedral coordination geometry. With Mg^{2+}

ions, the QM region comprised 65 atoms, with a total charge of -1, and includes, besides all the atoms involved in the breaking/forming of chemical bonds: the γ-phosphate group of the phosphorylated tale of the ATP molecule, the Asp166 side chain and, of course, the substrate serine side chain; the Lys168 side chain, and the two magnesium ions with all the residue side chains and water molecules first-coordinating them, that is, the phosphate groups from the ATP molecule, the side chain of residues Asn171 and Asp184, and three crystallographic waters (see Figure 2.3).

All cuts between QM and MM regions were applied in aliphatic C-C bonds, except that performed in the C5'-O5' bond of the ribose in ATP, which separates the complete triphosphate tail from the adenosine nucleoside moiety. The latter was treated at the MM level in order to keep the QM region small and computationally affordable. For the PKAc(1CDK)-Mg_2ATP-Kemptide and PKAc-Mg_2ATP-SP20 models a larger QM region was tasted including therein other enzyme residues interacting with ATP and Kemptide, as Thr201, Lys72 or Glu91 residues, but the new QM/MM partition caused no change in the calculated barrier heights for the phosphoryl-transfer step following an associative or dissociative mechanism. Therefore, it was decided to keep the original QM/MM region computationally more convenient. The fractional systems served as starting points for the QM/MM calculations.

All QM/MM calculations were performed with the modular program package ChemShell,[228] using TURBOMOLE[249] to obtain the quantum mechanical (QM) energies and gradients at the DFT level. In previous works, it has been shown that the B3LYP functional was a good choice for phosphorous-containing systems,[54] and that the QM(B3LYP[250-255]/6-31+G(d)[256-259])/CHARMM level of calculation provided good geometries and energies at reasonable computational time.[32,33] Specifically, for all the $Mg^{2+}$and Ca^{2+} containing models, the QM region was treated with the B3LYP approximation for the exchange-correlation functional, expanding wave-functions by means of the 6-31+G(d) Pople basis set. The Sr atom is not defined in Pople basis sets, so a B3LYP/def2-TZVP[260] level of calculation was established for the Sr^{2+}-containing models.

The remainder of the molecular system was described at the molecular mechanics level. The energies and gradients for the MM region were evaluated by DL_POLY,[261] which was accessed through the ChemShell package using the CHARMM22 force field.[247-248] It should be pointed out that the van der Waals parameters associated to the potential energy function used to model the interaction of Ca^{2+} and Sr^{2+} metal ions with water and biological ligands were taken from the study of Babu and Lim[262] on the developing of force fields for modelling metalloproteins in aqueous solution, since those parameters have proven to be consistent with the experimental structural and thermodynamical properties for such divalent metal ions.

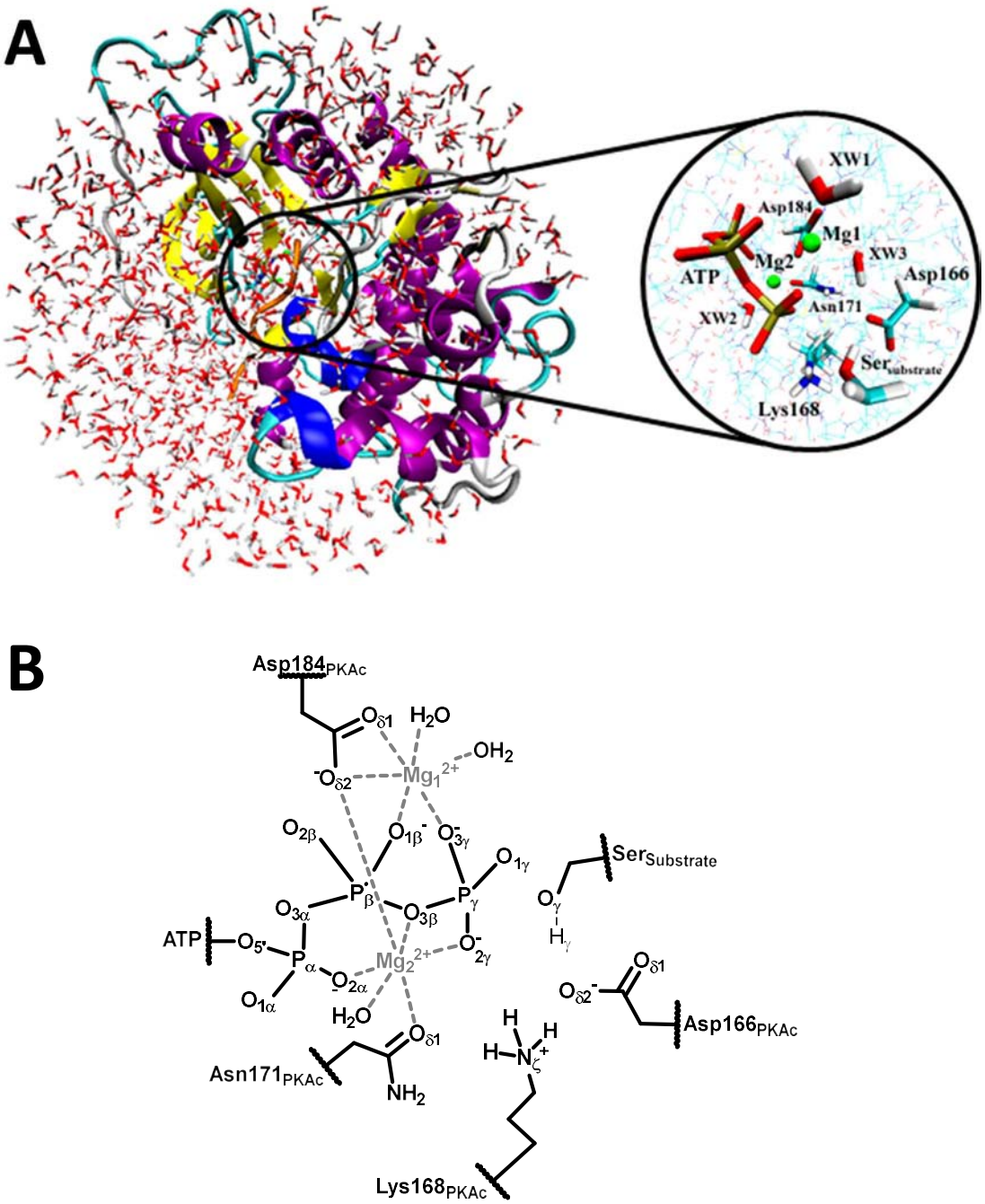

Figure 2.3. (A) Structure of the PKAc-Mg_2ATP-Substrate complex solvated with a 25 Å-radius sphere of water molecules. The black circle highlights the position of the active site. In the inset an enlarged view of the active site is shown in atomistic rendering with the QM atoms represented in licorice style and colored by atom type. **(B)** Schematic representation of the QM region within the active site of PKAc. All QM atoms are represented except for the hydrogen atoms of residues side chains. The nomenclature of PDB code 4IAC[76] X-ray crystallographic structure was adopted for the atom names. The wavy lines represent the frontier between QM and MM region (QM/MM electronic embedding scheme), employing hydrogen link atoms to cap the bonds crossing into the MM region (charge shift model).

An electronic embedding scheme[261] was adopted in the QM/MM calculations with the MM point charges being incorporated into the one-electron Hamiltonian during the QM calculation. No cutoffs were introduced for the non-bonding MM and QM/MM interactions. The

QM/MM boundary has been treated with the charge-shift model[263-265] so, according to the QM region defined above, six hydrogen link atoms were employed to cap the bonds crossing into the MM region. It is widely recognized that the charge-shift scheme reduces the overpolarization of the QM region by the MM point charges within link-atom models.[55-57] Energy minimizations were performed employing the L-BFGS[240,266] algorithm, while the transition state searches were carried out by means of the microiterative optimizer[229,243] combining the L-BFGS and the partitioned rational function optimizer (P-RFO) algorithm.[241-242] Both algorithms are implemented in the HDLCopt[229] module of ChemShell. The characteristic single imaginary frequency and the chemically proper transition vector were confirmed for all reported transition states by means of frequency calculations for the QM region. More accurate energy evaluations were obtained by single-point energy calculations at the QM(MP2[267-268]/aug-cc-pVTZ[269-270])/CHARMM level of theory for the Mg^{2+}-bound models, and QM(MP2/def2-TZVP)/CHARMM level of theory for the Ca^{2+} and Sr^{2+}-bound models.

From the corresponding initial model, reaction paths were scanned by constrained QM/MM optimizations along a reaction coordinate in steps of 0.2 Å. Different reaction coordinates were defined for the phosphoryl-transfer following one or the other proposed mechanism. For the associative mechanism the reaction coordinate equation involves the two anti-symmetrical combinations of the bonds to be broken and formed:

$$R4^{Associative} = r_1 - r_2 + r_3 - r_4 \quad (2.4)$$

where r_1 is the O3βATP-PγATP distance, r_2 is the $O\gamma Ser_{Substrate}$-PγATP distance, r_3 is the $O\gamma Ser_{Substrate}$-$H\gamma Ser_{Substrate}$ distance, and, finally, r_4 is the OiγATP-$H\gamma Ser_{Substrate}$ distance (see Figure 2.4A). Since the γ-oxygen atoms of ATP differ in their chemical environment, the three possibilities (i = 1,2,3) were taken into account when modeling the associative reaction path. The reaction coordinates were scanned, going forward and backward (from reactants to products and *vice versa*), until the convergence was reached, *i.e.* until the potential energy profile of one reaction path and the following were equal. This provided the appropriate starting structures for consequent full QM/MM optimization of all related stationary points (reactant complex, transition state, and product complex).

On the other hand, from the same initial model structure, the dissociative mechanism of the phosphoryl-transfer was also simulated by constrained QM/MM optimizations in steps of 0.2 Å according to the reaction coordinate defined as:

$$R4^{Dissociative} = r_1 - r_2 + r_3 - r_5 \quad (2.5)$$

where r_5 is the Oδ2Asp166-$H\gamma Ser_{Substrate}$ distance (see Figure 2.4B, phosphoryl-transfer step). The same convergence criterion was applied to the simulated reaction paths and relevant stationary

point optimizations from representative geometries were carried out as described above.

Subsequently, the optimized product of the dissociative phosphoryl-transfer path was then used as the starting structure for scanning the reaction path corresponding to the second step of the dissociative mechanism, that is, the proton ($HγSer_{Substrate}$) transfer from the just protonated carboxylate group of Asp166 side chain to one of the peripheral γ-oxygen atoms of the phosphate group already bonded to the substrate serine (*i.e.* phosphoserine). Thus, again in steps of 0.2 Å, constrained QM/MM optimizations were performed along the reaction coordinate defined as:

$$R2^{Dissociative} = r_5 - r_6 \quad (2.6)$$

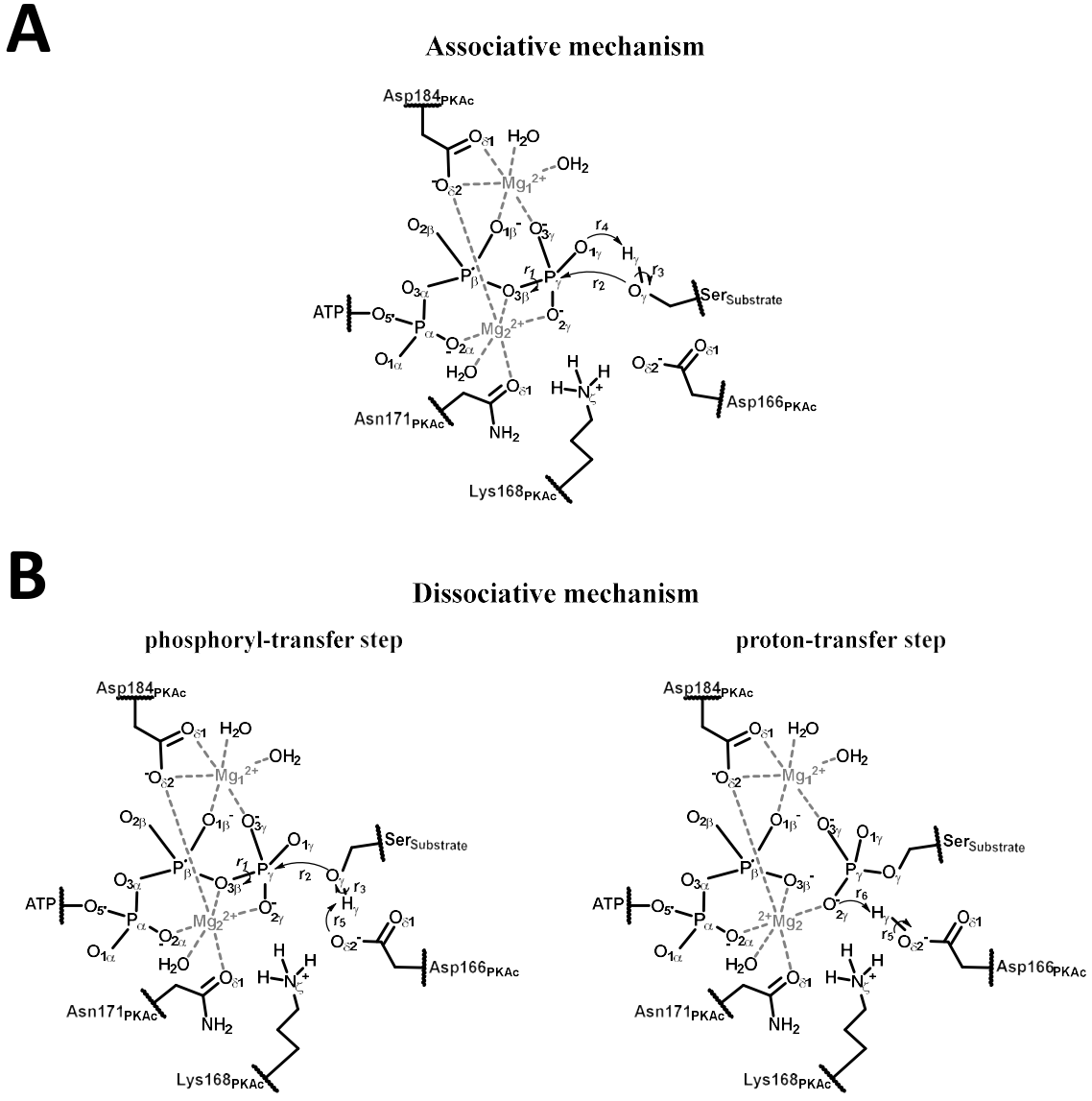

Figure 2.4. Schematic representation of the proposed mechanisms for the phosphorylation reaction catalyzed by PKAc. **(A)** Associative mechanism. **(B)** Dissociative mechanism: phosphoryl- and proton-transfer steps. All QM atoms within the active site of PKAc are represented, except the hydrogen atoms of substrates side chains. The wavy lines stand for the frontier between QM and MM regions.

where r_6 is the OiγATP-HγSer$_{Substrate}$ distance (i = 1,2,3; see Figure 2.4B, proton-transfer step).

When it was possible to simulate a converged proton-transfer path, it was confirmed that it yielded backwards the same optimized phosphoryl-transfer product –both geometrically and energetically– as the preceding phosphoryl-transfer path. That is, phosphoryl-transfer and proton-transfer reaction paths are connected through the same molecular complex. Finally, from the suitable structures in each case, the final product complex of PKAc catalyzed phosphoryl-transfer reaction was characterized and microiterative QM/MM TS search was performed.

The Figures showing molecular structures were generated using VMD version 1.8.7[271] and Chimera 1.8.1.[272]

Finally, two other computational techniques, briefly described here, were used to complete the analysis for the associative mechanism results obtained from the PKAc(1CDK)-Mg_2ATP-Kemptide model. 1) Recently, the analysis of the catalytic mechanism of phosphoryl-transfer from a basis of physical organic chemistry allied to enzyme biochemistry, and with a strong focus on the associative/dissociative nature of the reactions, is being complemented by structural studies. These studies juxtapose X-ray analysis with NMR spectroscopy allowing a new interpretation of the phosphoryl-transfer mechanism.[273] This new perspective is focused on understanding how enzyme have solved the problem of phosphate charge repulsion of the attacking nucleophile. In this sense, the charge balance hypothesis (CBH) has been established as a general explanation on how phosphoryl-transfer transition states are stabilized in several kinases.[217] Natural population analysis (NPA)[274] charges were determined from stationary points at the QM(B3LYP/6-31+G(d))/CHARMM level of theory, and applied in CBH calculations. 2) The contribution of different residues to the QM/MM energy along the associative reaction path was evaluated by setting their point charges to zero in additional energy calculations at the corresponding stationary points.

3. Results.

In this section the results of the computational study of the phosphoryl-transfer mechanism catalyzed by PKAc are presented. Both the associative and dissociative paths were profiled thoroughly in order to shed more light on the mechanistically relevant interactions found around the P-site residue that might make possible the catalytic process. This requires, for the associative mechanism, the simulation of the chemical step by which the proton of the hydroxyl group of the serine residue (Ser17 for Kemptide, Ser21 for SP20) of the substrate peptide (Kemptide or SP20) goes directly to one of the three γ-oxygen atoms of the ATP molecule along the phosphorylation step. For the dissociative mechanism, on the other hand, such proton goes to one oxygen of the carboxylate group of the closely located Asp166 residue in a specific point of the nucleophilic attack defining the phosphoryl-transfer reaction. Afterwards, the proton is transferred again but to one of the stereochemically accessible γ-oxygen atoms of the now phosphoserine product moiety, recovering with such second proton-transfer the initial charge of the enzyme (which does not changes along the associative mechanism). These comprehensive set of chemical processes taking place within the active site cleft of PKAc were modeled for all the systems with Mg^{2+} and the Kemptide substrate, implying initial models with different starting X-ray crystallographic structures (PDB Codes: 1CDK,[175] 1ATP,[142] and 4IAC[76]) to span both the phosphorylation state of PKAc and the relative position of the Gly-rich loop within the active site. With the 4IAC model, in addition, both SP20 and Kemptide were used to analyze the recently proposed substrate-dependence of the phosphoryl-transfer catalyzed by PKAc. Moreover, divalent alkali earth metal ions different than Mg^{2+} were considered occupying the two metal binding sites in order to check the recently suggested possibility of a PKAc-catalyzed phosphoryl-transfer under different metal ion conditions.

Since *a priori* none of the two mechanisms –associative and dissociative– proposed for PKAc have been discarded or ruled out, in order to properly follow the discussion of the results, it is important to distinguish between the three γ-oxygen atoms of ATP taking into account their chemical environment (see Figure 3.1). Here, the nomenclature of the 4IAC[76] PDB entry was adopted. Thus, in all the system models, O1γATP points towards the Gly-rich loop; O2γATP coordinates the M2 divalent metal ion and interacts with the positively charged ε-amino group of Lys168; and, finally, O3γATP coordinates the M1 divalent metal ion.

It has to be noticed that, at a geometry prone for the associative mechanism, the $H\gamma Ser_{Substrate}$ will point towards one of the three peripheral γ-oxygen atoms of ATP. Thus, for each Mg^{2+}-containing model, the proton-transfers between the ATP molecule and the substrate serine were simulated with the three OγATP atoms acting as the proton acceptor. Structural optimization on the B3LYP/6-31+G(d)/MM potential energy profile was performed as a function

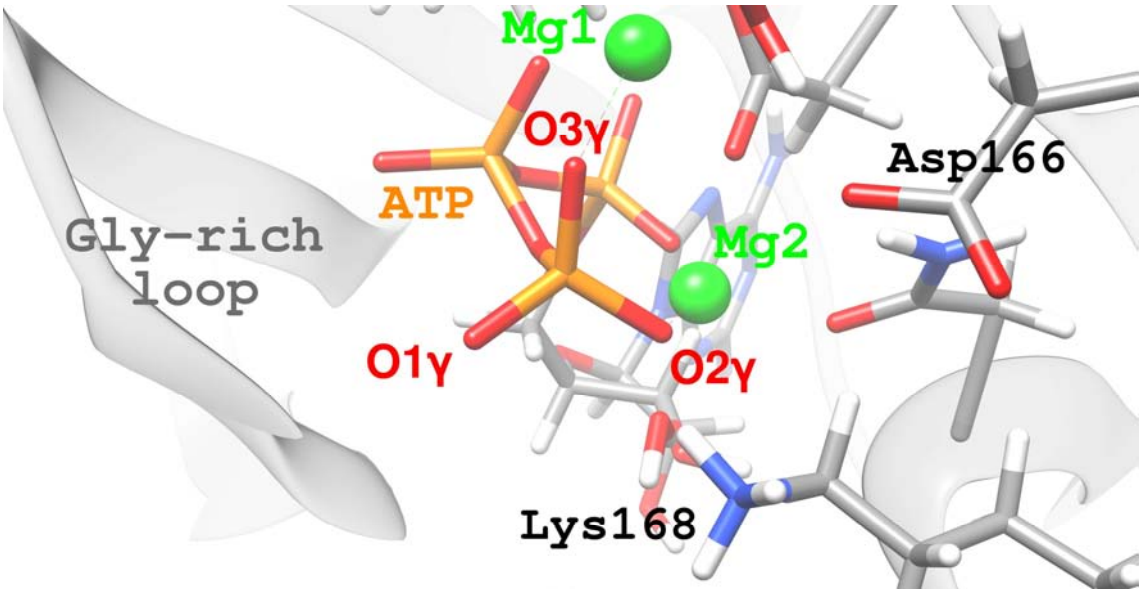

Figure 3.1. Schematic representation of the γ-oxygen atoms of ATP and the chemical environment that distinguishes each one within the active site cleft of PKAc (view from the perspective of substrate serine).

of the corresponding R4-reaction coordinate. That is, performing a sequence of geometry optimizations with a harmonic restraint applied on such reaction coordinate, the systems were driven from the reactants to the products configuration over the reaction barrier by optimizing the QM/MM active region at each given restrained value of the R4-reaction coordinate. Since the reaction coordinate was explored forward and backward several cycles until the one-dimensional potential energy curve reached convergence (*i.e.* until the energy profiles differ by < 0.1 kcal/mol), the methodology led for each case to a configuration conducive to form the O*i*γATP-HγSer$_{Substrate}$ (*i* = 1-3) hydrogen bond. Something similar happens when simulating the phosphoryl-transfer step of the dissociative mechanism, but reaching in this case geometries with an OγSer$_{Substrate}$-Oδ2Asp166 hydrogen bond clearly established. Then, the proton-transfer step from the carboxylate group of Asp166 to the phosphate group of substrate serine entails again the necessity of distinguishing between the γ-oxygen atoms.

It is worth mentioning that, with respect to previous theoretical studies on the phosphoryl-transfer reaction coordinates of the catalytic mechanism of PKAc, a more comprehensive approach is taken here since the extensive functionality provided by the ChemShell computational chemistry environment is used. In particular, the direct simulation of all the chemical steps involved along both the associative and the dissociative mechanisms could be studied with a more representative reaction coordinates than the ones used in a previous work of this research group.[148] Here it has not been necessary neither to optimize fractional coefficients in the R4 expression, nor to decompose the complex phosphoryl-transfer step, for instance, into simpler R2-reaction coordinates, as was carried out before.

3.1. PKAc(1CDK)-Mg_2ATP-Kemptide and PKAc(1ATP)-Mg_2ATP-Kemptide models.

3.1.1. Associative mechanism and D166A PKAc(1CDK)-Mg_2ATP-Kemptide mutant.

3.1.1.1. Energy analysis.

Specifically for the PKAc(1CDK)-Mg_2ATP-Kemptide model, Figure 3.2A shows the converged potential energy profiles obtained from the initial geometry models eq21 and M1 with O1γATP atom as the proton acceptor. Figure 3.2A also shows the converged potential energy profiles obtained from the eq71 geometry of the D166A mutant model with both the O1γATP and O3γATP as the proton acceptor atoms. The potential energy barrier obtained for the eq21 and M1 initial models are 21.3 and 27.6 kcal/mol, respectively, while for the D166A model, the potential energy profiles depict maxima of 31.8 and 32.1 kcal/mol for the simulations with the O1γATP and O3γATP atom, respectively. Figure 3.2B shows the results for other PKAc(1CDK)-Mg_2ATP-Kemptide initial models that result in higher potential energy barriers of about 40 kcal/mol. Two profiles correspond to the results obtained from initial geometry models eq21 and eq55 with the O3γATP as proton acceptor, and one to that obtained from the eq91 geometry with O1γATP as proton acceptor (with a potential energy maximum of 38 kcal/mol). In the same Figure 3.2B, but for the PKAc(1ATP)-Mg_2ATP-Kemptide model, the results for the eq4 initial geometry model with O1γATP as proton acceptor are shown too.

Interestingly, for all initial geometry models of both PKAc(1CDK)-Mg_2ATP-Kemptide and PKAc(1ATP)-Mg_2ATP-Kemptide when simulating the associative mechanism with O2γATP as the proton acceptor, the R4-reaction coordinate collapses around the expected R4 values for the transition state (-0.5 Å < R4 < +0.5 Å). This results in a set of distorted geometries with long PγATP-OγSer17 distances in which the O2γATP-HγSer bond-forming interaction disturbs both the O2γATP coordination to the M2 ion and the O2γATP-NζLys168 hydrogen bond interaction. The ε-amino group of Lys168 side chain is the only molecular fragment, other than the γ-phosphoryl group, whose position in the catalytic site changes notably along these collapsed reaction profile, and does so while not being able to maintain the O2γATP-NζLys168 interaction. Therefore, the observed incapability of the reactants to reach a catalytically competent configuration clearly points out to the role of Lys168 residue in the neutralization of the electron density accumulates in the reaction core during the phosphoryl-transfer from ATP to the substrate residue.

With respect to the results with O1γATP as the HγSer17 acceptor, it should be noted that eq55 is the only starting PKAc(1CDK)-Mg_2ATP-Kemptide geometry from which the R4-reaction coordinate simulation does not successfully reaches the products. In this particular case, from the beginning of the R4-reaction coordinate simulation the Oδ*i*Asp166–OγThr201 distance drastically decreases from 3.5 to 2.8 Å while the distance of residue Lys168 to the Ser17

substrate residue significantly increases (but neither to the γ-phosphoryl group of the ATP molecule nor to the Asp166 residue). Therefore, as the R4-reaction coordinate simulation moves toward the region of the transition state, the positively-charged ε-amino group of Lys168 gets increasingly distant from the Ser17 substrate residue. Thus, it is unable to correctly positioning the OH group of the substrate serine side chain for the proton-transfer and nucleophilic attack

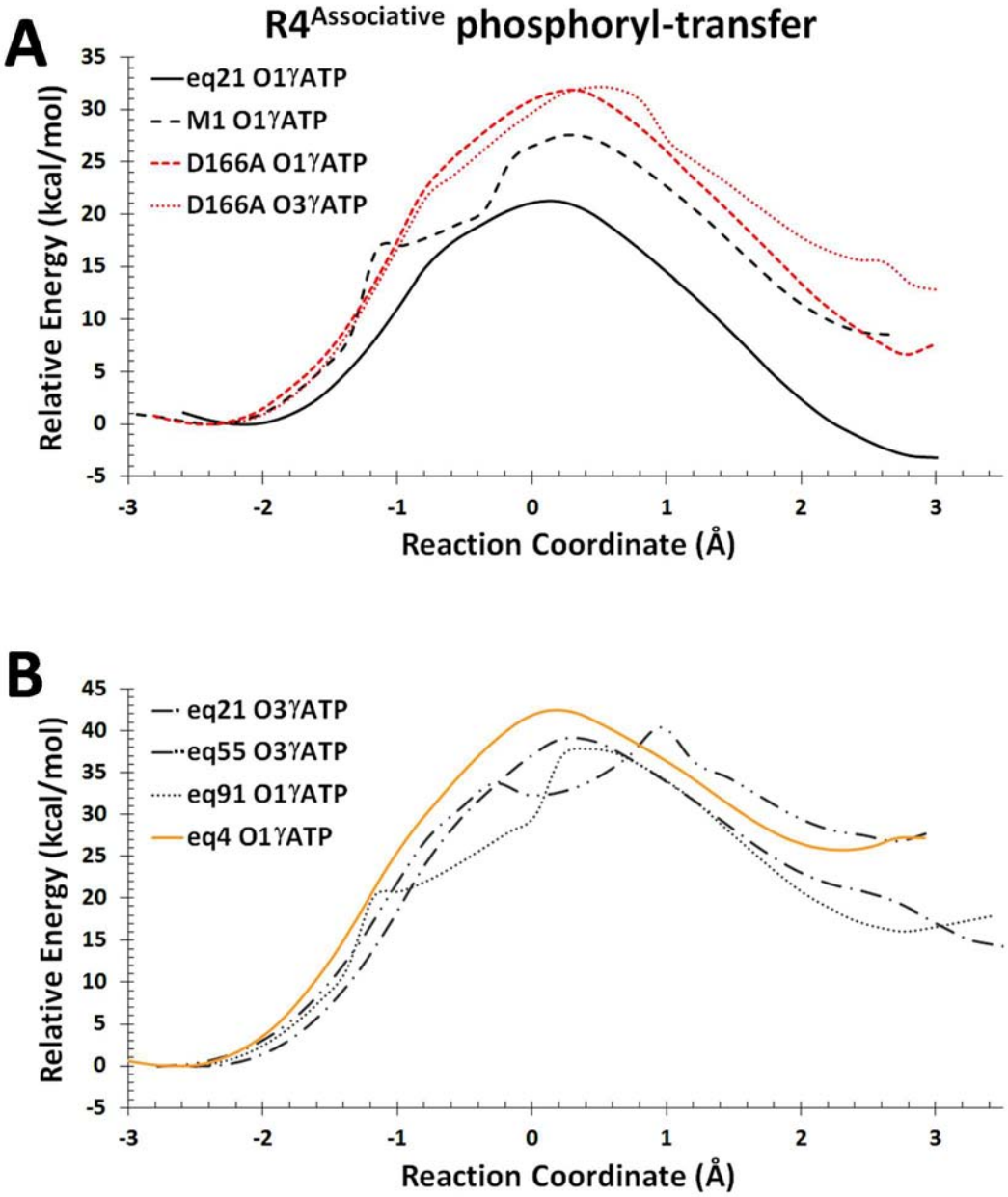

Figure 3.2. QM(B3LYP/6-31+G(d))/CHARMM potential energy profiles along the R4-reaction coordinate for the phosphoryl-transfer step via the associative mechanism. **(A)** Results corresponding to the PKAc(1CDK)-Mg_2ATP-Kemptide models that give the lowest potential energy barriers (built from geometries eq21 and M1) and for the D166A PKAc(1CDK)-Mg_2ATP-Kemptide mutant model (built from geometry eq71), with different γ-oxygen atoms of ATP as the HγSer17 acceptors. **(B)** Results corresponding to other PKAc(1CDK)-Mg_2ATP-Kemptide models that result in higher potential energy barriers (built from geometries eq21, eq55, and eq91) and one PKAc(1ATP)-Mg_2ATP-Kemptide model (built from geometry eq4), with different γ-oxygen atoms as the HγSer17 acceptors.

that takes place with the γ-phosphoryl group of ATP. Moreover, under such geometric conditions, Lys168 cannot partially neutralize either the negative charge that develops on the OγSer17 atom with the early proton-transfer. As a consequence, the system cannot approach to a product state configuration.

Regarding the simulations with O3γATP as the proton acceptor, from eq91 and M1 initial models the phosphoryl-transfer product is not reached. This is consequence of the unexpected HζLys168 abstraction by the OγSer17 atom which in turn prevents the nucleophilic attack on PγATP and causes the deviation of the reaction coordinate prior to reach R4 characteristic values of the transition state region. This result can be rationalized based on the importance of the Asp166-Lys168-Thr201 triad in the active site. The long Oγ1Thr201-Oδ1Asp166 distance (approximately 4.2 Å) in the eq91 and M1 initial geometries of the PKAc(1CDK)-Mg_2ATP-Kemptide model is directly related with the loss of the interactions of Oγ1Thr201 with NζLys168 and OγSer17 along the associative R4-reaction coordinate. Eventually, this also results in the strengthening of the active site interactions between the side chain of substrate serine and the ε-amino group of Lys168 side chain. That is, the gradual shortening of the OγSer17–NζLys168 distance leads to the consequent and inappropriate HζLys168 abstraction by the nucleophilic OγSer17 atom.

In conjunction, these first observations suggest that when the Thr201 residue is not in a suitable position for interacting with both Asp166 and Lys168 residues, the latter is not properly held within the reactive core. Since the position of Lys168 residue and its hydrogen bond network has a strong influence on the position and behavior of substrate serine side chain, variations in the relative position of the Asp166-Lys168-Thr201 triad result in distortion of the phosphoryl-transfer process along the associative reaction path.

Based on the potential energy profiles presented in Figure 3.2, the corresponding Michaelis complex structures were obtained by means of full structural optimization of the lowest-energy reactant geometry of each profile. The same procedure, but with a product-like geometry (R4 ≥ 2.5 Å, *i.e.* the ADP/phosphorylated-substrate region) as starting point, was used to localize an associative product structure for each reaction model. Finally, the structures corresponding to the energy maximum of reaction profiles were used as the starting point to locate the corresponding TS structures. The calculated potential energy differences between the localized stationary points (reactant complex, transition states and product complex) are listed in Table 3.1. From a methodologically point of view, the results in Table 3.1 suggest that the exploration of the R4-reaction coordinate forward and backward is an appropriate way to obtain a converged and smooth curve which provides suitable starting points for the direct location of the stationary points involved in the reaction.

Table 3.1. Potential energy barriers ($\Delta^{\neq}$) and potential reaction energies (ΔV_R) (in kcal/mol) for the different models of the PKAc(1CDK)-Mg_2ATP-Kemptide and its D166A mutant model at the QM(B3LYP/6-31+G(d))/CHARMM level of theory. Imaginary frequencies (in cm^{-1}) of the transition states are given in parentheses.

	O1γATP		O3γATP	
	$V^{\neq}$	ΔV_R	$V^{\neq}$	ΔV_R
eq21	21.3 (70i)	-3.2	39.0 (204i)	14.4
eq55	---	---	40.2 (74i)	26.6
eq91	37.9 (144i)	16.1	---	---
M1	27.6 (70i)	8.5	---	---
eq71 (D166A)	31.7 (123i)	4.5	32.1 (73i)	8.9

Hereinafter the results and discussion are focused on the associative mechanism of the PKAc(1CDK)-Mg_2ATP-Kemptide model with the O1γATP as the proton acceptor because the computed energy barriers given in Table 3.1 clearly favor these reaction channels over those obtained with O3γATP. Likely, within the associative mechanism, the HγSer17 transfer to O1γATP is favored over those to O3γATP and O2γATP, because the O1γATP-path causes the remaining γ-phosphoryl negative charge to accumulate in the O3γATP and O2γATP atoms, where it is more readily stabilized by means of the already existing coordination interactions with the $Mg2^{2+}$ ions. Moreover, with the O1γATP atom as the proton recipient, the system only loses the stabilizing interaction of this γ-oxygen atom of ATP with the hydroxyl group of Ser53 side chain, without directly disturbing the coordination sphere of the two Mg^{2+} ions in the nucleotide binding site.

The results obtained for the eq21 and M1 initial geometries for the PKAc(1CDK)-Mg_2ATP-Kemptide model will be analyzed in detail because there is a significant difference between their computed potential energy barriers, 21.3 and 27.6 kcal/mol, respectively. However, before focusing on them, it is important to remark that the higher potential energy barrier (37.9 kcal/mol) obtained from the eq91 initial geometry can be explained in terms of a shorter (approximately 0.2 Å) PγATP–OγSer17 distance at the transition state configuration in comparison to the eq21 model, combined with the shift of Ser17 away from the Asp166-Lys168-Thr201 triad all along the simulated reaction path. This last observation is particularly noticeable again for Lys168, whose negative charge neutralizing role within the reactive core as the γ-phosphoryl group passes from ATP to substrate serine is diminished in this particular case.

Concerning the D166A mutant system and the explanation of its residual activity in terms of the associative mechanism, the results with both the O1γATP and the O3γATP as HγSer17 final recipients (potential energy barrier of 31.7 and 32.1 kcal/mol, respectively) would be

considered here since the two chemically-distinguishable reaction channels are energetically equivalent.

In view of Figure 3.2 and Table 3.1, it is clear that the highlighted models (eq21 and M1) are energetically very different. For the eq21 model the reaction process is exergonic (with the product state located 3.2 kcal/mol below the reactant state), while for the M1 model it is endergonic (with the product state located 8.5 kcal/mol over the reactant state). For the D166A mutant models endergonic reaction profiles are also obtained, with an average potential reaction energy value of 7 kcal/mol. These differences in the results can be explained in terms of the transferred γ-phosphoryl group interactions and their evolution along the reaction profile, particularly at the product state region.

To complete the energetic analysis, single-point energy evaluations at the QM(MP2/cc-pVTZ)/CHARMM level of theory on the QM(B3LYP/6-31+G(d))/CHARMM stationary points of the selected PKAc(1CDK)-Mg_2ATP-Kemptide and D166A mutant models were performed (see Table 3.2). In all cases, the higher level potential energy barriers are lower than the DFT ones. Concerning the eq21 and M1 models, both potential energy barriers overestimate the phenomenological free energy barrier of 13.7 kcal/mol (derived from the experimental k_{cat} value of 500 s^{-1} at 296 K and pH 7[21,130]). However, in that phenomenological free energy barrier the contribution of the dissociative mechanism, and other effects, are included. In any case, the result at the QM(MP2/cc-pVTZ)/CHARMM level for the eq21 model through an O1γATP-associative path (which yields the lowest potential energy barrier among the different models studied), supports the plausibility of the associative mechanism. Moreover, when single-point energy calculations at the QM(MP2/aug-cc-pVTZ)/CHARMM level were carried out for this model, the potential energy barrier went down to 17.5 kcal/mol. In the same direction, when analyzing the two reaction coordinates simulated for the D166A mutant model, the single-point MP2 results help to explain the residual activity shown by the D166A mutation of PKAc (0.4% of the wild type specific activity in yeast PKAc)[137] in terms of the associative mechanism.

Table 3.2. Potential energy barriers and potential reaction energies corresponding to the QM(MP2/cc-PVTZ)/CHARMM single-point calculations on the QM(B3LYP/6-31+G(d))/CHARMM stationary points of the associative mechanism for the PKAc(1CDK)-Mg_2ATP-Kemptide and D166A mutant models. Energies are given in kcal/mol.

	$V^{\neq}$	ΔV_R
eq21 O1γATP	19.0	–4.8
M1 O1γATP	24.5	7.8
eq71 O1γATP (D166A)	29.1	7.4
eq71 O3γATP (D166A)	30.7	19.4

Table 3.3. Selected QM(B3LYP/6-31+G(d))/CHARMM bond distances (in Å) for the catalytic core in the optimized Michaelis complex (R), transition state (TS), and product (P) structures obtained from the energetically relevant PKAc(1CDK)-Mg_2ATP-Kemptide and D166A mutant models.

	eq21 O1γATP			M1 O1γATP			D166A eq71 O1γATP			D166A eq71 O1γATP		
	R	TS	P	R	TS	P	R	TS	P	R	TS	P
Interaction distances involved in R4												
O3βATP-PγATP	1.75	1.79	2.83	1.75	1.81	2.79	1.72	1.79	2.89	1.71	1.79	3.97
PγATP-OγSer17	3.14	2.32	1.66	3.39	2.30	1.69	3.33	2.22	1.65	3.29	2.26	1.65
OγSer17-HγSer17	0.99	1.66	2.83	0.99	1.73	2.50	0.99	1.72	2.93	0.99	1.96	2.83
O*i*γATP-HγSer17	1.77	1.01	0.99	1.77	1.00	0.99	1.80	1.00	0.99	1.78	0.98	0.98
Catalytic core interaction distances												
Oγ1Thr201-Oδ1Asp166	2.66	2.67	2.64	4.08	4.07	3.98	---	---	---	---	---	---
Oγ1Thr201-NζLys168	2.73	2.74	2.74	2.76	2.78	2.74	2.98	2.77	2.83	3.04	2.79	2.78
Oγ1Thr201-OγSer17	4.28	4.56	4.31	4.04	4.44	4.37	3.11	4.01	3.86	3.94	4.09	3.44
Oδ2Asp166-OγSer17	3.78	3.71	3.03	4.22	3.83	3.48	---	---	---	---	---	---
Oδ2Asp166-PγATP	4.27	4.22	3.68	4.20	4.16	3.74	---	---	---	---	---	---
Oδ2Asp166-OH2XW3	2.96	2.87	2.84	2.70	2.65	2.70	---	---	---	---	---	---
Oδ2Asp166-NζLys168	2.81	2.86	2.89	3.54	3.54	3.52	---	---	---	---	---	---
Oδ1Asp166-NζLys168	3.36	3.42	3.29	2.77	2.86	2.75	---	---	---	---	---	---
NζLys168-OγSer17	2.75	2.62	2.81	2.76	2.63	2.81	3.04	2.75	3.03	3.62	2.81	3.04
NζLys168-O2γATP	3.11	2.97	3.56	3.44	3.17	3.17	2.80	3.11	2.71	2.76	3.05	2.91

3.1.1.2. Interaction distances analysis.

The main structural changes taking place as the reaction goes from reactants to products through the transition state structure involve the motion of the γ-phosphoryl group of ATP, the side chain of the substrate serine, and the Mg2 ion (see Figure 3.1), in agreement with the results obtained by Valiev *et al*.[167] for a dissociative reaction pathway in their PKAc model. In this case, though, depending on the model from which the associative mechanism is simulated, there is a noticeable rearrangement of the catalytic core, mainly involving the relative position of Lys168 side chain.

The key bond distances of the QM(B3LYP/6-31+G(d))/CHARMM reactants, transition states, and products structures are listed in Table 3.3. The changes in the distances between the reactive atoms along the reaction paths indicate that in all models the simulated phosphoryl-transfer mechanism has a remarkably high associative character. From the calculated geometry of the transition state for both eq21 and M1 models, it can be seen that the distances between the γ-phosphorus and the leaving and entering γ-oxygens are 1.8 and 2.3 Å, respectively. This

means that the β-γ phosphoanhydride bond of ATP breaks late in the reaction and the nucleophilic attack of OγSer17 on PγATP occurs when the O3βATP-PγATP bond is, for all practical purposes, still formed (the equilibrium distance is 1.7 Å in the Michaelis complex structures). In this respect, the O3βATP-PγATP interaction distance is almost the same in the transition states structures localized for PKAc(1CDK)-Mg_2ATP-Kemptide and its D166A mutant models, and the same can be established for the length of the nascent PγATP-OγSer17 regardless of which γ-phosphoryl oxygen, O1γ or O3γ, acts as the proton acceptor. Furthermore, it is clear that to increase the nucleophilicity of OγSer17, the proton-transfer from the substrate hydroxyl group to one oxygen atom of the γ-phosphoryl group of ATP must happen prior the transition state configuration is achieved.

The comparison between the catalytic core interaction distance values in the second and third columns of Table 3.3 indicates that the structural parameter that clearly distinguishes eq21 from M1 model all along the simulation is the Oγ1Thr201-Oδ1Asp166 distance. Results in Table 3.3 indicate that along the entire simulated paths, the Oγ1Thr201-Oδ1Asp166 distance in the eq21 model is 1.4 Å shorter than in the M1 model, the former being that of a lower potential energy barrier (see Table 3.2). Specifically, it is observed a dependence of the Asp166 side chain orientation with respect to the substrate Ser17 and the enzyme Lys168 residue side chain positions when varying the length of the Oγ1Thr201-Oδ1Asp166 interaction. In the eq21 simulated path, Oδ1Asp166 remains farther away from the ε-amino group of Lys168 than it does along the M1 simulated path. That is because in M1 the Oδ1Asp166 atom practically does not interact with Oγ1Thr201, but does so and strongly with NζLys168 (see Oδ1Asp166-NζLys168 distance in Table 3.3). Obviously, the last interaction modifies the position of the other carboxylic oxygen in Asp166 side chain, namely Oδ2Asp166, which results in a longer Oδ2Asp166-OγSer17 and Oδ2Asp166-NζLys168 distances. Conversely, the Oδ2Asp166-PγATP distance is practically equal in both models; but, overall, in the M1 model the Asp166 side chain slightly distances from the reaction core region. In addition, Oδ2Asp166 interacts strongly with a conserved water molecule XW3 (named in the 1CDK crystallographic structure as XWAT536) through a hydrogen bond. This interaction is potentiated as a result of the direct coordination of XW3 molecule to the Mg1 ion, which activates in turn the hydrogen bond donor properties of the water molecule through strong polarization.

In the results presented here for the associative mechanism, the presence of short hydrogen bond interactions between the Lys168 side chain and both the γ-phosphate and the hydroxyl group of the substrate serine (last two rows in columns 2 and 3 of Table 3.3) suggests a contribution of Lys168 residue in the catalytic process. That is, Table 3.3 shows that from the reactants to the transition state structure of the PKAc(1CDK)-Mg_2ATP-Kemptide associative

reaction paths, the positive ε-amino group of Lys168 approaches to the serine residue of the substrate and to the ATP molecule, while keeping practically a constant distance with all the rest of residues within the catalytic core. However, in the product region, it comes back to a configuration similar to the initial one. Being the positioning of the γ-phosphate critical for catalysis, it is very significant that Lys168 is the catalytic-loop and active site residue that directly interacts with one of the γ-phosphate oxygen atoms along the phosphoryl-transfer, while remains close to the hydroxyl group of the substrate serine. In fact, there is even a strengthening of these interactions as the reaction proceeds to the transition state configuration. This can be explained by the Lys168 role in neutralizing the negative charge developed in the course of catalysis. Specifically, the nascent and rapidly increasing negative charge in OγSer17 atom during the early proton-transfer from the serine residue to the γ-phosphate of ATP. Further, in the transition state, the OγSer17 must perform a nucleophilic attack on the γ-phosphorous atom of ATP, which is surrounded by negatively-charged oxygen atoms. Hence, for the associative mechanism of PKAc, the Lys168 side chain is essential in making the nucleophilic attack easier by facilitating the correct orientation of the reactant molecular entities. That is, Lys168 residue plays a significant role in the positioning of the reactants, keeping them in close contact conformation, but also in reducing the repulsion between the negative moieties that must come close for the reaction to happen. In agreement with this catalytic role of Lys168, the mutant K168A has shown a significant reduction of the catalytic activity.[137]

When comparing the PKAc(1CDK)-Mg_2ATP-Kemptide results with those obtained for its D166A mutant model, it is observed (also in Table 3.3) that almost the unique interaction distance that differs is the Oγ1Thr201-OγSer17 one, which is clearly different all along the simulated profiles (0.5 Å longer in D166A simulations than in the eq21 and M1 models, approximately), together with the NζLys168-OγSer17 distance that is slightly longer in the D166A mutant. Specifically, in the transition state structures obtained for the D166A mutant models, all interactions of NζLys168 in Table 3.3 except the NζLys168-OγSer17 distance are equal to the calculated ones for the eq21 and M1 saddle points. Thus, in the D166A simulations, the Lys168 side chain starts moving away from ATP while approaching both Ser17 and Thr201 hydroxyl groups, but it does not get that close to the substrate serine as in the PKAc(1CDK)-Mg_2ATP-Kemptide models.

Now, the results summarized in Table 3.4 will be discussed with regard to the residues included in the conserved core of the catalytic domain. The results indicate that the Mg1 metal ion coordination shell is octahedral, consisting of a chelation interaction by 2β- and 1γ-oxygen atoms of ATP, the Asp184 side chain in a bidentate fashion, and two conserved water molecules. As it has been already mentioned, one of these water molecules forms a strong hydrogen bond

Table 3.4. Selected QM(B3LYP/6-31+G(d))/CHARMM distances (in Å) for the enzyme, nucleotide and metal ions interactions in the optimized reactant (R), transition state (TS), and product (P) structures obtained for the energetically relevant PKAc(1CDK)-Mg_2ATP-Kemptide and D166A mutant models.

	eq21 O1γATP			M1 O1γATP			D166A eq71 O1γATP			D166A eq71 O1γATP		
	R	TS	P	R	TS	P	R	TS	P	R	TS	P
NζLys72-O1αATP	2.76	2.75	2.76	2.72	2.72	2.70	2.75	2.74	2.75	2.74	2.73	2.72
NζLys72-O2βATP	2.84	2.87	2.86	2.83	2.84	2.80	2.85	2.86	2.89	2.89	2.87	2.83
NζLys72-Oε2Glu91	2.66	2.66	2.67	2.74	2.72	2.74	2.72	2.72	2.73	2.71	2.71	2.73
OγSer53-O3γATP	3.38	3.10	2.64	3.29	2.87	2.61	2.69	2.71	2.65	2.69	2.69	2.65
NSer53-O1βATP	2.90	2.81	2.76	2.89	2.81	2.87	2.75	2.73	2.76	2.78	2.78	2.79
NPhe54-O1βATP	2.79	2.80	2.77	2.85	2.83	2.84	2.75	2.76	2.79	2.76	2.75	2.80
Mg^{2+} ions coordination sphere												
Mg1-O1βATP	2.15	2.13	2.07	2.07	2.05	2.00	2.09	2.04	2.03	2.10	2.08	1.95
Mg1-O3γATP	2.02	2.06	2.13	2.03	2.09	2.14	2.12	2.19	2.13	2.05	2.11	3.73
Mg1-Oδ1Asp184	2.19	2.19	2.25	2.27	2.27	2.35	2.21	2.12	2.24	2.17	2.20	2.08
Mg1-Oδ2Asp184	2.23	2.24	2.19	2.20	2.22	2.16	2.26	2.24	2.24	2.27	2.25	2.23
Mg1-OH2XW3	2.16	2.14	2.18	2.11	2.08	2.11	2.08	2.07	2.10	2.05	2.07	2.09
Mg1-OH2XW1	2.06	2.06	2.07	2.14	2.15	2.17	2.04	2.04	2.07	2.06	2.05	2.04
Mg2-O2αATP	2.01	2.01	2.05	2.01	2.02	2.06	2.02	2.02	2.02	2.02	2.03	1.97
Mg2-O3βATP	2.33	2.28	2.03	2.25	2.20	2.01	2.28	2.20	1.99	2.34	2.24	1.98
Mg2-O2γATP	2.01	2.04	2.15	2.04	2.09	2.27	2.09	2.09	2.69	2.09	2.08	4.00
Mg2-Oδ2Asp184	2.12	2.11	2.12	2.15	2.16	2.14	2.10	2.14	2.08	2.08	2.09	2.14
Mg2-Oδ1Asn171	2.01	2.02	2.13	2.03	2.04	2.12	2.05	2.04	2.12	2.03	2.03	2.05
Mg2-OH2XW2	2.14	2.13	2.14	2.12	2.11	2.12	2.11	2.09	2.11	2.08	2.11	2.08

with Asp166 (see Table 3.3). This coordination scheme remains unchanged all along the reaction process (especially from the reactants to the transition state), what supports the importance of the Mg1 metal ion in nucleotide binding and in properly orientating ATP with respect to the nucleophilic hydroxyl group of substrate serine.[163,167]

On the other hand, in all the stationary point structures localized in this work, the Mg2 metal ion presents a distorted octahedral coordination sphere, rather than an incomplete fivefold coordination as indicated by X-ray and kinetic measurements.[21,129,147] This Mg^{2+} ion binds to the 2α-, 3β- and 2γ-oxygens of ATP, to a single carboxyl oxygen of Asp166, and to the side chain carbonyl oxygen of Asn171. Particularly, the Mg2-O3βATP interaction distance, which almost remains constant from the reactant (2.33 Å) to the transition state (2.28 Å), decreases more than ten percent of its initial value as the reaction proceeds towards the product region

(2.03 Å, see Table 3.4). That is, concomitant with the cleavage of the β-γ phosphoanhydride bond of ATP due the nucleophilic attack of OγSer17 on PγATP, the nascent and leaving ADP moiety is stabilized by the Lewis acid attack of Mg2. The initially weakly bound Mg2 metal ion strengthens its interaction with O3βATP screening in this way the negative charge which progressively accumulates on the β-γ bridging oxygen. In other words, along the associative reaction path, metal ion stabilization of the negative charge accumulation on the β-γ bridging oxygen occurs during the phosphoryl-transfer step.

As stated above, within the active site Thr201 anchors both Asp166 and Lys168 via hydrogen bonds to their side chains, such that the results of the study concerning the associative mechanism point toward the fundamental role of Thr201 being the correct spatial positioner of the versatile and catalytically functional Asp166-Lys168-Thr201 triad within the active site during the phosphorylation transfer step. In all the successful simulations carried out, the Lys168 residue bridges the ATP terminal phosphate to the substrate peptide, in a position maintained by its hydrogen bond interaction with the hydroxyl side chain of Thr201.

3.1.1.3. Electrostatic interaction energy analysis (by residue).

The relative electrostatic interaction energy of the MM residues was calculated by charge deletion analysis[51,275] as the phosphorylation reaction proceeds from the reactant complex to the transition state (based on the QM(B3LYP/6-31+G(d))/CHARMM geometries of the eq21, M1 and D166A mutant models). The results provide a good indication of the enzyme residues capability in stabilizing or destabilizing the transition state.

Accordingly, the electrostatic interaction energy between a given MM residue and the rest of the QM/MM system was determined with QM(B3LYP/6-31+G(d))/CHARMM single-point energy calculations for the reactant and the transition state structures, respectively. The difference between the corresponding reactant state and transition state results indicates the contribution of each residue to the reaction barrier.[165-166] The residue thus stabilizes the transition state if such difference yields a negative number, and vice versa. The results for the individual MM residues and for the conserved crystallographic water molecules within a 10 Å radius sphere from the PγATP atom are shown in Figure 3.3 for the different models of the enzyme-substrate system.

Results in Figure 3.3A (*i.e.* eq21 and M1 PKAc(1CDK)-Mg_2ATP-Kemptide models) show that the enzyme and substrate residues surrounding the active site up to 10 Å radius from the ATP γ-phosphorous, have a greater net contribution to the transition state stabilization through electrostatic interactions in the eq21 model than in the M1 one, as the total accumulated net stabilization effect is of -4.6 and -2.3 kcal/mol, respectively. This result helps to explain the lower

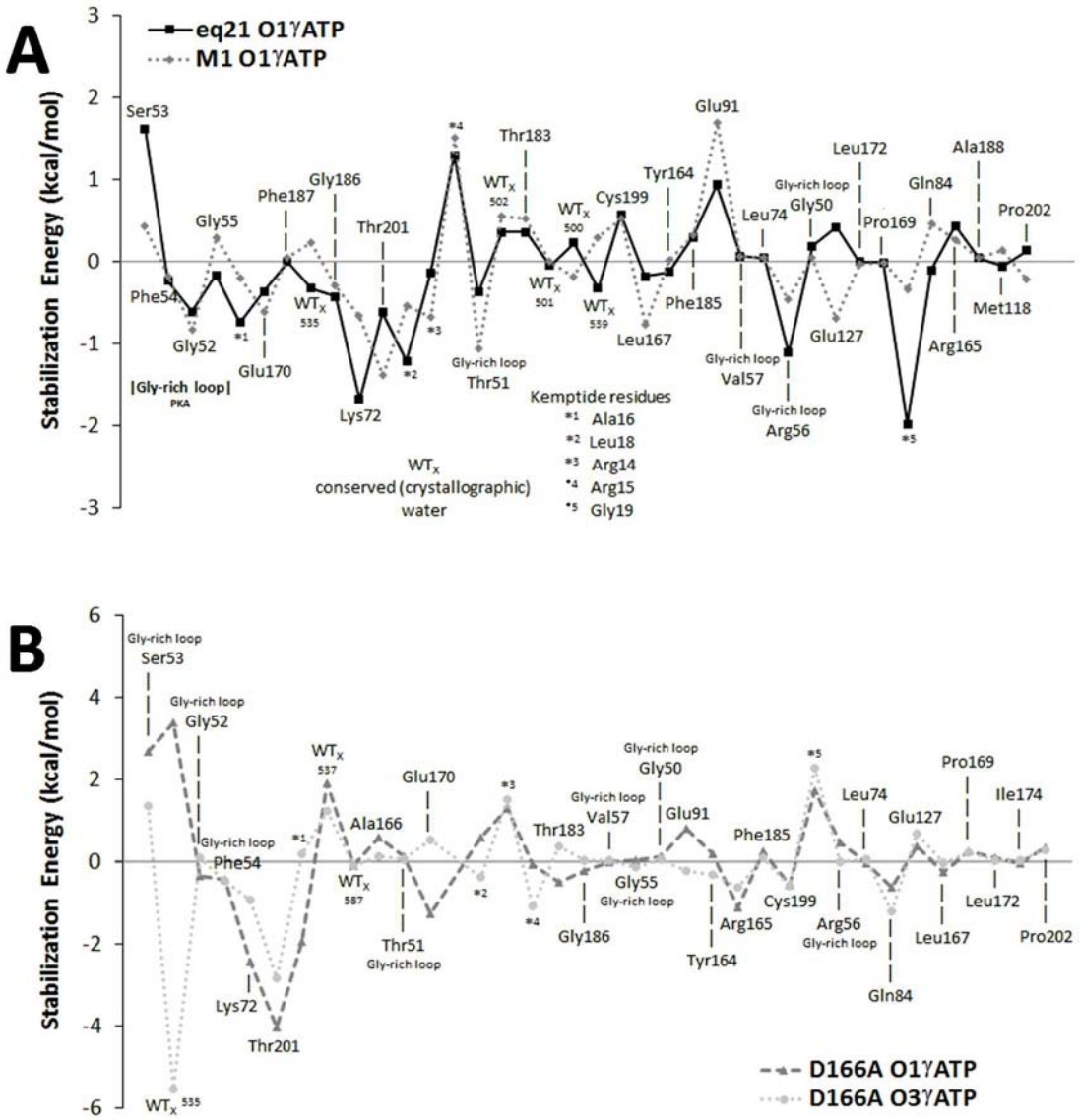

Figure 3.3. Individual MM-residue electrostatic contribution to the transition state stabilization and destabilization (residues are ordered as function to its appearance while moving away from PγATP. **(A)** eq21 and M1 PKAc(1CDK)-Mg_2ATP-Kemptide models (O1γATP as HγSer17 proton acceptor). **(B)** eq71 D166A mutant models with O1γATP and O3γATP as HγSer17 proton acceptors, respectively.

energy barrier obtained for the eq21 model simulated path. Such behavior is mainly due to a considerable catalytic advantage resulting from: (1) the Lys72 interaction with the ATP phosphate tail (detailed below); and (2) from substrate Kemptide residues interactions with motifs of the enzyme that directly bind the substrate, principally, with the Gly-rich loop and with the array of anionic Glu residues acting as peptide substrate-PKAc enzyme anchorage points (located along the small and large lobes that form the conserved core of the catalytic domain). That is, residues in the substrate peptide (some of which bear a charged side chain, as Arg15 and Arg16 do) affect the stabilization of the transition state, so that, to sum up, the overall catalytic effect of the Kemptide residues is to stabilize by 2.8 kcal/mol the eq21 model transition

state (in comparison, the net stabilizing effect in the M1 model is 0.2 kcal/mol). On the other hand, the results in Figure 3.3B show similar trends for all the MM residues in the two D166A mutant reaction pathways -with O1γATP and O3γATP atoms as the proton acceptors- thus, this analysis provides an explanation for their almost equal potential energy barriers.

The Gly-rich loop, owing to its extended ‘‘U’’ shape spatially aligned with ATP triphosphate tail, is capable of tightly enfolding the nucleotide by means of both hydrogen bonds and hydrophobic interactions. According to Figure 3.3, for the highlighted models of PKAc(1CDK)-Mg_2ATP-Kemptide and its D166A mutant, of the eight individual Gly-rich loop residues (50–57) present in this relative interaction energy analysis, only Ser53 exhibits a significant degree of transition state destabilization. In all simulated models, this particular residue interacts via its backbone amide hydrogen with the β-phosphate group and via the oxygen atom of the hydroxyl group of its side chain with the γ-phosphate group, specifically with the O1γATP atom, regardless if HγSer17 is transferred as a proton to that particular γ-oxygen atom of ATP or to the O3γATP one (see NSer53-O1βATP and OγSer53-O1γATP distances in Table 3.4). Experimentally,[153] it has been shown that the backbone interaction is the most important, because modifying the side chain scarcely alters the catalytic features of PKAc. However, for all the simulation models, it is the Ser53 side chain interaction with the terminal phosphate group which determines its optimal position for catalysis through the associative mechanism, thus supporting the structural role of Ser53.

Regarding the results obtained just for the PKAc(1CDK)-Mg_2ATP-Kemptide models, the higher destabilization in eq21 than in M1 might be due to the larger OγSer53-O3γATP distance in the former (see Table 3.4), so that in the latter the involved hydrogen bond represents a slightly higher stabilizing factor of the transition state. The other Gly-rich loop residues show a mild catalytic contribution, with the most prominent transition state stabilization coming from Arg56 residue for the eq21 model and from the Thr51 for the M1 model (although Gly52 also contributes significantly in both models). It is noteworthy, however, that for both PKAc(1CDK)-Mg_2ATP-Kemptide models almost every residue in the Gly-rich loop (with the clear exception of Ser53, as has been noted above) contributes to stabilize the transition state to some degree, indicating a collective influence and a contribution to the lowering of the potential energy barrier. That is, the simulation results indicate that the catalytic role of the Gly-rich loop comes from its effect as a whole, rather than from a single residue action. Summarizing, the net effect in the PKAc(1CDK)-Mg_2ATP-Kemptide models is that the transition state is stabilized by the Gly-rich loop with -0.6 kcal/mol in eq21 and -1.7 kcal/mol in M1. On the other hand, in the D166A models, additionally to Ser53 destabilization, only Gly52 and Phe54 show a small contribution to the transition state stabilization, while the other Gly-rich loop residues practically have no

influence at all on this regard. As a consequence, the reaction barrier is increased by 1.1 kcal/mol in the D166A O1γATP model and by 2.7 kcal/mol in the D166A O3γATP model.

Lys72 and Glu91 are another two conserved charged residues in the small lobe. The geometric results indicate that Lys72 anchors α- and β-phosphate and forms a salt bridge with Glu91 (see Table 3.4). The results in Figure 3.3 indicate that Lys72 substantially stabilizes the transition state through electrostatic interactions, whereas Glu91 causes a moderate opposite effect. The stabilization of the transition state by Lys72 is consistent with studies showing that K72A mutation led to an approximate 800-fold decrease in V_{max} with a fivefold increase in K_M (ATP), so that Lys72 facilitates the phosphorylation process without affecting the binding of ATP.[137] For Glu91, the results indicate that its role is to ensure the proper positioning of the flexible Lys72 side chain in order to maximize stabilizing interaction of the latter with the ATP phosphate tail, which in turn might counterbalance Glu91 destabilizing influence. Specifically, in the eq21 model the global contribution of those two PKAc conserved residues lowers the potential energy barrier by 0.74 kcal/mol, while in the M1 model a 1.04 kcal/mol destabilizing effect was calculated. Furthermore, for the D166A model the total contributions of Lys72 and Glu91 to lower the potential energy barrier are 1.1 and 1.6 kcal/mol for the O1γATP and D166A O3γATP associative reaction paths, respectively.

Accordingly to the electrostatic transition state stabilization results in Figure 3.3A, Thr201 encompasses additional potential energy barrier lowering in all PKAc(1CDK)-Mg_2ATP-Kemptide and D166A mutant simulated reaction paths. For the PKAc(1CDK)-Mg_2ATP-Kemptide simulations, taking into account that the Thr201 residue is farther away from Asp166 (see Table 3.3) in the M1 simulation than in the eq21 counterpart and the Asp166-Lys168-Thr201 triad is therefore not properly positioned within the active site (which explains the higher energy barrier for the corresponding M1 O1γATP reaction path), it is surprising that its electrostatic contribution to the transition state stabilization is higher in the M1 model. Here, it is proposed that the foregoing is a result of a more favorable position of Thr201 in the transition state in comparison with that in the reactant complex, something definitely not observed along the O1γATP reaction path for the eq21 model wherein Thr201 keeps a very stable configuration all along the simulation. Regarding the results for the D166A model, the Thr201 electrostatic contribution to the transition state stabilization is higher than in the eq21 and M1 PKAc(1CDK)-Mg_2ATP-Kemptide models, probably because in the mutated models the Oγ1Thr201–OγSer17 interaction is relatively stronger since the Oγ1Thr201–Oδ1Asp166 interaction is no longer present. In addition, in Figure 3.3B it can be seen that Thr201 is the residue within the MM region that contributes the most to the electrostatic stabilization of D166A O1γATP model transition state.

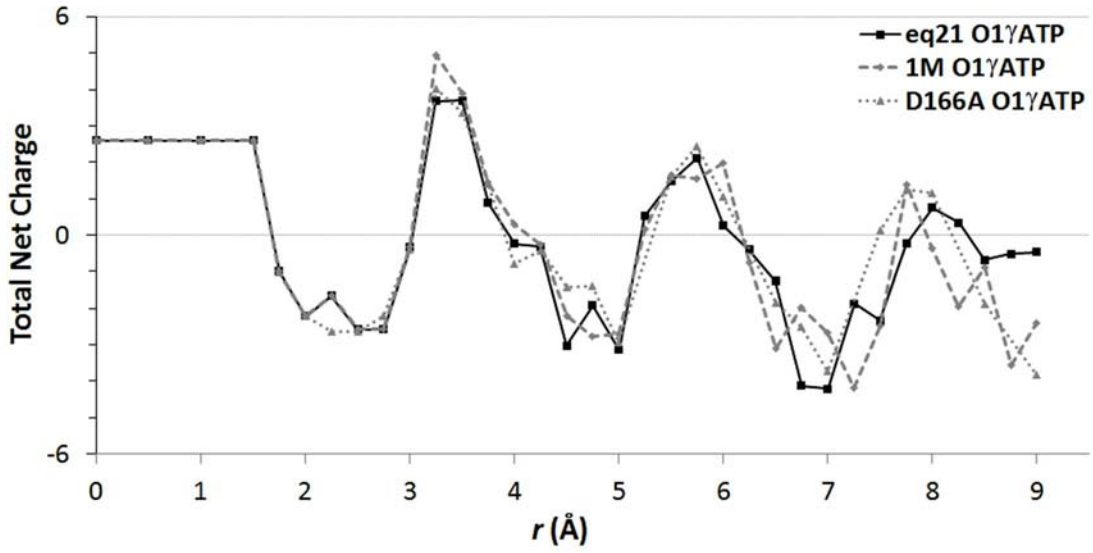

Figure 3.4. Charge balance calculation in the active site of the transition state structures localized for the phosphoryl-transfer reactions following an associative mechanism with the O1γATP atom as the recipient of the proton from substrate serine: PKAc(1CDK)-Mg_2ATP-Kemptide models eq21 (solid black line) and M1 (dotted square line), and D166A mutant model (dotted triangle line). The charge is summed over all atoms within a sphere of increasing radius *r*, the center of which is the transferring γ-phosphorous atom.

3.1.1.4. Charge balance hypothesis analysis.

In order to complete the study on the associative mechanism, the transition state complexes calculated and characterized for the reaction paths with O1γATP as the proton acceptor and for the eq21 and M1 PKAc(1CDK)-Mg_2ATP-Kemptide models, and the D166A mutant model, have been used to test the charge balance hypothesis in the phosphoryl-transfer reaction catalyzed by PKAc. The importance of electrostatic interactions in biological catalysis has been supported by experimental data for diverse enzymes. Specifically, in the case of the kinase-catalyzed phosphoryl-transfer, the charge balance is particularly important because the nucleophilic attack on a dianionic phosphate group is unfavorable in terms of an inherent Coulombic repulsion, condition described as the anionic shield.[217,276]

The charge distribution across the entire enzyme was calculated by summing up the partial charges within a sphere of a defined radius centered in the γ-phosphorous atom. For atoms within the QM region the NPA charges calculated at the QM(B3LYP/6-31+G(d))/CHARMM level were used, while for those in the MM region the charges used were the CHARMM22 parameters. Analysis of the charges in the vicinity of the transition state complexes active site fully supports the adherence of the PKAc(1CDK)-Mg_2ATP-Kemptide and its D166A mutant models to the charge balance hypothesis. In Figure 3.4, the net charge oscillates around a zero charge value for all models, being the trend and behavior slightly more similar for the M1 and the D166A mutant models. This observation is significant when considering the lower potential energy barrier obtained for the eq21 model, which also differs energetically from the other two

models. However, in general, the charge balance hypothesis contributes to make possible the nucleophilic attack on a dianionic phosphate group in spite of the Coulombic repulsion involved. Thus, it might be possible that kinases have evolved to counteract the repulsion through fine-tuning the active site to the charge of the transition state structure.

3.1.2. Dissociative mechanism.

As mentioned before, the same MD-generated structures of PKAc(1CDK)-Mg_2ATP-Kemptide and PKAc(1ATP)-Mg_2ATP-Kemptide models have also been considered here as appropriate starting points to simulate the reaction path of the dissociative phosphoryl-transfer catalyzed by PKAc. That is, it is considered here that reactive Ser17 side chain of substrate Kemptide, the γ-phosphoryl group of ATP, and the carboxylated side chain of Asp166 from PKAc are close enough to one another to allow both the associative and the dissociative mechanisms, neither directly favoring nor excluding any of them. Therefore, from each initial structure already chosen, the phosphoryl-transfer following a dissociative mechanism was simulated for several PKAc-Mg_2ATP-Kemptide models at the QM(B3LYP/6-31+G(d))/CHARMM level of theory.

However, as it happened for the associative counterpart, not all initial structures gave rise to reaction profiles appropriate for the analysis of the dissociative mechanism. Specifically, for the PKAc(1CDK)-Mg_2ATP-Kemptide model just the eq21 initial structure led to the simulation of both the phosphoryl- and proton-transfer steps with appropriate potential energy barriers, while for the PKAc(1ATP)-Mg_2ATP-Kemptide model the eq4 initial structure was the only one from which it was possible to define the phosphoryl-transfer step. The reason why most of the initial structures (eq55, eq91 and M1 for PKAc(1CDK)-Mg_2ATP-Kemptide model; eq49 and eq190 for PKAc(1ATP)-Mg_2ATP-Kemptide model) fail in the description of the dissociative mechanism is likely due to the distancing of Thr201 residue from the reaction core entities in all of them. In particular, for Asp166 and Lys168 residues losing their corresponding hydrogen bond to Thr201 results in their inability to maintain a fixed position within the active site. This, in turn, translates into a side chain conformations unsuitable to participate effectively, along the phosphoryl-transfer step, as a general-base catalyst (*i.e.* receiving the proton from the nucleophilic hydroxyl group of substrate serine) in the case of Asp166 residue, and as a positioning and charge stabilizing agent in the case of Lys168 residue.

On the other hand, in all the unsuccessful simulations of the phosphoryl-transfer step for the PKAc(1ATP)-Mg_2ATP-Kemptide model, without the spatial anchorage exerted by the Thr201 residue, the carboxylated side chain of the Asp166 residue showed a wide range of motion. Thus, while the proton-transfer from OγSer17 to Oδ2Asp166 takes place, the carboxylate group of Asp166 starts moving away from the reaction core, with Oδ2Asp166 progressively forming a

hydrogen bond to the ε-amino group of Lys168, which also lacks the interaction to Thr201. This happens concomitant with other changes in the hydrogen bond network within the active site. Oδ2Asp166 loses at the same time its hydrogen bond with the crystallographic water that is part of the Mg1 coordination too. When this interactions breaks down the crystallographic water then establishes a strong hydrogen bond with O2γATP atom, which loses in turn its coordination bond to Mg2. The latter likely represents a change in the structure of the reaction core so harsh that the reaction coordinate collapses even before phosphoryl-transfer completion.

3.1.2.1. Phosphoryl-transfer step.

3.1.2.1.1. Exploration of the potential energy surface.

As indicated in the Methodology section, the potential energy profiles have been calculated by means of constrained optimizations along the corresponding reaction coordinate and going forwards and backwards (from reactants to products and vice versa) until convergence to the reaction path with the lowest potential energy barrier is reached. That sequence of phosphoryl-transfer potential energy profiles calculated from the eq21 starting structure of PKAc(1CDK)-Mg_2ATP-Kemptide model are shown in Figure 3.5 as example. In this particular case, 12 potential energy profiles were computed (6 forward and 6 backward). Eight of those potential energy profiles are reaction paths for the phosphoryl-transfer step with the corresponding transition state structures but four of them are not.

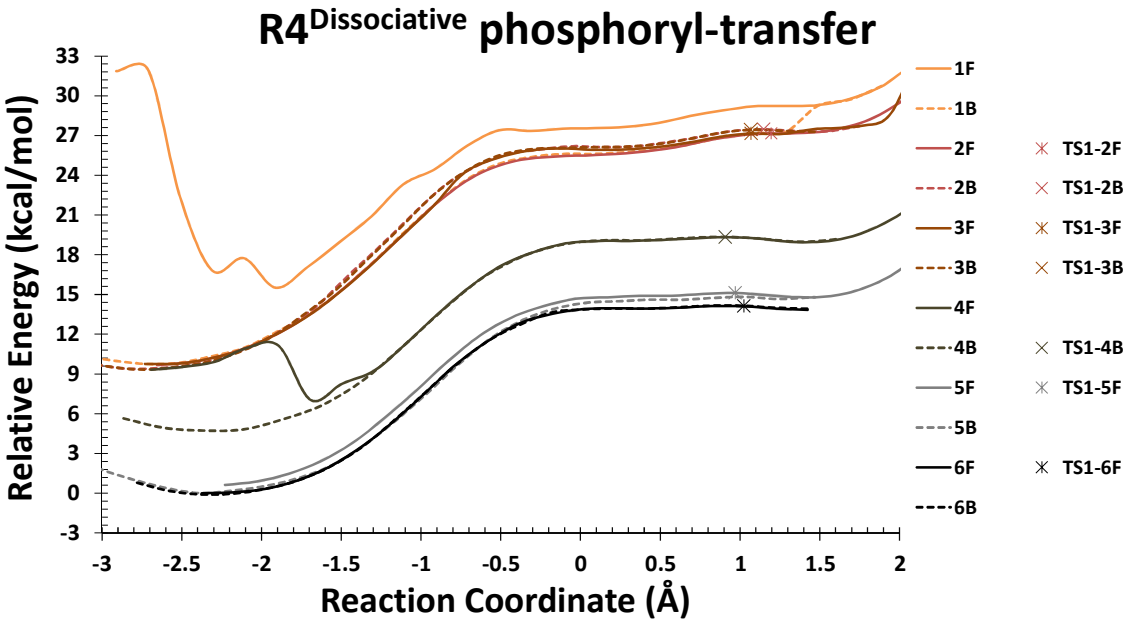

Figure 3.5. QM(B3LYP/6-31+G(d))/CHARMM potential energy profiles along the R4-reaction coordinate for the phosphoryl-transfer step following the dissociative mechanism. Results corresponding to the eq21 PKAc(1CDK)-Mg_2ATP-Kemptide model. The location of the transition state structures is indicated with asterisks following the color code of the potential energy profiles.

As can be seen in Figure 3.5, the first forward and backward potential energy profiles (1F and 1B, respectively) cannot be considered reaction paths because the corresponding transition states could not be located. In contrast, the potential energy profiles named as 2F, 2B, 3F, and 3B are phosphoryl-transfer reaction paths with a transition state structure which has been located for each one using as the starting point of the TS search the structure corresponding to the reaction path energy maximum. Those TS structures have been denoted, accordingly, TS1-2F, TS1-2B, TS1-3F and TS1-3B. The potential energy barriers for the phosphoryl-transfer step at those four transition states relative to their respective minima are quite similar (values in between 17.4 and 18.1 kcal/mol) and they are located at R4 values in between 1.07 and 1.20 Å (see Figure 3.5). Of the next six potential energy profiles only the one denoted as 4F cannot be considered as a reaction path for the phosphoryl-transfer process. In contrast, the potential energy profiles named conversely are reaction paths with their corresponding transition state structures (although TS1-6B is not shown because it coincides geometrically and energetically with TS1-6F). Those last transition states are located somewhat earlier on the R4-reaction coordinate and their corresponding potential energy barriers are lower (values in between 14.1 and 14.6 kcal/mol) in comparison with those of the previous set of transition states. Following this strategy the final obtained reaction path with the lowest potential energy barrier is the one denoted as 6F (as indicated above, 6B in the backward direction is coincident with 6F). The TS1–6F structure imposes the lowest barrier for the phosphoryl-transfer step with a value of 14.1 kcal/mol which practically matches the value corresponding to the potential energy maximum so validating the convergence of the reaction path. The analysis of this TS structure reveals that in the dissociative mechanism the proton is not promptly shifted from the substrate hydroxyl to the nascent phosphoryl group, rather it is delivered to the carboxylate group of the highly conserved Asp166 that is acting as a concerted catalytic base. This proton-transfer takes place in this PKAc(1CDK)-Mg_2ATP-Kemptide model without additional energy cost. As the formation of the bond between the γ-phosphoryl group and the serine side chain progresses, the acidity of the serine hydroxyl group increases, and that proton-transfer also increases the nucleophilicity of the substrate oxygen atom during its attack on the electrophilic γ-phosphorous atom.

As the rest of reaction paths, the 6F pathway describes an endoergic step, with the product of the phosphoryl-transfer having a potential energy of 13.8 kcal/mol over the reactant complex (so the potential energy barrier for going back to the reactant complex is really small, 0.3 kcal/mol). The reactant complex stationary point structure (R_a) was obtained by means of full DFT/MM structural optimization of the lowest-potential energy geometry of the 6F reaction path. The same procedure, but with a product-like geometry (R4 ≥ 1.0 Å *i.e.* the

ADP/phosphorylated-substrate region) as the starting point, was used to localize a phosphoryl-transfer product structure (P1). From those directly located stationary points an endoergicity of 13.8 kcal/mol was obtained. This value matches that obtained from the analysis of the reaction path, so confirming again its convergence.

At this point it should be discussed the physical meaning of the stationary points located along the 6F pathway. Both TS1 and P1 are mathematically well-characterized transition state and product structures, respectively, in what refers to the gradient and number of negative eigenvalues of their Hessian matrices, according to what is described in the methodology. However, the very small depth of the P1 well indicates that P1 cannot be considered as an actual minimum energy structure from the chemical point of view. As a matter of fact, the inclusion of the zero-point energy (ZPE) correction shows that the lowest vibrational level of P1 would already overcome the energy barrier imposed by TS1 (although it has to be noted that the harmonic approach used to calculate this ZPE is not adequate for such a shallow well). Anyway, beyond the strict mathematical topology of this region of the potential energy surface, it can be concluded that these results indicate the existence of a very flat potential energy region corresponding to the zone where the migrating phosphoryl group is already forming its new bond with the OγSer17. Thus, in this PKAc(1CDK)-Mg_2ATP-Kemptide model, P1 turns out merely to be a structure more advanced than TS1 along the reaction coordinate that can be useful to describe how the chemical process advances. This makes evident that this region does not contain the final stable phosphokemptide product yet.

The eq21 initial structure and the converged reaction path share in common a characteristic that resembles the trend already found for the associative mechanism. That is, the Thr201 residue anchors along the phosphoryl-transfer step both Asp166 and Lys168 via hydrogen bonds to their side chains, and thus, it is possible to hypothesize that the presence of the Asp166-Lys168-Thr201 catalytic triad stabilizes the phosphoryl-transfer transition state. This will be further analyzed below with respect to the interaction distance analysis. In contrast, the potential energy profiles obtained from the other initial structures, i.e. eq55, eq91 and M1, present maxima as high as 49.3, 38.7 and 23.7 kcal/mol at R4 values of 1.27, 1.20 and 0.52 Å, respectively. In view of these high potential energy values in comparison with the phenomenological free energy barrier for the phosphoryl-transfer process, these simulated reaction channels are discarded. However, the visual inspection of the reactant structures allows us to hypothesize about the reason for the unsuccessfulness of the mentioned structures. In all of them (eq55, eq91 and M1) and in comparison to the successful eq21 structure, the Thr201 residue is farther away from Asp166, and in the eq91 and M1 structures also from the Lys168 residue (see Table 3.5). On the other hand, in the eq55 structure, the value of the dihedral angle

Table 3.5. Interaction distances (in Å) within the three residues of the catalytic triad at the four PKAc(1CDK)-Mg_2ATP-Kemptide initial structures. Intermolecular dihedral (in degrees) between Asp166 and the γ-phosphorous atom of ATP.

	eq21	eq55	eq91	M1
Oγ1Thr201-Oδ1Asp166	2.73	3.78	4.09	4.01
Oγ1Thr201-NζLys168	2.79	2.75	3.66	3.32
Oδ2Asp166-NζLys168	4.15	2.81	3.46	3.55
Oδ2Asp166-OγSer17	2.64	3.50	2.84	2.93
NζLys168-O2γATP	3.41	3.42	2.97	2.83
NζLys168-OγSer17	2.67	3.03	2.83	2.83
$dihedral_{CβAsp166\text{-}CγAsp166\text{-}Oδ2Asp166\text{-}PγATP}$	144.12	-78.27	133.15	129.60

between Asp166 and the PγATP is significantly different from the value of such geometric parameter in the eq21 structure. Moreover, this geometric disposition is maintained along the whole phosphoryl-transfer profiles and indicates a clear difference in the orientation and interaction of the catalytic residues between the eq21 structure and the other models. In the case of eq55, corresponding to the highest potential energy profile obtained, the loose interactions between the active site residues result in a longer distance between the reactant moieties, and the potential energy profile exploration had to be initiated at R4 values of about -4 Å. In the properly-formed catalytic triad (that for PKAc(1CDK)-Mg_2ATP-Kemptide only appears in the eq21 initial structure), Thr201 anchors both Asp166 and Lys168, giving to Asp166 the appropriate orientation to act as an acid–base catalytic residue, and to Lys168 the appropriate position to bridge the reactant moieties together, that is, the Ser17 residue side chain and the γ-phosphoryl group of ATP. Therefore, from the analysis just described above, it is concluded that the unsuccessful phosphoryl-transfer profiles from eq55, eq91 and M1 initial structures might be associated to a distance of about 4 Å between Asp166 and Thr201 residues which prevents the formation of the catalytic triad. These results are in agreement with experimental observations.[147]

While performing the exhaustive exploration along the R4-reaction coordinate (Figure 3.5) in order to accomplish convergence to the reaction path with the lowest potential energy barrier, a different or geometrically distinguishable reaction zone was reached. This structural change is the cause of the energetic bump observed when following the potential energy profile denominated as 4F (see Figure 3.5), and it is a molecular rearrangement that is maintained in the following reaction paths (that is, 4B, 5F, 5B, 6F and 6B). From now on R_a it will be used to refer to the reactant complex stationary point of the 6F reaction path after the structural rearrangement, and R_b will denote the reactant complex stationary point of the 3F reaction path

before the structural change.

As shown in Figure 3.6, the main geometric difference between the R_a and R_b reactant complexes is the relative distance of the Lys168 side chain ε-amino group to the carboxylate group of the Asp166 side chain and to the O2γ atom of the terminal phosphate of ATP, along with the Lys168 side chain dihedral Cγ-Cδ-Cε-Nζ. In the reduced view of the active site at R_a shown in Figure 3.6A, Lys168 is in a more distant position to such groups than in the reduced view corresponding to R_b (Figure 3.6B). The Lys168 dihedral Cγ-Cδ-Cε-Nζ takes values of 161.41

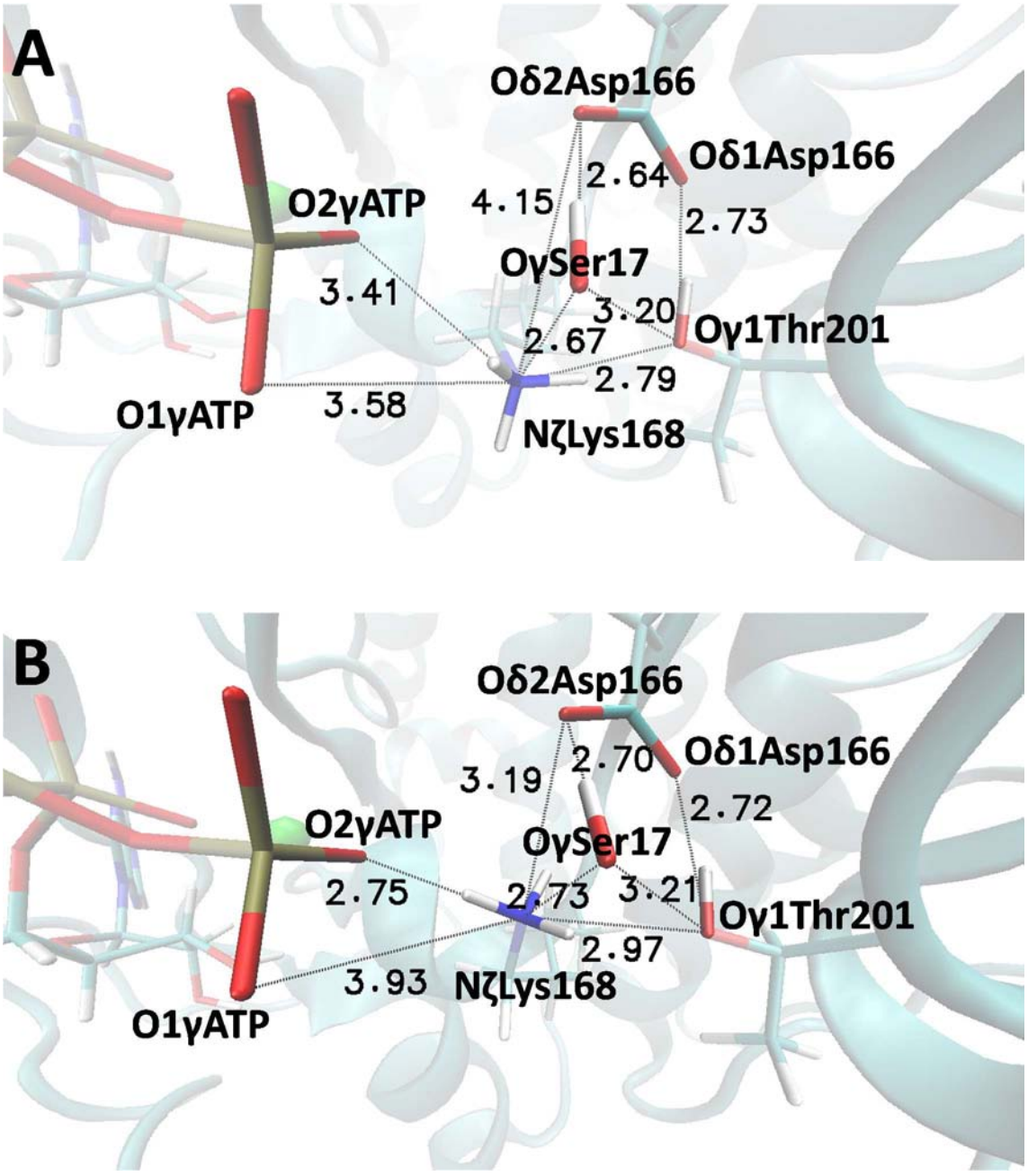

Figure 3.6. Hydrogen bond interactions and relevant heavy-heavy atom distances involving the three residues of the catalytic triad Asp166-Lys168-Thr201 and the O2γATP, O3γATPand OγSer17 atoms. **(A)** At the R_a minimum potential energy structure. **(B)** At the R_b minimum potential energy structure.

and 74.71 at R_a and R_b, respectively, which correlate with the different orientation of the Lys168 side chain in the two minima. Those differences are maintained along the whole phosphoryl-transfer profiles. Therefore, it is concluded that the phosphoryl-transfer step is energetically favored -potential energy barrier about 3 kcal/mol lower- as Lys168 is farther away from Asp166 and from the O2γATP atom (the latter particularly when the phosphoryl-transfer it is completed). This result can be seen as contradictory to the proposed catalytic role of the catalytic triad, but one has to realize that, first, the formation of the catalytic triad, that is, a bridge between Lys168 and Asp166 residues through the Thr201 residue, is independent of the Asp166-Lys168 distance; and second, a too short distance between Asp166 and Lys168 reduces the basic character of Asp166 and might be the cause of the higher potential energy barrier of the profiles related to R_b. In addition, and as will be discussed below, the NζLys168-O2γATP distance seems to determine the success of the overall reaction channel.

In summary, from the R_a structure we have obtained the lower potential energy barrier at the QM(B3LYP/6-31+G(d))/CHARMM level for the phosphoryl-transfer step related to the dissociative mechanism. So, from now on, only the results obtained from this structure will be reported and discussed in the main text for the PKAc(1CDK)-Mg_2ATP-Kemptide model, unless stated otherwise. To complete the energetic analysis we have performed single-point energy evaluations at the QM(MP2/cc-pVTZ)/CHARMM level of theory on the QM(B3LYP/6-31+G(d))/CHARMM stationary points. The high level potential energy barrier and reaction potential energy values (10.9 kcal/mol and 10.4 kcal/mol, respectively) are somewhat lower than the DFT ones.

3.1.2.1.2. Structural analysis comparison between theory and experiments.

The increasing number of crystallographic structures available in the Protein Data Bank for diverse complexes of the wild type PKAc with several ligands give us the opportunity to compare some of our theoretically localized stationary point structures (reactants, transition states and products) with crystallographic models of the different steps of the catalytic phosphoryl-transfer. This is especially applicable to the models based on the 1ATP crystallographic structure,[100,171] because Taylor and coworkers have crystallized PKAc complexes of the same species (*Mus musculus*) that serve as transition state and ATP-hydrolysis product analogs, with ID numbers 1L3R[79] and 4DH5,[164] respectively. However, the successful model in this Thesis comes from the *Sus scrofa* PKAc (1CDK crystallographic structure).[175] The structural comparison between the reactant complex (R_a) defined in this work for the eq21 PKAc(1CDK)-Mg_2ATP-Kemptide model and that obtained from the eq4 PKAc(1ATP)-Mg_2ATP-Kemptide model it is shown in Figure 3.7. The RMSD between both structures calculated for all backbone atoms

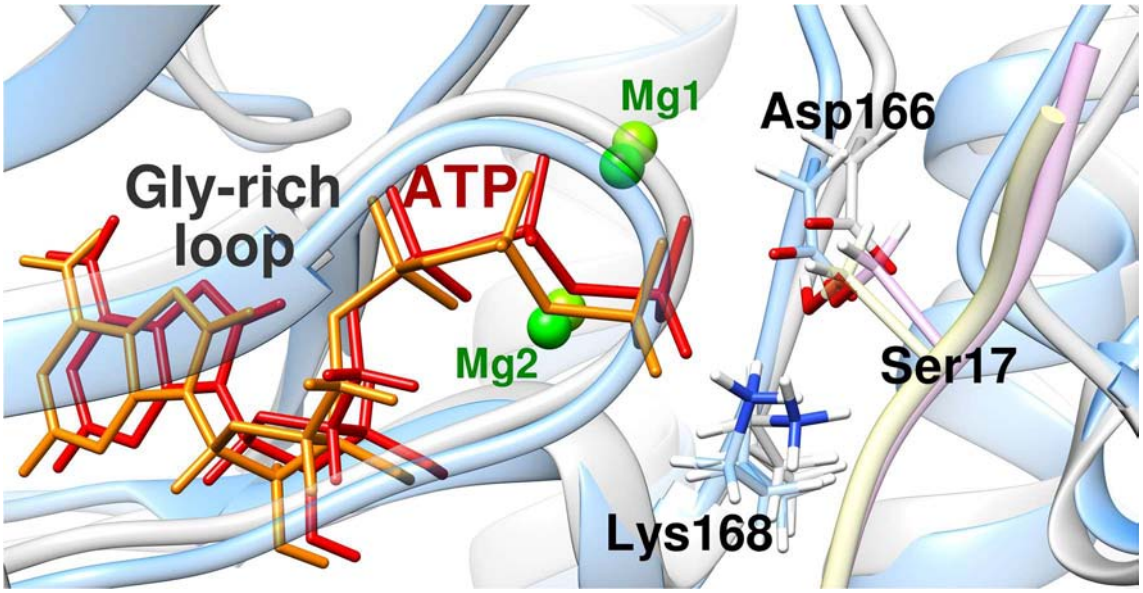

Figure 3.7. Overlay between the eq21 PKAc(1CDK)-Mg_2ATP-Kemptide model at R_a and that obtained from eq4 PKAc(1ATP)-Mg_2ATP-Kemptide model as initial structure. In R_a, PKAc is depicted in ribbon style and colored in light purple, the Mg^{2+} ions are shown as lime balls, the ATP molecule is depicted in licorice style and red color, and side chains of Ser17, Asp166 and Lys168 are depicted in licorice style and colored by atom type. Same depiction styles are used for the eq4 initial structure but PKAc is colored in light cyan, the Mg^{2+} ions in green, and the ATP molecule in orange.

within a sphere of 15 Å centered at the PγATP atom is 0.924 Å. Such value confirms the similarity between the two compared stationary points.

The significance of this similarity is that it allows to use the *Mus musculus* PKAc crystals as a reference for the theoretical 1CDK-derived model. Consequently, we present in Figures 3.8A and B the overlay images of our theoretically determined transition state and product complex of the phosphoryl-transfer step and the corresponding crystallographic structures.

As for the phosphoryl-transfer transition state comparison (Figure 3.8A), the RMSD between both structures was calculated. The small value obtained of 0.764 Å reflects the similarity between the crystallographic and the PKAc(1CDK)-Mg_2ATP-Kemptide model-based structures. The most notable difference entails the relative position of the metal-trifluoride that mimics the γ-phosphoryl group in the 1L3R[79] transition state analogue structure (which from now on will be referred as TSA) and that of the γ-phosphoryl group in our calculated geometry (TS1). In TSA, the metal-trifluoride has a planar configuration and is in an equidistant position (about 2.3 Å) to the donor and recipient oxygen atoms (O3βATP and OγSer21, respectively), which in turn occupy the apical positions of the trigonal bipyramidal coordination of the metal atom. In TS1, the γ-phosphoryl group also has a planar configuration with the phosphorus atom bearing a similar trigonal bipyramidal coordination, but the distances to the donor and recipient oxygen atoms are 2.84 and 1.86 Å, respectively (see Table 3.6). The foregoing points toward a more dissociative character for TS1 than for TSA.

Regarding the 4DH5 product analog, Kovalevsky *et al.*[164] pointed out that it represents a transient stage in the reaction after the hydrolysis of ATP but before the complete transfer of the released γ-phosphoryl group to the substrate Ser21 residue. This group imposes in turn an electrostatic effect on the surrounding residues due to its large negative charge. This fact may explain the difference in the relative positions of the highlighted residues in the superposition of such product analog and our calculated P1 structure (see Figure 3.8B), although the calculated RMSD value is quite small (0.691 Å). Meaningfully, within the active site of both structures, the

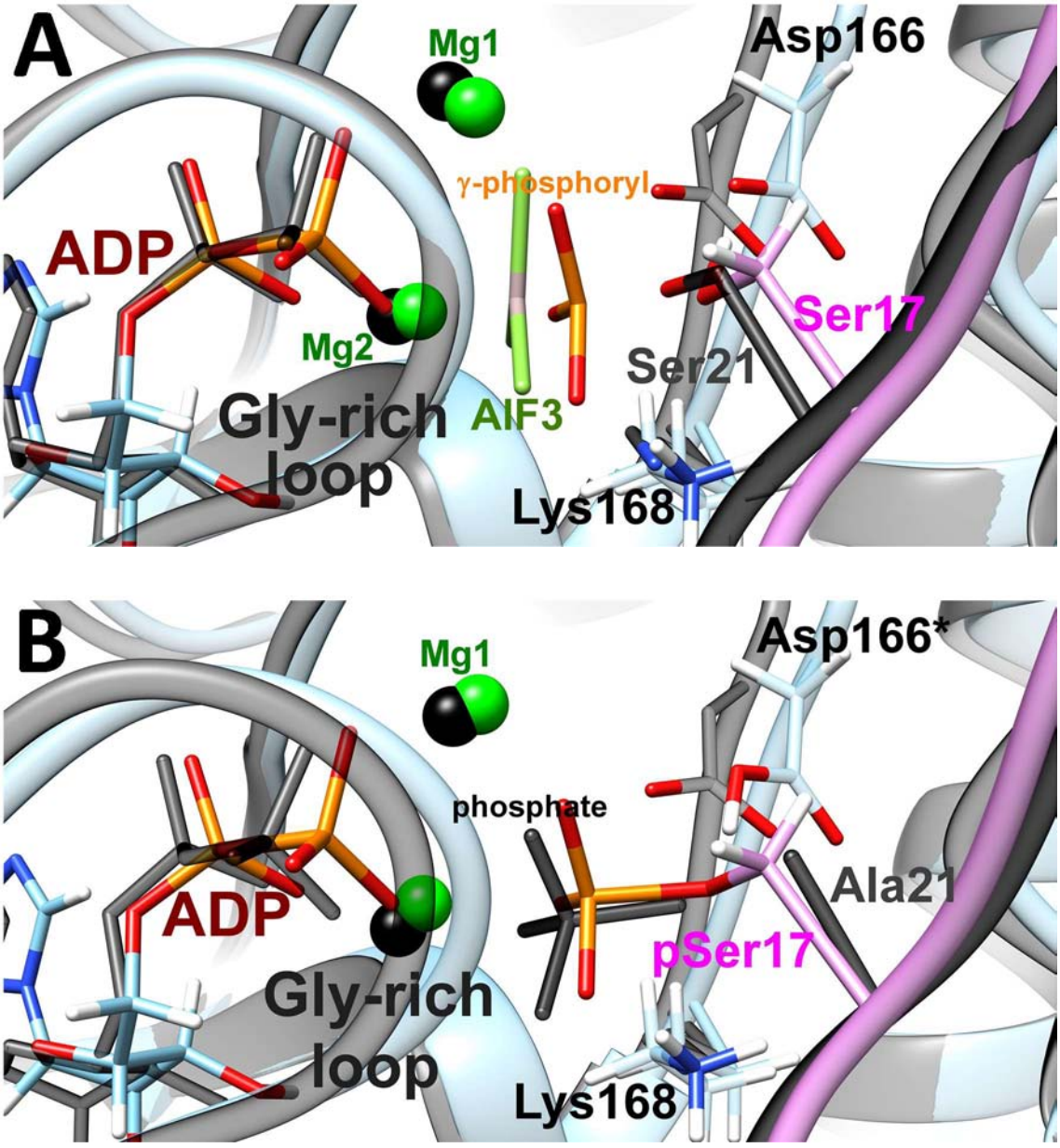

Figure 3.8. (A) Active site view of the overlay between the eq21 PKAc(1CDK)-Mg_2ATP-Kemptide model at TS1 and the transition state analog (TSA) crystallographic structure (PDB code 1L3R,[79] depicted in black color). **(B)** Active site view of the overlay between the eq21 PKAc(1CDK)-Mg_2ATP-Kemptide model at P1 and the ATP-hydrolysis product analog crystallographic structure (PDB code 4DH5,[164] depicted in black color).

Table 3.6. QM(B3LYP/6-31+G(d))/CHARMM interaction distances (in Å) involved in R4- and R2-reaction coordinates for the catalytic core at the reactant Michaelis complex (R_a), transition states, and product structures for the phosphoryl- and proton-transfers steps (eq21 PKAc(1CDK)-Mg_2ATP-Kemptide model). Intermolecular dihedral (in degrees) between Asp166 and O2γATP.

		phosphoryl-transfer		proton-transfer	
	R_a	TS1	P1	TS2	P2
O3βATP-PγATP	1.77	2.84	2.91	3.05	2.88
PγATP-OγSer17	3.48	1.86	1.80	1.70	1.68
OγSer17-HγSer17	0.99	1.22	1.39	2.15	2.43
Oδ2Asp166-HγSer17	1.65	1.18	1.07	1.01	1.80
O2γATP-HγSer17	3.39	2.81	2.85	1.79	0.99
$dihedral_{Asp166(Cβ\text{-}Cγ\text{-}Oδ2)\text{-}O2γATP}$	121.07	122.96	124.18	178.37	-173.79

nucleotide moieties and residues' side chains have the same orientation and, consequently, are held together by the same hydrogen-bonding interactions.

3.1.2.1.3. Geometric analysis of the main interactions along the phosphoryl-transfer step.

Next, in order to rationalize the calculated potential energy differences between the localized stationary points, we will compare the evolution of the main interaction distances along the reaction profile (Figure 3.5) that represents the phosphoryl-transfer path.

The values corresponding to the distances involved in the R4-reaction coordinate are listed in Table 3.6. In the optimized structure of *Ra* the PγATP-OγSer17 distance was found to be 3.48 Å, an intermediate value among those obtained from MD simulations,[166,190] QM cluster calculations,[190] and QM/MM approaches[166-167] of the phosphorylation reaction in other catalytic subunit models of PKAc with other substrates. The length of the ATP O3β-Pγ bond, 1.77 Å, is in good agreement with the value defined as ''natural'' by Valiev *et al*.[167] for the ATP-Mg complex in the active site of PKAc within the limits of DFT description. Furthermore, prior to the phosphorylation reaction, the angle O3βATP-PγATP-OγSer17 is almost linear (176.9°), thereby confirming the in-line nature of the phosphoryl-transfer mechanism observed in PKAc. On the other hand, as expected for a dissociative mechanism conducive initial structure, the hydroxyl group of the Ser17 side chain is rotated toward –and interacting with, through a 2.64 Å hydrogen bond– the carboxylate group of Asp166 (the angle OγSer17-HγSer17-Oδ2Asp166 is 176.9°), and also forming a 2.67 Å hydrogen bond with the Nζ atom of the ammonium side chain of Lys168 (Figure 3.6A).

The R4 interaction distances (Table 3.6) confirm the dissociative character for the phosphoryl-transfer transition state (TS1), so that the segment of the reaction coordinate that

describes the evolution of R_a to TS1 mainly involves the movement, up to an asymmetrical position, of the terminal phosphoryl group, from the β-γ bridging oxygen of ATP to the substrate hydroxyl oxygen. Specifically, in the TS1 structure, the O3βATP-PγATP bond is already broken (2.84 Å) and the bond between the phosphorous atom of the γ-phosphoryl-transferring group and the oxygen atom of the nucleophilic hydroxyl group of the substrate serine is almost formed (1.86 Å). On the other hand, the position of the HγSer17 between the donor OγSer17 and the acceptor Oδ2Asp166 (distances of 1.22 and 1.18 Å, respectively) clearly indicates that such proton-transfer is in its halfway stage and occurs after the nucleophilic displacement. Frequency calculations within the QM/MM description of the system confirmed a single imaginary frequency mode of 160i cm^{-1}, whose transition vector shows a contribution from the evolution of the bonds O3βATP-PγATP and PγATP-OγSer17, and the movement of the serine hydroxyl hydrogen towards the carboxylate side chain of Asp166. It is important to note that in TS1 the γ-phosphoryl group has a planar configuration and the angle O3βATP-PgγATP-OγSer17 retains its linear character (176.6°). That is, the reaction proceeds through a trigonal bipyramidal pentacoordinated transition state.

Energetically, as mentioned above, P1 is scarcely 0.3 kcal/mol below TS1 (Figure 3.5) and, consequently, this point is structurally very similar to TS1 in what concerns the phosphoryl-transfer, with the PγATP–OγSer17 distance just 0.06 Å shorter and maintaining the same trigonal bipyramidal pentacoordination. In contrast, the structural quantities related to the proton-transfer from the hydroxyl group of Ser17 to the carboxylate group of Asp166, undergo the most significant changes as the TS1 evolves to P1 along this flat potential energy region. In the P1 structure, the protonated Asp166 side chain establishes a short hydrogen bond with the now phosphorylated substrate oxygen (Oδ2Asp166-OγSer17 distance of 2.45 Å and a hydrogen bond angle of 165.7°), and the HγSer17 is 2.85 and 3.11 Å away from –and not directed towards– O2γATP and O1γATP, respectively. It is noteworthy that the PγATP-OγSer17 and Oδ2Asp166-HγSer17 bond distances are slightly longer than those reported previously for the same intermediate product structure of 1ATP-SP20 based PKAc models.[166-167]

Hereinafter, we will analyze the interactions made by enzyme residues with each other and with the ligands (substrate Kemptide and ATP molecules), which have been collected in Table 3.7. In addition, Figure 3.9 is a reduced view of the active site at TS1 where we can distinguish the location of the residues involved in the interaction distances commented in the following paragraphs.

The first twelve rows of Table 3.7 are dedicated to the interaction distances of residues that comprise the triad Asp166-Lys168-Thr201, whose catalytic role has already been mentioned and highlighted above for the associative and dissociative mechanisms. It should be

recalled that Thr201 belongs to the peptide positioning loop of PKAc, whereas Asp166 and Lys168 are located in the catalytic loop. Table 3.7 indicates that Thr201 forms hydrogen bond interactions with the non-proton accepting side of the carboxylate group of Asp166 side chain (Oδ1Asp166 atom) and with the ammonium group of the Lys168 side chain, while it interacts weakly with the substrate serine γ-oxygen atom. The hydrogen bonds with Asp166 and Lys168 residues are maintained throughout the phosphoryl-transfer reaction profile, while the interaction with the substrate Ser17 residue seems to decrease when going from the R_a structure -passing through TS1- to the P1 structure.

Table 3.7. Selected QM(B3LYP/6-31+G(d))/CHARMM distances (in Å) for the enzyme, nucleotide, and substrate interactions at the reactants, transition state, and product complex structures along the phosphoryl- and proton-transfer steps (eq21 PKAc(1CDK)-Mg_2ATP-Kemptide model).

		phosphoryl-transfer		proton-transfer	
	R_a	TS1	P1	TS2	P2
Oγ1Thr201-Oδ1Asp166	2.73	2.72	2.74	2.74	2.70
Oγ1Thr201-NζLys168	2.79	2.83	2.85	2.84	2.71
Oγ1Thr201-OγSer17	3.20	3.45	3.47	3.49	4.00
Oδ2Asp166-OγSer17	2.64	2.39	2.45	2.80	3.09
Oδ2Asp166-PγATP	4.26	3.46	3.47	3.31	3.54
Oδ2Asp166-OH2XW3	2.79	2.88	2.91	2.90	2.83
Oδ2Asp166-NζLys168	4.15	4.58	4.65	4.49	4.01
Oδ1Asp166-NζLys168	4.33	4.49	4.52	4.36	3.97
NζLys168-OγSer17	2.67	3.01	3.02	3.15	2.86
NζLys168-PγATP	3.97	3.42	3.39	3.36	3.64
NζLys168-O2γATP	3.41	3.28	3.27	3.22	3.28
NζLys168-O1γATP	3.58	2.99	2.97	2.88	3.68
Nδ2Asn171-O2γATP	3.44	3.11	3.09	3.21	3.62
Nδ2Asn171-Oδ2Asp166	3.86	3.99	4.01	3.15	3.07
NζLys72-O1αATP	2.75	2.75	2.75	2.75	2.75
NζLys72-O1βATP	2.89	2.86	2.85	2.85	2.86
NζLys72-Oε2Glu91	2.66	2.68	2.68	2.68	2.67
OγSer53-O1γATP	2.65	2.64	2.64	2.64	2.64
NSer53-O2βATP	2.79	2.74	2.75	2.73	2.78
NPhe54-O2βATP	2.80	2.77	2.77	2.78	2.82
NGly55-O2βATP	2.88	2.85	2.84	2.85	2.88

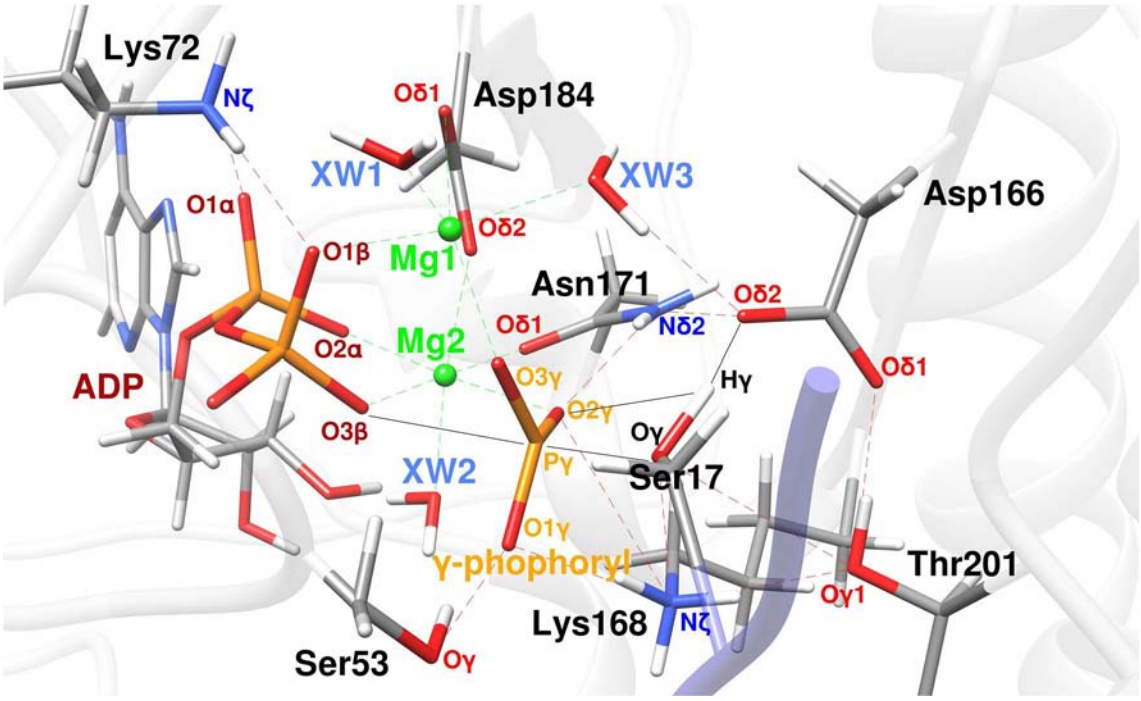

Figure 3.9. Reduced view of the active site at the TS1 structure for the phosphoryl-transfer step of eq21 PKAc(1CDK)-Mg_2ATP-Kemptide model. The most relevant interactions presented in Tables 3.6, 3.7, and 3.8 are depicted in broken lines.

In turn, besides the obvious and already described interaction with the nucleophilic OH group of the Ser17 side chain, Asp166 also interacts via hydrogen bonds with a conserved water molecule (coordinated to the Mg1 ion) and with the conserved Asn171 residue through its proton accepting carboxylic oxygen (Oδ2Asp166 atom). Both interactions do not show important variations along the stationary points defined from the phosphoryl-transfer reaction profile. Moreover, as explained above, the Asp166 residue is detectably away (see Figure 3.6A) from the Lys168 ammonium group, although these two residues are anchored by the residue Thr201.

Now, to finish the description of the three members of the catalytic triad, the analysis is focused on Lys168 interactions. In going from the reactant to the transition state and product zones, in addition to its interaction with Thr201, Lys168 maintains its interaction with the OγSer17 atom, although with increasing distances. The analysis of the values reported in Table 3.7 for the NζLys168-PγATP distance shows that the distance of this residue to the phosphoryl group diminishes about 0.6 Å in going from the reactant to the product. That is, Lys168 slightly approaches the γ-phosphoryl group along the phosphoryl-transfer step. Specifically in R_a, the closest γ-oxygen atom of ATP to NζLys168 is the O2γ atom (the one coordinated to Mg2). However, at TS1 and P1 structures, this interaction has clearly longer distance values than the corresponding one for the O1γATP atom, which seems to be related to the progressive distancing of the Lys168 ε-amino group from the reaction core as the phosphoryl-transfer step

occurs (see Oδ2Asp166-NζLys168 and NζLys168-OγSer17 distances in Table 3.7).

At this point, it is worth comparing the results obtained here with those from Montenegro *et al.*[148] on the dissociative mechanism using the PKAc(1CDK)-Mg_2ATP-Kemptide model. As indicated above, that previous calculations of the phosphoryl-transfer reaction path were carried out at the AM1/d-PhoT/MM level with a rather rigid R4-reaction coordinate expression in which fixed coefficients were used to account for the contributions of the four different distances (*r1* or O3βATP-PγATP, *r2* or PγATP-OγSer17, *r3* or OγSer17-HγSer17, and *r4* or Oδ2Asp166-HγSer17) involved in the chemical process. The potential energy was then corrected along the reaction path by means of single-point energy calculations at the B3LYP/6-31+G(d)/MM level. However, the DFT-corrected potential energy profile based on the weighted R4-reaction coordinate was so rugged that it was not possible for the authors to use it to locate the phosphoryl-transfer stationary points. Finally, by means of a strategy based on the calculation of a corrected 2D-surface obtained from the difference between the high level B3LYP/6-31+G(d)/MM and the low level AM1/d-PhoT/MM 2D-PESs, and by fitting these difference values through a two dimensional cubic spline function, the three stationary points, reactant (R), transition state (TS) and product (P), were located. The nature of the dissociative transition state is the same in both studies, and the interaction distances O3βATP-PγATP and PγATP-OγSer17, involved in the R4-reaction coordinate, at TS and TS1 are then practically identical. However, the dual-level potential energy barrier and reaction energy values of the phosphoryl-transfer process in the work by Montenegro *et al.*[148] differ from the converged energetic values obtained in the present study at the B3LYP/6-31+G(d)/MM level with the new flexible R4-reaction coordinate. The reason is that several interactions that have been identified as very important for the energetics of the phosphoryl-transfer process on the B3LYP/6-31+G(d)/MM potential energy surface were not present on the DFT-corrected AM1/d-PhoT/MM counterpart. For instance, the triad Asp166-Lys168-Thr201 was not correctly formed in the structures along the phosphoryl-transfer reaction path of that preceding study. Moreover, when comparing the Lys168 hydrogen bond interactions at the TS1 and P1 structures with those at the corresponding structures, TS and P, respectively,[148] it is clear that in the ternary structures obtained in the present study the Lys168 amino group is more distant from the carboxylate group of Asp166 and the hydroxyl group of Ser17. The foregoing, besides enhancing the basic character of Asp166, also increases the nucleophilicity of the Ser17 attacking oxygen atom, then promoting the phosphoryl-transfer reaction. Moreover, such configuration of the Lys168 side chain within the active site allowed the simulation of the final step of the dissociative mechanism, in which the protonation of the phosphorylated product by Asp166 takes place, something that has been carried out for the PKAc-Mg_2ATP-Kemptide system for the first time in

this Thesis. Therefore, the NζLys168-O2γATP distance is longer at the P1 structure than at the P structure, so the basic character of the O2γATP atom is stronger in the former, such that it can really act, in the phosphoryl group already transferred to the substrate Ser17, as the acceptor oxygen for the final proton-transfer step.

Following with the analysis of Table 3.7, we will now focus on the interactions that hold and stabilize the nucleotide moieties within the active site. The O3γATP atom has no interaction besides being one of the ligands in the Mg1 coordination sphere. The O2γATP forms a hydrogen bond with the Nδ2Asn171 atom (interaction which is strengthened as the phosphoryl-transfer reaction takes place), the interaction mentioned above with Lys168, and, in addition, it belongs to the coordination sphere of Mg2. The O1γATP oxygen also interacts via a hydrogen bond with the side chain hydroxyl group of Ser53, located in the Gly-rich loop. Another oxygen atom of ATP is responsible of other interactions with the glycine-rich loop: the O2βATP atom, which interacts with the main chain nitrogen atoms of Ser53, Phe54, and Gly55 residues. Finally, both O1α and O1β atoms of ATP form hydrogen bonds with the ε-amino group of Lys72, which is also hydrogen-bonded to the ε-carbonyl group of Glu91.

Regarding both Mg^{2+} ions within their corresponding metal binding site, the Mg1 ion binds the 1β- and 3γ-oxygens of ATP, the carboxylate group of Asp184 side chain in a bidentate fashion, and two conserved water molecules, while the Mg2 ion binds the 2α-, 3β-and 2γ-oxygens of ATP, a single carboxyl oxygen of Asp184, and the side chain carbonyl oxygen of Asn171 (see Table 3.8). Specifically, the octahedral coordination sphere of the metal ions does not significantly vary along the phosphoryl-transfer reaction, with the exception of the O3βATP and O2γATP interaction distances for the Mg2 ion. As described for the associative mechanism, concurrent with the cleavage of the β-γ phosphoanhydride bond of ATP due to the nucleophilic attack of OγSer17 on PγATP, the nascent and leaving ADP moiety is stabilized by the increased interaction with the Mg2 metal ion. That is, the O3βATP-Mg2 interaction is strengthened and, consequently, its distance shortened during the phosphoryl-transfer step. Simultaneously, as a result of the movement of the γ-phosphoryl group almost 2 Å towards Ser17, in both the transition state and product regions the O2γATP-Mg2 distance increases almost ten percent of its initial value.

3.1.2.2. Proton-transfer step.

3.1.2.2.1. Exploration of the potential energy surface.

As seen above, P1 does not correspond to a stable final structure. An additional chemical step is required to reach a stable phosphokemptide. In this section, the potential energy profile at the QM(B3LYP/6-31+G(d))/CHARMM level corresponding to the proton-transfer of HγSer17

Table 3.8. QM(B3LYP/6-31+G(d))/CHARMM interaction distances (in Å) between the two Mg^{2+} ions and the ligands of their corresponding coordination spheres along the phosphoryl- and proton-transfer steps (eq21 PKAc(1CDK)-Mg_2ATP-Kemptide model).

		phosphoryl-transfer		proton-transfer	
	R_a	TS1	P1	TS2	P2
Mg1-O1βATP	2.13	2.04	2.04	2.03	2.05
Mg1-O3γATP	2.06	2.13	2.12	2.11	2.13
Mg1-Oδ1Asp184	2.23	2.29	2.31	2.34	2.27
Mg1-Oδ2Asp184	2.23	2.19	2.18	2.21	2.22
Mg1-OH2XW3	2.12	2.18	2.18	2.18	2.19
Mg1-OH2XW1	2.07	2.07	2.07	2.07	2.06
Mg2-O2αATP	2.00	2.06	2.06	2.07	2.02
Mg2-O3βATP	2.29	2.04	2.04	2.02	2.01
Mg2-O2γATP	2.02	2.20	2.21	2.44	2.48
Mg2-Oδ2Asp184	2.11	2.10	2.10	2.08	2.08
Mg2-Oδ1Asn171	2.01	2.10	2.10	2.11	2.09
Mg2-OH2XW2	2.13	2.16	2.17	2.16	2.14

from the Asp166 residue to the O2γATP atom of the γ-phosphoryl group already bonded to the substrate Ser17 is described. As indicated in the methodology, this second step of the dissociative mechanism has been calculated using the R2 coordinate from the P1 structure. The complete potential energy profile is shown in Figure 3.10, and encompasses the phosphoryl- and the proton-transfer steps along the R4- and R2-reaction coordinates, respectively, with the

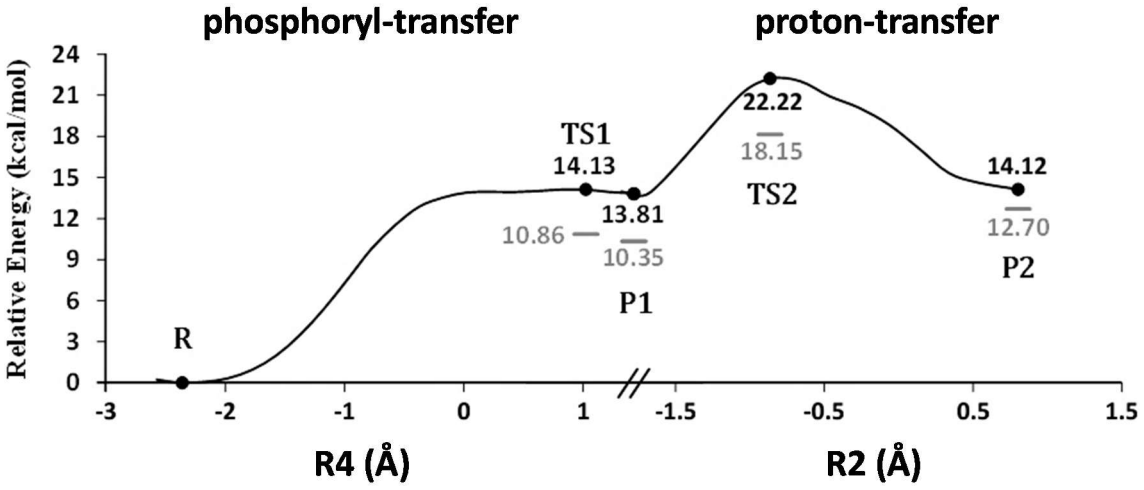

Figure 3.10. QM(B3LYP/6-31+G(d))/CHARMM complete potential energy profile encompassing the phosphoryl- and proton-transfer steps along the corresponding reaction coordinate (eq21 PKAc(1CDK)-Mg_2ATP-Kemptide model). The single-point energy results at the QM(MP2/cc-PVTZ)/CHARMM level on the QM(B3LYP/6-31+G(d))/CHARMM stationary point structures are depicted in grey.

phosphorylated serine of substrate Kemptide and protonated side chain of Asp166 of PKAc in the product complex (P1) as a common point. The same Figure 3.10 also includes the QM(MP2/cc-PVTZ)/CHARMM//QM(B3LYP/6-31+G(d))/CHARMM single-point energies for all the calculated stationary points.

As can be seen in Figure 3.10, the proton-transfer step is explored from R2 values of about -1.9 Å at the P1 zone, with the obtained potential energy profile reaching its maximum at R2 = -0.78 Å with a potential energy value of 8.4 kcal/mol with respect to P1. It describes a nearly isoergic process. Based on the converged potential energy profile presented in Figure 3.10, a product-like geometry (R2 = 0.8 Å) as the starting point was used to localize a proton-transfer product structure, *i.e.* the ADP/protonated-phosphokemptide structure (P2). Finally, the structure corresponding to the potential energy maximum of the reaction profile obtained for the proton-transfer step was used as the starting point for the corresponding transition state (TS2) search. The final potential energy barrier for the proton-transfer step and the reaction potential energy with respect to P1 are 8.4 kcal/mol and 0.3 kcal/mol, respectively, at the QM(B3LYP/6-31+G(d))/CHARMM level. The single-point energy calculations at the QM(MP2/cc-PVTZ)/CHARMM level on the QM(B3LYP/6-31+G(d))/CHARMM TS2, P1 and P2 stationary points, gave values for the potential energy barrier and reaction potential energy of 7.8 and 2.4 kcal/mol, respectively. It has to be noted that P2, which corresponds to a protonated phosphokemptide, has to be considered as the final stable product from which the phosphokemptide release occurs.

Pre-steady state kinetics has revealed a very rapid phosphoryl-transfer step in PKAc using Kemptide as a substrate. From those experiments a rate constant of 500 s^{-1} was determined, and the kinetic measurements indicate that the rapid phosphorylation of Kemptide occurs in a single observable step.[130] On the other hand, the phosphorylation of Kemptide by PKAc was monitored over time taking advantage of the fact that the fluorescence emission spectrum of PKAc is quenched differentially by ATP and ADP.[140] Fitting of the pre-steady state kinetic transient for Kemptide phosphorylation to a double exponential function gave rate constants of 500 s^{-1} and 60 s^{-1}, corresponding to a fast and a slow phase, respectively. The first phase was assigned to the evolution over time of the phosphoryl group transfer from ATP to Kemptide. The second phase was tentatively associated to a large conformational change of the enzyme, and could include the very fast phosphokemptide release. The phenomenological free energy barrier corresponding to the experimental rate constant of the first phase, obtained by applying conventional transition state theory, gives a value of 13.8 kcal/mol at 300 K, which is not too far from the potential energy barrier of TS2 with respect to R calculated in this work (18.1 kcal/mol at the MP2 level; see Figure 3.10).

As indicated in the Introduction, only Díaz and Field[190] have calculated the potential energy profile for the proton-transfer step that protonates the phosphorylated peptide and that recovers the protonation state of the active site residues. With their cluster model, Díaz and Field[190] obtained a potential energy barrier and a reaction potential energy of 7.0 and 0.9 kcal/mol, respectively, at the B3LYP/6-31+G(d,p) level. In agreement with their results we have obtained using a complete model of the ternary complex a small potential energy difference between the product complexes before (P1, deprotonated phosphoryl group) and after (P2, protonated phosphoryl group) proton-transfer. In contrast, Valiev *et al*.[187] considered that the structure corresponding to P1 is the unique stable protonation state of the product complex of the dissociative mechanism locating that structure 9 kcal/mol below the reactant complex in an 82-atom cluster with $HOCH_2CH_3$ as a substrate model. That result is likely an artifact because the coordination sphere of the Mg1 ion was not complete in the cluster model used by Valiev *et al*.[187] resulting in an overstabilized product complex. More recent theoretical studies using complete models of the ternary PKA-ATP-Mg_2-SP20 system have also considered the P1 structure as the final protonation state of the product complex but with different results concerning the reaction energy (7.4, 9.5, and 11.9 kcal/mol in terms of potential energy, or -3 kcal/mol in terms of free energy).[166-167]

3.1.2.2.2. Geometric analysis of the main interactions along the proton-transfer step.

Next, the potential energy differences between the localized stationary points along the proton-transfer step will be analyzed by comparing the evolution of the main interaction distances along the corresponding reaction profile (Figure 3.10) as it has been done for the phosphoryl-transfer path.

The main geometric variables involved in the R2 coordinate are given in Table 3.6 and the structure of TS2 is depicted in Figure 3.11. It can be inferred by inspection of the structural evolution that the potential energy barrier corresponds to the rotational movement of the protonated carboxylate group of the Asp166 residue which displaces from a location with a Asp166(Cβ-Cγ-Oδ2)-O2γATP dihedral angle value of 124.2° at P1 to 178.4° at TS2 reaching a configuration more suitable for proton-transfer (see Figure 3.11). Concomitant with the rotation of the Asp166 side chain, the O2γATP-HγSer17(Asp166) distance decreases from 2.85 Å at P1 to 1.79 Å at TS2, while the OγSer17-HγSer17 distance increases from 1.39 Å at P1 to 2.15 Å at TS2. However, the proton-transfer has not yet begun at TS2 with the distance Oδ2Asp166-HγSer17 being only 1.01 Å. In fact, the actual proton-transfer from the protonated Asp166 to O2γATP begins rather late in the reaction pathway (a R2 value of about -0.27 Å) in the downhill region quite close to the P2 product structure.

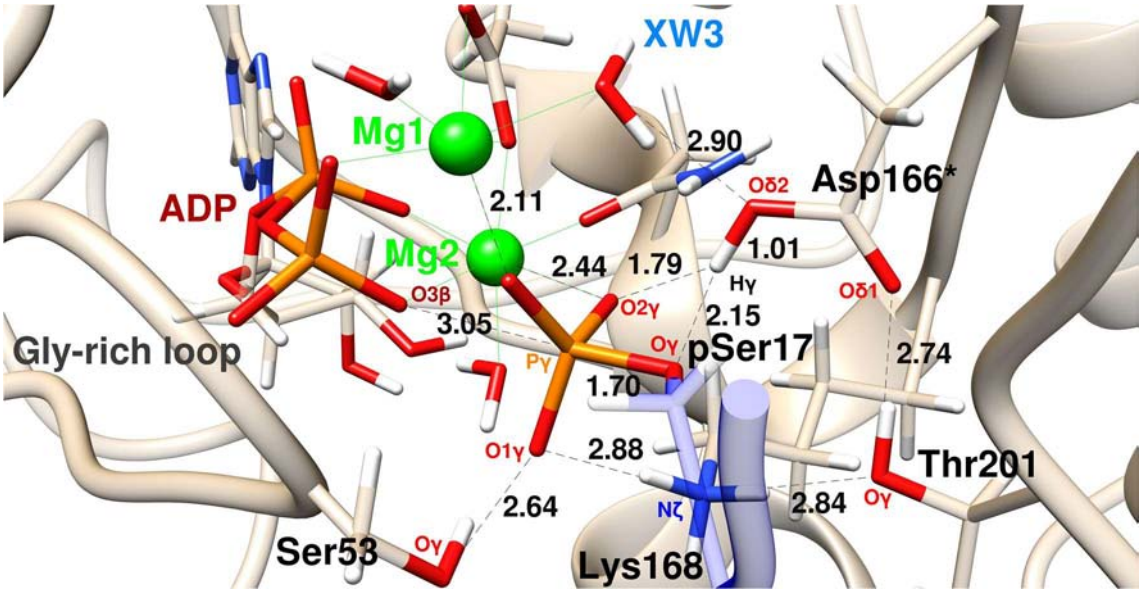

Figure 3.11. Reduced view of the active site at the TS2 structure for the phosphoryl-transfer step of eq21 PKAc(1CDK)-Mg_2ATP-Kemptide model. The main interaction distances (given in Å) are depicted with black broken lines. Metal coordination is shown as green solid lines.

The proton-transfer from Asp166 to O2γATP is favored with respect to the protonation of O3γATP because, as indicated previously, along the movement of the γ-phosphoryl group towards Ser17 in the phosphoryl-transfer step, the O2γATP-Mg2 distance increases and the negative charge on O2γATP becomes less stabilized (the Mg2-O2γATP distance increases from 2.02 Å at R_a to 2.21 Å at P1 and to 2.44 Å at TS2). A relevant change in the coordination sphere of the Mg2 ion along the catalytic mechanism has been recently observed in two crystallographic structures of the PKAc-Mg_2ADP-pSP20 complex showing partial or total phosphoryl-transfer (structures with PDB codes 4HPU and 4HPT, respectively).[102] In contrast, the O3γATP atom which is somewhat more distant from Asp166 than O2γATP (the O3γATP-Oδ2Asp166 distance is 3.65 Å while the O2γATP-Oδ2Asp166 distance is 3.43 Å) is also more stabilized by its interaction with the Mg1 ion. That is, O3γATP has not such a basic character as O2γATP because O3γATP does not distance from Mg1 along the phosphoryl-transfer step. The Mg1-O3γATP distance only changes from 2.06 Å at R_a to 2.12 Å at P1 and to 2.11 Å at TS2. Moreover, the conformation adopted by Lys168 is also crucial for the viability of the proton-transfer step to O2γATP. As noted above from the values given in Table 3.7 and Figure 3.6A and B, at R_a Lys168 is farther away from O2γATP (3.41 Å) than at R_b (2.85 Å) which contributes to enhance the basic character of O2γATP.

Thus, using a complete model of the solvated ternary complex PKAc-Mg_2ATP-Kemptide, it is demonstrated in this Thesis that the role of Asp166 as a general acid–base catalyst is viable in agreement with mutagenesis experiments. As indicated in the Introduction, the important reduction in phosphorylation and phosphopeptide release rate constants measured in the Asp149Asn mutant of PhK was explained by the incapability of Asn to ionize like Asp149.[85] The

proton-transfer from Ser17 of Kemptide to Asp166 (acting as a base catalyst) facilitates the phosphoryl-transfer while the proton-transfer from Asp166 (acting as an acid catalyst) to O2γATP regenerates the original protonation state of the enzyme. Anyway it has to be noted that Asp166 does not act as a conventional acid catalyst because its proton-transfer begins after the corresponding transition state structure of the process. Moreover, it has also been suggested that the repulsion between the negatively charged Asp166 and the phosphopeptide product could facilitate the phosphopeptide dissociation and could also contribute in part to the rotation of the Gly-rich loop.[73] This is one of the conformational changes needed for the opening of the active site and the departure of the phosphorylated product and ADP.

It should be pointed out that the theoretical results for the phosphorylation reaction catalyzed by PKAc in the PKAc(1CDK)-Mg_2ATP-Kemptide model via the associative and dissociative mechanisms can be found published in references 277 (which includes the D166A mutant model results) and 278, respectively.

3.2. Study on the substrate dependence of the PKAc catalytic mechanism: *in silico* models derived from the 4IAC crystallographic structure.

As mentioned in the Introduction, the aim of the work presented in this section is to simulate the phosphoryl-transfer process (both the associative and the dissociative mechanisms) from the pseudo-Michaelis complex analogue PKAc-Mg_2AMPPCP-SP20, determined experimentally by Gerlits *et al*.[76] The initial theoretical model, PKAc-Mg_2ATP-SP20, was built up as close as possible to the experimental X-ray coordinates (PDB code 4IAC[76]) in order to be able to compare the results with it and with the related PKAc X-ray structures: the transition state mimic of the catalytic subunit (PDB code 1L3R[79]), and the product of the phosphoryl-transfer reaction (PDB code 4IAF[76]). In addition, the setup of the PKAc(4IAC)-Mg_2ATP-Kemptide model, also from the 4IAC crystallographic structure was carried out (in this case, using since the beginning of the *in silico* methodology the SP20 substrate as a template for modelling the Kemptide substrate). The simulation of the complete mechanistic scheme with both *in silico* models, PKAc-Mg_2ATP-SP20 and PKAc(4IAC)-Mg_2ATP-Kemptide, will provide some insights into the suggested dependence[76] of the kinase-catalyzed phosphorylation reaction mechanism on the particular substrate bound in the active site.

3.2.1. Comparison between the initial theoretical models: PKAc-Mg_2ATP-SP20 and PKAc(4IAC)-Mg_2ATP-Kemptide.

As in the starting 4IAC crystallographic structure, in both QM/MM optimized PKAc-Mg_2ATP-SP20 and PKAc(4IAC)-Mg_2ATP-Kemptide initial models structures, the O1γATP atom interacts with crystallographic water molecules, and it is positioned in front of the Gly-rich loop but around 5 Å away from it (thus it does not interact directly with the Ser53 residue as it does in the PKAc(1CDK)-Mg_2ATP-Kemptide and PKAc(1ATP)-Mg_2ATP-Kemptide models); the O2γATP atom coordinates the Mg2 ion and forms a 2.8 Å hydrogen bond with the ε-ammonium group of Lys168; and, finally, the O3γATP atom coordinates the Mg1 ion.

The superposition of the QM/MM optimized PKAc-Mg_2ATP-SP20 and PKAc(4IAC)-Mg_2ATP-Kemptide initial model structures (from now on $i_{model}S_{Mg}$ and $i_{model}K_{Mg}$, respectively) is shown in Figure 3.12 for its direct comparison. It can be observed that the configuration of the active site is very similar in both initial model structures, being the main difference the position of the crystallographic water molecules interacting with the phosphorylated-tale of ATP and residues Ser53, Phe54, and Gly55 of the Gly-rich loop. For two crystallographic waters, in particular, this comprises, in turn, a different set of hydrogen bond interactions with the β- and γ-phosphates of ATP, whose bridging O3βATP-PγATP bond breaks along the phosphoryl-transfer with distinctive features according to the mechanism followed (*i.e.* associative or dissociative,

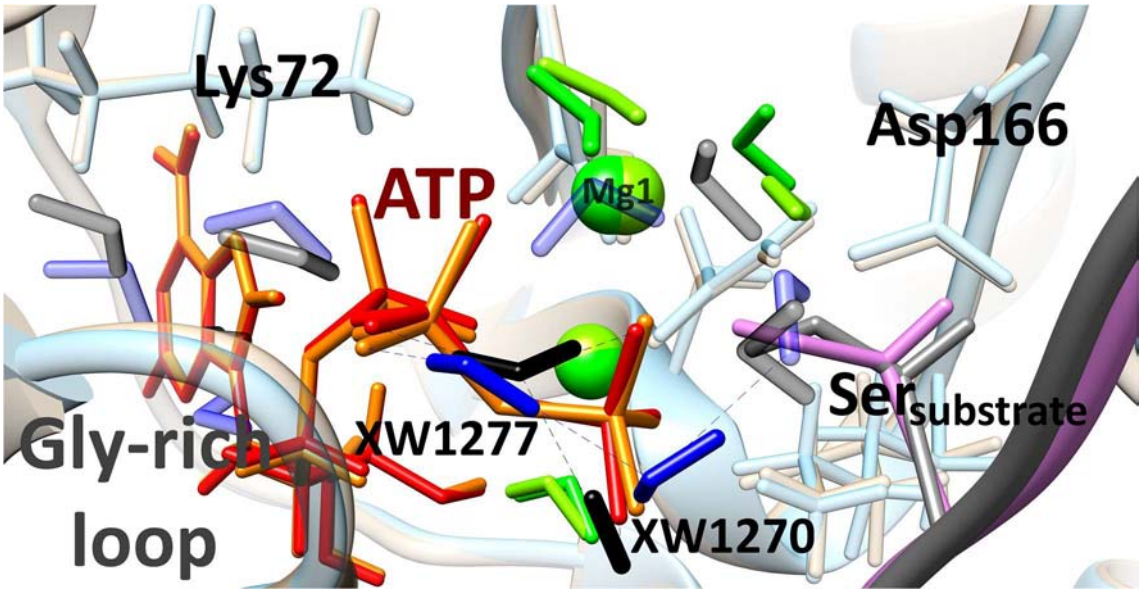

Figure 3.12. Superposition of the active sites of the optimized initial model structures of PKAc-Mg_2ATP-SP20 ($i_{model}S_{Mg}$; PKAc colored in tan, SP20 in dark gray, ATP in red, Mg^{2+} ions with coordinating water molecules in lime, and water molecules within the active site in black) and PKAc(1CDK)-Mg_2ATP-Kemptide ($i_{model}K_{Mg}$; PKAc colored in cyan, Kemptide in purple, ATP in orange, Mg^{2+} ions with coordinating water molecules in green, and water molecules within the active site in blue).

Table 3.9. Selected QM(B3LYP/6-31+G(d))/CHARMM bond distances (in Å), bond angles (in deg), and dihedral (in deg) in the PKAc-Mg_2ATP-SP20 and PKAc(4IAC)-Mg2ATP-Kemptide initial model structures ($i_{model}S_{Mg}$ and $i_{model}K_{Mg}$, respectively). Comparison with values from the pseudo-Michaelis complex X-ray crystallographic structure (PDB code 4IAC[76]) used as model template.[a]

	4IAC[76]	$i_{model}S_{Mg}$	$i_{model}K_{Mg}$
O3βATP-PγATP	1.8*	1.70	1.68
PγATP-OγSer$_{Substrate}$	3.5	3.76	3.62
OγSer$_{Substrate}$-HγSer$_{Substrate}$	---	0.98	0.99
Oδ2Asp166-HγSer$_{Substrate}$	---	4.23	3.03
O2γATP-HγSer$_{Substrate}$	---	3.52	3.74
OγSer$_{Substrate}$-Oδ2Asp166	4.4	4.28	4.48
Oδ2Asp166-O2γATP	3.8	3.93	3.95
angle$_{O3βATP-PγATP-OγSerSubstrate}$	148.2*	141.3	137.5
angle$_{OγSerSubstrate-HγSerSubstrate-Oδ2Asp166}$	---	86.4	105.4
angle$_{Oδ2Asp166-HγSerSubstrate-O2γATP}$	---	60.2	60.2
d.$_{SerSubstrate(N-Cα-Cβ-Oγ)}$	64.0	68.7	58.5
d.$_{Asp166(Cβ-Cγ-Oδ2)-O2γATP}$	160.0	167.2	173.4

[a]For 4IAC[76] * is O3βATP=CβAMPPCP

see Figure 1.11). Thus, in the $i_{model}S_{Mg}$ structure, employing the nomenclature of the 4IAC[76] PDB entry, the crystallographic water XW1277 is directly bridging the O2βATP and O3γATP atoms

while interacting with the crystallographic water XW1270 too, which in turn is hydrogen bonded to the O1γATP atom. On the other hand, in the $i_{model}K_{Mg}$ structure, the XW1277 and the XW1270 water molecules bridge in conjunction the O2βATP and O1γATP atoms, so that in this case the O3γATP atom does not interact with any crystallographic water. Finally, the subtle difference in the position of the substrate serine side chain (*i.e.* in the value of the Oγ-Cβ-Cα-N torsion angle, as it will be pointed out below) is likely due to the OγSer17-OXW1270 hydrogen bond that is only formed in the $i_{model}K_{Mg}$ structure.

3.2.2. Comparison between the initial models and the X-ray crystallographic model.

It is also worth comparing the 4IAC X-ray structure of the PKAc-Mg_2AMPPCP-SP20 complex with the QM/MM optimized $i_{model}S_{Mg}$ and $i_{model}K_{Mg}$ structures (see Table 3.9). One geometric feature of the starting 4IAC crystallographic structure, specially noted by Gerlits *et al*.,[76] was the relative orientation of the OH group of the substrate Ser21, which directly affected the assembly of hydrogen bonds within the chemically active region. Thus, as referred by the authors[76] and summarized in Table 3.9, in the 4IAC crystallographic structure the hydroxyl group of the substrate serine is at 3.5 Å from the γ-phosphorus atom of ATP, it lacks the hydrogen bond to Asp166, and it is rotated toward O3γATP (the γ-oxygen atom also coordinated to Mg1) forming a hydrogen bond with a OγSer21-O3γATP distance of 2.7 Å. The authors also reported a Ser21 Oγ-Cβ-Cα-N torsion angle of 64°. As expected, the active site of the computationally obtained initial structures is geometrically comparable to that of the crystallographic structure. The $O\gamma Ser_{Substrate}$-O3γATP distance (2.7 Å in $i_{model}S_{Mg}$ and $i_{model}K_{Mg}$), which corresponds to a $H\gamma Ser_{Substrate}$-O3γATP distance of 1.81 and 1.73 Å in $i_{model}S_{Mg}$ and $i_{model}K_{Mg}$, respectively, and the long $O\gamma Ser_{Substrate}$-Oδ2Asp166 distances (4.3 and 4.5 Å in $i_{model}S_{Mg}$ and $i_{model}K_{Mg}$, respectively) are maintained, with almost identical substrate serine Oγ-Cβ-Cα-N torsion angles (69° and 59° in $i_{model}S_{Mg}$ and $i_{model}K_{Mg}$, respectively). From a geometric point of view, all structures (4IAC, $i_{model}S_{Mg}$ and $i_{model}K_{Mg}$) could be considered to be prone to the associative phosphoryl-transfer path, with the O3γATP as the direct proton acceptor in the incoming phosphate group.

On the other hand, it is also important to highlight that the presence of ATP in the $i_{model}S_{Mg}$ and $i_{model}K_{Mg}$ structures did not modify the Gly-rich loop position found in the starting 4IAC crystallographic structure, with this loop in all of them somewhat displaced relative to its position in most of the other crystallographic[73,79,100,164,175] and theoretical[148,166-167,187,190] structures characterized for the different stages of the phosphoryl-transfer reaction. Such displacement is considered by Gerlits *et al*.[76] to be due to the strong steric effects of the β,γ-methylene group in AMPPCP, acting as ATP-analogue, in such a way that the Gly-rich loop is pushed farther from the phosphorylated tail of the ATP kinase cofactor. In contrast, the fact of

restituting the β,γ-bridging oxygen of ATP results in the recovery of the octahedral coordination of the Mg2 ion (Mg2-O3βATP distance of 3.3 Å in 4IAC, 3.0 Å in $i_{model}S_{Mg}$, and 3.1 Å in $i_{model}K_{Mg}$), whereas the Mg2 ion coordination in 4IAC is trigonal bipyramidal due to the incapacity of the β,γ-bridging CH_2 group in AMPPCP to bind to a metal ion.[76] Moreover, due the shorter distance of the β,γ-bridging bond in ATP than in AMPPCP, the γ-phosphate group in the $i_{model}S_{Mg}$ and the $i_{model}K_{Mg}$ structures retracts into the ADP moiety (PγATP-OγSer$_{Substrate}$ distance of 3.5 Å in 4IAC, 3.8 Å in $i_{model}S_{Mg}$, and 3.6 Å in $i_{model}K_{Mg}$; see Table 3.9).

3.2.3. Reaction paths and stationary points computationally determined.

From the $i_{model}S_{Mg}$ and $i_{model}K_{Mg}$ structures, it was possible to simulate both the associative and dissociative mechanisms. In fact, as detailed below, the calculations show the viability of two of the three analyzed associative reaction pathways, each one involving a particular γ-oxygen atom of ATP as the proton acceptor, specifically, O1γATP and O3γATP. It is worth mentioning that when simulating the O2γATP-associative path with both SP20 and Kemptide as substrates, the HγSer$_{Substrate}$ atom was transferred to Oδ2Asp166, so following a dissociative path instead of being transferred directly to the recipient γ-oxygen atom of ATP.

For both O1γATP- and O3γATP-associative paths with SP20 as substrate, three forward/backward cycles of associative R4-reaction coordinate scans were sufficient to reach a converged potential energy profile. In contrast, with Kemptide as substrate, both the O1γATP and O3γATP potential energy profiles converged after two cycles. It has to be underlined that this concatenation of successive forward/backward cycles along the corresponding reaction coordinate up to convergence, considerably relaxes the system and contributes to eliminate artificial strains.

On the other hand, for the dissociative mechanism with SP20, also two of the three possible pathways for the second step of the mechanism were found to be plausible, each one involving as the final proton acceptor a particular γ-oxygen atom of the phosphoryl group already bonded to the substrate Ser21, specifically, O2γATP and O3γATP. For the common phosphoryl-transfer step with SP20 as substrate, four forward/backward cycles of dissociative R4-reaction coordinate scans were needed to obtain a converged potential energy profile. Further, for the second step of the dissociative mechanism, that is, the proton-transfer from the protonated Asp166 to the already phosphorylated substrate, four and three forward/backward cycles of dissociative R2-reaction coordinate scans were needed to reach a converged potential energy profile with O2γATP and O3γATP as proton acceptor, respectively. As described below, when analyzing the results for the dissociative phosphoryl-transfer, the O1γATP-path for this proton-transfer step is sterically hindered with any substrate.

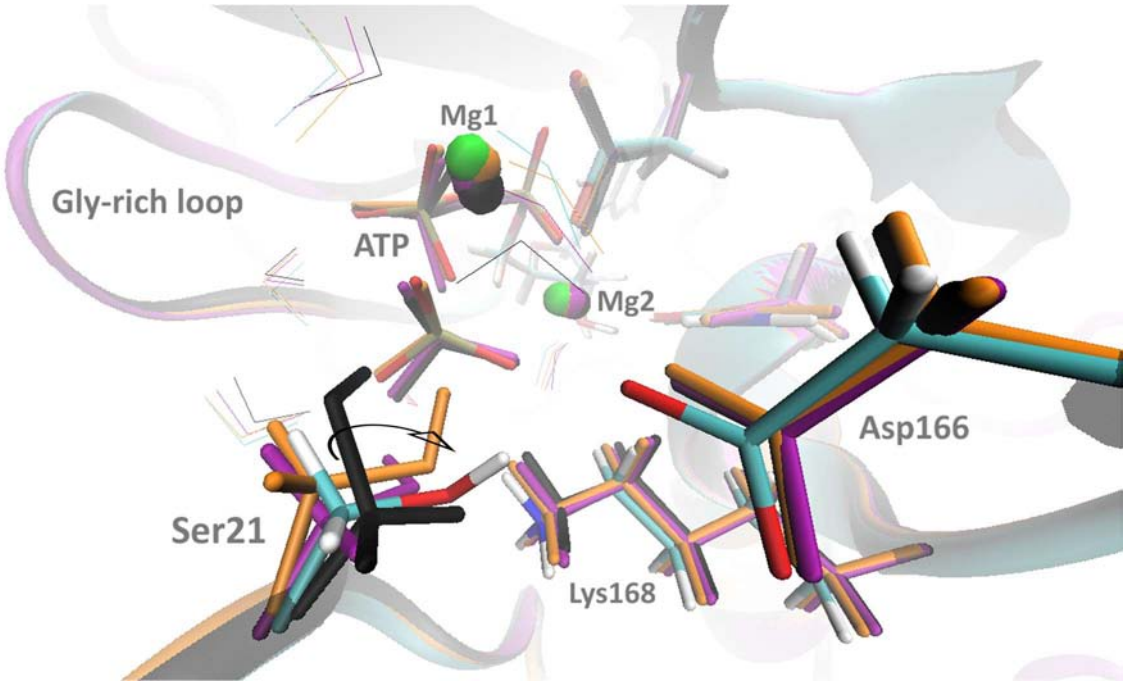

Figure 3.13. Superposition of the active sites of the optimized initial model ($i_{model}S_{Mg}$, colores in black), O1γATP-associative reactive complex ($Ra1_S$, colored in purple), O3γATP-associative reactive complex ($Ra3_S$, colored in orange), and dissociative reactive complex (Rd_S, colored by atom type).

As a result of scanning until convergence the reaction coordinates required to model the aforementioned mechanistic alternatives of the catalyzed phosphoryl-transfer reaction, specific Michaelis complexes were characterized in each case, with significant geometric differences in the active site between them and the corresponding $i_{model}S_{Mg}$ and $i_{model}K_{Mg}$ structures (see complete geometric data in Tables A1-A8 in the Appendix).

For example, in the geometry of all the Michaelis complexes localized in the simulated phosphoryl-transfer QM/MM reaction paths with SP20 as substrate, the hydroxyl group of substrate serine is rotated toward the carboxylate group of Asp166, presenting a Oγ-Cβ-Cα-N torsion angle of –39°, –39°, and –57° in the O1γATP-associative ($Ra1_S$), O3γATP-associative ($Ra3_S$), and dissociative (Rd_S) reactive complex, respectively (see Figure 3.13). Moreover, although in such structures the β,γ-bridging bond of ATP does not change from its value in $i_{model}S_{Mg}$ (1.7 Å), the PγATP-OγSer21 distance does change: the oxygen atom of the nucleophilic hydroxyl group is closer to the phosphorus atom of the γ-phosphate of ATP in $Ra1_S$ (3.1 Å), $Ra3_S$ (3.3 Å), and Rd_S (3.4 Å) structures, than in the 4IAC crystallographic starting structure (3.5 Å) and $i_{model}S_{Mg}$ (3.8 Å). In addition, the PγATP-OγSer21 interaction is almost aligned to the β,γ-bridging bond of the ATP molecule (see $angle_{O3\beta ATP\text{-}P\gamma ATP\text{-}O\gamma Ser21}$ in Tables 3.10–3.13, which takes values closer to 180° than those present in the $i_{model}S_{Mg}$ and 4IAC structures). In addition, the hydroxyl group of the Ser21 side chain interacts through a 2.9 Å hydrogen bond with O1γATP and O3γATP in $Ra1_S$ and $Ra3_S$, respectively, whereas in Rd_S it interacts with the Oδ2Asp166 through a 2.8 Å

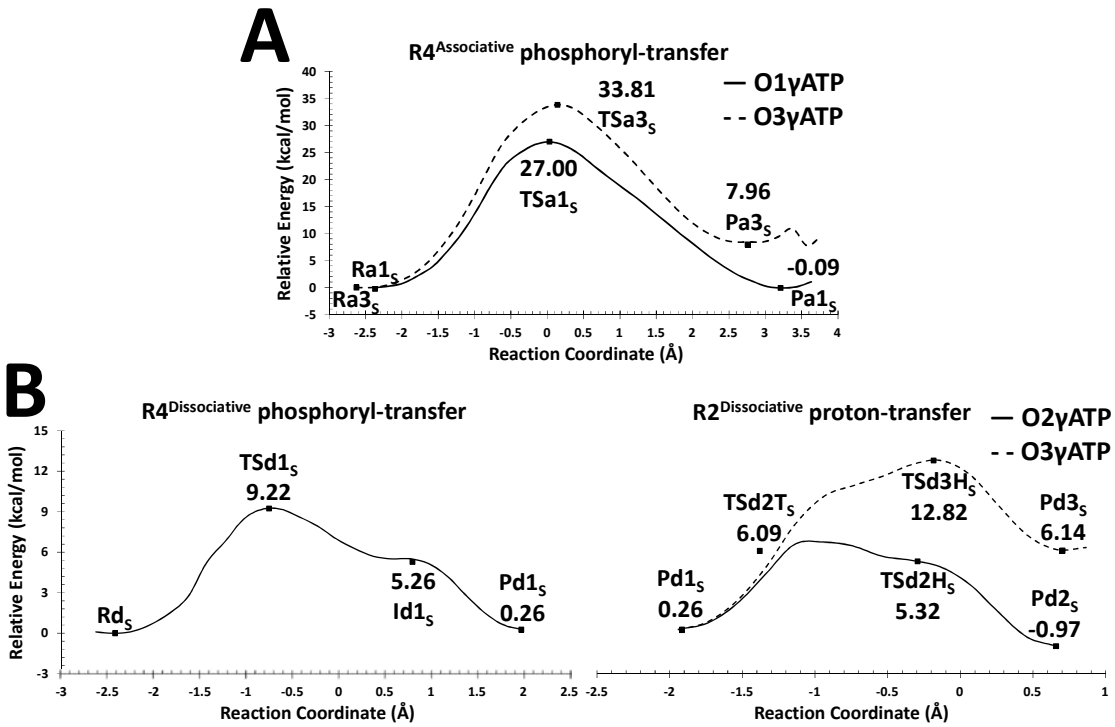

Figure 3.14. Calculated QM(B3LYP/6-31+G(d))/CHARMM potential energy profiles, potential energy barriers, and potential reaction energies for the PKAc-Mg_2ATP-SP20 model along **(A)** the R4-reaction coordinate for the associative phosphoryl-transfer, and **(B)** the R4- and R2-reaction coordinates for the dissociative phosphoryl-transfer and proton-transfer steps, respectively. The γ-oxygen atom in the transferred phosphate group acting as the proton (HγSer21) acceptor is indicated in each case.

hydrogen bond (all those values correspond to O-O distances).

Thus, compared to the $i_{model}S_{Mg}$ and regardless of the phosphoryl-transfer reaction channel that each one defines geometrically, it is clear that all three converged reactive complexes have been reached after a conformational change in the Ser21 side chain. Moreover, with this new configuration the terminal phosphate group of the ATP cofactor is closer to the nucleophilic γ-oxygen atom of substrate serine. Thus, the computationally obtained ternary complex structures seem to be more directed towards the corresponding chemical step than the preceding model structures (4IAC and $i_{model}S_{Mg}$ structures).

The QM/MM potential energy profiles at the (B3LYP/6- 31+G(d))/MM level along: (A)the associative, and (B) the dissociative reaction coordinates for the PKAc-Mg_2ATP-SP20 model are shown in Figure 3.14. For the associative profiles, the γ-oxygen atom of ATP acting as the proton acceptor is indicated in each case. The dissociative potential energy profile includes the simulation of the second proton-transfer, from the Oδ2Asp166 atom to both the O2γATP and the O3γATP atoms of the γ-phosphate group of the just phosphorylated substrate serine (then, the change in the reaction coordinate variable should be noted). The related QM/MM potential energy barriers and potential reaction energies are depicted in the corresponding reaction profile.

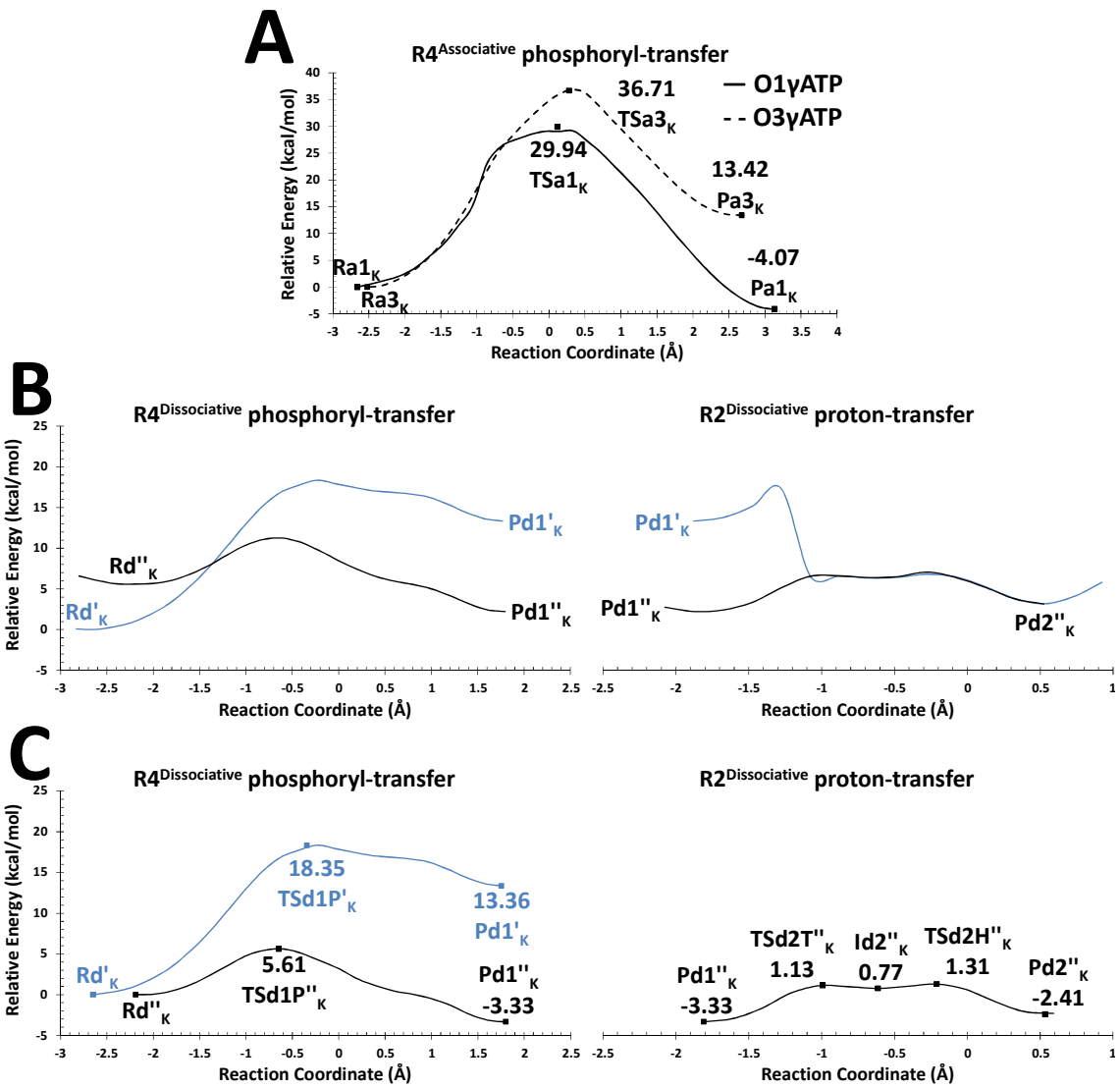

Figure 3.15. Calculated QM(B3LYP/6-31+G(d))/CHARMM potential energy profiles, potential energy barriers, and potential reaction energies for the PKAc(4IAC)-Mg_2ATP-Kemptide model. **(A)** Along the R4-reaction coordinate for the associative phosphoryl-transfer. **(B)** Along the R4- and R2-reaction coordinates for the dissociative phosphoryl-transfer and proton-transfer steps, respectively, relative to the Rd'$_K$ reactant complex. **(C)** Along the R4- and R2-reaction coordinates for the dissociative phosphoryl-transfer and proton-transfer steps, respectively, relative to the corresponding reactant complex energy. The γ-oxygen atom in the transferred phosphate group acting as the proton (HγSer21) acceptor is indicated in each case.

Regarding the PKAc(4IAC)-Mg_2ATP-Kemptide model, the QM/MM potential energy profiles at the (B3LYP/6- 31+G(d))/MM level along the associative, and dissociative reaction coordinates are shown in Figure 3.15A and C. Again, for the associative profiles, the γ-oxygen atom of ATP acting as the proton acceptor is indicated in each case.

For the phosphoryl-transfer step with Kemptide as substrate, three forward/backward cycles of dissociative R4-reaction coordinate scans were needed to obtain a converged potential energy profile, depicted in blue color in the R4 inlet in Figure 3.15B. However, for this PKAc(4IAC)-Mg_2ATP-Kemptide model, when simulating the proton-transfer from the

Oδ2Asp166 atom to the O2γATP atom of the already phosphorylated substrate, using as starting point the Pd1'$_K$ phosphoryl-transfer product complex of the converged potential energy profile, a Pd2''$_K$ final product complex is reached (line in blue color, R2 inlet in Figure 3.15B) which does not connect to the original Pd'1 when simulating backwards the R2-reaction coordinate (line in black color, R2 inlet in Figure 3.15B). Instead, a different but also appropriate intermediate product is characterized (Pd1''$_K$), which in turn defines a different reactant complex (Rd''$_K$) when simulating backwards the R4 dissociative reaction coordinate (line in black color, R4 inlet in Figure 3.15B; the potential energy values are given relative to the Rd'$_K$ reactant complex). Rd'$_K$ is 5.6 kcal/mol more stable than Rd''$_K$. After two forward/backward cycles of dissociative R4 and R2-reaction coordinate scans, respectively, the same converged potential energy profiles were obtained, confirming a thorough phosphoryl-transfer process through a completely different reaction path. In absolute energy, TSd1P''$_K$ is 7.1 kcal/mol more stable than TSd'$_K$, while Pd1''K is almost 11 kcal/mol more stable than Pd1'$_K$. The related QM/MM potential energy barriers and reaction energies for the dissociative reaction profiles (relative to the corresponding reactant complex energy) are presented in Figure 3.15C.

With Kemptide as substrate the dissociative mechanism results only include the simulation of the second proton-transfer from the Oδ2Asp166 atom to the O2γATP atom, since it wasn't possible to simulate the proton-transfer to the O3γATP atom from either of the two Pd1 phosphoryl-transfer products already outlined. Specifically, instead of describing such proton-transfer, the proton is transferred from the Oδ2Asp166 atom back to the nucleophilic γ-oxygen atom of substrate serine. This methodological setback could not be then overcome either by employing different starting points for the simulation or by modifying the numerical parameters, the implementation options or the operation modes for the commands within the constrained R2-reaction coordinate optimization.

3.2.4. Associative pathway.

3.2.4.1. Substrate SP20.

As can be seen in Figure 3.14A, the reaction path that was characterized from the O1γATP-associative reactive complex is energetically favored over that defined from the O3γATP-associative reactive complex (27.0 and 33.8 kcal/mol potential energy barriers, respectively). This was not the expected result considering that the geometry of the preceding $i_{model}S_{Mg}$ and 4IAC crystallographic structures pointed out to a reactive path in which the hydroxyl group of substrate serine side chain could directly protonate O3γATP before the phosphoryl-transfer. Moreover, both associative reaction paths involve higher potential energy barriers for the phosphoryl-transfer than the dissociative counterpart (9.2 kcal/mol, Figure 3.14B). The

calculated reaction potential energies describe two almost isoergic processes for both the O1γATP-associative and the dissociative phosphoryl-transfer paths (−0.1 and 0.3 kcal/mol, respectively), whereas that for the O3γATP-associative is endoergic (8.0 kcal/mol). A general point to be noted is that along all the obtained reaction paths, the significant structural changes within the reactive core occur with no rearrangement in the rest of the ternary complex model.

The $Ra1_S$ and $Ra3_S$ associative reactant complexes evolve to their corresponding product complexes, through the $TSa1_S$ and $TSa3_S$ transition states, respectively. The geometric parameters presented in Tables 3.10 (O1γATP-associative path) and 3.11 (O3γATP-associative path) show that the nucleophilic attack in both reaction channels takes place with an O3βATP-PγATP-OγSer21 bond angle of 167° and 165° at $TSa1_S$ and $TSa3_S$, respectively, and when ADP and the γ-phosphate leaving group are still bonded (O3βATP-PγATP bond distance of 1.8 Å at $TSa1_S$ and $TSa3_S$). To reach those structures, the proton-transfer -from the nucleophilic hydroxyl group of Ser21 to the corresponding γ-oxygen atom of the terminal phosphate group of ATP- anticipates the phosphoryl-transfer. Consequently, the distance from the OγSer21 atom to the proton-acceptor γ-oxygen atom decreases to 2.3 Å along the initial segment of the reaction coordinate. This, in turn, facilitates the breaking of the β,γ-bridging bond of ATP along the nucleophilic displacement.

Table 3.10. Selected QM(B3LYP/6-31+G(d))/CHARMM bond distances (Å), bond angles (deg), and dihedrals (deg) in the optimized reactants ($Ra1_S$), transition state ($TSa1_S$), and products ($Pa1_S$) for the associative mechanism with the O1γATP as the proton acceptor in the PKAc-Mg_2ATP-SP20 model. Comparison with values from X-ray crystallographic structures characterizing different stages of the phosphoryl-transfer mechanism catalyzed by the PKAc with SP20 as substrate and Mg^{2+} ions.[a]

	4IAC[76]	$i_{model}S_{Mg}$	Ra1	TSa1	Pa1	1L3R[79]	4IAF[76]
O3βATP-PγATP	1.8*	1.70	1.70	1.76	2.93	2.3*	4.1
PγATP-OγSer21	3.5	3.76	3.11	2.27	1.64	2.3*	1.6
OγSer21-HγSer21	---	0.98	0.98	1.57	2.91	---	---
O1γATP-HγSer21	---	3.12	1.94	1.03	0.99	---	---
OγSer21-Oδ2Asp166	4.4	4.28	4.01	4.2	3.5	2.5	4.7
$angle_{O3\beta ATP\text{-}P\gamma ATP\text{-}O\gamma Ser21}$	148.2*	141.3	174.2	167.1	171.8	162.6*	159.8
$angle_{O\gamma Ser21\text{-}H\gamma Ser21\text{-}O1\gamma ATP}$	---	153.6	151.8	130.7	59.1	---	---
$d._{Ser21(N\text{-}C\alpha\text{-}C\beta\text{-}O\gamma)}$	64.0	68.7	-39.3	-40.9	-46.5	-64.8	74.0
							-119.2*
$d._{Asp166(C\beta\text{-}C\gamma\text{-}O\delta2)\text{-}O2\gamma ATP}$	160.0	167.2	158.7	147.9	142.3	117.8*	-152.5*
							-104.8*

[a] For 4IAC * is O3βATP=CβAMP-PCP; for 1L3R * γPO3=AlF3; for 4IAF * means that is not possible to establish the chemical correspondence of the O*i*γATP atoms in relation to the 4IAC[76] nomenclature.

Table 3.11. Selected QM(B3LYP/6-31+G(d))/CHARMM bond distances (Å), bond angles (deg), and dihedrals (deg) in the optimized reactants ($Ra3_S$), transition state ($TSa3_S$), and products ($Pa3_S$) for the associative mechanism with the O1γATP as the proton acceptor in the PKAc-Mg_2ATP-SP20 model. Comparison with values from X-ray crystallographic structures characterizing different stages of the phosphoryl-transfer mechanism catalyzed by the PKAc with SP20 as substrate and Mg^{2+} ions.[a]

	4IAC[76]	$i_{model}S_{Mg}$	Ra3	TSa3	Pa3	1L3R[79]	4IAF[76]
O3βATP-PγATP	1.8*	1.70	1.70	1.78	2.89	2.3*	4.1
PγATP-OγSer21	3.5	3.76	3.27	2.26	1.64	2.3*	1.6
OγSer21-HγSer21	---	0.98	0.98	1.64	2.50	---	---
O3γATP-HγSer21	---	1.81	2.04	1.01	0.99	---	---
OγSer21-Oδ2Asp166	4.4	4.28	3.40	3.63	3.54	2.5	4.7
$angle_{O3\beta ATP\text{-}P\gamma ATP\text{-}O\gamma Ser21}$	148.2*	141.3	166.5	164.6	171.2	162.6*	159.8
$angle_{O\gamma Ser21\text{-}H\gamma Ser21\text{-}O3\gamma ATP}$	---	153.6	145.2	127.5	80.3	---	---
$d._{Ser21(N\text{-}C\alpha\text{-}C\beta\text{-}O\gamma)}$	64.0	68.7	-69.9	-59.2	-48.7	-64.8	74.0
							-119.2*
$d._{Asp166(C\beta\text{-}C\gamma\text{-}O\delta2)\text{-}O2\gamma ATP}$	160.0	167.2	159.0	154.1	148.6	117.8*	-152.5*
							-104.8*

[a] For 4IAC * is O3βATP=CβAMP-PCP; for 1L3R * γPO3=AlF3; for 4IAF * means that is not possible to establish the chemical correspondence of the O*i*γATP atoms in relation to the 4IAC nomenclature.

However, although this preliminary proton-transfer process increases the nucleophilicity of OγSer21, it also involves important geometric constraints, particularly for the HγSer21-OγSer21-PγATP-OiγATP ring.[190] Thus, an extra energy penalty must be overcome by the reacting atoms to reach a configuration prone for the nucleophilic attack, *i.e.* with a short enough PγATP-OγSer21 distance, and an almost linear O3βATP-PγATP-OγSer21 bond angle, as in both $TSa1_S$ and $TSa3_S$ structures. In comparison, for the associative reaction pathway from a specific MD simulation snapshot of the PKAc(1CDK)-Mg_2ATP-Kemptide model, namely eq21, a potential energy barrier of 21.3 kcal/mol is reported in this Thesis for the reaction channel with the O1γATP atom as the proton acceptor (it should be recall that the more extensive the MD simulation time was, the corresponding initial geometry gave place to higher potential energy barriers upon calculation of the reaction coordinate). The lower potential energy barrier in that case is likely a consequence of a less restrained transition state compared to the $TSa1_S$ structure. In both $TSa1_S$ and $TSa3_S$, the calculated transition vectors (with associated imaginary frequencies of 141i and 228i cm^{-1}, respectively) clearly characterize the nucleophilic substitution, although with some remnant contribution from the movement of the shifted proton. Finally, the PγATP-OγSer21 bond is clearly formed in $Pa1_S$ and $Pa3_S$ (1.64 Å) phosphorylation product complexes, and a 2.9 Å O3βATP-PγATP distance in both of them is in clear agreement with previous

theoretical results for which the phosphoryl-transfer process has been considered effectively completed.[166-167,190]

As mentioned before, within the associative mechanism and for the PKAc-Mg_2ATP-SP20 model, the computed energy barriers given in Figure 3.14A clearly favor the reaction channel with the O1γATP atom as the proton acceptor over that obtained with O3γATP. This trend is in agreement with the results with Kemptide as substrate and PKAc described by the 1CDK crystallographic structure. In summary, the transfer of HγSer21 to O1γATP causes the remaining γ-phosphoryl negative charge to accumulate in the O2γATP and O3γATP atoms, where it is more readily stabilized by means of the already existing coordination interactions with the Mg^{2+} ions (see Mg^{2+} ions coordination sphere in Table A1). On the contrary, the transfer of HγSer21 to O3γATP disturbs the coordination sphere of the Mg1 ion to which that γ-oxygen atom is bonded (see Mg^{2+} ions coordination sphere in Table A2).

Regarding the O3γA-and O1γATP-associative product complexes (the $Pa3_S$ and $Pa1_S$ structures, respectively), it can be observed that the coordination of both Mg^{2+} ions is octahedral, and it is almost identical to that in the corresponding reactant complex structures ($Ra3_S$ and $Ra1_S$, respectively), with the exception of the Mg2−O3βATP interaction. Specifically, such interaction is strengthened due to the stabilization by the Mg2 metal ion of the negative charge that accumulates on the β,γ-bridging oxygen as the β,γ-phosphoanhydride bond of ATP breaks due the nucleophilic attack of OγSer21 on PγATP (see Mg^{2+} ions coordination sphere in Tables A1 and A2). Moreover, as it is also observed in all the optimized stationary points along the O1γATP- and O3γATP-associative paths, the NζLys168 atom forms strong hydrogen bonds with OγSer21 and O2γATP (see the catalytic core interaction distances in Tables A1 and A2). This observation will be further developed when comparing the final product complexes of the dissociative mechanism with the 4IAF structure, because those interactions are also found there.

3.2.4.2. Substrate Kemptide.

Similarly to the model with SP20 as substrate, the O1γATP-associative path is energetically favored over the one defined for the associative phosphoryl-transfer with the O3γATP atom as recipient of HγSer17, by almost 7 kcal/mol (with potential energy barriers of 29.9 and 36.7 kcal/mol, respectively). Thus, for both substrates -SP20 and Kemptide- in their corresponding initial model (as well as in the 4IAC crystallographic structure used as model template), the configuration of the substrate serine side chain relative to the γ-phosphate of ATP, prone to an O3γATP-associative phosphoryl-transfer path, does not evolve to an effective reaction channel. Moreover, the O1γATP-associative path itself involves an almost 12 kcal/mol higher potential energy barrier than the one calculated initially for the dissociative phosphoryl-transfer path

(18.4 kcal/mol, blue profile in Figure 3.15C), and 24 kcal/mol higher than the one for the energetically favored dissociative path (5.6 kcal/mol, black profile in Figure 3.15C). The calculated reaction potential energies describe an exoergic process for the O1γATP-associative path (-4.1 kcal/mol), whereas that for the O3γATP-associative path is highly endoergic (13.4 kcal/mol). Both results agree with those determined for the model with SP20 as substrate.

The geometric parameters included in Tables A5 and A6 show the structural evolution of the reaction core and its surroundings along the O1γATP- and O3γATP-associative paths, respectively. In $Ra1_K$ the side chain of substrate serine is clearly directed towards the γ-phosphoryl group of ATP, while in the $Ra3_K$ it does in a much lesser degree (O3βATP-PγATP-OγSer17 angle of 177 and 147°, respectively), with the OγSer17 atom closer to the PγATP atom in $Ra1_K$ than in $Ra3_K$ (2.85 and 3.43 Å, respectively). Further, the reactive core is packed together more closely in $Ra1_K$ than in $Ra3_K$, with the side chains of Asp166, Lys168, and Thr201 interacting stronger with the side chain of the substrate serine. Particularly relevant is the difference in the NζLys168-OγSer17 distance (2.82 and 4.68 Å in $Ra1_K$ and $Ra3_K$, respectively). These distinctive geometric conditions within the reactive core remain throughout the course of the corresponding reaction coordinate. A loose reactive core in the O3γATP-associative path might explain its higher potential energy barrier.

In both $TSa1_K$ and $TSa3_K$ transition states, the characteristic linear alignment of atoms participating in the nucleophilic displacement of the phosphoryl-transfer is displayed (the nucleophilic substitution is characterized by transition vectors with associated imaginary frequencies of 153i and 184i cm^{-1}, respectively). In fact, with the exception of the position of the Asp166-Lys168-Thr201 triad relative to Ser17 in the O3γATP-path, the geometric parameters of the reactive core with Kemptide as substrate are practically identical to those obtained with SP20 in the corresponding associative path. This holds true for the final phosphorylation product complexes too.

The structural resemblance is likely a consequence of both the use of the SP20 molecular fragment within the 4IAC crystallographic structure as template for the *in silico* modelling of Kemptide, and also due to the fact that none subsequent MD simulation as a geometry-relaxation methodology was carried out. It is important to note that at this point of the study we decided to take directly the X-ray crystallographic results instead of relaxing it through MD simulations because of the non-reactive structures generated previously by the MD simulations on the PKAc(1CDK)-Mg_2ATP-Kemptide and PKAc(1ATP)-Mg_2ATP-Kemptide models. Thus, although SP20 (an icosapeptide) and Kemptide (an heptapeptide) differ substantially at the molecular level -with the exception of the kinase phosphorylation consensus recognition sequence- and, therefore, they may establish a different set of substrate-enzyme interactions

with PKAc (irrespective of the crystallographic structure used as starting point for the protein kinase), the approach employed here for the setup and simulation of the phosphoryl-transfer process with both substrates and the same crystallographic model of PKAc (in this case, 4IAC), does not translate, at least with regard to the associative mechanism, into significant structural changes within the reactive core. Moreover, this might help to explain the very similar associative potential energy barriers obtained with both substrates. On the other hand, the explanation for the deviation with respect to the results with the eq21-snapshot of the PKAc(1CDK)-Mg_2ATP-Kemptide model, follows what has already been described regarding a less restrained transition state in that case.

3.2.5. Dissociative pathway.

3.2.5.1. Substrate SP20.

The calculated potential energy barriers and reaction potential energies for the complete dissociative mechanism on the PKac-Mg_2ATP-SP20 ternary complex appear summarized in Figure 3.14B. For the phosphoryl-transfer step (see R4 Dissociative phosphoryl-transfer profile), besides the corresponding transition state ($TSd1P_S$) and product complex ($Pd1_S$), it was also characterized an intermediate structure ($Id1_S$) connecting both of them (see structures in Figure 3.16A-C).

The inspection of the $TSd1P_S$ structure (Table 3.12) reveals that the nucleophilic attack takes place when the γ-phosphoryl group –in a planar configuration– is in a quasi-symmetrical position between the leaving O3βATP (2.31 Å) and the entering OγSer21 (2.36 Å) oxygen atoms. That is, within a trigonal bipyramidal coordination around the reacting γ-phosphorus atom, in the $TSd1P_S$ structure, the O3βATP-PγATP bond is almost completely broken when the PγATP-OγSer21 bond-forming interaction begins to strengthen. These results are in excellent agreement with that for the TS mimic 1L3R X-ray crystallographic structure,[79] in which the γ-phosphoryl group is replaced by the planar AlF_3 group, showing distances of 2.3 Å to the ADP moiety and substrate serine (see structural data given in Table 3.12 and Figure 3.17). The same concordance can be established for the O3βATP-PγATP-OγSer21 angle (consistent with a nearly in-line mechanism) and for the orientation of Asp166 side chain relative to the γ-phosphoryl group (Asp166(Cβ-Cγ-Oδ2)-O2γATP dihedral).

The most significant difference between both structures is related with the conformation of the Gly-rich loop shown in Figure 3.17B. However, it is relevant to highlight that both loop conformations with Ser53-Gly186 distances of 11.01 Å for $TSd1P_S$ and 10.38 Å for 1L3R, respectively, clearly belong to the so-called closed conformational state defined by Ser53-Gly186 distances within the range 11±2 Å.[43] In fact, recent MD simulations have also shown that

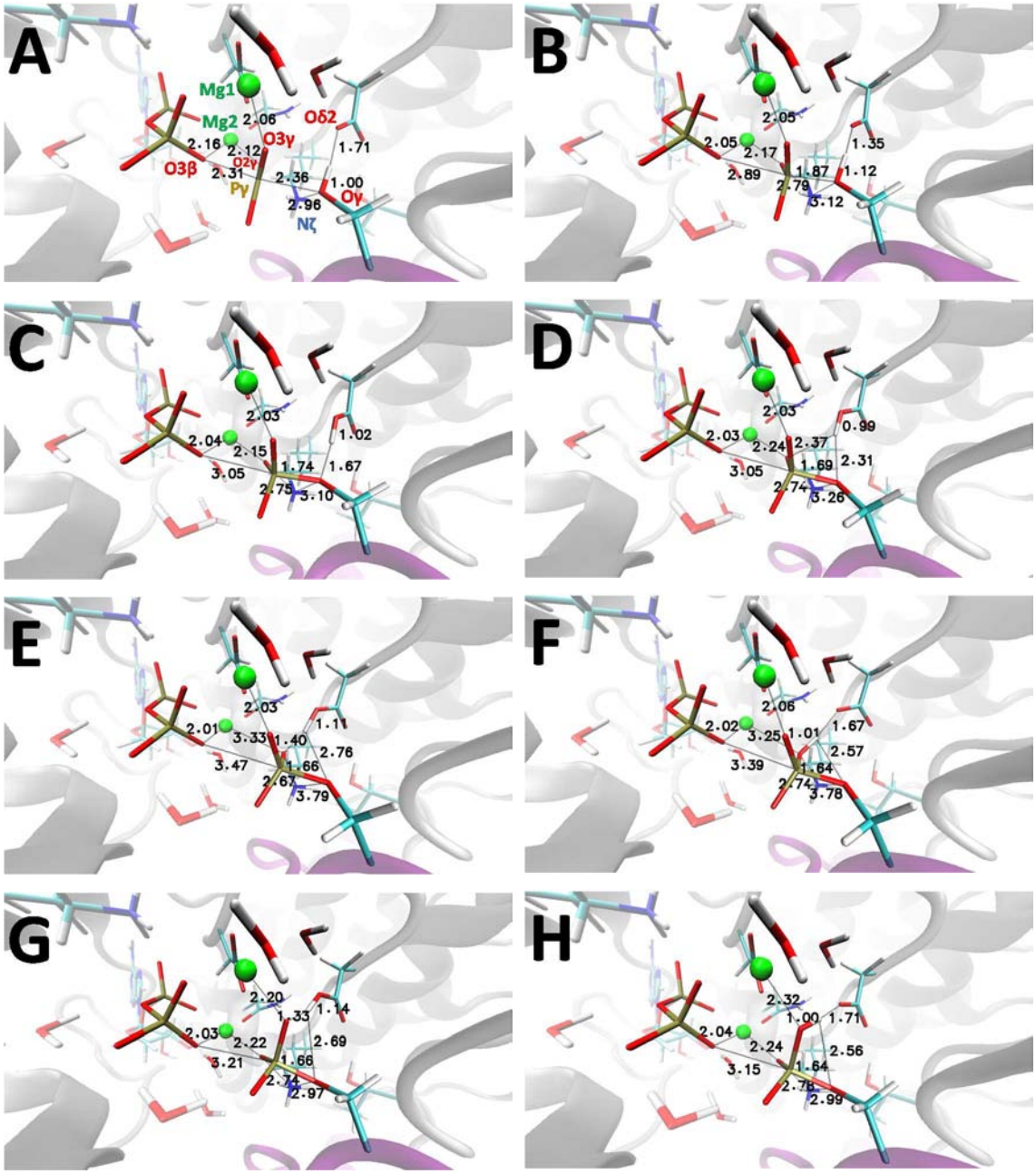

Figure 3.16. Active sites of the QM(B3LYP/6-31+G(d))/CHARMM optimized **(A)** TSd1P$_S$, **(B)** Id1$_S$, **(C)** Pd1$_S$, **(D)** TSd2T$_S$, **(E)** TSd2H$_S$, **(F)** Pd2$_S$, **(G)** TSd3H$_S$, and **(H)** Pd3$_S$ for the dissociative mechanism simulation on the PKAc-Mg$_2$ATP-SP20 model. The QM region together with some relevant residues side chains and water molecules in the active site are represented as sticks. Selected distances (in Å) are also indicated.

the ternary complex PKAc-ATP-substrate displays higher root-mean-square fluctuation (RMSF) values for all the relevant catalytic loops and, in particular, for the Gly-rich loop in comparison with the dynamics of the PKA-ATP-inhibitor complex.[43-45,149] The flexibility of the Gly-rich loop is then a dynamic feature of the reactive closed conformations of the PKA-ATP-substrate. The results in this Thesis suggest that this motion is not catalytically relevant if the closed conformation is maintained.

Frequency calculations confirmed a single imaginary frequency mode of 75i cm^{-1}, with the

transition vector accounting for the nucleophilic attack exclusively and, therefore, without showing any contribution related with the movement of the proton of the hydroxyl group of substrate serine toward the carboxylate group of Asp166 side chain.

Thus, along the phosphoryl-transfer step of the dissociative mechanism, HγSer21 is not promptly shifted from the substrate hydroxyl to the nascent phosphoryl group. It is rather delivered to the carboxylate group of the highly conserved Asp166 residue after the phosphoryl-transfer. Then, in going from the $TSd1P_S$ to the $Pd1_S$ phosphoryl-transfer product complex, the reaction path describes a plateau (0.5 Å < R4 < 1.0 Å values) involving a set of geometries that were used as starting points for searching a transition state structure that could characterize such proton-transfer to the Asp166 side chain. However, such structure was not found. The related $Id1_S$ intermediate structure lays 4.0 kcal/mol below $TSd1P_S$ and 5.0 kcal/mol above $Pd1_S$.

Table 3.12. Selected QM(B3LYP/6-31+G(d))/CHARMM bond distances (Å), bond angles (deg), and dihedrals (deg) in the optimized reactants (Rd_S), phosphoryl-transfer transition state ($TSd1P_S$), proton shift intermediate ($Id1_S$), phosphoryl-transfer products ($Pd1_S$), protonated Asp166 side chain-rotation transition state ($TSd2T_S$), proton-transfer transition state ($TSd2H_S$), and proton-transfer products ($Pd2_S$) for the dissociative mechanism with the O2γATP as the final proton acceptor in the PKAc-Mg_2ATP-SP20 model. Comparison with values from X-ray crystallographic structures characterizing different stages of the phosphoryl-transfer mechanism catalyzed by the PKAc with SP20 as substrate and Mg^{2+} ions.[a]

	Rd	$TSd1P_S$	$Id1_S$	$Pd1_S$	$TSd2T_S$	$TSd2H_S$	$Pd2_S$	1L3R	4IAF
O3βATP-PγATP	1.76	2.31	2.89	3.02	3.05	3.47	3.39	2.3*	4.1
PγATP-OγSer21	3.36	2.36	1.87	1.74	1.69	1.66	1.64	2.3*	1.6
OγSer21-HγSer21	0.99	1.00	1.12	1.67	2.31	2.76	2.57	---	---
Oδ2Asp166-HγSer21	1.81	1.71	1.35	1.02	0.99	1.11	1.67	---	---
O2γATP-HγSer21	3.26	2.82	2.76	2.93	2.37	1.40	1.01	---	---
OγSer21-Oδ2Asp166	2.80	2.71	2.46	2.66	3.17	3.49	3.57	2.5	4.7
									3.3*
Oδ2Asp166-O2γATP	3.82	3.59	3.47	3.52	3.11	2.49	2.68	3.1*	5.4*
									5.8*
a.$_{O3\beta ATP\text{-}P\gamma ATP\text{-}O\gamma Ser21}$	167.7	168.4	166.2	166.3	170.8	178.3	172.0	162.6*	159.8
a.$_{O\gamma Ser21\text{-}H\gamma Ser21\text{-}O\delta 2Asp166}$	173.3	172.0	169.3	162.2	145.3	123.0	113.1	---	---
a.$_{O\delta 2Asp166\text{-}H\gamma Ser21\text{-}O2\gamma ATP}$	93.6	101.6	110.8	117.8	130.8	164.4	172.5	---	---
d.$_{Ser21(N\text{-}C\beta\text{-}C\gamma\text{-}O\gamma)}$	-56.8	-48.1	-42.9	-43.2	-60.7	-73.5	-70.1	-64.8	74.0
									-119.2*
d.$_{Asp166(C\beta\text{-}C\gamma\text{-}O\delta 2)\text{-}O2\gamma ATP}$	119.6	118.4	118.7	124.5	145.8	172.4	175.0	117.8*	-152.5*
									-104.8*

[a] For 1L3R * γPO3=AlF3; for 4IAF * means that is not possible to establish the chemical correspondence of the O*i*γATP atoms in relation to the 4IAC nomenclature.

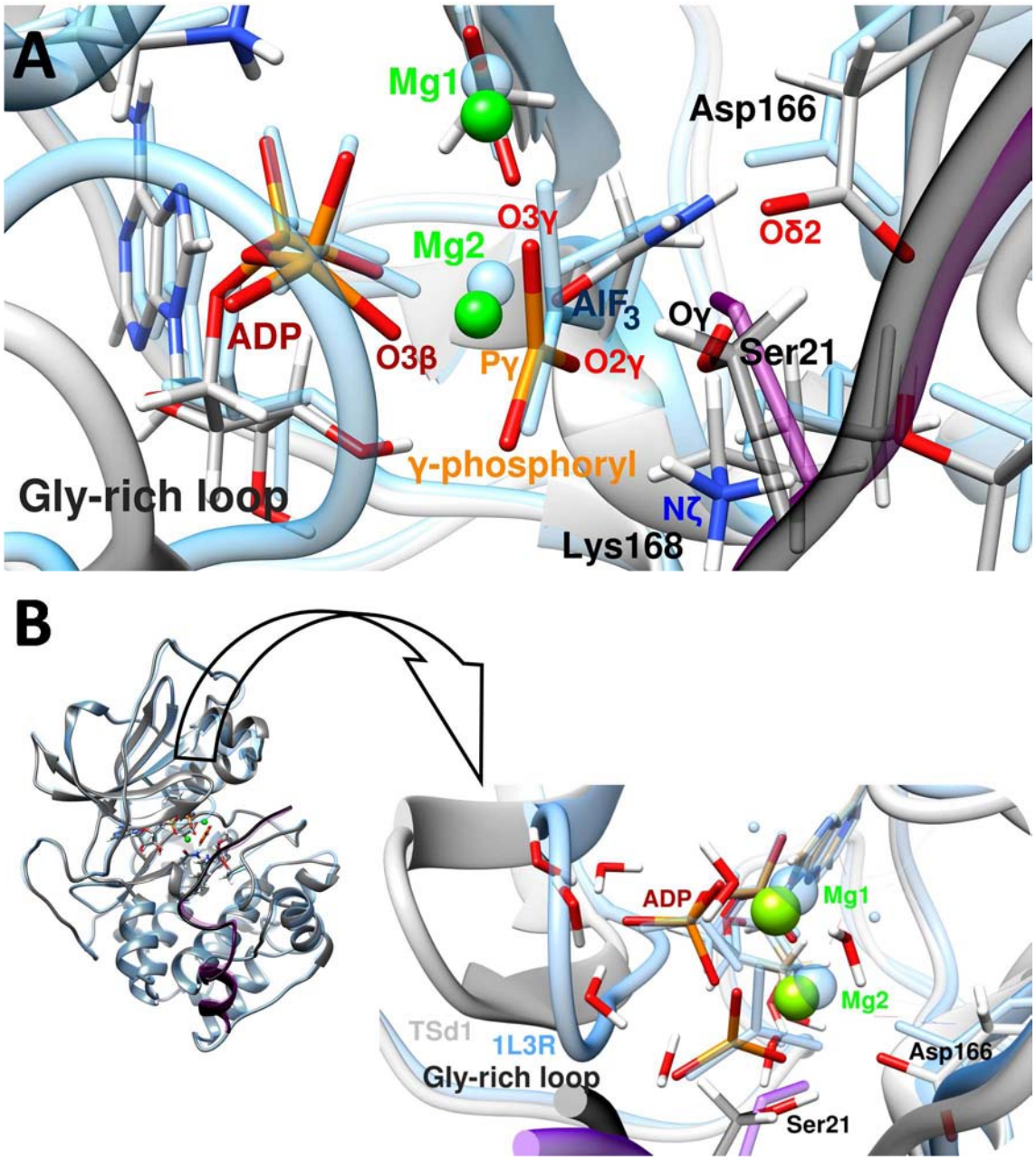

Figure 3.17. (A) Superposition of the active sites in the phosphoryl-transfer transition state structure of the dissociative mechanism (TSd1P$_S$) for the PKAc-Mg$_2$ATP-SP20 model (as sticks colored by atom type) and transition state mimic crystallographic structure (1L3R, as black sticks). **(B)** Global overlay of the TSd1P$_S$ (gray) and 1L3R (light blue) structures. In the inset, an enlarged view of the active site showing the different conformations of the Gly-rich loop in both structures (sticks colored by atom type correspond to the TSd1P$_S$ structure and sticks in light blue correspond to the 1L3R structure).

Although Id1$_S$ formally fulfills the conditions for a shallow minimum, it should be rather considered as a shoulder along the reaction path. Essentially, while the γ-phosphoryl group continues moving away from ADP (O3βATP-PγATP 2.89 Å) and its bond with the substrate serine is significantly formed (PγATP-OγSer21 1.87 Å), when arriving at the Id1$_S$ structure, the OγSer21 atom interacts through a very short hydrogen bond with the Oδ2Asp166 atom (2.46 Å), so that the related proton-transfer event takes place without any additional energy cost. Further, in the

$Pd1_S$ structure the OH bond of the substrate serine is completely broken (1.67 Å), but the hydrogen bond interaction between the now protonated Oδ2Asp166 and the phosphorylated OγSer21 (2.66 Å) is still present, though it is not as short as in $Id1_S$ (see Table 3.12).

Regarding the octahedral coordination for both Mg^{2+} ions (see Mg^{2+} ions coordination sphere section in Table A3), it remains practically unchanged throughout the phosphoryl-transfer step, except for the Lewis acid attack of Mg2 that stabilizes the nascent and leaving ADP moiety. Thus, the initially weakly bound Mg2 metal ion strengthens its interaction with O3βATP by screening the negative charge which accumulates on the β,γ-bridging oxygen concomitant with the cleavage of the O3βATP-PγATP bond. Specifically, the Mg2-O3βATP distance decreases almost to its final value as the molecular complex evolves through the transition state region ($TSd1P_S$).

On the other hand, in $Pd1_S$, the O2γATP and O3γATP atoms of the phosphorylated Ser21 are both reachable (from a sterically point of view) from the just protonated Oδ2Asp166, whereas the O1γATP is much farther away, and the proton-transfer to such oxygen atom would have to occur through –or in the immediate vicinity of– the newly formed PγATP-OγSer21 bond, thus distorting it severely. Therefore, only the proton-transfer paths corresponding to the protonation of the phosphorylated SP20 substrate at O2γATP and O3γATP were explored (see Figure 3.14B, R2 Dissociative proton-transfer profiles).

Specifically, the O2γATP-path goes through a transition state structure ($TSd2T_S$) that represents a potential energy barrier of 6.1 kcal/mol (*i.e.* 5.8 kcal/mol over $Pd1_S$ and approximately 3 kcal/mol lower than the barrier corresponding to the phosphoryl-transfer step). The $TSd2T_S$ structure is characterized by a transition vector (44i cm^{-1}) that corresponds to the rotation of the protonated side chain of Asp166 toward the O2γATP atom. This movement, from $Pd1_S$ to $TSd2T_S$, can also be assessed from the increase of the Asp166(Cβ-Cγ-Oδ2)-O2γATP dihedral and the decrease in the Oδ2Asp166-O2γATP distance (see Table 3.12; accordingly, the OγSer21-Oδ2Asp166 distance increases).

After passing $TSd2T_S$, these trends continue, and the molecular complex evolves through another transition state structure, the $TSd2H_S$ (localized around a R2 value of –0.25 Å), whose transition vector (179i cm^{-1}) characterizes the proton-transfer from the carboxylic group Asp166 to O2γATP. Specifically, Oδ2Asp166 and O2γATP interact strongly through a short hydrogen bond (2.49 Å). Furthermore, a Oδ2Asp166-HγSer21-O2γATP angle of 164° and a Asp166(Cβ-Cγ-Oδ2)-O2γATP dihedral of 172° also account for the clear orientation of the protonated carboxylic oxygen of Asp166 side chain toward the proton-acceptor O2γATP atom of the phosphorylated Ser21. Energetically, $TSd2H_S$ represents a 5.3 kcal/mol potential energy barrier with respect to the reactant complex structure. That is, 5 kcal/mol over $Pd1_S$ and 0.8 kcal/mol more stable than

the preceding $TSd2T_S$ structure. The efforts to computationally define a stable intermediate connecting both transition state structures were unsuccessful.

Finally, after going through $TSd2H_S$, the HγSer21 proton is completely transferred to O2γATP (1.01 Å), forming the $Pd2_S$ final product structure, in which the Oδ2Asp166 and O2γATP atoms are still tightly hydrogen-bonded (at a distance of 2.68 Å, and with an Oδ2Asp166-HγSer21-O2γATP angle of 173°). Moreover, the final PγATP-OγSer21 distance at $Pd2_S$ of 1.64 Å is in good agreement with that in the 4IAF X-ray structure of the PKAc-Mg_2ADP-pSP20 ternary complex. The global reaction potential energy is -1.0 kcal/mol with respect to the reactant complex, so that the overall dissociative phosphoryl-transfer mechanism is slightly exoergic when following the O2γATP-path for the second proton-transfer.

On the other hand, regarding the O3γATP-path for the proton-transfer step, although the protonated carboxylate group of Asp166 side chain also rotates toward O3γATP when evolving from $Pd1_S$, the rotation takes place now along the uphill region of the corresponding potential energy profile (around a R2 value of -1.0 Å, see Figure 3.14B), in such a way that it does not constitute an independent chemical step by itself. Thus, the O3γATP-path reaches the $TSd3H_S$ transition state structure that characterizes the proton-transfer with a transition vector (710i cm^{-1}) with a unique contribution from the movement of the transferred proton. Energetically, $TSd3H_S$ is 12.8 kcal/mol less stable than the reactive complex Rd_S (a potential energy barrier almost 7 kcal/mol higher than $TSd2T_S$ and $TSd2H_S$). As it happens in $TSd2H_S$, the HγSer21 proton is completely transferred to O3γATP (with a O3γATP-HγSer21distance of 1.00 Å), and the Oδ2Asp166 atoms interacts strongly with O3γATP through a short hydrogen bond (2.43 Å, see Table A4). The proton-transfer to the O3γATP of the phosphorylated substrate results in the formation of the $Pd3_S$ product complex structure, which entails a 6.1 kcal/mol reaction potential energy. That is, the O3γATP-path for the proton-transfer step gives a final product 7 kcal/mol less stable than the O2γATP-path.

The proton-transfer from Oδ2Asp166 to O2γATP clearly destabilizes the Mg2−O2γATP interaction: the Mg2-O2γATP distance increases from 2.15 Å at $Pd1_S$ to 3.33 Å at $TSd2H_S$, and then remains almost constant, attaining a value of 3.25 Å at $Pd2_S$ (see Table A3). In contrast, the protonation of O3γATP does not entail such a separation from Mg1: the Mg1-O3γATP distance only increases from 2.03 Å at $Pd1_S$ to 2.20 Å at $TSd3H_S$, and then to 2.32 Å at $Pd3_S$ (see Table A4). That is, after the phosphoryl-transfer step, the negative charge on O2γATP is less stabilized by Mg2 than the negative charge on O3γATP by Mg1, and then O2γATP has a stronger basic character -with respect to the HγSer21 protonating the carboxylate group of Asp166 side chain- than O3γATP. This explains why the O2γATP-path for the proton-transfer step is favored over the O3γATP-path.

The comparison of the dissociative final product complex structures with the 4IAF crystallographic product complex, reveals significant differences related with the stage of the catalytic cycle represented in each case. In the $Pd2_S$ structure, although O2γATP is farther from Mg2 than in the $Pd3_S$ structure, it is not far enough to completely lose its interaction to Mg2. On the other hand, NζLys168 is strongly hydrogen-bonded to the O2γATP throughout the dissociative phosphoryl-transfer and both proton-transfer O2γATP- and O3γATP-paths (see Tables A3 and A4). Moreover, along the dissociative phosphoryl-transfer, NζLys168 also forms a hydrogen bond with the OγSer21. This interaction remains strong all through the proton-transfer O3γATP-path, and is somewhat weaker along the O2γATP-path. In very good agreement, both interactions are also present in the PKAc TS mimic and the PKAc ATP-hydrolysis products crystallographic structures (PDB codes 1L3R[79] and 4DH5[164] respectively). In contrast, these geometric features significantly differ from what is observed in the PKAc product complex 4IAF crystallographic structure. According to Gerlits *et al*.,[76] as a consequence of the displacement of the γ-phosphate onto the Ser21, in 4IAF the Mg2 ion no longer interacts with the O2γATP but does so with a new water molecule. This relevant change in the coordination sphere of the Mg2 ion along the catalytic mechanism has been recently observed also in two crystallographic structures of PKA-Mg2AMPPNP-SP20 showing partial or total phosphoryl-transfer (4HPU and 4HPT structures, respectively).[102] It is likely that the changes in the Mg2 coordination sphere along the dissociative reaction pathway might correlate with the beginning of the structural changes that take the catalytic system to the product complex 4IAF crystallographic structure.

Thus, after the phosphoryl-transfer step, the Mg2 metal ion strengthens its interaction with O3βATP, increasing its binding to the ADP moiety of ATP, whereas Mg1 presents a more labile coordination all the way through. These differences in the coordination spheres of the two Mg ions seem plausible, taking into account that it has recently been proposed and confirmed that only Mg2 remains bound in the active site with ADP after product release.[146] Once the last proton-transfer step to O2γ takes place, the Mg2-O2γATP distance clearly increases, and this vacant ligand position could be the one occupied by a water molecule in the 4IAF, as well as in the 4HPU and 4HP crystal structures to maintain the octahedral coordination. On the contrary, the Mg1 coordination sphere does not change so much along the chemical process, so the changes observed in the different experimental product complex structures (mostly due to the growing distance of Asp184) must be more related with the product release process.

Further, in 4IAF the phosphate group now bonded to Ser21 does not form any hydrogen bond with Asp166 or with Lys168, but it does form a bond with the OH group of Ser53 side chain, interaction that is neither present in the 4IAC starting structure, nor in the $i_{model}S_{Mg}$ nor along the

associative and dissociative paths and the corresponding optimized stationary points here reported. Gerlits *et al*.[76] relate these observations with the fact that the CβSer21-OγSer21 bond is rotated away from the reaction core toward the bulk solvent so that the product can be released from the enzyme. In this manner, the results presented in this Thesis suggest that while the product complex structures theoretically calculated correspond to the final stage of the phosphoryl-transfer chemical reaction, the 4IAF structure would represent a snapshot of the phosphorylated substrate release progression. Moreover, that seems to be the reason why –in contrast to what is found in the 4IAF crystallographic structure– the interaction between Ser53 residue and the phosphate group of Ser21 in it is not found in either of the theoretically determined product complexes ($Pd2_S$ and $Pd3_S$ structures). These structures are the final products of the complete dissociative phosphoryl-transfer from ATP to the substrate, and in both of them, the now phosphate group of Ser21 is still interacting, via hydrogen bond, with the carboxylate group of Asp166. From this point, the substrate is ready to evolve to its release from the active site.

Then, the dynamic character of a protein system allows the rotation of the Ser21 Cα-Cβ bond of the substrate whose progression might eventually break the hydrogen bond between the phosphate group of Ser21 and Asp166 residue and lead the phosphate to interact with Ser53 in the Gly-rich loop. The visual inspection of the $Pd2_S$ and $Pd3_S$ product structures indicates that this rotation is possible in their active site, and it would had probably occurred if the product release step had been studied by molecular dynamics simulation. However, this is beyond the scope of this Thesis, which in this particular section is focused on the simulation of the complete phosphoryl-transfer from ATP to the SP20 substrate catalyzed by the PKAc enzyme.

To complete the energetic analysis we have performed single-point energy evaluations at the QM(MP2/aug-cc-pVTZ)/CHARMM level of theory on the QM(B3LYP/6-31+G(d))/CHARMM stationary points, while for only the dissociative mechanism results the QM(MP2/def2-TZVP)/CHARMM level of theory was also considered (see Table 3.13). The results confirm the manifest preference of the dissociative mechanism over the associative mechanism, with quite comparable potential energy barrier results at the DFT and MP2 levels (in general, higher potential energy barrier and reaction potential energy results are obtained with the def2-TZVP basis set than with the aug-cc-pVTZ basis set). However, for the second step of the dissociative mechanism, the QM(MP2/aug-cc-pVTZ)/CHARMM high level potential energy barrier at $TSd2H_S$ (that characterizes the proton-transfer to O2γATP as the final proton acceptor), is just 2 kcal/mol lower than that for the proton-transfer to O3γATP at $TSd3H_S$ (6.8 and 8.8 kcal/mol, respectively), while at the DFT level, such difference is 7.5 kcal/mol (5.3 and 12.8 kcal/mol, respectively). Furthermore, the overall potential reaction energy at the QM(MP2/aug-cc-pVTZ)/CHARMM

level of theory is also very similar (1.5 and 3.2 kcal/mol for the O2γATP- and O3γATP-dissociative paths, respectively), whereas this is not the case at the DFT level (–1.0 and 6.1 kcal/mol, respectively). The difference in the proton-transfer barriers when comparing the MP2 and DFT results could be attributed either to the fact that MP2 barriers derive from single-point energy calculations or to an overpolarization of the QM electron density by the MM point charges when using the B3LYP functional and diffuse functions that tend to delocalize the extra electron corresponding to the total charge of the QM region (–1).

3.2.5.2. Substrate Kemptide.

As can be seen in Figure 3.15C, the potential energy barrier for the dissociative phosphoryl-transfer path first calculated (in blue in Figure 3.15C) is 18.35 kcal/mol, and its reaction potential energy is heavily endoergic (13.4 kcal/mol), whereas that with the lower-potential energy barrier (5.61 kcal/mol) is exoergic (-3.3 kγcal/mol). In both cases, the hydrogen atom from the hydroxyl group of substrate Ser17 side chain is clearly oriented to the carboxylate group of Asp166 side chain all along the phosphoryl-transfer step, and the trigonal bipyramidal coordination around the γ-phosphorous atom in a nearly in-line mechanism for the nucleophilic attack is confirmed in both transition state structures, $TSd1P'_K$ and $TSd1P''_K$ (see the O3βATP-PγATP-OγSer17 angle and active core geometric features in Tables A7 and A8, respectively).

Table 3.13. Potential energy barriers and reaction potential energies (in kcal/mol) corresponding to the QM(MP2/aug-cc-pVTZ)/CHARMM and QM(MP2/def2-TZVP)/CHARMM (in brackets) single-point calculations on the QM(B3LYP/6-31+G(d))/CHARMM stationary points in the PKAc-Mg_2ATP-SP20 model.

O1γATP-Associative		O3γATP-Associative		Dissociative	
phosphoryl-transfer		*phosphoryl-transfer*		*phosphoryl-transfer*	
$Ra1_S$	---	$Ra3_S$	---	Rd_S	---
$TSa1_S$	23.26	$TSa3_S$	31.30	$TSd1P_S$	9.52 (11.02)
$Pa1_S$	-3.88	$Pa3_S$	6.42	$Id1_S$	2.26 (3.57)
				$Pd1_S$	-2.68 (-1.79)
				proton-transfer to O2γATP	
				$TSd2T_S$	2.17 (2.95)
				$TSd2H_S$	6.84 (5.05)
				$Pd2_S$	1.47 (-0.01)
				proton-transfer to O3γATP	
				$TSd3H_S$	8.80 (9.34)
				$Pd3_S$	3.19 (4.28)

Although the relative energy varies widely from one phosphoryl-transfer path to the other, the configuration of the active site residues, ATP (or its moieties, ADP and γ-phosphoryl group), and the Mg ions, is almost identical in both of them (for example, see the comparison of the active site of reactant complexes in Figure 3.18A, where Rd'K has PKAc colored in blue with the rest of the system by atom type, and Rd''K is all colored in black). Thus, what chemically distinguishes one reactant complex configuration from the other at the beginning of the phosphoryl-transfer dissociative-path, is the conformation of five water molecules within the reactive core. That is, their specific positions and the particular hydrogen bond interactions they form among themselves and with the β- and γ-phosphate groups of ATP along the stationary points defined in each case. In Figure 3.18B, again for the Rd'_K and Rd''_K structures, these water molecules are highlighted from the set of water molecules which clearly occupy the relative position that the tip of the Gly-rich loop holds in a more closed conformation of the PKAc active site, like the ones featured by PKAc in the phosphoryl-transfer studies with the PKAc(1CDK)-Mg_2ATP-Kemptide models in this Thesis. It can be inferred from the visual inspection of the latter image and attested from the hydrogen bond data in Figure 3.18C, that the hydrogen bond distances that match up in both configurations of the reactant complex have, in general, the same length. Conversely, the other hydrogen bond distances differ "in nature" from Rd'_K to Rd''_K, with significant implications in its length. In the same Figure 3.18C, the clear displacement of water 3 in Rd''_K relatively to its position in Rd'_K is depicted too. The length of the discrepant hydrogen bond interactions are shown more clearly in Figure 3.18D. From this geometrical data, it can be established that in this particular region of the reactive core there is one more hydrogen bond at Rd'_K (the most stable reactant complex configuration) than at Rd''_K. Specifically, O1γATP (marked with an asterisk in Figure 3.18D) forms one more hydrogen bond with the surrounding water molecules in Rd'_K than in Rd''_K. In Rd''_K the water 5 loses its interaction with that particular γ-oxygen atom of ATP because of the movement of water 3, whose translation in Rd''_K, relative to its position in Rd'_K, seems to be, in turn, a consequence of a small movement of water 2. In particular, in Rd'_K the water 2 interacts with the O3γATP atom and water 3, which in turn bridges the O2βATP and O1γATP atoms. On the other hand, in Rd''_K the water 2 bridges the O2βATP and O3γATP atoms, while the water 3 interacts with the O3βATP (the oxygen atom bridging the β- and γ-phosphates in ATP) and O1γATP atoms. Thus, the extra hydrogen bond for O1γATP likely represents the stabilization factor that makes Rd'_K 5.6 kcal/mol more stable than Rd''_K. Moreover, such subtle difference in the hydrogen bond network around the solvent-exposed phosphorylated-tale of ATP could also help to explain the slightly different position, relative to the Ser17 side chain, of the γ-phosphate group. Namely, in Rd'_K the extra hydrogen bond likely holds the γ-phosphoryl moiety more tightly bound in a rearmost position.

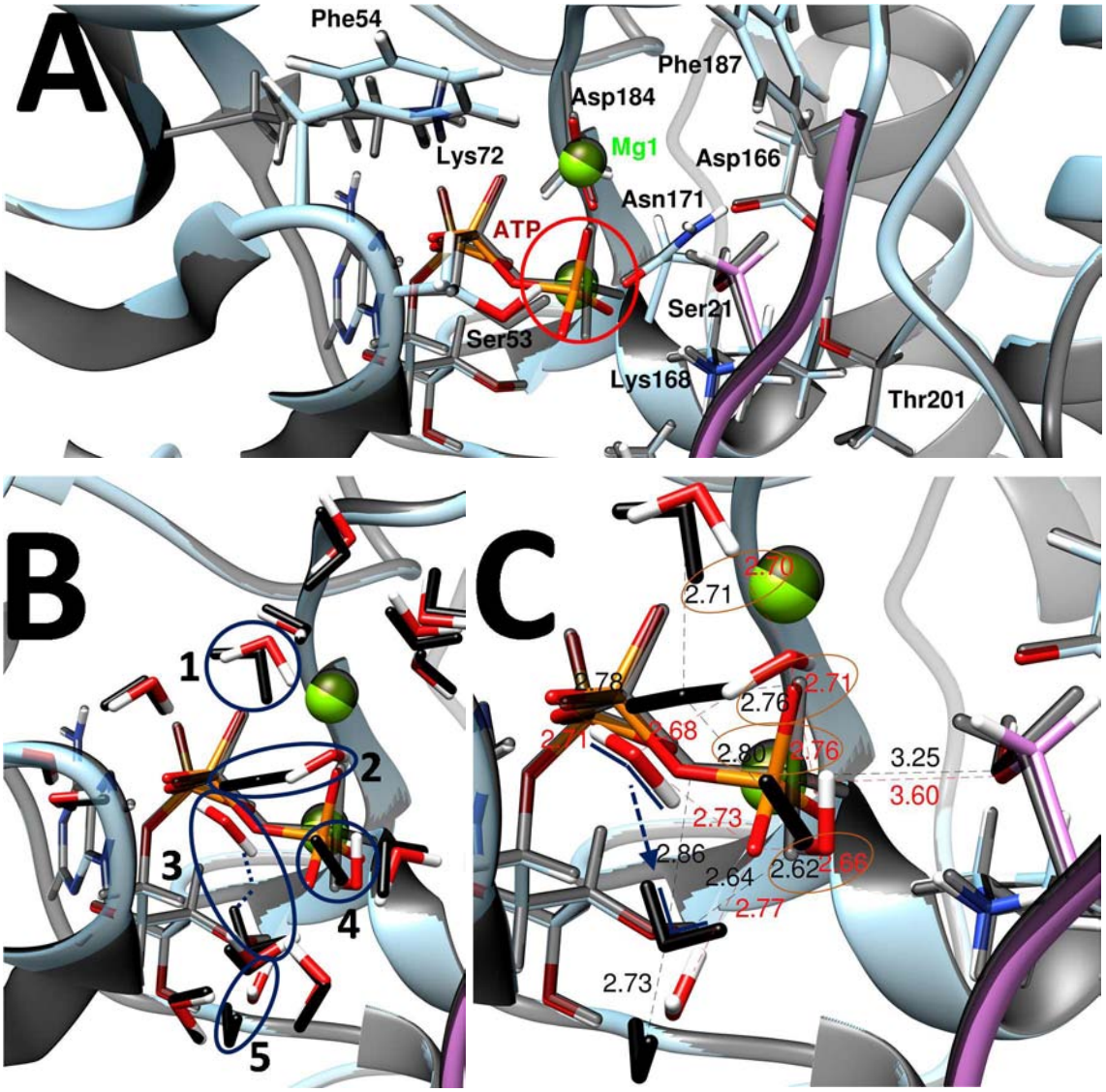

Figure 3.18. Superposition of the active site at the QM(B3LYP/6-31+G(d))/CHARMM optimized reactants (Rd'$_K$ and Rd''$_K$) for the dissociative mechanism in the PKAc(4IAC)-Mg_2ATP-Kemptide model. Rd'$_K$ has PKAc colored in blue and the rest of the system by atom type; Rd''$_K$ is all colored in black. QM region together with relevant residues and crystallographic water molecules in the active site are represented as sticks. Selected distances (in Å) are also indicated. **(A)** Active site comparison. **(B)** Crystallographic water molecules within the active site. The crystallographic water molecules that chemically distinguish one reactant complex configuration from the other (due to their specific positions and the particular hydrogen bond interactions they form among themselves and with the β- and γ-phosphate groups of ATP) are highlighted and numbered. **(C)** Hydrogen bond distances for highlighted crystallographic water molecules. Those matching up in both reactants complex are highlighted. The clear displacement of water 3 in Rd''$_K$ relatively to is position in Rd'$_K$ it is also depicted. **(D)** The hydrogen bond distances differing in nature and length are shown exclusively.

Interestingly, when performing the same geometrical analysis in the corresponding transition state structures (TSd1P'$_K$ and TSd''$_K$, see Figure 3.19), with almost all reaction and active site geometric features being very similar, a significant change in the hydrogen bond network around the phosphate groups of ATP it is evident: the O1γATP atom in TSd1P'$_K$ loses its interaction with the water 5 (see the underlined hydrogen bond distance in Figure 3.18D and

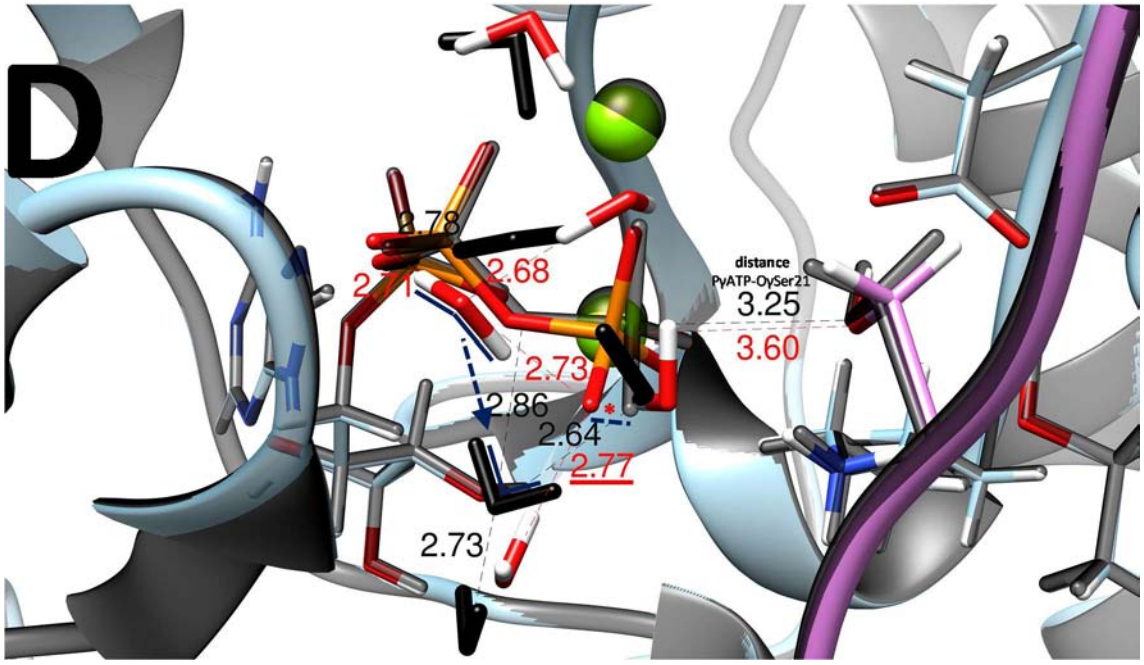

Figure 3.18. *Cont.*

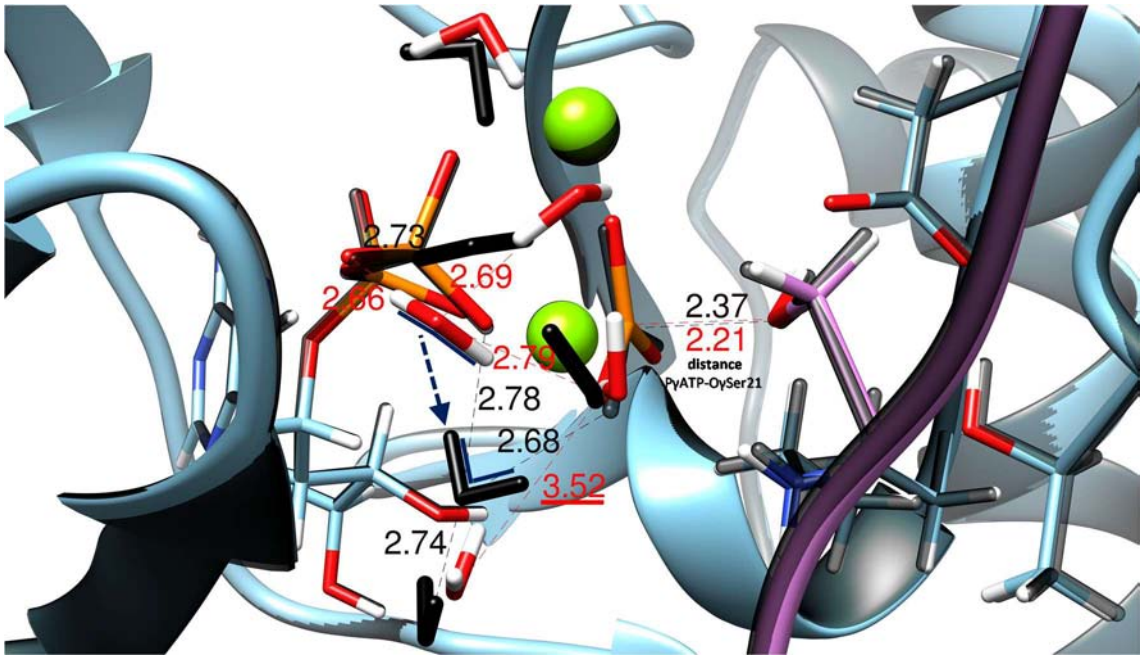

Figure 3.19. Superposition of the active site at the QM(B3LYP/6-31+G(d))/CHARMM phosphoryl-transfer transition states (TSd1P'$_K$ and TSd1P''$_K$) for the dissociative mechanism in the PKAc(4IAC)-Mg_2ATP-Kemptide model. Tsd1P'$_K$ has PKAc colored in blue and the rest of the system by atom type; TSd1P''$_K$ is all colored in black. QM region together with relevant residues and crystallographic water molecules in the active site are represented as sticks. Selected distances (in Å) are also indicated. The hydrogen bond distances differing in nature and length between TSd1P'$_K$ and TSd1P''$_K$ are shown (see the main text).

Figure 3.19). Accordingly, the stabilization factor that an extra water to γ-phosphate hydrogen bond likely meant for Rd'$_K$ with respect to Rd''$_K$ it is also lost. Moreover, the water 3 in TSd1P''$_K$ strengthens its hydrogen bond interaction with O3βATP, stabilizing the negative charge that

accumulates on the β,γ-bridging oxygen as the β,γ-phosphoanhydride bond of ATP breaks due the nucleophilic attack of OγSer17 on PγATP. Thus, in the TSd1P''$_K$ structure, the β-phosphate of ADP and the γ-phosphoryl group are further stabilized by the hydrogen bond network of the surrounding water molecules than in the TSd1P'$_K$ structure. As a result, the less stable reactant complex conformation, Rd''$_K$, gives place, after the simulation of a converged dissociative phosphoryl-transfer reaction coordinate, to a transition state structure that is 7.2 kcal/mol more stable in total energy than that defined from Rd'$_K$, and which also implies a 13 kcal/mol lower potential energy barrier.

On the other hand, in the TSd1P''$_K$ structure the nucleophilic attack takes place with the γ-phosphoryl group in fully planar configuration and with the PγATP in a quasi-symmetrical position between the leaving O3βATP (2.33 Å) and the entering OγSer17 (2.37 Å) oxygen atoms. In comparison, in the TSd1P'$_K$ structure the γ-phosphoryl group is not completely planar, and the O3βATP-PγATP and PγATP-OγSer17 distances differ from each other (2.44 and 2.21 Å, respectively). That is, the TSd1P''$_K$ structure is very similar to the corresponding stationary point with the SP20 as substrate, and the TSd1P'$_K$ structure occurs later in the dissociative phosphoryl-transfer reaction coordinate. Frequency calculations confirmed a single imaginary frequency mode of 73i cm^{-1} for TSd1P'$_K$ and 66i cm^{-1} for TSd1P''$_K$, with the transition vector accounting in both cases for the nucleophilic attack and showing some contribution of the transfer of the HγSer17 of substrate serine hydroxyl group toward the carboxylate group of Asp166 side chain, which takes place immediately afterwards without any additional energy cost. Moreover, like for the model with SP20, it was not possible to characterize a transition state structure for such proton-transfer taking as starting points the set of geometries defined in the reaction path interval of 0.5 Å < R4 < 1.0 Å. In fact, with Kemptide as substrate -and in contrast with SP20- not even a related proton shift intermediate structure was characterized in the aforementioned reaction coordinate range.

Both reaction coordinates reach Pd1'$_K$ and Pd1''$_K$ at R4 value of about 1.6 Å. In the already phosphorylated substrate serine (with PγATP-OγSer17 distances of 1.76 and 1.75 Å in Pd1'$_K$ and Pd1''$_K$, respectively), the OH bond is completely broken (1.57 and 1.55 Å, respectively) and the hydrogen bond interaction between the now protonated Oδ2Asp166 and the phosphorylated OγSer17 (2.58 and 2.56 Å, respectively) is still present. Comparing Pd1'$_K$ and Pd1''$_K$ conformations, as for the preceding stationary points, almost identical reaction and active site geometric parameters are found (see Tables A7 and A8, respectively). In fact, within both geometries, the hydrogen bond network around the β-phosphate group of ADP and the phosphate group at Ser17 it is the same as in the preceding transition state structures (even the trend for the referred lost hydrogen bond in TSd1P'$_K$ is maintained). Thus, with the energy gap

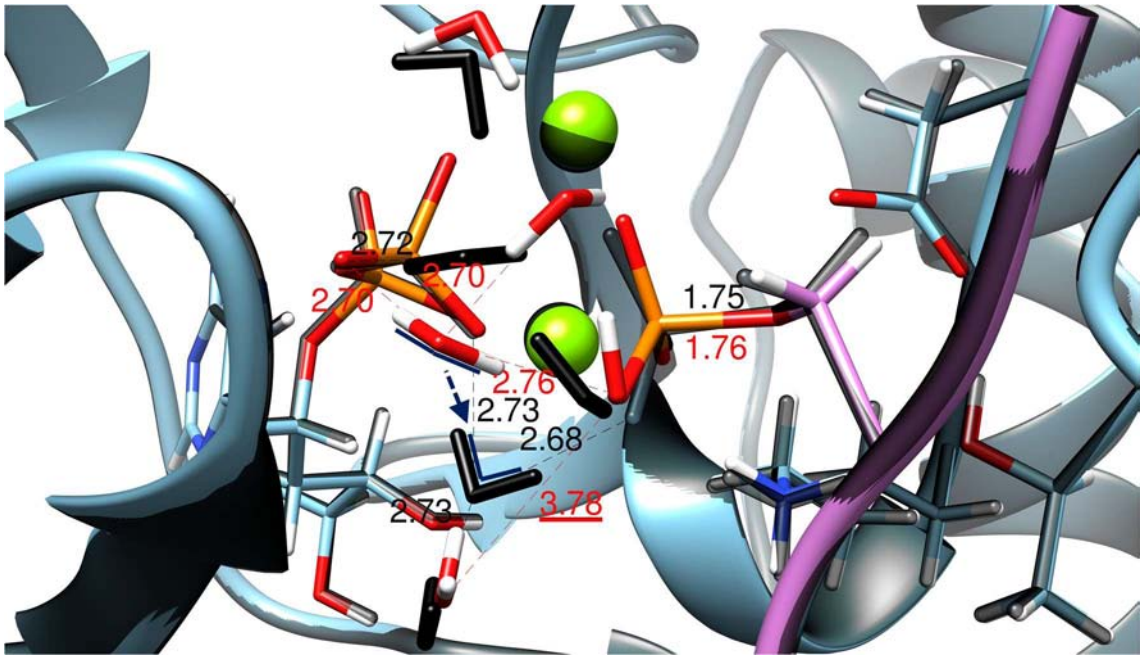

Figure 3.20. Superposition of the active site at the QM(B3LYP/6-31+G(d))/CHARMM phosphoryl-transfer products (Pd1'$_K$ and Pd1''$_K$) for the dissociative mechanism in the PKAc(4IAC)-Mg_2ATP-Kemptide model. Pd1'$_K$ has PKAc colored in blue and the rest of the system by atom type; Pd1P''$_K$ is all colored in black. QM region together with relevant residues and crystallographic water molecules in the active site are represented as sticks. Selected distances (in Å) are also indicated. The hydrogen bond distances differing in nature and length between Pd1'$_K$ and Pd1''$_K$ are shown (see the main text).

between both intermediate product conformations favoring Pd1''$_K$ over Pd1'$_K$, the aforementioned differences in the hydrogen bond network around the reactive phosphate groups explain the further stabilization for the intermediate product complex of the phosphoryl-transfer path with the lowest potential energy barrier.

As already mentioned for the other studied models following either an associative or a dissociative mechanism, the octahedral coordination for both Mg^{2+} ions remains constant throughout the phosphoryl-transfer step with the exception of the Mg2-O3βATP coordination interaction, which strengthens due the Lewis acid attack of Mg2 that screens the negative charge that accumulates on the β,γ-bridging oxygen concomitant with the cleavage of the O3βATP-PγATP bond.

In contrast to the PKAc-Mg_2ATP-SP20 model, the O2γATP-proton-transfer path of phosphorylated Kemptide (see Figure 3.15C, R2 Dissociative proton-transfer profile) is characterized by a stable intermediate complex (Id2''$_K$) connecting the transition state structure of rotation -toward the O2γATP atom- of the protonated side chain of Asp166 (TSd2T''$_K$), and the transition state structure of proton-transfer from Oδ2Asp166 to O2γATP (TSd2H''$_K$). Both critical points are characterized by their proper transition vector (33i cm^{-1} and 280i cm^{-1} for TSd2T''$_K$ and TSd2H''$_K$, respectively). The evolution of the proton-transfer is clearly depicted by the decrease in the Oδ2Asp166-O2γATP distance and the increase in the Oδ2Asp166-HγSer17-

O2γATP angle and Asp166(Cβ-Cγ-Oδ2)-O2γATP dihedral (see Table A8). The TSd2T''$_K$ lies 4.5 kcal/mol over Pd1''$_K$ (a value almost 1 kcal/mol lower than with SP20 as substrate) and corresponds to a relative potential energy very close to that of Id2''$_K$ and TSd2H''$_K$ (1.13, 0.77, and 1.31 kcal/mol, respectively). Thus, the region of the O2γATP-potential energy profile that goes from TSd2T''$_K$ to TSd2H''$_K$ (a R2-value range from -1 to 0 Å) is more planar than the same region with SP20 as substrate. Geometrically, at the beginning of the proton-transfer path with Kemptide as substrate, the hydroxyl group from the now carboxylic group of Asp166 side chain is more oriented to the O2γATP atom of phosphorylated-serine than with SP20 (see O2γATP-HγSer17 distance and dihedral$_{Asp166(Cβ-Cγ-Oδ2)-O2γATP}$ in Tables A8 and 3.12 for Kemptide and SP20, respectively). Further, in comparison to the model with SP20 as substrate, all along the proton-transfer path with Kemptide as substrate the ε-amino group of Lys168 side chain is approximately 0.3 Å further from the proton-transfer region, and almost 1.0 Å closer to O1γATP atom (see distances of NζLys168 atom to Oδ2Asp166, O2γATP, and O1γATP atoms in Tables A8 and A4 for Kemptide and Sp20, respectively). Moreover, and applying this statement for the phosphoryl-transfer too, since the Gly-rich loop is more distanced from the phosphorylated tail of ATP with Kemptide than with SP20, the active region is then slightly more open with the heptapeptide than with the latter.

The complete proton-transfer to O2γATP gives place to the Pd2''$_K$ product complex, in which the Oδ2Asp166 and O2γATP atoms keep their strong interaction (a distance of 2.60 Å and an Oδ2Asp166-HγSer17-O2γATP angle of 170°) and the final PγATP-OγSer17 distance is 1.64 Å, all being practically identical to what is reported above with SP20 as substrate. Energetically, the global reaction potential energy for the dissociative phosphoryl-transfer mechanism following the O2γATP-path for the back-proton-transfer is exoergic (–2.4 kcal/mol) with respect to its corresponding Rd''$_K$ reactant complex (but endoergic, 3.2 kcal/mol, with respect to the Rd'$_K$ reactant complex).

To complete the energetic analysis, single-point energy evaluations at the QM(MP2/aug-cc-pVTZ)/CHARMM level of theory were performed on the QM(B3LYP/6-31+G(d))/CHARMM stationary points, while for only the dissociative mechanism results the QM(MP2/def2-TZVP)/CHARMM level of theory was also considered (see Table 3.14). As for the model with SP20 as substrate, these results clearly point to a categorical predisposition of the system to follow a phosphoryl-transfer dissociative mechanism. In this case, unlike what was obtained with SP20, the potential energy barrier and reaction potential energy results at the DFT and MP2 levels differ substantially, particularly for the proton-transfer to O2γATP of the dissociative mechanism at the MP2/aug-cc-pVTZ level of theory, for which much lower potential energy barrier and reaction potential energy results are obtained. Moreover, at the DFT and MP2 levels of theory

Table 3.14. Potential energy barriers and reaction potential energies (in kcal/mol) corresponding to the QM(MP2/aug-cc-pVTZ)/CHARMM and QM(MP2/def2-TZVP)/CHARMM (in brackets) single-point calculations on the QM(B3LYP/6-31+G(d))/CHARMM stationary points for the PKAc(4IAC)-Mg_2ATP-Kemptide model.

O1γATP-Associative		O3γATP-Associative		Dissociative			
phosphoryl-transfer		*phosphoryl-transfer*		*phosphoryl-transfer*			
$Ra1_K$	---	$Ra3_K$	---	Rd'_K	---	Rd''_K	---
$TSa1_K$	32.39	$TSa3_K$	34.98	$TSd1P'_K$	16.14 (19.43)	$TSd1P''_K$	3.52 (6.93)
$Pa1_K$	-3.58	$Pa3_K$	11.52	$Pd1'_K$	7.73 (11.00)	$Pd1''_K$	-9.91 (-6.04)
					proton-transfer to O2γATP		
						$TSd2T''_K$	-7.61 (-2.80)
						$Id2''_K$	-8.64 (-3.45)
						$TSd2H''_K$	-7.49 (-3.15)
						$Pd2''_K$	-7.94 (-4.36)

the relative potential energy differences for the $TSd2T''_K$, $Id2''_K$ and $TSd2H''_K$ are very similar. The potential energy from $TSd2H''_K$ to $Pd2''_K$ is very small at the high levels (-0.45 and -1.21 kcal/mol at QM(MP2/aug-cc-pVTZ)/CHARMM and QM(MP2/def2-TZVP)/CHARMM levels, respectively, whereas it is -3.72 kcal/mol at the QM(B3LYP/6-31+G(d))/CHARMM level), thus depicting a quite planar profile for the proton-transfer to O2γATP up to the final product.

3.2.6. Discussion.

In this Thesis, the two proposed mechanisms, dissociative and associative, for the phosphorylation reaction catalyzed by PKA have been analyzed by means of QM(MP2/aug-cc-pVTZ)/CHARMM//QM(B3LYP/6-31+G(d))/CHARMM calculations using several completely solvated models of the PKAc-Mg_2ATP-substrate enzymatic system (with SP20 or Kemptide as substrate). Flexible reaction coordinates have been used in order to properly explore the potential energy surface for this reaction.

Using the 4IAC[76] X-ray structure of the PKAc-Mg_2AMPPCP-SP20 complex as initial template for the *in silico* calculations, four (two associative and two dissociative) reaction pathways for the phosphorylation reaction were found connecting reactants and products. In agreement with the results for the phosphorylation of the heptapeptide Kemptide substrate presented in section 3.1 this Thesis for the PKAc(1CDK)-Mg_2ATP-Kemptide model, the associative mechanism consists of a one-step reaction with a transition state corresponding to the transfer of the γ-phosphoryl group from ATP to the nucleophilic hydroxyl group of substrate serine. The nucleophilicity of the attacking oxygen atom is enhanced by an early proton-transfer

to one of the γ-oxygen atoms of ATP. For all the PKAc models from which it was possible to carry out successful phosphoryl-transfer simulations, of the three possible associative pathways only the two corresponding to O1γATP and O3γATP acting as proton acceptors have been located on the potential energy surface. The O1γATP-pathway is favored over the O3γATP one because the negative charge excess on the phosphate group is better stabilized over O2γATP and O3γATP which belong to the coordination spheres of Mg2 and Mg1, respectively.

On the other hand, the dissociative mechanism consists of two steps which are related with two different molecular processes. The first step is the phosphoryl-transfer that imposes the first potential energy barrier. In this mechanism, the nucleophilicity of the hydroxyl group of substrate serine is enhanced in part by the hydrogen bond between such hydroxyl group and the carboxylate group of the highly conserved Asp166 residue. Following the phosphoryl-transfer, a proton migration from the OH group to the carboxylate group of Asp166 residue takes place without potential energy barrier even though an intermediate structure for this proton-transfer has been located and characterized with a very short hydrogen bond. In the second step, Asp166 delivers back the proton to the phosphorylated product. In this way, Asp166 behaves as a base catalyst favoring the phosphoryl-transfer and as an acid catalyst protonating the phosphorylated substrate, thus regenerating the original protonation state of the kinase. Of the three possible proton-transfer pathways, only the two corresponding to O2γATP and O3γATP as proton acceptors have been located. Their respective potential energy barriers are quite similar. Anyway, it has to be mentioned that Asp166 acts neither as a conventional base catalyst nor a conventional acid catalyst in the dissociative mechanism, because both proton-transfers happen quite late along the corresponding reaction paths. The late proton-transfer when Asp166 behaves as a base catalyst is consistent with previous results.[79,166-167,187,190] However, the proton-transfer from substrate serine to Asp166 and then the protonation of the phosphorylated product by Asp166 are required for the enzyme reaction to proceed through a full dissociative mechanism.

In agreement with the calculations with Kemptide, the dissociative mechanism results are clearly favored with respect to the associative process. For both substrates, the dissociative mechanism presents the same two steps, that is, phosphoryl-transfer and protonation of the phosphorylated substrate serine. In fact, the potential energy barriers for each one of these two mechanistic steps are quite similar for both substrates: 9.5 and 10.9 kcal/mol for the phosphoryl-transfer with SP20 and Kemptide, respectively, and 6.8 (or 8.8) and 7.8 kcal/mol for the protonation of phosphorylated SP20 and phosphorylated Kemptide, respectively. So this study, based on the molecular simulation of the phosphorylation reaction, demonstrates that the PKAc catalytic mechanism is not substrate-dependent as previously suggested. However, the product

complexes, with the unprotonated (for the first step) and the protonated phosphorylated peptide (for the second step) of the mechanism, are clearly better stabilized in the active site in the case of SP20. This would be in agreement with the tighter binding of the phosphorylated SP20 in comparison with phosphokemptide that dissociates very fast.[73] In fact, Taylor and coworkers have attributed their own recent success of trapping stable PKAc-Mg_2ADP-pSP20 product complexes in crystals to the unique binding properties of this substrate peptide.[76,102] In addition, the greater stabilization of the unprotonated phosphorylated SP20 peptide in the calculations presented here, which are related with lower potential energy barriers, allows to predict that the global chemical process for the SP20 phosphorylation is faster than for Kemptide.

On the other hand, the comparison between the phosphoryl-transfer transition state structures for SP20 and Kemptide reveals significant differences. In the dissociative reaction paths, at the corresponding transition state, the nucleophile and leaving groups are bonded to the γ-phosphorus to a rather differing extent. The phosphoryl-transfer transition state for SP20 presents very similar O3βATP-PγATP bond-breaking and PγATP-OγSer21 bond-forming distances, whereas at the corresponding transition state for Kemptide, the O3βATP-PγATP distance is much longer than the PγATP-OγSer17 one. At both transition states, though, the γ-phosphoryl group (γ-PO_3^{2-}) has a planar configuration with the phosphorus atom bearing a similar trigonal bipyramidal coordination. The degree of coupling between the phosphoryl-transfer process and the proton-transfer from substrate serine to Asp166 is different in the two transition states. So, the transition vector of the SP20 transition state accounts for the nucleophilic attack exclusively, whereas there is a clear contribution related with the movement of the serine hydroxyl hydrogen toward the carboxylate side chain of Asp166 in the transition vector of the corresponding transition state for Kemptide.

The comparison of the stationary points structures for the SP20 phosphorylation by PKA, located along the QM/MM reaction pathway, with the crystallographic structures of the PKAc-Mg_2AMPPCP-SP20 complex (4IAC), with the transition state mimic (1L3R), and with the PKAc-Mg_2ADP-pSP20 complex (4IAF), reveals very interesting details of the different molecular stages of the PKA catalytic cycle. First, it is confirmed that 4IAC can be a good structure to be taken as starting point to progress not only via the associative pathway, as suggested by Gerlits *et al*.,[76] but also along the dissociative mechanism. The substrate serine Oγ-Cβ-Cα-N torsion angle (defined by Gerlits *et al*. as the "reaction driving force")[76] is confirmed here as an important geometrical parameter to characterize the structural advance of the catalytic process. The Ser21 hydroxyl group is directed outward the catalytic core (toward the solvent) at 4IAC, but it rotates toward the carboxylate group of Asp166 when the chemical reaction initiates and remains in

this orientation all along the chemical steps of the associative and dissociative pathways. The same orientation of the Ser21 hydroxyl group is found in the 1L3R crystallographic structure corresponding to a transition state mimic of the phosphorylation reaction. The excellent agreement between the 1L3R structure and the geometry of the dissociative transition state stationary point located on the dissociative pathway validates, on one hand, the *in silico* model, and supports the preference for the dissociative mechanism, although representative conformations of the Michaelis complex could follow both mechanisms. In the 4IAF structure, the phosphoryl group transferred to Ser21 is directed again outward the catalytic core (toward the solvent), indicating that the 4IAF structure could represent a more advanced stage of the catalytic cycle, specifically, that when the phosphorylated substrate release takes place. On the other hand, the product complex structures located on the calculated reaction pathways correspond to the final stage of the chemical process. Obviously, a complete study of the reaction mechanism of this highly flexible enzyme would require an extensive treatment of the dynamics of the system. The calculation of only reaction paths is not enough for the enzyme to visit all thermally accessible nuclear configurations of the system and to describe the effect of all possible reorientations of the different residues within the active site and its surroundings. However, the results in this Thesis describe a reaction path that can help to understand the main trends of the reaction, and that turns out to be quite plausible when compared with the available crystal structures.

Furthermore, these calculations show for the first time the viability of the SP20 phosphorylation process in a conformation of the PKAc-Mg_2ATP-SP20 ternary complex in which the Gly-rich loop is somewhat displaced with respect to the fully closed conformation of the PKAc-Mg_2ATP-IP20 complex. Many recent experimental and theoretical results have revealed the high degree of flexibility of the Gly-rich loop, so the possibility that this loop might adopt different conformations in the reactive ternary complexes is not discarded. Along the associative and dissociative paths here simulated from the models derived from the 4IAC[76] crystallographic structure, the Gly-rich loop maintains its initial conformation at the crystallographic structure. Therefore, it is not really a flap at the mouth of the active site cleft like in more closed conformations, even though it cannot be described as an open configuration either. Further, despite the fact that the apparently preferred Gly-rich loop position for the catalytic reaction is not restituted, the phosphorylated tail of ATP can still be stabilized through strong hydrogen bonds with three crystallographic waters all along the characterized stationary points of the PKA-catalyzed phosphoryl-transfer. The presence of those water molecules substitutes the stabilizing interactions between the Gly-rich loop residues and ATP previously observed in more closed conformations. In particular, the results shown here confirm, in agreement with

mutagenesis experiments,[153] that the hydroxyl group of Ser53 side chain is not needed for the catalytic reaction taking place in the active site of PKAc. In fact, in this conformation of the Gly-rich loop none of the interactions between the backbone-nitrogen atoms of residues Ser53, Phe54, and Gly55 of PKAC with the Oβ and Oγ atoms of ATP are present.

While this Thesis was written, new crystallographic structures were determined by several of the authors that obtained the 4IAC[76] X-ray structure.[80] As indicated by these authors, the search of new crystallographic structures is motivated by the objective of finding a better model of the ternary PKAc-M_2ATP-SP20 Michaelis complex. Previous crystallographic structures mimicking the reactant complex had been obtained either with peptide inhibitors or ATP analogues, as is the case of the 4IAC structure. The recent crystallization of the ternary complex PKAc-Ca_2ATP-CP20, where, with respect to 4IAC, the substrate Ser21 has been substituted by Cys21, Mg^{2+} by Ca^{2+}, and AMPPCP by ATP, results in a structure (PDB code 4XW5[80]) where the main artifact caused by the presence of an ATP analogue in 4IAC is overcome. That is, the Cys21 is now facing Asp166, ready to undergo the phosphoryl-transfer step assisted by the base catalyst Asp166. At this point it is worthy to mention that the optimized reactant structure labeled as Rd_S in this Thesis is validated by the 4XW5 structure, because the orientation of the catalytic residues in both structures is highly comparable (see Figure 3.21). Remarkably, the substrate Ser21 is orientated toward the catalytic residue Asp166 in the optimized structure (interaction distance of 2.8 Å) analogously to Cys21 toward Asp166 in the 4XW5 structure (interaction distance of 3.2 Å). Thus, in spite of the initial position of Ser21, rotated by ≈110° away from Asp166 in both the 4IAC and $i_{model}S_{Mg}$ structures, the reaction coordinate scanning

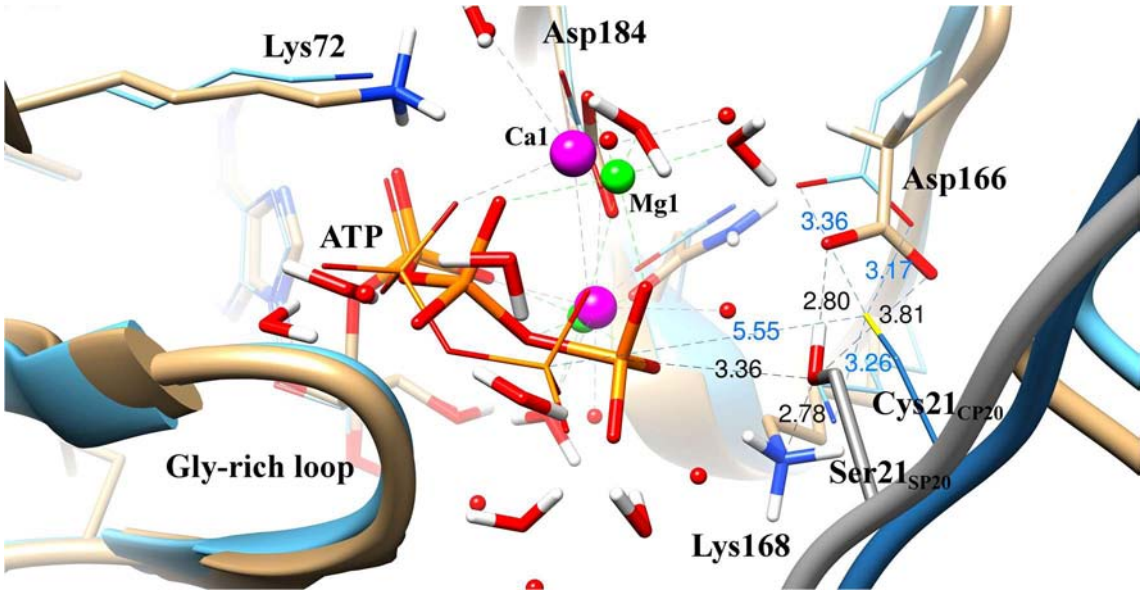

Figure 3.21. Superposition of the active sites in Rd_S (tan) and 4XW5 (black) structures. The catalytic cores of Rd_S (colored by atom type) and 4XW5 are represented in thick- and thin-sticks, respectively.

process has driven Ser21 to a position where it forms a hydrogen bond with Asp166, which is a necessary step to initiate the phosphoryl-transfer via the dissociative mechanism.

Figure 3.21 allows to compare two more interaction distances found in both the Rd_S reactant and the 4XW5 structure. In both cases, Lys168 forms a hydrogen bond with the side chain of the residue 21 of the substrate, and the measured distances are comparable: 2.8 Å for the Lys168-OγSer21 distance in Rd_S, in comparison to a Lys168-SγCys21 distance of 3.4 Å in 4XW5. The different sizes of sulfur and oxygen atoms may explain the difference between those two distances. In contrast, the comparison of the distance between the Pγ atom of ATP and the substrate nucleophile atom (Oγ or Sγ in SP20 or CP20, respectively) seems to indicate that the 4XW5 crystallographic structure represents a previous stage, in comparison to the Rd_S structure, of the catalytic cycle process. That is, the reactive fragments are still far away (5.6 Å) from each other in 4XW5, whereas they are clearly at a near attack conformation (3.4 Å interaction distance) in Rd_S. Finally, it is clear from inspection of Figure 3.21 that the Gly-rich loop position (see the bottom-left side of the Figure) is comparable in both structures.

On the other hand, Figure 3.22 compares the recent X-ray crystallographic structure of the PKAc-Mg_2ADP-PO4-CP20 ternary complex (PDB code 4XW6[80]), which mimics a product state immediately after the phosphoryl-transfer has taken place, with our $Pd2_S$ product structure. As mentioned above in relation to the Rd_S and 4XW5 structures, the new 4XW6 structure validates the model of the phosphoryl-transfer product. In both $Pd2_S$ and 4XW6, the catalytic Asp166 residue is facing the phosphoryl group, in agreement with its proposed role as the acid catalyst that protonates the phosphate group now bonded to the substrate serine. The comparison of

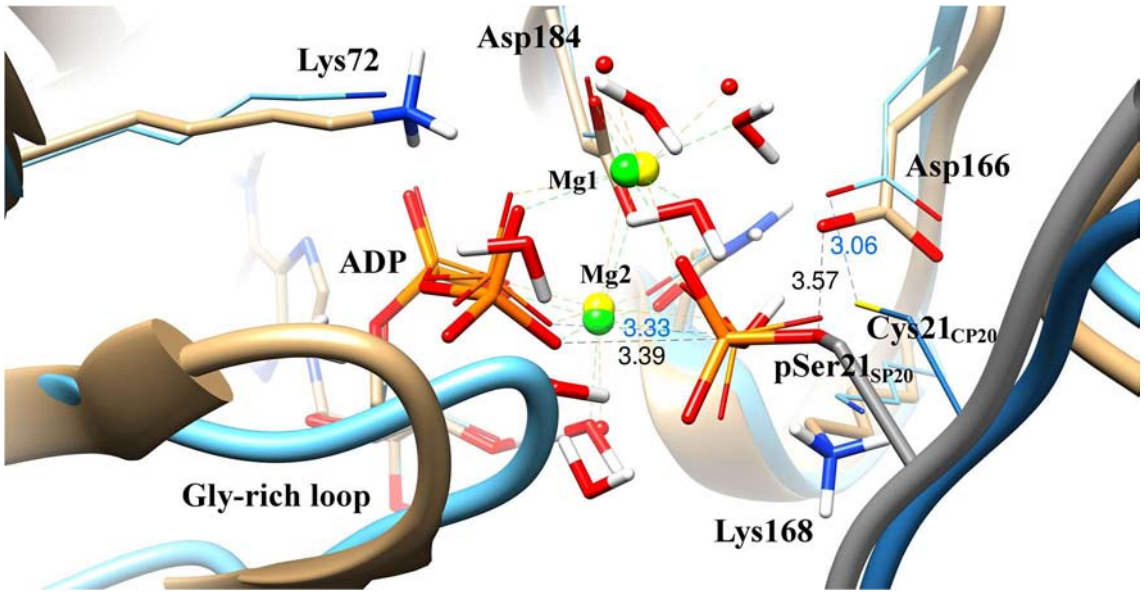

Figure 3.22. Superposition of the active sites in $Pd2_S$ (tan) and 4XW6 (black) structures. The catalytic cores of $Pd2_S$ (colored by atom type) and 4XW6 are represented in thick- and thin-sticks, respectively.

the distances, shown in Figure 3.22, between Asp166 and the OγSer21 and SγCys21 atoms in $Pd2_S$ and 4XW6 structures, respectively, together with the broken O3βATP-PγATP bond distances in both structures, give us a quantitative indication of the correspondence between the crystallographic and the computationally determined structures. Thus, and in contrast to the 4IAF structure, these results indicate that the recently determined 4XW6 structure and the optimized model of the phosphoryl-transfer product represent the same stage of the catalytic cycle.

Regarding the PKAc(4IAC)-Mg_2ATP-Kemptide model, several causes might explain the differences in the potential energy profiles obtained from this model and from the PKAc(1CDK)-Mg_2ATP-Kemptide one (see section 3.1.2). First, it is necessary to recall that the 4IAC crystallographic structure corresponds to a catalytic subunit of the Protein Kinase A with SP20 as substrate, which for this particular model was substituted by the much smaller Kemptide. As detailed in the methodology, such *in silico* substrate substitution was not followed by an MD simulation that could have allowed the Kemptide molecule to explore different locations within the active site of PKAc. Conversely, in the study of the PKAc(1CDK)-Mg_2ATP-Kemptide model, the MD simulation, from which selected snapshots were used as starting point geometries, might have helped the substrate to accommodate itself in the substrate binding site of PKAc. In this respect, those initial reactant structures might represent stabilized geometries of the equilibrated PKAc(1CDK)-Mg_2ATP-Kemptide Michaelis complex from which a smooth potential energy profile for the global reaction process was obtained after several progressively converging forward/backward scan cycles of the corresponding complex reaction coordinates. In this case, the highest potential energy point corresponds to the proton-transfer step region. In contrast, the PKAc(4IAC)-Mg_2ATP-Kemptide initial structure could correspond to a near-attack geometry of the Michaelis complex from which a final converged potential energy profile was also obtained but with much lower barriers for both the phosphoryl-transfer and the proton-transfer steps. In this respect, very recent electronic measurements of single-molecule catalysis by PKAc using Kemptide as substrate,[132] have resulted in a wide range of measured rate constants which together depict a highly dynamic enzymatic system with turnover rates varying over 2 orders of magnitude. These single-molecule experiments caution us to correlate bulk kinetic values like k_{cat} with the time it takes each individual Kemptide molecule to go through a particular conformational change or chemical reaction. On the other hand, it must also be taken into account that in the 4IAC crystallographic structure, as opposed to the 1CDK and 1ATP crystallographic structures, the Gly-rich loop position is such that it allows the entry of several water molecules. As detailed carefully in the corresponding results section, when comparing the optimized geometries characterizing both potential energy profiles of the phosphoryl-transfer

step explored with the PKAc(4IAC)-Mg_2ATP-Kemptide model, such water molecules and the hydrogen bond network they establish, end up having a different role in the degree of stabilization of the ADP and the γ-phosphoryl group moieties, and, therefore, can contribute to explain the energetic difference between the two potential energy profiles.

It should be pointed out that some the theoretical results for the phosphorylation reaction catalyzed by PKAc in the PKAc-Mg_2ATP-SP20 model via the associative and dissociative mechanisms can be found published in reference 279.

3.3. Dependence of the phosphoryl-transfer mechanism on the alkali earth metal ions.

The objective of the theoretical study presented in this section is to simulate the chemistry of the phosphoryl-transfer reaction catalyzed by PKAc from a Michaelis complex PKAc-M_2ATP-Substrate, where M is either Ca^{2+} or Sr^{2+}, and Substrate is either SP20 or Kemptide. We have built our theoretical models from the experimental X-ray crystallographic structure with PDB code 4IAC[76] (pseudo-Michaelis complex PKAc-Mg_2AMPPCP-SP20) in order to compare our results with the related X-ray crystallographic structures of PKAc in complex with different divalent metals ions before and after the phosphoryl-transfer reaction,[76,80] and with our previous results for the PKAc-Mg_2ATP-SP20 model. The nomenclature of the 4IAC[76] PDB entry is used again, which is particularly important to distinguish between the γ-oxygen atoms of ATP. Thus, O1γATP interacts with crystallographic waters toward the Gly-rich loop; O2γATP coordinates the divalent metal ion occupying M2 site and forms a hydrogen bond with the ε-ammonium group of Lys168; and, finally, O3γATP coordinates the divalent metal ion bound in M1 site. The theoretical studies reported previously in this Thesis give support to the dissociative mechanism for the SP20 and Kemptide phosphorylation reaction catalyzed by PKAc with Mg^{2+} bound in the active site, so we have discarded the associative mechanism in the study with divalent metal ions. Moreover, for the dissociative mechanism, those results described the proton-transfer path corresponding to the protonation of the phosphorylated substrate serine at the O2γATP atom with a lower potential energy barrier than the one calculated for the O3γATP atom, the other oxygen atom chemically suitable as final proton acceptor of the phosphorylation process. Thus, for the following PKAc ternary complex models only the dissociative O2γATP-path was explored.

Importantly, for the models setup, the coordination sphere of the two metal binding sites was not changed manually in any way. The structures obtained by our setup procedure were subjected to QM/MM geometry optimization. The resulting enzyme-reactants complexes are denoted as $i_{model}X_M$, where X can be S or K, for SP20 and Kemptide, respectively, and M is the corresponding divalent metal ion. All of these initial model structures featured the OH group of the substrate serine adopting a conformation very similar to that observed in the 4IAC[76] structure, that is, rotated away from the Asp166 and directed toward the O3γATP. Moreover, the Gly-rich loop occupies an analogous/equivalent position in the 4IAC[76] in all our theoretical initial models. The superposition of the $i_{model}X_{Ca}$ and $i_{model}X_{Sr}$ structures is depicted in Figure 3.23A with respect to the $i_{model}S_{Mg}$, also constructed from the 4IAC pseudo-Michaelis complex and following the same procedure. As a result of the QM/MM optimization there are differences in the coordination geometry and metal-ligand distances for the M1 site as the metal ionic radii varies for the divalent alkali earth metal ions (see Table 3.15 for key bond distances, bond angles,

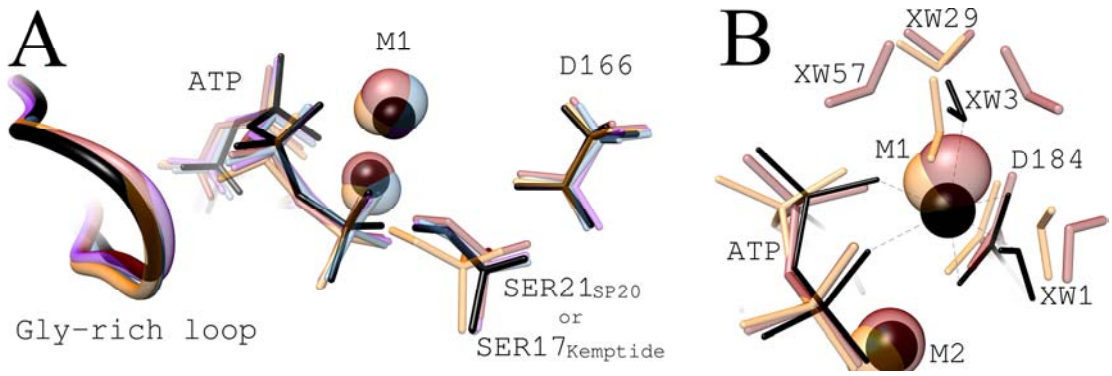

Figure 3.23. (A) Superposition of the active sites in the initial model structures of PKAc-Ca_2ATP-SP20 ($i_{model}S_{Ca}$, colored in orange), PKAc-Sr_2ATP-SP20 ($i_{model}S_{Sr}$, colored in dark red), PKAc-Ca_2ATP-Kemptide ($i_{model}K_{Ca}$, colored in purple), PKAc-Sr_2ATP-Kemptide ($i_{model}K_{Sr}$, colored in blue), and PKAc-Mg_2ATP-SP20 ($i_{model}S_{Mg}$ shown for comparison, colored in black). **(B)** Superposition of the coordination sphere for the M1 site in the initial model structures of PKAc-Ca_2ATP-SP20 (colored in orange), PKAc-Sr_2ATP-SP20 (colored in dark red), and PKAc-Mg_2ATP-SP20 (colored in black).

and dihedrals in the initial model structures). Regardless of the substrate, in the two initial models with Ca^{2+} ions, the M1 site is surrounded by seven ligands, while in those two structures with Sr^{2+} ions eight ligand surround the M1 site. The crystallographic water XW29 is responsible of the extra ligand in the calcium-bound models, while XW29 and XW57 are responsible in the strontium-bound ones (in Figure 3.23B, the coordination sphere for the M1 site in the initial model structures with SP20 as substrate and Ca^{2+} or Sr^{2+} ions bound in the active site are compared to the octahedral geometry for Mg^{2+} ions in the $i_{model}S_{Mg}$ structure). On the other hand, the M2 site shows the same octahedral coordination in all initial models regardless of the substrate or divalent metal ions bound in the active site, with longer metal-ligand distances as the metal ionic radii increases. In the 4IAC structure used as a template, the Mg2 ion has a trigonal bipyramidal coordination due to the incapacity of the β,γ-methylene group in the AMPPCP molecule (used as ATP-analogue) to bind to a metal ion. With the PKAc-Mg_2ATP-SP20 model, we observed that the restitution of the β,γ-bridging oxygen atom of ATP (O3βATP) resulted in immediate recovery of the octahedral coordination for the Mg2 ion. Here, the presence of ATP in the model structures also led to the formation of the M2-O3βATP interaction after the setup and initial QM/MM minimization. It was expected that such procedures would allow the Ca^{2+} or Sr^{2+} ions bound in the M2 site to fulfill their coordination sphere as it happened for such ions bound in the M1 site. However, no changes in the coordination sphere of the M2 site when occupied by different divalent metal ions are observed. This can be partially explained by the fact that after each stage of the setup procedure there are neither protein residues nor water molecules in close proximity that could provide, along the initial QM/MM minimization, additional coordination to this metal site.

On the other hand, in all the initial model structures the Gly-rich loop is located rather far

from the phosphorylated tail of the ATP kinase cofactor, approximately 3.0 Å displaced from its position in most of the crystallographic[73,78-79,100,102,142-144,164,171,175,179] and theoretical[148,166-167,187,190] structures characterized for the different stages of the PKA-catalyzed phosphorylation

Table 3.15. Selected QM(B3LYP/6-31+G(d)/CHARMM bond distances (Å), bond angles (deg), and dihedrals (deg) of the calcium-bound initial model structures. Selected QM(B3LYP/def2-TZVP)/CHARMM bond distances (Å), bond angles (deg), and dihedrals (deg) of the strontium-bound initial model structures. Comparison with values from pseudo-Michaelis complex 4IAC[76] X-ray crystallographic structure (used as model template) and PKAc-Mg_2ATP-SP20 initial model structure (QM(B3LYP/6-31+G(d))/CHARMM level). $Ser_{substrate}$ holds for Ser21 and Ser17 in SP20- and Kemptide-bound ternary complex models, respectively.

	4IAC	$i_{model}S_{Mg}$	$i_{model}S_{Ca}$	$i_{model}S_{Sr}$	$i_{model}K_{Ca}$	$i_{model}K_{Sr}$
O3βATP-PγATP	1.8*	1.70	1.72	1.70	1.74	1.70
PγATP-O$\gamma Ser_{substrate}$	3.5	3.76	3.59	3.70	3.68	3.59
O$\gamma Ser_{substrate}$-H$\gamma Ser_{substrate}$	---	0.98	0.99	0.99	1.00	0.99
Oδ2Asp166-H$\gamma Ser_{substrate}$	---	4.23	4.69	4.23	4.24	4.40
O2γATP-H$\gamma Ser_{substrate}$	---	3.52	3.47	3.23	3.31	3.39
O$\gamma Ser_{substrate}$-Oδ2Asp166	4.4	4.28	4.93	4.24	4.30	4.60
a.$_{O3\beta ATP\text{-}P\gamma ATP\text{-}O\gamma SerSubs.}$	148.2*	141.3	143.2	142.2	141.7	146.6
a.$_{O\gamma SerSubs.\text{-}H\gamma SerSubs.\text{-}O\delta 2Asp166}$	---	86.4	98.0	83.8	86.6	95.3
a.$_{O\delta 2Asp166\text{-}H\gamma SerSubs.\text{-}O2\gamma ATP}$	---	60.2	57.1	67.0	64.8	63.9
d.$_{Ser21(N\text{-}C\alpha\text{-}C\beta\text{-}O\gamma)}$	64.0	68.7	61.2	68.7	70.8	69.1
d.$_{Asp166(C\beta\text{-}C\gamma\text{-}O\delta 2)\text{-}O2\gamma ATP}$	160.0	167.2	-179.7	-177.8	178.2	-153.6
M1-O1βATP	2.2	2.08	2.38	2.54	2.38	2.53
M1-O3γATP	2.3	2.16	2.47	2.74	2.47	2.48
M1-Oδ1Asp184	2.4	2.21	2.47	2.63	2.49	2.56
M1-Oδ2Asp184	2.3	2.20	2.58	2.77	2.53	2.68
M1-OH2XWAT1003	2.2	2.07	2.44	2.64	2.43	2.60
M1-OH2XWAT1001	2.2	2.02	2.43	2.63	2.45	2.52
M1-OH2XWAT1029	4.0	3.94	2.51	2.66	2.42	2.52
M1-OH2XWAT1057	6.1	4.97	4.55	2.59	4.20	2.62
M2-O2αATP	2.2	1.99	2.32	2.41	2.32	2.40
M2-O3βATP	3.3*	2.96	2.65	2.89	2.55	2.91
M2-O2γATP	2.2	2.00	2.35	2.42	2.39	2.47
M2-Oδ2Asp184	2.2	2.10	2.37	2.47	2.38	2.46
M2-Oδ1Asn171	2.2	2.01	2.30	2.39	2.30	2.43
M2-OH2XWAT1002	2.3	2.12	2.41	2.53	2.40	2.53

For 4IAC[76] * stands for O3βATP = CβAMPPCP.

reaction. Thus, the restitution of ATP when setting-up the ternary complex models and the ensuing initial QM/MM optimization did not modify the position that the Gly-rich loop holds in the starting 4IAC[76] crystallographic structure, which was considered by its authors as a consequence of the strong steric effects of the β,γ-methylene group in the AMPPCP nucleotide. Moreover, because the β,γ-bridging bond in ATP is shorter than in AMPPCP, the γ-phosphate group in all four initial model structures retracts into the ADP moiety while moves away from the substrate serine nucleophilic hydroxyl group (see O3βATP-PγATP and PγATP-OγSer$_{substrate}$ distances in Table 3.15).

The mechanistic studies at the QM/MM level started from the enzyme-reactants complexes defined by the initial model structures. The dissociative mechanism discussed in the following consists of: (1) the phosphoryl-transfer from ATP to serine substrate almost concomitant to the proton-transfer from the hydroxyl group of substrate serine to the carboxylate group of the Asp166 residue, and (2) the proton-transfer from the just protonated side chain of Asp166 residue to the phosphate group of the just phosphorylated serine, which first entails the rotation of the carboxylic group of protonated Asp166 residue toward the recipient oxygen atom of the transferred phosphate. These successive steps of the PKAc-catalyzed phosphorylation reaction mechanism will be respectively discussed in its corresponding section. The potential energy values and geometric data given here were obtained using, as QM treatment in the DFT/CHAMM calculations, the B3LYP functional and the 6-31+G(d) and def2-TZVP basis sets for the calcium- and strontium-bound models, respectively. To complete the energetic analysis we also carried out single-point QM(MP2/def2-TZVP)/CHARMM calculations at the corresponding stationary points.

Phosphoryl-transfer step.

To reach a converged potential energy profile, the phosphoryl-transfer reaction paths required three forward/backward cycles of dissociative R4-reaction coordinate scans from the $i_{model}S_{Ca}$, two cycles from $i_{model}S_{Sr}$, and three cycles from $i_{model}K_{Ca}$. From the $i_{model}K_{Sr}$ structure not even one potential energy scan along the reaction coordinate was computed due to convergence failure in the initial steps of the phosphoryl-transfer reaction path. In this regard, we manually modified the $i_{model}K_{Sr}$ structure by rotating the hydroxyl group of substrate serine toward the carboxylate group of Asp166 to force the molecular system to reach a different QM/MM minimum from which the dissociative R4-reaction coordinate could be scanned. However, the calculation of a potential energy profile from this new starting geometry also broke down for the same convergence issues at the beginning of the phosphoryl-transfer reaction path. Therefore, the mechanism of the phosphorylation reaction of Kemptide catalyzed

by PKAc with Sr^{2+} ions bound in the active site will not be discussed hereinafter. For the second step of the dissociative mechanism, that is, the proton-transfer from the protonated Asp166 residue to the just phosphorylated substrate serine with the O2γATP as proton acceptor, two forward/backward cycles of R2-reaction coordinate were needed to reach a converged potential energy profile for the PKAc-Ca_2ATP-SP20, PKAc-Sr_2ATP-SP20, and PKAc-Ca_2ATP-Kemptide models (denoted hereinafter as the Ca/SP20, Sr/SP20, and Ca/Kemptide models, respectively).

The resulting QM/MM potential energy curves along the dissociative mechanism are summarized in Figure 3.24A together with that for the PKAc-Mg_2ATP-SP20 model (from now on, Mg/SP20 model) as comparison. These include both the phosphoryl-transfer and the proton-transfer (from Oδ2Asp166 to O2γATP) steps, so the change in the reaction coordinate variable should be noted. Figures 3.24B, C, and D show the potential energy profile for the Ca/SP20, Sr/SP20, and Ca/Kemptide models, respectively, together with the evolution of the R4- and R2-reaction coordinate distances for the phosphoryl-transfer and proton-transfer steps, respectively. For each model, the related QM/MM potential energy barriers and reaction energies are depicted on the appropriate reaction profile in Figure 3.25 along with the results of single-point QM(MP2/def2-TZVP)/CHARMM calculations at the corresponding stationary points. The relative energies were calculated with respect to the energy of the specific Michaelis complex that was characterized in each case. Key bond distances, bond angles, and dihedrals within the active core that change during the phosphorylation reaction are given in Tables 3.16, 3.17, and 3.18 for Ca/SP20, the Sr/SP20, and the Ca/Kemptide models, respectively (complete active core geometric features, catalytic core interaction distances, and Mg^{2+} ions coordination sphere distances at the stationary points characterized for all models are given in Tables A9, A10, and A11 for the Ca/SP20, the Sr/SP20, and the Ca/Kemptide models, respectively). The stationary points considered in this study are labeled as follows: reactant complex, Rd; phosphoryl-transfer transition state, TSd1P; proton shift intermediate, Id1; proton shift transition state, TSd1H; phosphoryl-transfer products, Pd1; protonated Asp166 side chain-rotation transition state, TSd2T; back proton-transfer transition state, TSd2H; and, proton-transfer products, Pd2. The divalent metal ion and the substrate are indicated by subscripts in the stationary point labels, with S and K standing for SP20 and Kemptide, respectively.

In order to reach the converged reactant ternary complex structure from the corresponding initial model structure, the substrate serine side chain undergoes an energetically favorable conformational change. Specifically, in all the optimized Michaelis complexes (whose active sites are depicted in Figures 3.26A, B, and C for $Rd_{Ca/S}$, $Rd_{Sr/S}$ and $Rd_{Ca/K}$, respectively) the hydroxyl group of substrate serine is rotated toward the carboxylate group of Asp166 side chain (Asp166 N-Cα-Cβ-Oγ torsion angle of -55°, -53°, and -48° in the $Rd_{Ca/S}$, $Rd_{Sr/S}$, and $Rd_{Ca/K}$ reactant

complexes, respectively), interacting strongly with the Oδ2Asp166 atom through a hydrogen bond of about 2.8 Å. In this way, besides gaining the stabilizing factor due to the electrostatic

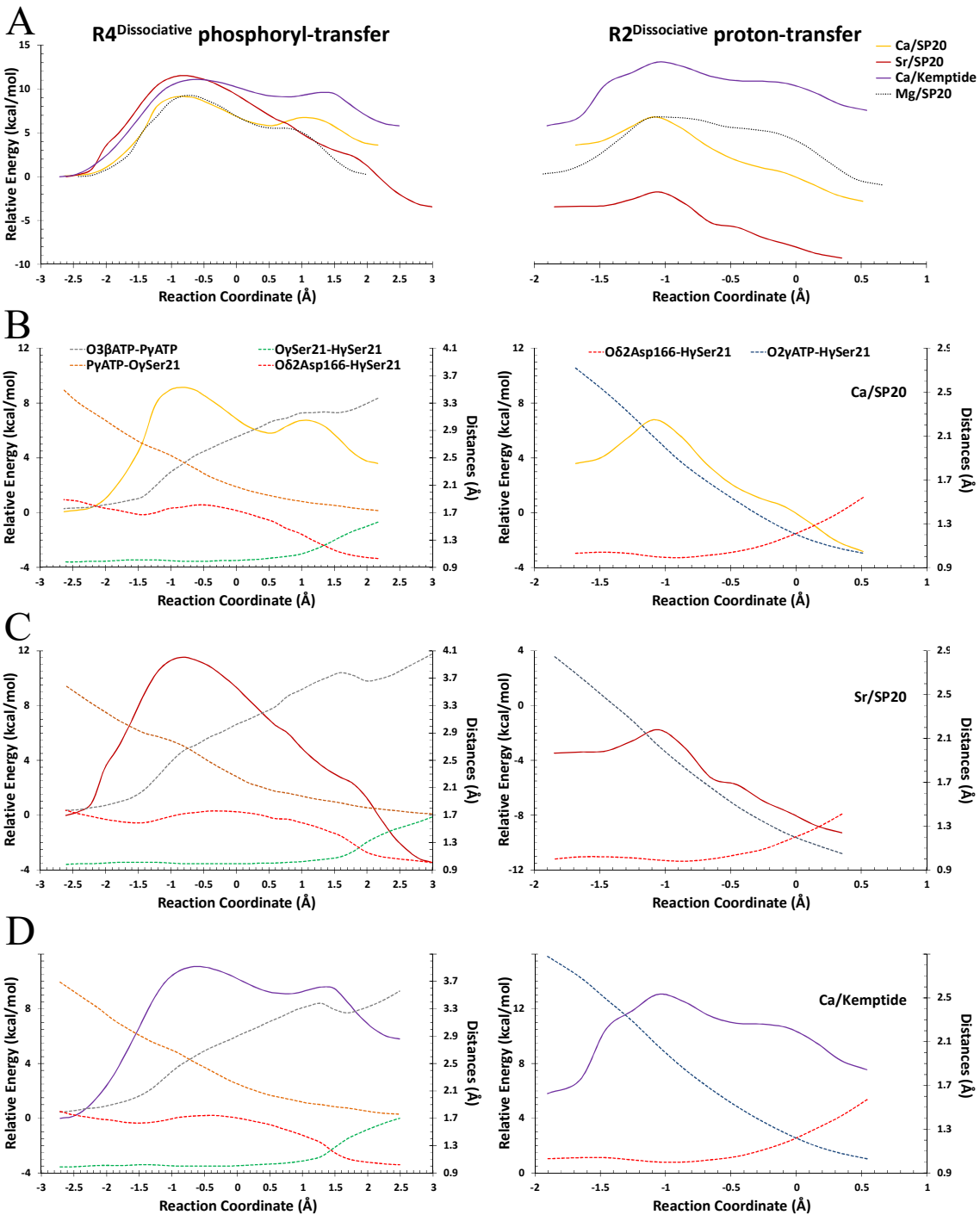

Figure 3.24. (A) For the phosphoryl-transfer and proton-transfer steps using the R4 and R2 reaction coordinates: QM(B3LYP/6-31+G(d)/CHARMM potential energy profile for PKAc-Ca_2ATP-SP20 (Ca/SP20) and PKAc-Ca_2ATP-Kemptide (Ca/Kemptide) models; QM(B3LYP/def2-TZVP)/CHARMM potential energy profile for PKAc-Sr_2ATP-SP20 (Sr/SP20) model; and, QM(B3LYP/6-31+G(d)/CHARMM potential energy profile for PKAc-Mg_2ATP-SP20 (Mg/SP20, shown for comparison). The potential energy profile and the variation of the interatomic distances involved in the phosphoryl-transfer and proton-transfer step are depicted conveniently in: **(B)** for PKAc-Ca_2ATP-SP20 (Ca/SP20) model; **(C)** for PKAc-Sr_2ATP-SP20 (Sr/SP20) model model; and **(D)** for PKAc-Ca_2ATP-Kemptide (Ca/Kemptide).

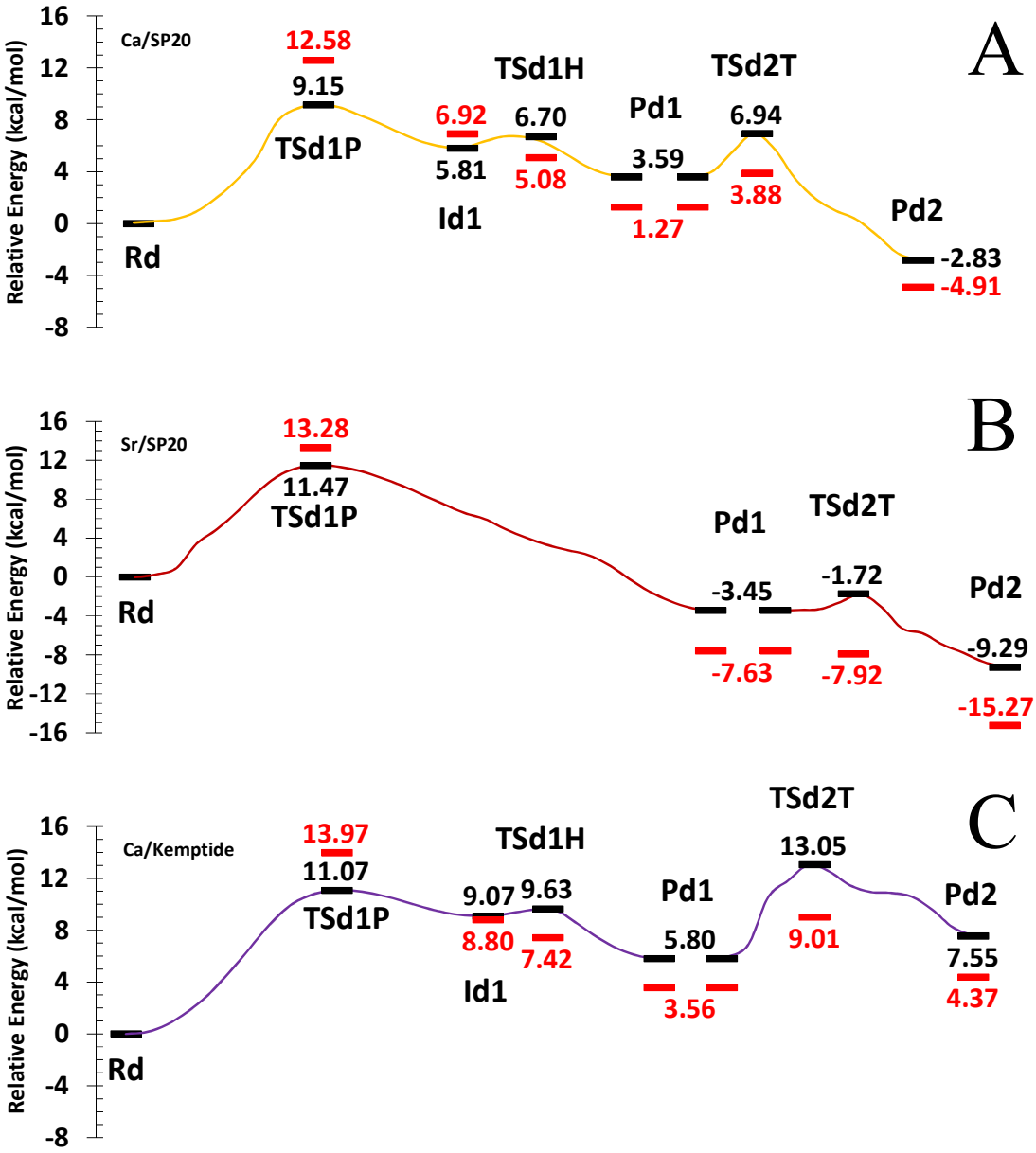

Figure 3.25. Potential energy profile, potential energy barriers, and potential reaction energies along the R4- and R2-reaction coordinates for the dissociative phosphoryl-transfer and proton-transfer steps, respectively, for: **(A)** PKAc-Ca_2ATP-SP20 (Ca/SP20) model, calculated at QM(B3LYP/6-31+G(d)/CHARMM; **(B)** PKAc-Sr_2ATP-SP20 (Sr/SP20) model, calculated at QM(B3LYP/def2-TZVP/CHARMM; and PKAc-Ca_2ATP-Kemptide (Ca/Kemptide) model, calculated at QM(B3LYP/6-31+G(d)/CHARMM. The single-point energy results at the MP2/def2-TZVP level on the corresponding stationary point structures are depicted in red

dipole-dipole interaction, the hydroxyl oxygen atom points in the proper direction to follow a dissociative phosphoryl-transfer pathway, so that the proton-transfer to the Oδ2Asp166 atom can take place almost concomitant to the nucleophilic attack on the γ-phosphorous atom of ATP. In this regard, in the optimized reactant complex structures the oxygen atom of the nucleophilic hydroxyl group is closer to the γ-phosphate group and it is more linearly aligned to the β,γ-bridging bond of the ATP cofactor than in the corresponding initial model structure. Thus, the

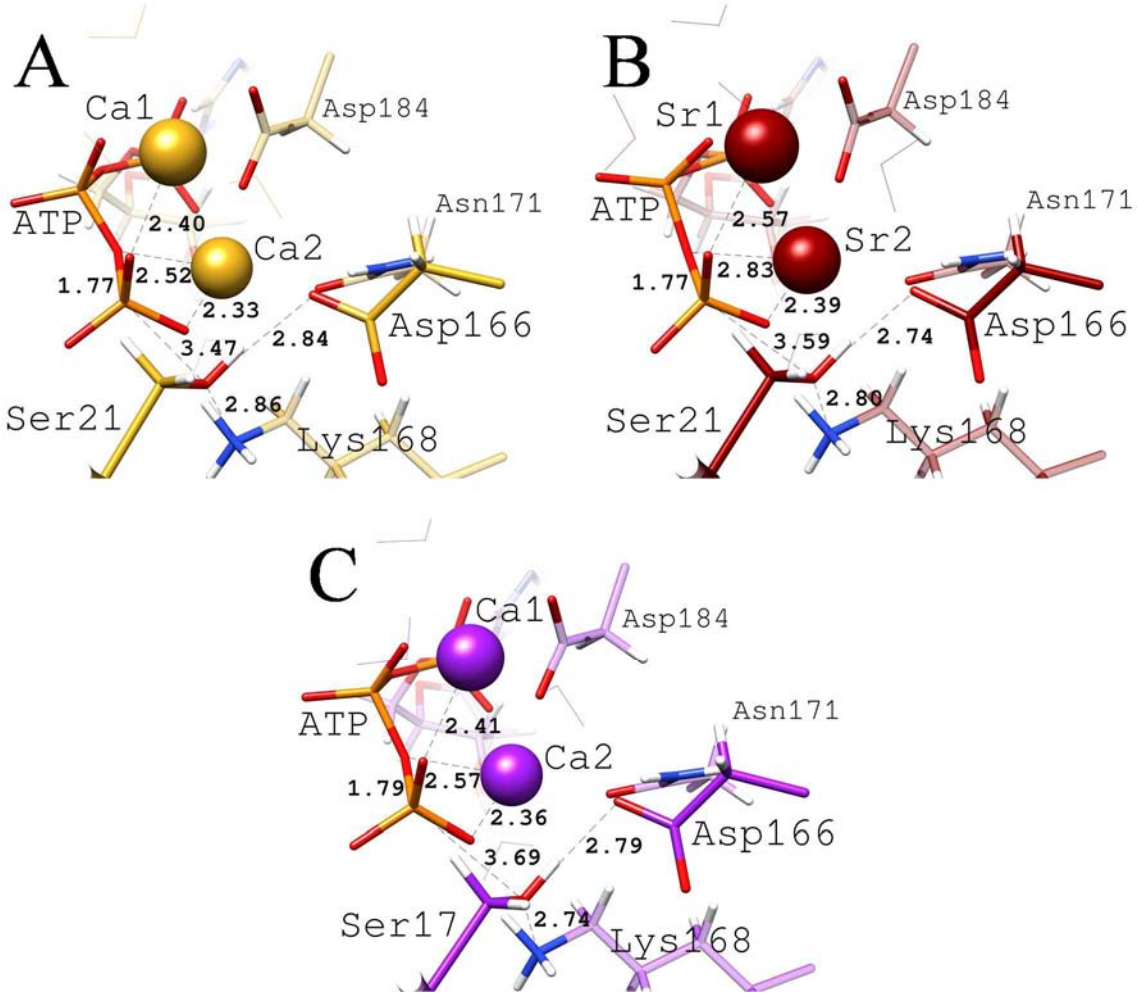

Figure 3.26. Active site structures at: **(A)** QM(B3LYP/6-31+G(d))/CHARMM optimized $Rd_{Ca/S}$; **(B)** QM(B3LYP/def2-TZVP)/CHARMM optimized $Rd_{Sr/S}$; and **(C)** QM(B3LYP/6-31+G(d))/CHARMM optimized $Rd_{Ca/K}$. Selected distances are given in Å.

computationally obtained reactant ternary complex structures are more directed to the energetically favored dissociative pathway of the phosphoryl-transfer catalyzed by PKAc than the preceding initial model structures and the 4IAC crystallographic structure used as model template.

The geometric features described so far for the corresponding Michaelis complexes are very similar to those for the PKAc-Mg_2ATP-SP20 and PKAc(4IAC)-Mg_2ATP-Kemptide optimized Rd structures. However, the ionic radii of the Ca^{2+} (1.14 Å) and Sr^{2+} (1.26 Å) are significantly longer than that of Mg^{2+} (0.72 Å), and changes in the geometry of the active site of their reactant complexes can be partially explained by the variations in the metal ionic radii. One consequence is evident for the PγATP-OγSer$_{Substrate}$ distance, which defines the nucleophilic attack and the bond-forming interaction of the phosphoryl-transfer. In the Michaelis complex structures of the magnesium-bound models the latter distance is 3.36 and 3.48 Å with SP20 and Kemptide as substrate, respectively. With SP20 substrate, such bond-forming interaction increases its length

Table 3.16. Selected QM(B3LYP/6-31+G(d))/CHARMM bond distances (Å), bond angles (deg), and dihedrals (deg) in the stationary points characterizing the different stages of the phosphoryl-transfer dissociative mechanism for the PKAc-Ca_2ATP-SP20 model.

	$Rd_{Ca/S}$	$TSd1P_{Ca/S}$	$Id1_{Ca/S}$	$TSd1H_{Ca/S}$	$Pd1_{Ca/S}$	$TSd2T_{Ca/S}$	$Pd2_{Ca/S}$
O3βATP-PγATP	1.77	2.40	3.04	3.21	3.37	3.35	3.35
PγATP-OγSer21	3.47	2.45	1.94	1.84	1.73	1.69	1.63
OγSer21-HγSer21	0.98	0.99	1.04	1.20	1.56	2.01	2.62
Oδ2Asp166-HγSer21	1.87	1.78	1.57	1.25	1.03	1.00	1.53
O2γATP- HγSer21	3.26	2.86	2.74	2.78	2.72	2.06	1.03
OγSer21-Oδ2Asp166	2.84	2.77	2.60	2.44	2.58	2.91	3.55
$a._{O3\beta ATP\text{-}P\gamma ATP\text{-}O\gamma Ser21}$	155.4	164.6	166.1	169.1	175.4	173.6	174.1
$a._{O\gamma Ser21\text{-}H\gamma Ser21\text{-}O\delta 2Asp166}$	170.7	176.4	172.0	171.0	169.5	148.8	114.7
$a._{O\delta 2Asp166\text{-}H\gamma Ser21\text{-}O2\gamma ATP}$	103.0	107.1	111.5	114.5	112.1	129.7	172.6
$d._{Ser21(N\text{-}C\alpha\text{-}C\beta\text{-}O\gamma)}$	-54.9	-56.1	-46.1	-46.1	-52.9	-56.3	-55.7
$d._{Asp166(C\beta\text{-}C\gamma\text{-}O\delta 2)\text{-}O2\gamma ATP}$	144.2	130.5	125.8	124.6	120.3	137.8	170.8

Table 3.17. Selected QM(B3LYP/def2-TZVP)/CHARMM bond distances (Å), bond angles (deg), and dihedrals (deg) in the stationary points characterizing the different stages of the phosphoryl-transfer dissociative mechanism for the PKAc-Sr_2ATP-SP20 model.

	$Rd_{Sr/S}$	$TSd1P_{Sr/S}$	$Pd1_{Sr/S}$	$TSd2T_{Sr/S}$	$Pd2_{Sr/S}$
O3βATP-PγATP	1.77	2.60	4.05	4.21	4.34
PγATP-OγSer21	3.59	2.73	1.72	1.67	1.61
OγSer21-HγSer21	0.98	0.99	1.67	2.03	2.64
Oδ2Asp166-HγSer21	1.77	1.72	1.01	0.99	1.41
O2γATP- HγSer21	3.27	2.98	2.89	2.11	1.05
OγSer21-Oδ2Asp166	2.74	2.71	2.66	2.93	3.47
$a._{O3\beta ATP\text{-}P\gamma ATP\text{-}O\gamma Ser21}$	154.1	158.5	161.5	164.3	152.9
$a._{O\gamma Ser21\text{-}H\gamma Ser21\text{-}O\delta 2Asp166}$	170.2	178.4	166.6	149.7	114.5
$a._{O\delta 2Asp166\text{-}H\gamma Ser21\text{-}O2\gamma ATP}$	105.7	110.2	124.6	131.4	174.3
$d._{Ser21(N\text{-}C\alpha\text{-}C\beta\text{-}O\gamma)}$	-53.3	-42.2	-39.4	-49.9	-51.3
$d._{Asp166(C\beta\text{-}C\gamma\text{-}O\delta 2)\text{-}O2\gamma ATP}$	160.5	140.0	130.8	133.9	155.9

to 3.47 and 3.59 Å when Ca^{2+} ions and Sr^{2+} ions are bound, respectively, in the active site of the corresponding Rd structure. Finally, with Kemptide and Ca^{2+} in the reactant ternary complex of PKAc, the PγATP-OγSer17 distance extends up to 3.69 Å. That is, for the same substrate peptide, the longer the ionic radii of the divalent metal ion bound in the active site, the farther is the γ-phosphoryl group from the nucleophilic hydroxyl group of substrate serine. Therefore, the R4-

Table 3.18. Selected QM(B3LYP/6-31+G(d))/CHARMM bond distances (Å), bond angles (deg), and dihedrals (deg) in the stationary points characterizing the different stages of the phosphoryl-transfer dissociative mechanism for the PKAc-Ca_2ATP-Kemptide model.

	$Rd_{Ca/K}$	$TSd1P_{Ca/K}$	$Id1_{Ca/K}$	$TSd1H_{Ca/K}$	$Pd1_{Ca/K}$	$TSd2T_{Ca/K}$	$Pd2_{Ca/K}$
O3βATP-PγATP	1.79	2.62	3.26	3.39	3.56	3.65	3.66
PγATP-OγSer17	3.69	2.53	1.97	1.89	1.76	1.71	1.65
OγSer17-HγSer17	0.99	1.00	1.05	1.18	1.70	2.05	2.50
Oδ2Asp166-HγSer17	1.80	1.74	1.52	1.28	1.02	1.00	1.57
O2γATP- HγSer17	3.27	2.83	2.68	2.75	2.92	2.00	1.03
OγSer17-Oδ2Asp166	2.79	2.74	2.56	2.46	2.71	2.91	3.28
$a._{O3βATP\text{-}PγATP\text{-}OγSer17}$	148.7	157.4	161.2	161.7	161.2	171.6	170.2
$a._{OγSer17\text{-}HγSer17\text{-}Oδ2Asp166}$	174.3	173.5	170.3	171.1	167.0	142.1	105.0
$a._{Oδ2Asp166\text{-}HγSer17\text{-}O2γATP}$	108.7	112.8	115.4	117.6	126.4	139.1	175.4
$d._{Ser17(N\text{-}Cα\text{-}Cβ\text{-}Oγ)}$	-48.1	-33.1	-33.8	-34.7	-33.7	-36.2	-36.5
$d._{Asp166(Cβ\text{-}Cγ\text{-}Oδ2)\text{-}O2γATP}$	152.9	141.1	132.6	131.1	136.9	154.6	171.8

reaction coordinate begins from a more negative value as the ionic radii of the divalent metal ion increases (see Figure 3.24, $R4^{Dissociative}$ phosphoryl-transfer section). Another feature of the active site that changes because of the nature of the divalent metal ion bound is the linear alignment of the OH group of substrate serine with respect to the β,γ-bridging bond of the ATP molecule. This linear arrangement, which affects the starting point of the nucleophilic attack, is less evident as the ionic radii increases. These changes in the active site geometry of different metal complexes can also be due to the increment in the coordination number at metal binding site M1 (six, seven, and eight for Mg^{2+}, Ca^{2+}, and Sr^{2+}, respectively): the larger the coordination sphere, the longer the metal-ligand distances, and consequently the terminal phosphate of ATP and the nucleophilic hydroxyl group of substrate serine are then pushed apart. In summary, the metal size and electronic structure of the divalent metal ion not only impinges on the coordination sphere, metal-ligand distances, and metal hydration between the reactant complexes, it does too to some extend on the relative position of reactive moieties within the active site at the beginning of the phosphorylation reaction catalyzed by PKAc. On the other hand, the active site geometry of the computationally obtained Michaelis complexes for the same divalent metal ion also varies depending on the nature of the substrate peptide. Again, the relative position of the reactive γ-phosphate group of ATP undergoes the most significant variations, being farther and less linearly aligned to the OH group of substrate serine with Kemptide than with SP20.

Interestingly, only in $Rd_{Sr/S}$ the ε-amino group of Lys72, besides forming hydrogen bonds

with the O1α and O1β atoms of ATP, and with the ε-carbonyl group of Glu91, it is also hydrogen-bonded (2.8 Å) to the XW1029 crystallographic water molecule, which in turn is part of the 8-fold coordination sphere of the Sr1 metal ion (see catalytic core interaction distances and Sr^{2+} ion coordination sphere in Table A10).

As can be seen in Figure 3.24, the obtained phosphoryl-transfer potential energy paths show at a R4 value close to -0.9 Å an energy maximum of about 9.1, 11.5 and 11.1 kcal/mol for the Ca/SP20, Sr/SP20 and Ca/Kemptide models, respectively. The distances depicted in Figures 3.24A, B, and C show that the phosphorylation reaction starts with the approach of the OH group of substrate serine to the terminal phosphoryl group of ATP. However, it is the breakage of the β,γ-phosphoanhydride bond of ATP (from a R4 value of approximately 1.5 Å) which accounts for nearly all the potential energy barrier associated with the phosphoryl-transfer step. Note that for the three models under study, the energy maximum region coincides clearly with the crossing point of the progression of the phosphoryl-transfer distances (O3βATP-PγATP and PγATP-OγSer$_{Substrate}$) while the coupled proton-transfer distances (OγSer$_{Substrate}$-HγSer$_{Substrate}$ and Oδ2Asp166-HγSer$_{Substrate}$) remain almost unchanged up to such region. There is a subtle decrease in the Oδ2Asp166-HγSer$_{Substrate}$ distance at the very beginning of the R4-reaction coordinate and extending up to a R4 value of 1.5 Å. From this point, Oδ2Asp166-HγSer$_{Substrate}$ distance almost recovers its initial value. This shows that the hydrogen bond interaction between the hydroxyl group of substrate serine and the carboxylate group of Asp166 residue enhances the nucleophilic character of the oxygen atom when its approach to the γ-phosphoryl group starts. However, it is clear that the nucleophilic attack anticipates the proton-transfer from the nucleophilic hydroxyl group of substrate serine to the side chain of Asp166 (which acts as an acid/base catalyst).

TS searches starting from the maximum-energy geometries were successful. The active sites of the optimized TS structures are shown in Figures 3.27A, B and C for TSd1P$_{Ca/S}$, TSd1P$_{Sr/S}$ and TSd1P$_{Ca/K}$, respectively. Frequency calculations from the resulting TS structures confirmed a single imaginary frequency mode (58i, 58i and 62i cm^{-1} for TSd1P$_{Ca/S}$, TSd1P$_{Sr/S}$ and TSd1P$_{Ca/K}$, respectively) with the transition vector consistent with the nucleophilic attack, and without any contribution related with the transfer of the serine hydroxyl proton toward the carboxylate side chain of Asp166. The O3βATP-PγATP and PγATP-OγSer$_{substrate}$ distances are almost equal in each of the TSd1P structures, revealing that the γ-phosphoryl group, in a trigonal-planar configuration, is in a quasi-symmetrical position between the leaving and the nucleophilic oxygen atoms. That is, in terms of its progression, the approach of the attacking nucleophile to the phosphorous is comparable to the departure of the leaving group before the TS. Therefore, the PγATP-OγSer$_{substrate}$ bond begins to strengthen only when the O3βATP-PγATP bond is almost

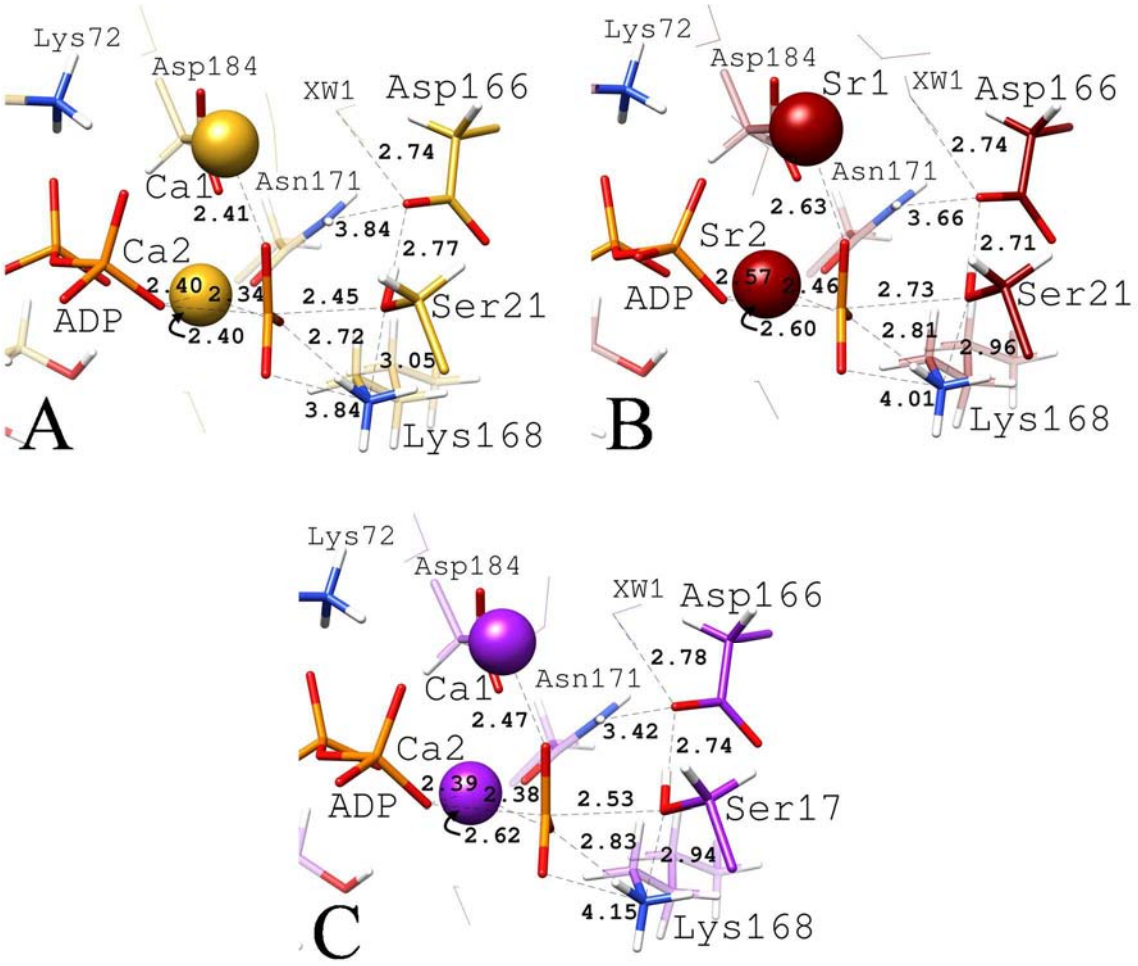

Figure 3.27. Active site structure at: **(A)** QM(B3LYP/6-31+G(d))/CHARMM optimized TSd1P$_{Ca/S}$; **(B)** QM(B3LYP/def2-TZVP)/CHARMM optimized TSd1P$_{Sr/S}$; and **(C)** QM(B3LYP/6-31+G(d))/CHARMM optimized TSd1P$_{Ca/K}$. Selected distances are given in Å.

completely broken. It can be observed though that the dissociative character of the TS increases along the earth alkali metals group: Mg^{2+} < Ca^{2+} < Sr^{2+}, with SP20 as substrate. Further, the relative positions of the three atoms -O3βATP, PγATP and OγSer$_{substrate}$- are suitable for a nearly in-line nucleophilic substitution at the γ-phosphorous atom, which then shows a trigonal bipyramidal coordination. These results are, qualitatively, identical to those obtained for the TSd1P$_S$ structure. For that, it is plausible to establish that, in the phosphorylation reaction catalyzed by PKAc, an almost perfect compensation between bond-making and bond-breaking processes regulates the formation of an almost symmetrical, metaphosphate-like transition state for the phosphoryl-transfer step following a dissociative mechanism, regardless of the substrate or the alkali earth divalent metal ion bound in the active site.

The hydrogen bond network and the positions of the residues side chains within the active site are also very similar in these critical point structures. However, the nature of the substrate and of the metal cations do affect the geometry of the active site of these dissociative TS complexes. For the SP20-bound complexes in particular, the O3βATP-PγATP and PγATP-OγSer21

distances (that are 2.31 and 2.36 Å, respectively, in the $TSd1P_S$, see Table 3.12) increase in going from Mg^{2+} to Sr^{2+}, being such increase more noticeable for the $TSd1P_{Sr/S}$. As the O3βATP, PγATP and OγSer21 atoms are located in a nearly straight line at the TS structures, the O3βATP···OγSer21 separation also increases: from 4.6 Å in $TSd1P_S$ to 4.8 and to 5.2 Å in $TSd1P_{Ca/S}$ and $TSd1P_{Sr/S}$, respectively. On the other hand, the trend in the O3βATP···OγSer21 separation is not as pronounced -if any- for the reactant complexes (5.1, 5.1 and 5.2 Å for Rd_S, $Rd_{Ca/S}$ and $Rd_{Sr/S}$, respectively). Characterizing here the variation of the active site length upon going from the reactant complex to the phosphoryl-transfer TS structures as the change in the O3βATP···OγSer21 separation, then the contraction is significant for the Mg/SP20 and Ca/SP20 models (-0.45 and -0.32 Å, respectively) and insignificant for the Sr/SP20 model (-0.01 Å). Taking into account that the reactive species (*i.e.* ADP leaving group, transferring γ-phosphoryl group, and the nucleophilic hydroxyl group of substrate serine) are the same in all models, then the extent of the active site contraction in the phosphoryl-transfer TS structures is likely related to the electron density of the metaphosphate-like group and its delocalization by the divalent metal ions through the M1-O3γATP and M2-O2γATP coordination interactions. That is, the more effectively such effect is exerted by the metal cations, the less negative charge accumulates on the transferring γ-phosphoryl group and, consequently, lower are the repulsive forces between the leaving group and the nucleophile (*i.e.* the terminal β-phosphate group of ADP and the hydroxyl group of substrate serine, respectively). This fact then results in a smaller O3βATP···OγSer21 separation. It is thus clear that the smaller the size of the divalent metal ion (*i.e.* harder Lewis acid character), the more polarized is the electron density on the metaphosphate-like group and more compact and further stabilized is the active site in dissociative phosphoryl-transfer TS structures.

The almost identical geometry, as well as the comparable contraction, of the active site at both $TSd1P_S$ and $TSd1P_{Ca/S}$ structures, explains the same QM(B3LYP/6-31+G(d))/CHARMM potential energy barrier (9.2 kcal/mol) for the nucleophilic attack. For all models, the QM(MP2/def2-TZVP)/CHARMM single-point calculations on the TSd1P structures gave higher potential energy barriers (see values in red color in Figures 3.25A, B, and C for the Ca/SP20, Sr/SP20, and Ca/Kemptide models). For the Ca/SP20 model the high-level value is 12.6 kcal/mol, while for the Mg/SP20 model is 11.0 kcal/mol at the same level of theory.

On the other hand, the Ca^{2+} ions-bound TSd1P structures show that the extent of active site contraction is lower with Kemptide than with SP20 (*e.g.* longer O3βATP-PγATP distance with Kemptide as substrate). Moreover, interaction distance of the ε-amino group of Lys168 residue with the oxygen atom of the γ-phosphoryl group is shorter in $TSd1P_{Ca/S}$ than in $TSd1P_{Ca/K}$. In

contrast, the NζLys168-OγSer$_{Substarte}$ distance is longer. For the PKAc-Mg_2ATP-SP20 and PKAc-Mg_2ATP-Kemptide models, we have proven the significant catalytic role of the Lys168 residue hydrogen bond interactions in the phosphorylation reaction catalyzed by PKAc, particularly in the geometry and electronic stabilization of related transition states. Firstly, in bridging together the reactant moieties (*i.e.* the γ-phosphoryl group and the nucleophilic hydroxyl group of substrate serine), so facilitating its correct orientation and keeping them in a close contact conformation. Secondly, in reducing the energetically unfavorable large repulsion force between such molecular entities by partially neutralizing their inherent -and rapidly increasing- negative charge. Thus, a slightly longer NζLys168-OγSer$_{Substrate}$ distance in TSd1P$_{Ca/S}$ might entail a somewhat stronger nucleophilic character for the attacking oxygen atom of Ser21 with respect to that of Ser17. And the shorter NζLys168-O1γATP and NζLys168-O2γATP distances in TSd1P$_{Ca/S}$ indicate that in this structure the positively charged Lys168 residue exerts a higher stabilization factor than it does in TSd1P$_{Ca/K}$. In fact, despite differing in both the substrate and the divalent metal ion bound, the active and catalytic cores at the TSd1P$_{Ca/K}$ structure are geometrically very much alike to the active and catalytic cores at the TSd1P$_{Sr/S}$ counterpart. Both systems represent very similar potential energy barrier for the phosphoryl-transfer step (11.1 and 11.5 kcal/mol at TSd1P$_{Ca/K}$ and TSd1P$_{Sr/S}$, respectively). Quite comparable potential energy barriers at the QM(MP2/def2-pVTZ)/CHARMM level were calculated from these stationary point geometries (14.0 and 13.3 kcal/mol, respectively).

For all three models, after the TSd1P region, the potential energy goes down because the formation and strengthening of the PγATP-OγSer$_{Substrate}$ bond while the γ-phosphoryl group continues moving away from the ADP leaving group. The evolution of the R4-reaction coordinate distances (Figures 3.24A, B, and C) shows that the coupled proton-transfer from the nucleophilic-attacking oxygen atom to the carboxylate group of the Asp166 residue just begins around R4 = 0.5 Å, when PγATP-OγSer$_{Substrate}$ bond is almost completely formed (length of 2.0 Å, approximately). From this point in the dissociative R4-reaction coordinates, there is a meaningful difference in the potential energy profiles depending on the divalent metal ion bound in the active site.

With Ca^{2+} ions, the corresponding phosphoryl-transfer path describes a shallow minimum from which it was possible to characterize a proton shift intermediate structure, Id1$_{Ca/S}$ and Id1$_{Ca/K}$ for SP20 and Kemptide as substrates, respectively. The Id1$_{Ca/S}$ and Id1$_{Ca/K}$ structures lay around 3 and 2 kcal/mol below the corresponding TSd1P structure, respectively. These structures are geometrically very similar, with a short (2.6 Å) OγSer21-Oδ2Asp166 hydrogen bond and an O3βATP-PγATP distance slightly longer than 3 Å, particularly in Id1$_{Ca/K}$. They also are geometrically quite close to the Id1$_S$ structure, although in that case the active core is a little

more contracted than the $Id1_{Ca/S}$ (*e.g.* shorter O3βATP-PγATP, PγATP-OγSer21 and OγSer21-Oδ2Asp166 distances). The proton-transfer to the Asp166 side chain is at a more advanced stage (a markedly short Oδ2Asp166-HγSer21 distance, almost corresponding to a properly formed bond). In fact, in the Mg/SP20 model, the proton shift intermediate structure instead of fulfilling the conditions for a shallow minimum represents the shoulder of a plateau in the phosphoryl-transfer reaction path (0.0 Å < R4 < 1.0 Å). Moreover, from the set of geometries within such R4-reaction coordinate region, unsuccessful TS searches were carried out trying to characterize the proton-transfer from the substrate hydroxyl group to the Asp166 side chain. Thus, in going from the transition state to the product complex of the phosphoryl-transfer step, the coupled proton-transfer event takes place without any additional energy cost. By contrast, for the Ca/SP20 and Ca/Kemptide models, the corresponding dissociative phosphoryl-transfer potential energy paths describes a local maximum (at R4 values of 1.0 and 1.3 Å, respectively) before reaching the products region. Major changes in the $OγSer_{Substrate}$-$HγSer_{Substrate}$ and Oδ2Asp166-$HγSer_{Substrate}$ distances occur around this particular region and successful TS searches starting from these local maximum-energy geometries were carried out. The corresponding $TSd1H_{Ca/S}$ and $TSd1H_{Ca/K}$ structures were identified with a single imaginary frequency mode (634i and 570i cm^{-1}, respectively) consistent with the transfer of the serine hydroxyl proton toward the carboxylate side chain of Asp166. In terms of the potential energy of the corresponding previous intermediate structure, the $TSd1H_{Ca/S}$ and $TSd1H_{Ca/K}$ structures represent a 0.9 and 0.6 kcal/mol potential energy barrier, respectively. Note in Figures 3.24B and D that the TSd1H position along the R4-reaction coordinate clearly coincides with the crossing point of $OγSer_{Substrate}$-$HγSer_{Substrate}$ and Oδ2Asp166-$HγSer_{Substrate}$ distances curve progression (*i.e.* where their lengths are practically equal). Beyond this point, for the Ca/SP20 and Ca/Kemptide models the potential energy goes down again –due the formation of the Oδ2Asp166-$HγSer_{Substrate}$ bond- and finally reaches the product complex region. The characterized $Pd1_{Ca/S}$ and $Pd1_{Ca/K}$ structures pose an endoergic potential reaction energy of 3.6 and 5.8 kcal/mol, respectively (for the Mg/SP20 model the potential reaction energy is 0.3 kcal/mol). That is, they lay 3.1 and 3.8 kcal/mol below the $TSd1H_{Ca/S}$ and $TSd1H_{Ca/K}$ structures, respectively (or, in turn, 5.6 and 5.3 kcal/mol below $TSd1P_{Ca/S}$ and $TSd1P_{Ca/K}$ structures, respectively). Interestingly, the QM(MP2/def2-TZVP)/CHARMM single-point energy evaluations for Ca/SP20 and Ca/Kemptide models (see Figures 3.25A and C), indicate that the high-level potential energy of the corresponding TSd1H structure are energetically below the corresponding proton shift intermediates. This indicates that the progression along the reaction path from the phosphoryl-transfer TS structure to the phosphoryl-transfer product complex occurs directly, and the supposed potential energy barrier for the proton migration from $OγSer_{Substrate}$ to Oδ2Asp166 might be related with a short

hydrogen bond. In our calculations for Mg^{2+} and Ca^{2+} ions-bounded models, the $O\gamma Ser_{Substrate}$-Oδ2Asp166 distance shortens from 2.8 Å near the phosphoryl-transfer transition state down to 2.4 Å at most along the reaction path to product complex region (2.6 Å for the Sr/SP20 model). Shorts hydrogen bonds have been detected using neutron diffraction and have proven to provide stabilization along enzymatic processes either through an electrostatic effect or resonance effect (low-barrier hydrogen bond).[280] The intrinsic protein fluctuations could modulate the $O\gamma Ser_{Substrate}$-Oδ2Asp166 distance, thus allowing the enzymatic system the use of a very limited space in an energetically efficient manner. The high-level potential reaction energies at the phosphoryl-transfer product complex, Pd1, is 1.3 and 3.6 kcal/mol for the Ca/SP20 and Ca/Kemptide models, respectively (-1.8 kcal/mol for the Mg/SP20 model at the same level of theory).

On the other hand, for the Sr/SP20 model, in going from $TSd1P_{Sr/S}$ to $Pd1_{Sr/S}$ the potential energy profile decreases smoothly (see Figure 3.24C) without describing any other R4-reaction coordinate region prone to stationary point convergence. The phosphoryl-transfer step in this case is exoergic, with a potential reaction energy of -3.5 kcal/mol (then, $Pd1_{Sr/S}$ lays 15 kcal/mol below the $TSd1P_{Sr/S}$ structure). The phosphoryl-transfer step for the Sr/SP20 model is even more exoergic at the MP2 level of theory (potential reaction energy of -7.6 kcal/mol). The evolution of $O\gamma Ser_{Substrate}$-$H\gamma Ser_{Substrate}$ and Oδsp166-$H\gamma Ser_{Substrate}$ distances shows that the proton shift from $O\gamma Ser_{Substrate}$ to Oδ2Asp166 occurs at a R4 value of approximately 1.8 Å and when the length of the O3βATP-PγATP distance is already 3.7 Å.

In all three optimized phosphoryl-transfer product complexes, the PγATP-OγSer21 bond is practically formed (1.7 Å) and the hydrogen bond between the phosphorylated OγSer21 and the now protonated Oδ2Asp166 is still present and remains quite short (2.6-2.7 Å). The coordination scheme of Ca1 and Ca2 sites remains practically unchanged throughout the phosphoryl-transfer step, with the exception of the Ca-O3βATP interaction, which strengthens (see Ca^{2+} ions coordination sphere in Tables A9 and A11 for the Ca/SP20 and Ca/Kemptide models, respectively). Our calculations indicate that the Ca-O3βATP distance decreases almost to its final value at the phosphoryl-transfer transition state structures. Thus, through this Lewis acid attack, the leaving ADP moiety screens the negative charge that accumulates as a consequence of the breakage of the β,γ-phosphoanhydride bond of ATP. The same holds true for the Sr/SP20 phosphoryl-transfer step. Nevertheless, it should be noted that in $Pd1_{Sr/S}$ the ε-amino group of Lys72 loses its hydrogen bond interaction to the β-phosphate group of ADP (a 3.2 Å NζLys72-O1βATP distance, see catalytic core interaction distances in Table A10) such that from this phosphoryl-transfer product complex structure, Lys72 interacts with the α-phosphate of ATP, the δ-amide group of Glu91, and the XW1029 crystallographic water molecule

exclusively. In addition to consider the proximity of the XW1029 molecule coordinating the Sr1 metal ion as a forgone conclusion, the change in the hydrogen bond network of Lys72 in $Pd1_{Sr/S}$ relative to $Rd_{Sr/S}$ (and to its common assembly stabilizing the α- and β-phosphates of the nucleotide while being properly positioned by Glu91), is likely due to the change in the relative position and interactions of the O1βATP atom. This β-oxygen atom coordinates the M1 metal ion all along the phosphorylation process regardless the divalent metal ion bound. In $Pd1_{Sr/S}$, however, without losing its coordination interaction to Sr1, the O1βATP atom is approximately 1 Å closer to Sr2 relatively to its position with respect to Mg2 in $Pd1_S$. This results in a 2.8 Å coordinating Sr2-O1βATP distance in $Pd1_{Sr/S}$, whereas Mg2 is almost 4 Å away from such β-oxygen atom in $Pd1_S$. This slight displacement of the O1βATP atom after the phosphoryl-transfer step distances such atom from the ε-amino group of Lys72 while increases the coordination number of the Sr2 metal ion to seven relatively to the octahedral (six-fold) coordination geometry seen around Sr2 in the preceding $Rd_{SR/S}$ and $TSd1P_{Sr/S}$ stationary points (with Sr2-O1βATP distances of 3.7 and 3.6 Å, respectively).

The size of the divalent metal ions bound in the active site directly affects the length of the just broken β,γ-phosphoanhydride bond (approximately 3.0, 3.5, and 4.0 Å with Mg^{2+}, Ca^{2+}, and Sr^{2+} ions, respectively) because the longer the metal-ligands distances, the larger the coordination sphere, and consequently the terminal phosphoryl groups of ADP and phosphorylated substrate serine are pushed farther away from each other. The length (4.1 Å) to which the O3βATP-PγATP increases due to the size of Sr^{2+} ions correlates with the large R4 value (almost 3 Å) and the exoergic process defined at $Pd1_{Sr/S}$. Moreover, the active core elongation because of the size of metal cations have a notable effect of the relative position and hydrogen bond interactions of the side chains of catalytically relevant residues. In particular, taking as reference the $Pd1_S$ structure, with Ca^{2+} and Sr^{2+} ions the ε-amino group of Lys168 residue in the corresponding phosphoryl-transfer product complex gets closer to the γ-phosphate group now bonded to substrate serine and is pushed farther apart from the carboxylated group of Asp166 side chain.

Proton-transfer step

In Pd1 structures, the O2γATP and O3γATP atoms of the phosphorylated substrate serine are sterically appropriate for acting as recipient in the proton-transfer from protonated Oδ2Asp166 atom. The O1γATP atom, besides being much farther away, presuppose a phosphoryl-transfer path distorting the newly formed phosphor ester bond. For the Mg/SP20 model, a slightly smaller potential energy barrier was calculated for the path with O2γATP as final proton acceptor, suggesting that the proton-transfer step of the dissociative mechanism

will most probably proceed via this reaction channel. For that, only the proton-transfer path corresponding to the protonation of the phosphorylated substrate serine at O2γATP was explored in each model (see Figure 3.24A, $R2^{Dissociative}$ proton-transfer profiles).

The evolution of bond breaking/forming distances along the R2-reaction coordinate is depicted in Figures 3.24B, C, and D for the Ca/SP20, Sr/SP20, and Ca/Kemptide models, respectively. Along the converged reaction profiles, the potential energy of the system first rises to a maximum value (of about 3.2, 1.7, and 7.2 kcal/mol with respect to the corresponding phosphoryl-transfer product complex, that is, over $Pd1_{Ca/S}$, $Pd1_{Sr/S}$, and $Pd1_{Ca/K}$, respectively) around at a R2 value of -1.1 Å. TS state search starting from these maximum-potential energy geometries were successful. Specifically, the proton-transfer O2γATP-paths go through a transition state structure (TSd2T) characterizing the rotation of protonated Asp166 side chain toward the O2γATP atom. The $TSd2T_{Ca/S}$, $TSd2T_{Sr/S}$, and $TSd2T_{Ca/K}$ structures are identified with one imaginary frequency (233i, 195i, and 137i cm^{-1}, respectively) consistent with such rearrangement of protonated Asp166 moiety within the active core. In fact, the Oδ2Asp166-$H\gamma Ser_{Substrate}$ and O2γATP-$H\gamma Ser_{Substrate}$ distances show a null progression and a readily decrease, respectively, up to a R2 value of almost -0.5 Å. Moreover, from Pd1 to TSd2T corresponding structures, the movement of the carboxylic group of protonated Asp166 moiety can also be assessed from the increase in both the Asp166(Cβ-Cγ-Oδ2)-O2γATP dihedral and the $O\gamma Ser_{Substrate}$-Oδ2Asp166 distance, as well as from the decrease in the Oδ2Asp166-O2γATP distance (see Tables 3.16, 3.17 , and 3.18 for the Ca/SP20, Sr/SP20, and Ca/Kemptide models, respectively). Thus, rotation of protonated Asp166 side chain in order to bring the donor and acceptor oxygen atoms closer and properly aligned is the main factor for the potential energy barrier associated with the dissociative proton-transfer step. In particular, the $TSd2T_{Ca/S}$ structure represents a potential energy barrier of 3.3 kcal/mol with respect to the mechanistically preceding $Pd1_{Ca/S}$ structure (2.6 kcal/mol at the MP2 level). For the Sr/SP20 model, in turn, this barrier is only 1.7 kcal/mol height, while the high-level results discard such energy requirement. Finally, relative to the aforegoing $Pd1_{Ca/K}$ structure, the potential energy barrier at the $TSd2T_{Ca/K}$ structure is 7.3 kcal/mol (5.5 kcal/mol at the MP2 level).

After the protonated Asp166 side chain-rotation transition state, the potential energy profiles drop smoothly for all three systems, reaching their corresponding minimum value at R2 close to 0.5 Å. The decrease of the potential energy reflects the gradual approach of the donor and acceptor oxygen atoms and the proton-transfer process itself. That is, for each model, the molecular complex evolves directly to the corresponding final proton-transfer product complex structure (Pd2). For the Ca^{2+} ions-bound models in particular, there is a bump in the downhill region of the corresponding potential energy profile that defines a quite planar region and

clearly coincides with the point where Oδ2Asp166-HγSer$_{Substrate}$ and O2γATP-HγSer$_{Substrate}$ distances are equal (that is, at a R2 value of 0 Å, see Figure 3.24B and D). TS search from geometries around this point did not succeed in defining stable stationary points characterizing specifically the proton-transfer from the protonated Oδ2Asp166 to O2γATP. For the Mg/SP20 model, the transition state structure characterizing the proton-transfer to O2γATP was indeed defined, and the corresponding MP2 level single-point calculations pointed out its potential energy as the relevant barrier for the proton-transfer step (*i.e.* a computed potential energy higher than that of the TSd2T$_S$ structure).

At the Pd2 structures, the HγSer$_{Substrate}$ is completely transferred to O2γATP, which is still tightly hydrogen-bonded to Oδ2Asp166 (in general, a Oδ2Asp166-O2γATP distance and a Oδ2Asp166-HγSer$_{Substrate}$-O2γATP angle of about 2.5 Å and 175°, respectively). At these final product complex structures, the size of the metal cations has a notorious impact in, firstly, the length of the O3βATP-PγATP distance, being about 1 Å longer with Sr^{2+} ions than with Mg^{2+} and Ca^{2+} ions. And, secondly, in the relative position and strength of the hydrogen bond interactions of the positively charged Lys168 side chain with the peripheral γ-oxygen atoms of phosphorylated substrate serine, particularly with the O1γATP atom. The global potential reaction energy, with respect to the corresponding Rd reactant complex structure, is -2.8, -9.3, and 7.6 kcal/mol for the Ca/SP20, Sr/SP20, and Ca/Kemptide models, respectively. The high-level potential reaction energy at Pd2$_{Ca/S}$, Pd2$_{Sr/S}$, and Pd2$_{Ca/K}$ is -4.9, -15.3, and 4.4 kcal/mol, respectively. The global potential reaction energy calculated for the Mg/SP20 model was -1.0 kcal/mol. Then, the larger the ionic radii of the divalent metal cations bound in the active site, the more exoergic is the PKA-catalyzed phosphoryl-transfer process following a dissociative reaction path.

The superposition of the active sites of the Rd$_{Ca/S}$ structure with the X-ray crystallographic structure of the pseudo-Michaelis complex PKAc-Ca_2ATP-CP20 (PDB code 4XW5[80]) is shown in Figure 3.28. In both structures, which are aligned with RMSD of 0.51 Å, the Ca1 and Ca2 metal ions have coordination numbers of seven and six, respectively, and the catalytically important residues occupy similar positions. The main difference is the conformation of the phosphorylated tale of the nucleotide and the relative conformation of the Gly-rich loop. A displacement of approximately 1.5 Å of the phosphates groups of ATP in Rd$_{Ca/S}$ relatively to 4XW5 sets the β-phosphate in Rd$_{Ca/S}$ closer to Ca2 metal ion, allowing the formation -as in the other models- of the Ca2-O3βATP coordination interaction which is not present in 4XW5. This coordination site of Ca2 in 4XW5 is thus occupied by a crystallographic water molecule (2.6 Å) positioned at an intermediate point between the Ca2 itself, the carboxylate group of Asp166, and the γ-sulfur atom of the Cys20 thiol group. The retracted position of the phosphorylated tail

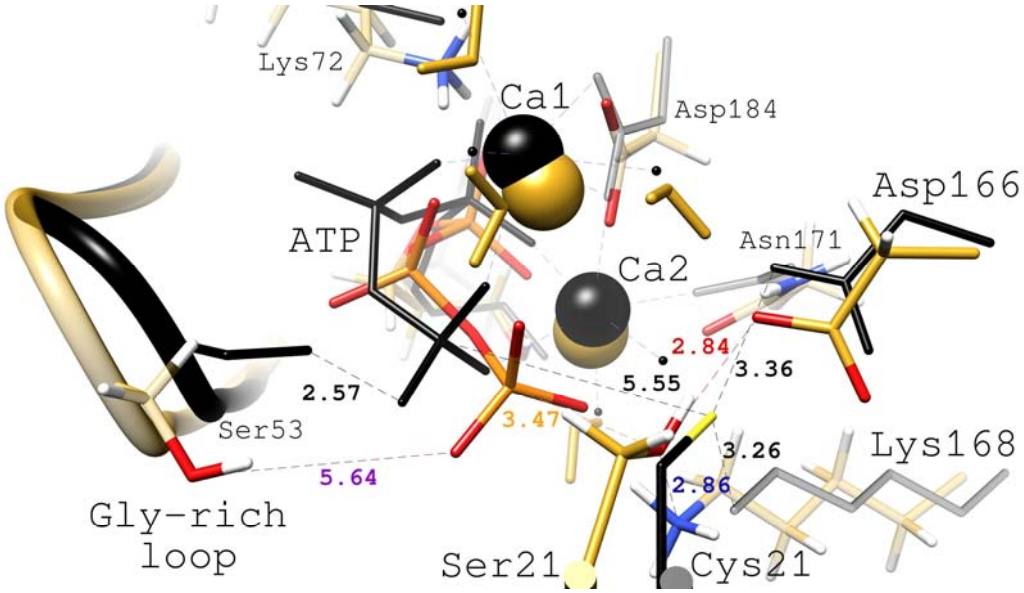

Figure 3.28. Superposition of the active sites in $Rd_{Ca/S}$ (pale yellow) and 4XW5 (black) structures. The catalytic cores of $Rd_{Ca/S}$ (colored by atom type) and 4XW5 are represented in thick- and thin-sticks, respectively. Selected distances are given in Å, using different colors for $Rd_{Ca/S}$ and only black for 4XW6. Relevant distances, hydrogen bonds and the Ca^{2+} coordination specifically in 4XW5 are shown as dashed lines.

of ATP in 4XW5 enables a hydrogen bond of the γ-phosphate group to Ser53 which is not formed in $Rd_{Ca/S}$ (a 2.6 and 5.6 Å O1γATP-OγSer53 distance, respectively). This difference might explain the displacement of about 1.5 Å at the tip of the Gly-rich loop in 4XW5[80] toward the active site relative to its position in $Rd_{Ca/S}$. Most importantly, the side chains of Ser21 and Cys21 have very similar conformations, both facing Asp166 and at hydrogen bond distances from the carboxylic group of its side chain (OγSer21-Oδ2Asp166 and SγCys21-Oδ2Asp166 distances of 2.8 and 3.4 Å, respectively). Furthermore, they also form a hydrogen bond with the ε-amino group of Lys168 side chain (OγSer21-NζLys168 and SγCys21-NζLys168 distances of 1.9 and 3.3 Å, respectively). The different sizes of oxygen and sulfur atoms may explain in part the length difference (van der Waals radius of sulfur is 1.9 Å compared with oxygen that is 1.3 Å). Finally, in both $Rd_{Ca/S}$ and 4XW5 active sites, the nucleophilic hydroxyl group of residue 21 of the substrate, the apical O3βATP leaving group, and the PγATP atom adopt an in-line configuration (with O3βATP-PγATP-OγSer21 and O3βATP-PγATP-SγCys21 angles of about 160°). However, the PγATP-OγSer21 distance is much shorter than the PγATP-SγCys21 distance (3.5 and 5.6 Å, respectively), and the CβSer21-OγSer21-PγATP angle (106°) is closer to 109.5° than the CβCys21-OγCys21-PγATP angle (94°). Thus, in $Rd_{Ca/S}$ the reactive fragments display the correct near attack conformation, with a Ser21 side chain configuration in which a lone electron pair of the OγSer21 atom is clearly directed toward the PγATP atom, maximizing orbital overlap in the nucleophilic attack. In contrast, although the extended PγATP-SγCys21 distance might be explained in part by the larger

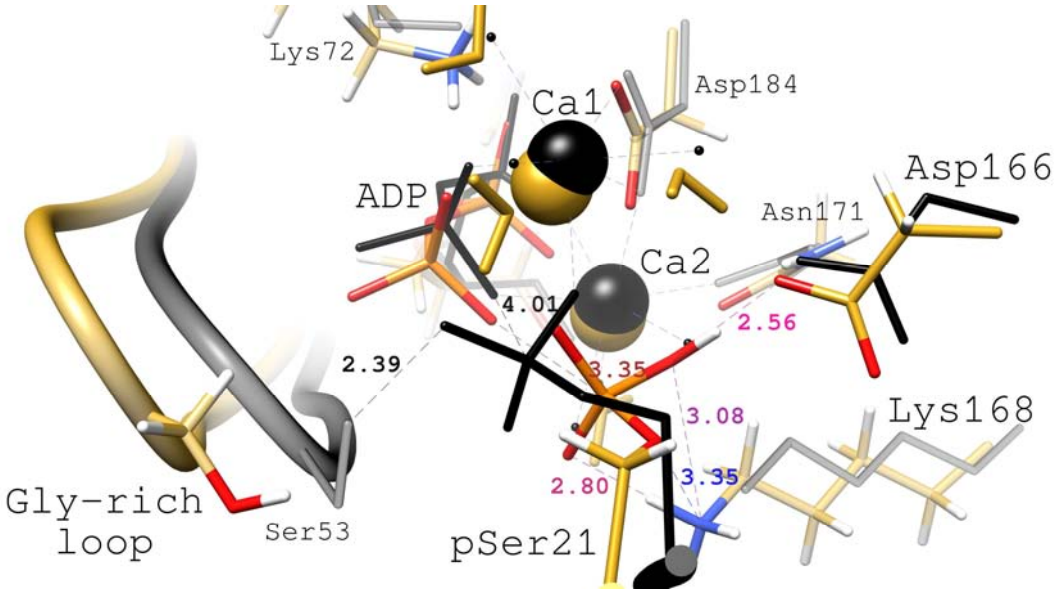

Figure 3.29. Superposition of the active sites in $Pd2_{Ca/S}$ (pale yellow) and 4IAI (black) structures. The catalytic cores of $Pd2_{Ca/S}$ (colored by atom type) and 4IAI are represented in thick- and thin-sticks, respectively. Selected distances are given in Å, using different colors for $Rd_{Ca/S}$ and only black for 4XW6. Relevant distances, hydrogen bonds and the Ca^{2+} coordination specifically in 4IAI are shown as dashed lines.

size of sulfur compared with oxygen, it is more likely that the 4XW5 crystallographic structure represents a preliminary stage of the catalytic process.

The active sites of the $Pd2_{Ca/S}$ structure and the X-ray crystallographic structure of the PKAc-Ca_2ADP-pSP20 product complex (PDB code 4IAI[76]) are geometrically comparable (see Figure 3.29, RMSD of 0.39 Å for the structure alignment). The most relevant difference is the orientation of the CβSer21-OγSer21 bond. In $Pd2_{Ca/S}$, the CβSer21-OγSer21 bond is oriented toward the Asp166 (as well as in all the computationally determined structures in this Thesis for the phosphorylation process catalyzed by PKAc), with the O2γATP of the phosphate group on Ser21 forming a strong hydrogen bond with Oδ2Asp166. This is due to the fact that Asp166 has just transferred the HγSer21 proton to the phosphorylated substrate, thereby restoring the original protonation state of the kinase after completing the catalyzed phosphorylation reaction through a dissociative mechanism. Moreover, in $Pd2_{Ca/S}$ Lys168 interacts through hydrogen bonds with OγSer21, O1γATP, and O2γATP of phosphorylated serine. In 4IAI, conversely, the CβSer21-OγSer21 bond is rotated away from the active site, pointing toward the bulk solvent and forming a strong hydrogen bond with the hydroxyl group of Ser53 (2.4 Å). This underscores another important difference between these structures. In $Pd2_{Ca/S}$, Ca1 and Ca2 have the same coordination numbers (seven and six, respectively) and ligands they had in the reactant complex, with only the Ca2-O2γATP coordination interaction showing a slight increase from its initial value. In 4IAI, Ca1 has the same seven ligands in its coordination sphere whereas Ca2 gains an

extra crystallographic water molecule (coordination number of seven). Furthermore, in 4IAI Ca2 loses completely its interaction with the transferred γ-phosphate and instead does so with a crystallographic water molecule. In fact, the relative position of the O2γATP atom in $Pd2_{Ca/S}$ and such crystallographic water in 4IAI is practically the same. In the same line of thought, the extra crystallographic water coordinated to Ca2 in 4IAI occupies a relative position very close to that of the O1γATP in $Pd2_{Ca/S}$, although the latter does not get to be part of the coordination sphere of Ca2 (3.44 Å). Finally, the orientation of the transferred phosphoryl group and its hydrogen bond network is reflected in the relative position of the Gly-rich loop in the two structures. In $Pd2_{Ca/S}$ the Gly-rich loop is approximately 2 Å farther away from the metals and ADP relatively to its position in 4IAI.

The superposition of the active sites of the $Pd2_{Sr/S}$ structure with the low temperature and room temperature X-ray crystallographic structures of the product complex PKAc-Sr_2ATP-pSP20 (PDB codes 4IAK[76] and 4IAY[76], respectively) are shown in Figure 3.30A (RMSD of 0.32 Å for the structure alignment) and B (RMSD of 0.48 Å for the structure alignment), respectively. In both 4IAK and 4IAY structures (as it is also the case for the product complex crystal structures with Mg^{2+} and Ca^{2+} ions, PDB codes 4IAF and 4IAI, respectively) the phosphoryl group on Ser21 is similarly oriented toward the bulk solvent, reducing the number of interactions with the active site, including contacts with the Sr2 metal and hydrogen bonds with Asp166 and Lys168, while forming a hydrogen bond with the OH group of Ser53 in the Gly-rich loop. These geometric features differ completely from those observed in the $Pd2_{Sr/S}$ structure. However, as has been explained already for the Mg/SP20 and Ca/SP20 models, the final product complex of our simulations correspond to the stage right after the proton-transfer step, in which the previously protonated Asp166 acts as an acid that protonates the phosphate group on Ser21. The charge repulsion between the negatively charged protonated phosphoserine and the carboxylate group of Asp166 side chain may in turn trigger the phosphate rotation away from the active site to the configuration shown in both 4IAK and 4IAY (from which the product release accompanied by opening of the Gly-rich loop is possible). Nevertheless, there is a striking good correspondence in the rest of the active sites geometries of these PKAc-Sr_2ATP-pSP20 crystallographic and computationally determined structures. In the three structures the catalytically important residues and the Gly-rich loop occupy very similar positions and, most importantly, both Sr1 and Sr2 metal ions are surrounded by eight ligands. Specifically, the Sr2 metal ion, which before the phosphoryl-transfer step had already increased its coordination number to seven due to its interaction with O1βATP, has in $Pd2_{Sr/S}$ an extra coordination contact with the phosphate on Ser21 through the O1γATP atom (see Figures 3.30A and B and Sr^{2+} ions coordination sphere in Table A10). In 4IAK and 4IAY, the lost interactions of Sr2 due to the rotation of the phosphate

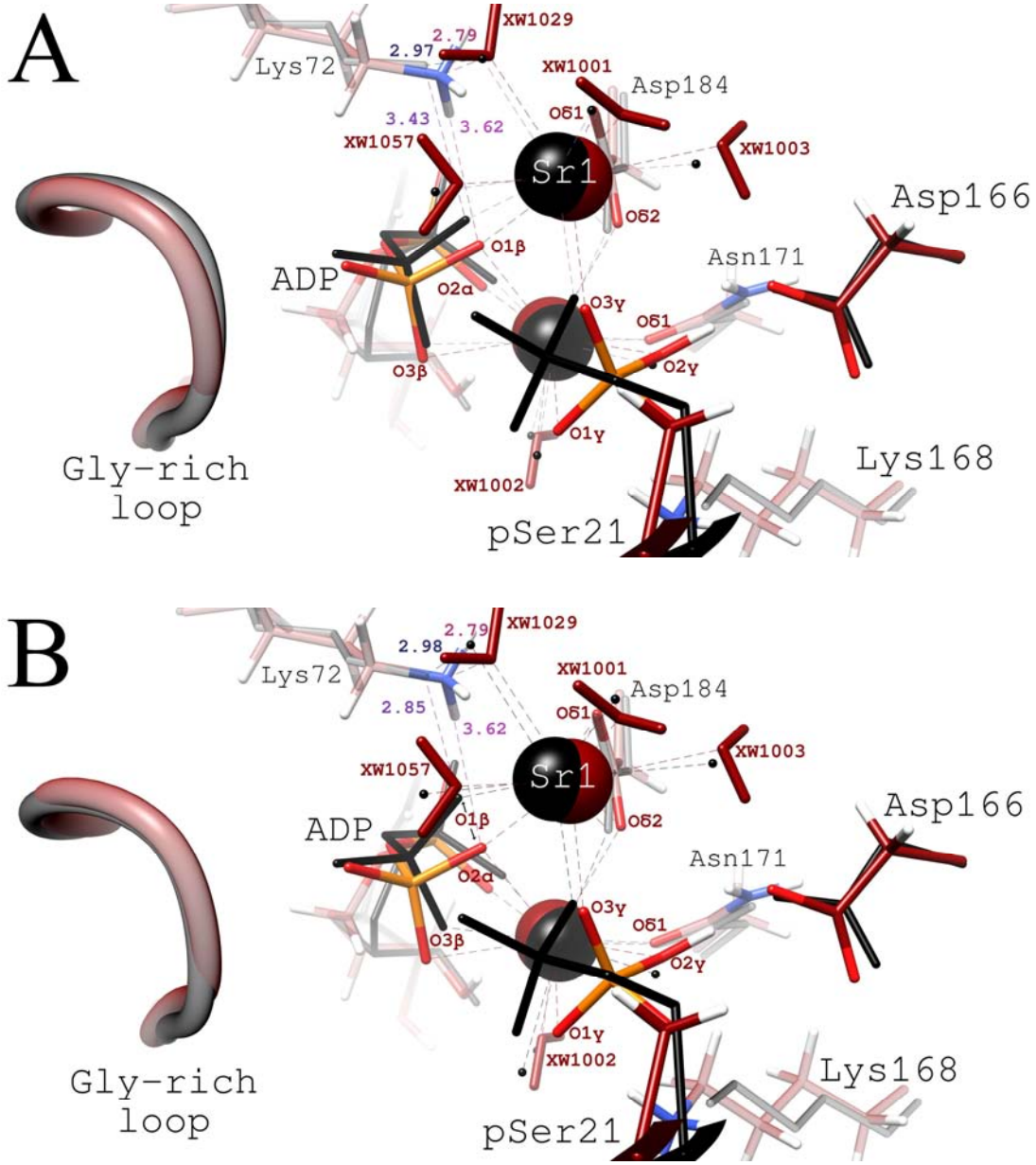

Figure 3.30. Superposition of the active sites in $Pd2_{Sr/S}$ (dark red) and: **(A)** 4IAK (black) structures; **(B)** 4IAY (black) structures. The catalytic cores of $Pd2_{Sr/S}$ (colored by atom type) and X-ray crystallographic structures are represented in thick- and thin-sticks, respectively. Selected distances are given in Å, using different colors for $Pd2_{Sr/S}$ and only black for 4IAK and 4IAY. Relevant distances, hydrogen bonds and the Sr^{2+} coordination are shown as dashed gray lines.

on Ser21 are provided by water molecules, whose relative positions match those of O1γATP and O2γATP in $Pd2_{Sr/S}$. Finally, the relative positions of the ε-amino group of Lys72 and the β-phosphate group of ADP in $Rd2_{Sr/S}$ and 4IAK (see Figure 3.30A and NζLys72 interaction distances in Table A10) confirm the slight displacement of the O1βATP atom toward the Sr2 along the phosphorylation process. Thus, for the Sr/SP20 model, our simulation of the dissociative mechanism of phosphoryl-transfer accurately describes the experimentally determined Sr^{2+} ions

coordination sphere and the structural changes defining the active site organization after the phosphorylation reaction.

4. Conclusions.

1.1. The QM/MM approach at the B3LYP/CHARMM level can be used to describe the different reaction mechanisms on the potential energy hypersurface of the global phosphoryl-transfer reaction catalyzed by PKAc using a complete solvated model of the biomolecular system.

1.2. The optimized structures for the stationary points at the B3LYP/CHARMM level along with single-point energy corrections at the MP2//B3LYP/CHARMM level represent a clear improvement of the chemical reaction paths over previous calculations of the same mechanisms using semiempirical methods for the QM part.

1.3. The converged reaction paths for the different catalytic mechanisms have been obtained by using several techniques and algorithms in ChemShell, specially designed for treating systems with a large number of degrees of freedom. The use of more flexible reaction coordinates, the location of the stationary points with the hybrid delocalized internal coordinate system, and the microiterative method to locate transition state structures are very efficient computational tools to explore the potential energy hypersurface of biomolecular systems.

2. The simulation of the associative mechanism on a complete solvated model of the PKAc-Mg_2ATP-Kemptide ternary complex built from the 1CDK X-ray crystallographic structure demonstrate that:

2.1. The associative mechanism reaction channel has an active role in the phosphoryl-transfer reaction catalyzed by PKAc.

2.2. The D166A mutant model shows residual activity in agreement with the experimental data.

2.3. The correct spatial positioning of the triad Asp166-Lys168-Thr201 and the hydrogen bond network these residues establish within the active site are essential for catalysis.

2.4. The transition state structures of the associative mechanism accomplish the charge balance hypothesis.

3. The simulation of the dissociative mechanism on a complete solvated model of the PKAc-Mg_2ATP-Kemptide ternary complex built from the 1CDK X-ray crystallographic structure demonstrate that:

3.1. With Kemptide as substrate, the dissociative mechanism (involving two consecutive steps: phosphoryl-transfer and back protonation of the phosphorylated substrate or proton-transfer) is more favorable than the associative one.

3.2. The Asp166 residue behaves as a base catalyst by abstracting the proton from the hydroxyl group of substrate serine which, in turn, enhances the nucleophilic character of the hydroxyl group, thus facilitating the phosphoryl-transfer step.

3.3. In the proton-transfer step, the Asp166 residue acts as an acid catalyst by donating the proton just accepted from the hydroxyl group of substrate serine specifically to the O2γATP atom of the phosphorylated substrate, thus regenerating the original protonation state of the enzyme.

3.4. The charge repulsion between the negatively charged protonated phosphokemptide and the carboxylate group of Asp166 could facilitate the product release in agreement with mutagenesis experiments.

3.5. The precise location and orientation of the Asp166-Lys168-Thr201 triad have a relevant contribution to the stabilization of the phosphoryl-transfer and proton-transfer steps by modulating electrostatic and hydrogen bond interactions.

4. The simulation of both the associative and the dissociative mechanisms on a complete solvated model of the PKAc-Mg_2ATP-SP20 and the PKAc-Mg_2ATP-Kemptide ternary complexes built from the 4IAC X-ray crystallographic structure demonstrate that:

4.1. The main features of the catalytic mechanism are not substrate dependent. However, the product complexes are better stabilized in the active site in the case of SP20, which may explain why phosphokemptide dissociates much faster. Moreover, with SP20 as substrate both O2γATP and O3γATP act as final proton acceptors.

4.2. Regardless of the substrate and the phosphorylation state of the PKAc, the dissociative mechanism is clearly more favorable than the associative one.

4.3. A fully closed conformation of the Gly-rich loop is not a requirement for catalysis.

4.4. The theoretically determined reaction paths are comparable with X-ray crystallographic structures that have been suggested as tentative snapshots of the evolution of the enzyme system along the catalytic reaction. Our results complete the data experimentally determined about the phosphoryl-transfer transition state and underscore the relevant geometric features of the chemical step and its relation with the enzyme dynamics.

5. The simulation of the dissociative mechanism on a complete solvated model of the PKAc-Ca_2ATP-SP20 and the PKAc-Sr_2ATP-SP20 ternary complexes built from the 4IAC X-ray crystallographic structure demonstrate for the first time that:

5.1. The catalyzed phosphoryl-transfer is plausible with alkali earth metal ions other than Mg^{2+} ions.

5.2. The results confirm, in the case of the Ca^{2+} ions, the recent experimental results where the physiological role of Ca^{2+} in kinase activity has been proposed.

5.3. For all metals studied, the phosphoryl-transfer step is energetically comparable, although the dissociative character of the transition state increases in going from Mg^{2+} to Sr^{2+}.

5.4. In contrast, the proton-transfer step is metal dependent making more exoergic the global chemical process in going from Mg^{2+} to Sr^{2+}.

5.5. Finally, the very good agreement between the theoretically determined structures and the crystallographic studies validates the above conclusions for the Ca^{2+} and Sr^{2+} models.

Appendix. Structural information.

Nomenclature is based on the pseudo-Michaelis complex PKAc-Mg_2AMPPCP-SP20 X-ray crystallographic structure (PDB code 4IAC[76]).

For 4DH3[164] * is OγSer21=CβAla21 (or XSer21=XAla21); for 4DH8[164] * is O3βATP=NβAMPPNP and OγSer21=CβAla21 (or XSer21=XAla21); for 4IAC[76] * is O3βATP=CβAMPPCP: for 1L3R[79] * γPO_3=AlF_3; for 4IAF[76] * means that is not possible to establish the chemical correspondence of the O*i*γATP atoms in relation to the 4IAC[76] nomenclature; for 4DH52 * is OγSer21=OH2 and ~ is OγSer21=CβAla21 (or XSer21=XAla21).

Table A1. For the PKAc-Mg_2ATP-SP20 model, selected QM(B3LYP/6-31+G(d))/CHARMM bond distances (Å), bond angles (deg), and dihedrals (deg) in the optimized reactants ($Ra1_S$), transition state ($TSa1_S$), and products ($Pa1_S$) for the associative mechanism with the O1γATP as the proton acceptor (O1γATP-associative path). Comparison with values from X-ray crystallographic structures characterizing different stages of the phosphoryl-transfer mechanism catalyzed by the PKAc with SP20 as substrate and Mg^{2+} ions.

Active core geometric features	4DH3[164]	4DH8[164]	4IAC[76]	$i_{model}S_{Mg}$	$Ra1_S$	$TSa1_S$	$Pa1_S$	1L3R[79]	4IAF[76]	4DH5[164]
O3βATP-PγATP	1.68	1.74*	1.83*	1.70	1.70	1.76	2.93	2.31*	4.06	3.55
PγATP-OγSer21	3.80*	4.09*	3.49	3.76	3.11	2.27	1.64	2.27*	1.63	1.67*
OγSer21-HγSer21	---	---	---	0.98	0.98	1.57	2.91	---	---	---
O1γATP-HγSer21	---	---	---	3.12	1.94	1.03	0.99	---	---	---
O2γATP-HγSer21	---	---	---	3.52	3.04	2.88	3.43	---	---	---
O3γATP-HγSer21	---	---	---	1.81	2.88	2.84	2.78	---	---	---
OγSer21-Oδ2Asp166	4.00*	3.94*	4.40	4.28	4.01	4.15	3.47	2.48	4.67	2.70*
Oδ2Asp166-O2γATP	3.40	3.47	3.81	3.93	3.87	3.78	3.68	3.31*	3.34*	3.09
Oδ2Asp166-O3γATP	4.21	4.16	4.31	4.49	4.53	4.44	4.38	3.36*	5.38* 5.78*	3.53
$angle_{O3\beta ATP\text{-}P\gamma ATP\text{-}O\gamma Ser21}$	160.8*	170.7*	148.2*	141.3	174.2	167.1	171.8	162.6*	159.8	168.0*
$angle_{O\gamma Ser21\text{-}H\gamma Ser21\text{-}O1\gamma ATP}$	---	---	---	150.3	151.8	130.7	59.1	---		---
$angle_{O\gamma Ser21\text{-}H\gamma Ser21\text{-}O3\gamma ATP}$	---	---	---	153.6	100.2	68.9	53.8	---	---	---
$d._{Ser21(N\text{-}C\alpha\text{-}C\beta\text{-}O\gamma)}$	---	---	64.0	68.7	-39.3	-40.9	-46.5	-64.8	74.0	---
$d._{Asp166(C\beta\text{-}C\gamma\text{-}O\delta2)\text{-}O2\gamma ATP}$	158.6	162.1	160.0	167.2	158.6	147.9	142.3	117.8*	-119.2*	129.34
$d._{Asp166(C\beta\text{-}C\gamma\text{-}O\delta2)\text{-}O3\gamma ATP}$	-117.2	-107.6	-105.5	-96.1	-96.9	-95.1	-97.8	-88.4*	-152.5* -104.8*	-140.6

$d._{phiAsp166}$	-141.3	-148.0	-149.2	-128.2	-131.3	-132.5	-133.0	-148.5	-148.2	-142.4
$d._{psiAsp166}$	48.6	47.6	43.5	68.2	67.8	66.9	63.1	44.2	39.9	40.7
	4.05*$^{i=1}$	3.98*$^{i=1}$	3.29$^{i=1}$	4.00$^{i=1}$	2.85$^{i=1}$	2.38$^{i=1}$	2.54$^{i=1}$	3.08*$^{i=F3}$	2.63*	2.75*$^{i=1}$
OγSer21-OiγATP	3.69*$^{i=2}$	4.03*$^{i=2}$	4.07$^{i=2}$	4.36$^{i=2}$	3.27$^{i=2}$	2.66$^{i=2}$	2.48$^{i=2}$	2.81*$^{i=F1}$	2.53*	2.72*$^{i=2}$
	3.17*$^{i=3}$	3.53*$^{i=3}$	2.67$^{i=3}$	2.73$^{i=3}$	3.20$^{i=3}$	2.74$^{i=3}$	2.58$^{i=3}$	2.78*$^{i=F2}$	2.66*	2.59*$^{i=3}$
Catalytic core interaction distances	4DH3[164]	4DH8[164]	4IAC[76]	$i_{model}S_{Mg}$	$Ra1_S$	$TSa1_S$	$Pa1_S$	1L3R[79]	4IAF[76]	4DH5[164]
Oγ1Thr201-Oδ1Asp166	2.91	2.85	2.62	2.68	2.71	2.75	2.73	2.76	3.13	3.28
Oγ1Thr201-NζLys168	3.16	2.78	2.99	2.79	2.76	2.72	2.71	2.86	2.80	2.92
Oγ1Thr201-OγSer21	4.26*	4.06*	5.27	4.63	3.41	4.15	3.74	3.56	5.59	3.70*
Oδ2Asp166-PγATP	4.39	4.47	4.66	4.83	4.76	4.53	4.03	3.60*	4.63	3.22
Oδ2Asp166-OH2XWAT1003	2.85	2.74	2.53	2.69	2.70	2.69	2.68	2.47	2.82	2.81
Oδ2Asp166-Nδ2Asn171	3.15	2.97	3.05	2.91	2.93	2.99	3.04	3.29	3.06	3.07
Oδ2Asp166-NζLys168	4.03	3.62	3.46	3.63	3.72	3.88	3.92	4.26	4.12	4.46
Oδ1Asp166-NζLys168	4.17	3.84	4.86	4.34	4.31	4.33	4.32	4.04	4.02	4.26
NζLys168-OγSer21	4.53*	4.23*	4.81	4.70	2.77	2.70	2.91	3.12	5.20	2.90*
NζLys168-PγATP	4.24	4.09	3.98	3.82	3.93	3.98	3.61	3.82*	5.20	3.32
NζLys168-O2γATP	2.87	2.78	2.77	2.83	2.97	3.14	3.06	2.92*$^{i=F1}$	4.73*	3.32
NζLys168-O1γATP	4.55	4.24	4.08	3.88	3.93	4.23	4.05	4.12*$^{i=F3}$	4.82* 6.78*	3.38
Nδ2Asn171-O2γATP	4.37	4.23	4.53	4.37	4.31	4.10	3.94	3.11*$^{i=F1}$	> 5	3.05
NζLys72-O1αATP	2.64	2.84	2.87	2.72	2.73	2.73	2.76	2.76	2.88	2.83
NζLys72-O1βATP	2.80	2.95	3.13	2.84	2.77	2.75	2.76	2.78	2.85	3.11
NζLys72-Oε2Glu91	2.72	2.71	2.72	2.66	2.66	2.66	2.67	2.79	2.67	2.55
OγSer53-O1γATP	3.46	3.68	5.42	5.69	5.37	5.29	5.26	3.47*$^{i=F3}$	2.77*	4.01

OγSer53-OγSer21	4.51*	4.51*	5.55	5.70	6.20	5.91	6.21	5.20	3.02	5.23*
OγSer53-OSer21	2.87*	2.72*	5.14	4.29	4.21	3.95	4.07	2.62	2.92	3.99~
OγSer53-NSer21	3.51*	3.41*	6.35	5.73	5.28	5.14	5.27	3.23	3.67	3.35~
NSer53-O2βATP	3.24	3.48	4.16	4.23	4.16	4.15	4.22	3.31	3.98	3.95
NSer53-O1γATP	2.55	2.83	5.63	5.41	5.26	5.02	5.24	2.67*$^{i=F3}$	2.94*	4.43
NPhe54-O2βATP	3.02	3.16	5.35	5.45	5.34	5.41	5.48	2.94	4.50	3.82
NGly55-O2βATP	3.08	3.04	5.82	5.95	5.77	5.87	5.83	3.06	5.30	3.68
Oδ1Asp24^{SP20}-Cε1His87	7.67	7.49	6.24	5.28	5.26	5.25	5.25	6.68	> 11	3.08
Oδ1Asp24^{SP20}-Nε2Gly84	4.79	4.66	3.58	2.80	2.80	2.80	2.80	6.56	> 10	3.17
Oε1Gly84-Nδ1His87	2.80	2.83	2.67	2.70	2.71	2.71	2.72	2.85	2.78	2.72
O2pThr197-Nε2His87	2.63	2.71	2.64	2.66	2.64	2.65	2.64	2.72	2.75	2.71
Mg^{2+} ions coordination sphere	4DH3[164]	4DH8[164]	4IAC[76]	$i_{model}S_{Mg}$	$Ra1_S$	$TSa1_S$	$Pa1_S$	1L3R[79]	4IAF[76]	4DH5[164]
Mg1-O1βATP	2.39	2.14	2.20	2.08	2.09	2.09	2.03	2.13	2.27	2.23
Mg1-O3γATP	2.25	2.17	2.25	2.16	2.10	2.12	2.21	1.97*$^{i=F2}$	2.29*	2.14
Mg1-Oδ1Asp184	2.60	2.45	2.40	2.21	2.20	2.17	2.20	2.22	2.44	2.67
Mg1-Oδ2Asp184	2.35	2.31	2.29	2.20	2.19	2.19	2.14	2.32	2.27	2.40
Mg1-OH2XWAT1003	2.08	2.10	2.17	2.07	2.08	2.08	2.10	2.36	2.39	2.27
Mg1-OH2XWAT1001	2.10	2.11	2.16	2.02	2.05	2.05	2.05	2.12	2.36	2.13
Mg2-O2αATP	2.43	2.09	2.18	1.99	1.99	2.00	2.05	1.88	2.35	2.40
Mg2-O3βATP	2.67	2.48*	3.26*	2.96	2.89	2.52	2.06	2.06	2.27	2.32
Mg2-O2γATP	2.52	2.42	2.19	2.00	2.00	2.02	2.16	1.97*$^{i=F1}$	2.27*^{OH2}	1.99
Mg2-Oδ2Asp184	2.48	2.27	2.22	2.10	2.12	2.14	2.14	2.00	2.30	2.26
Mg2-Oδ1Asn171	2.39	2.22	2.19	2.01	2.00	2.02	2.16	2.11	2.32	2.37
Mg2-OH2XWAT002	2.06	2.04	2.27	2.12	2.11	2.11	2.17	2.18	2.24	2.13

Table A2. For the PKAc-Mg_2ATP-SP20 model, selected QM(B3LYP/6-31+G(d))/CHARMM bond distances (Å), bond angles (deg), and dihedrals (deg) in the optimized reactants ($Ra3_S$), transition state ($TSa3_S$), and products ($Pa3_S$) for the associative mechanism with the O3γATP as the proton acceptor (O3γATP-associative path). Comparison with values from X-ray crystallographic structures characterizing different stages of the phosphoryl-transfer mechanism catalyzed by the PKAc with SP20 as substrate and Mg^{2+} ions.

Active core geometric features	4DH3[164]	4DH8[164]	4IAC[76]	$i_{model}S_{Mg}$	$Ra3_S$	$TSa3_S$	$Pa3_S$	1L3R[79]	4IAF[76]	4DH5[164]
O3βATP-PγATP	1.68	1.74*	1.83*	1.70	1.70	1.78	2.89	2.31*	4.06	3.55
PγATP-OγSer21	3.80*	4.09*	3.49	3.76	3.27	2.26	1.64	2.27*	1.63	1.67*
OγSer21-HγSer21	---	---	---	0.98	0.98	1.64	2.50	---	---	---
O1γATP-HγSer21	---	---	---	3.12	3.30	3.00	3.37	---	---	---
O2γATP-HγSer21	---	---	---	3.52	2.96	2.77	2.97	---	---	---
O3γATP-HγSer21	---	---	---	1.81	2.04	1.01	0.99	---	---	---
OγSer21-Oδ2Asp166	4.00*	3.94*	4.40	4.28	3.40	3.63	3.54	2.48	4.67	2.70*
Oδ2Asp166-O2γATP	3.40	3.47	3.81	3.93	4.03	4.05	3.75	3.31*	3.34*	3.09
Oδ2Asp166-O3γATP	4.21	4.16	4.31	4.49	4.06	4.05	3.73	3.36*	5.38* 5.78*	3.53
$angle_{O3\beta ATP\text{-}P\gamma ATP\text{-}O\gamma Ser21}$	160.8*	170.7*	148.2*	141.3	166.5	164.6	171.2	162.6*	159.8	168.0*
$angle_{O\gamma Ser21\text{-}H\gamma Ser21\text{-}O1\gamma ATP}$	---	---	---	150.3	94.7	65.7	49.3	---		---
$angle_{O\gamma Ser21\text{-}H\gamma Ser21\text{-}O3\gamma ATP}$	---	---	---	153.6	145.2	127.5	80.3	---	---	---
$d._{Ser21(N\text{-}C\alpha\text{-}C\beta\text{-}O\gamma)}$	---	---	64.0	68.7	-69.9	-59.2	-48.7	-64.8	74.0	---
$d._{Asp166(C\beta\text{-}C\gamma\text{-}O\delta2)\text{-}O2\gamma ATP}$	158.6	162.1	160.0	167.2	159.0	154.1	148.6	117.8*	-119.2*	129.34
$d._{Asp166(C\beta\text{-}C\gamma\text{-}O\delta2)\text{-}O3\gamma ATP}$	-117.2	-107.6	-105.5	-96.1	-101.1	-97.7	-115.0	-88.4*	-152.5* -104.8*	-140.6
$d._{phiAsp166}$	-141.3	-148.0	-149.2	-128.2	-130.3	-132.5	-132.9	-148.5	-148.2	-142.4
$d._{psiAsp166}$	48.6	47.6	43.5	68.2	67.6	67.2	61.9	44.2	39.9	40.7

	4.05*$^{i=1}$	3.98*$^{i=1}$	3.29$^{i=1}$	4.00$^{i=1}$	3.52$^{i=1}$	2.77$^{i=1}$	2.57$^{i=1}$	3.08*$^{i=F3}$	2.63*	2.75*$^{i=1}$
OγSer21-OiγATP	3.69*$^{i=2}$	4.03*$^{i=2}$	4.07$^{i=2}$	4.36$^{i=2}$	3.39$^{i=2}$	2.64$^{i=2}$	2.49$^{i=2}$	2.81*$^{i=F1}$	2.53*	2.72*$^{i=2}$
	3.17*$^{i=3}$	3.53*$^{i=3}$	2.67$^{i=3}$	2.73$^{i=3}$	2.90$^{i=3}$	2.40$^{i=3}$	2.53$^{i=3}$	2.78*$^{i=F2}$	2.66*	2.59*$^{i=3}$
Catalytic core interaction distances	4DH3[164]	4DH8[164]	4IAC[76]	$i_{model}S_{Mg}$	$Ra3_S$	$TSa3_S$	$Pa3_S$	1L3R[79]	4IAF[76]	4DH5[164]
Oγ1Thr201-Oδ1Asp166	2.91	2.85	2.62	2.68	2.73	2.75	2.74	2.76	3.13	3.28
Oγ1Thr201-NζLys168	3.16	2.78	2.99	2.79	2.77	2.72	2.76	2.86	2.80	2.92
Oγ1Thr201-OγSer21	4.26*	4.06*	5.27	4.63	3.28	4.03	3.43	3.56	5.59	3.70*
Oδ2Asp166-PγATP	4.39	4.47	4.66	4.83	4.66	4.61	4.01	3.60*	4.63	3.22
Oδ2Asp166-OH2XWAT1003	2.85	2.74	2.53	2.69	2.68	2.67	2.60	2.47	2.82	2.81
Oδ2Asp166-Nδ2Asn171	3.15	2.97	3.05	2.91	2.92	2.97	3.00	3.29	3.06	3.07
Oδ2Asp166-NζLys168	4.03	3.62	3.46	3.63	3.84	3.88	4.20	4.26	4.12	4.46
Oδ1Asp166-NζLys168	4.17	3.84	4.86	4.34	4.27	4.24	4.34	4.04	4.02	4.26
NζLys168-OγSer21	4.53*	4.23*	4.81	4.70	2.97	2.73	2.96	3.12	5.20	2.90*
NζLys168-PγATP	4.24	4.09	3.98	3.82	3.92	3.89	3.52	3.82*	5.20	3.32
NζLys168-O2γATP	2.87	2.78	2.77	2.83	2.87	3.05	2.83	2.92*$^{i=F1}$	4.73*	3.32
NζLys168-O1γATP	4.55	4.24	4.08	3.88	4.24	4.41	4.35	4.12*$^{i=F3}$	4.82* 6.78*	3.38
Nδ2Asn171-O2γATP	4.37	4.23	4.53	4.37	4.41	4.31	4.02	3.11*$^{i=F1}$	> 5	3.05
NζLys72-O1αATP	2.64	2.84	2.87	2.72	2.73	2.71	2.72	2.76	2.88	2.83
NζLys72-O1βATP	2.80	2.95	3.13	2.84	2.78	2.77	2.74	2.78	2.85	3.11
NζLys72-Oε2Glu91	2.72	2.71	2.72	2.66	2.65	2.65	2.66	2.79	2.67	2.55
OγSer53-O1γATP	3.46	3.68	5.42	5.69	5.12	5.04	4.92	3.47*$^{i=F3}$	2.77*	4.01
OγSer53-OγSer21	4.51*	4.51*	5.55	5.70	6.55	6.25	6.36	5.20	3.02	5.23*
OγSer53-OSer21	2.87*	2.72*	5.14	4.29	4.26	4.10	4.17	2.62	2.92	3.99~

OγSer53-NSer21	3.51*	3.41*	6.35	5.73	5.43	5.37	5.41	3.23	3.67	3.35~
NSer53-O2βATP	3.24	3.48	4.16	4.23	4.22	4.19	4.22	3.31	3.98	3.95
NSer53-O1γATP	2.55	2.83	5.63	5.41	4.91	4.82	4.96	2.67*$^{i=F3}$	2.94*	4.43
NPhe54-O2βATP	3.02	3.16	5.35	5.45	5.37	5.39	5.40	2.94	4.50	3.82
NGly55-O2βATP	3.08	3.04	5.82	5.95	5.88	5.94	5.86	3.06	5.30	3.68
Oδ1Asp24^{SP20}-Cε1His87	7.67	7.49	6.24	5.28	5.25	5.23	5.24	6.68	> 11	3.08
Oδ1Asp24^{SP20}-Nε2Gly84	4.79	4.66	3.58	2.80	2.81	2.80	2.81	6.56	> 10	3.17
Oε1Gly84-Nδ1His87	2.80	2.83	2.67	2.70	2.71	2.71	2.71	2.85	2.78	2.72
O2pThr197-Nε2His87	2.63	2.71	2.64	2.66	2.64	2.64	2.64	2.72	2.75	2.71
Mg^{2+} ions coordination sphere	4DH3^{164}	4DH8^{164}	4IAC^{76}	$i_{model}S_{Mg}$	$Ra3_S$	$TSa3_S$	$Pa3_S$	1L3R^{79}	4IAF^{76}	4DH5^{164}
Mg1-O1βATP	2.39	2.14	2.20	2.08	2.09	2.05	1.97	2.13	2.27	2.23
Mg1-O3γATP	2.25	2.17	2.25	2.16	2.05	2.12	2.29	1.97*$^{i=F2}$	2.29*	2.14
Mg1-Oδ1Asp184	2.60	2.45	2.40	2.21	2.15	2.09	2.09	2.22	2.44	2.67
Mg1-Oδ2Asp184	2.35	2.31	2.29	2.20	2.24	2.23	2.20	2.32	2.27	2.40
Mg1-OH2XWAT1003	2.08	2.10	2.17	2.07	2.11	2.10	2.23	2.36	2.39	2.27
Mg1-OH2XWAT1001	2.10	2.11	2.16	2.02	2.07	2.06	2.06	2.12	2.36	2.13
Mg2-O2αATP	2.43	2.09	2.18	1.99	2.00	1.99	2.05	1.88	2.35	2.40
Mg2-O3βATP	2.67	2.48*	3.26*	2.96	2.64	2.48	2.05	2.06	2.27	2.32
Mg2-O2γATP	2.52	2.42	2.19	2.00	2.04	2.04	2.17	1.97*$^{i=F1}$	2.27*^{OH2}	1.99
Mg2-Oδ2Asp184	2.48	2.27	2.22	2.10	2.14	2.17	2.18	2.00	2.30	2.26
Mg2-Oδ1Asn171	2.39	2.22	2.19	2.01	2.03	2.04	2.19	2.11	2.32	2.37
Mg2-OH2XWAT002	2.06	2.04	2.27	2.12	2.11	2.11	2.16	2.18	2.24	2.13

Table A3. For the PKAc-Mg_2ATP-SP20 model, selected QM(B3LYP/6-31+G(d))/CHARMM bond distances (Å), bond angles (deg), and dihedrals (deg) in the optimized reactants (Rd_S), phosphoryl-transfer transition state ($TSd1P_S$), proton shift intermediate ($Id1_S$), phosphoryl-transfer products ($Pd1_S$), protonated Asp166 side chain-rotation transition state ($TSd2T_S$), proton-transfer transition state ($TSd2H_S$), and proton-transfer products ($Pd2_S$) for the dissociative mechanism with the O2γATP as the final proton acceptor (O2γATP-dissociative path). Comparison with values from X-ray crystallographic structures characterizing different stages of the phosphoryl-transfer mechanism catalyzed by the PKAc with SP20 as substrate and Mg^{2+} ions.

Active core geometric features	4DH3	4DH8	4IAC[76]	$i_{model}S_{Mg}$	Rd_S	$TSd1P_S$	$Id1_S$	$Pd1_S$	$TSd2T_S$	$TSd2H_S$	$Pd2_S$	1L3R	4IAF	4DH5
O3βATP-PγATP	1.68	1.74*	1.83*	1.70	1.76	2.31	2.89	3.05	3.05	3.47	3.39	2.31*	4.06	3.55
PγATP-OγSer21	3.80*	4.09*	3.49	3.76	3.36	2.36	1.87	1.74	1.69	1.66	1.64	2.27*	1.63	1.67*
OγSer21-HγSer21	---	---	---	0.98	0.99	1.00	1.12	1.67	2.31	2.76	2.57	---	---	---
Oδ2Asp166-HγSer21	---	---	---	4.23	1.81	1.71	1.35	1.02	0.99	1.11	1.67	---	---	---
O1γATP-HγSer21	---	---	---	3.12	4.10	3.62	3.57	4.02	4.19	3.83	3.44	---	---	---
O2γATP-HγSer21	---	---	---	3.52	3.26	2.82	2.76	2.93	2.37	1.40	1.01	---	---	---
O3γATP-HγSer21	---	---	---	1.81	3.20	2.92	2.83	2.95	3.10	2.98	2.83	---	---	---
OγSer21-Oδ2Asp166	4.00*	3.94*	4.40	4.28	2.80	2.71	2.46	2.66	3.17	3.49	3.57	2.48	4.67	2.70*
Oδ2Asp166-O2γATP	3.40	3.47	3.81	3.93	3.82	3.59	3.47	3.52	3.11	2.49	2.68	3.31*	3.34*	3.09
Oδ2Asp166-O3γATP	4.21	4.16	4.31	4.49	3.81	3.61	3.39	3.33	3.50	3.53	3.80	3.36*	5.38* 5.78*	3.53
$angle_{O3\beta ATP\text{-}P\gamma ATP\text{-}O\gamma Ser21}$	160.8*	170.7*	148.2*	141.3	167.7	168.4	166.2	166.3	170.8	178.3	172.0	162.6*	159.8	168.0*
$angle_{O\gamma Ser21\text{-}H\gamma Ser21\text{-}O\delta 2Asp166}$	---	---	---	86.4	173.3	172.0	169.3	162.2	145.3	123.0	113.1	---	---	---
$angle_{O\delta 2Asp166\text{-}H\gamma Ser21\text{-}O2\gamma ATP}$	---	---	---	60.2	93.6	101.6	110.8	117.8	130.8	164.4	172.5	---	---	---
$angle_{O\delta 2Asp166\text{-}H\gamma Ser21\text{-}O3\gamma ATP}$	---	---	---	86.2	94.9	99.0	102.4	102.9	105.4	110.9	112.5	---	---	---
$d._{Ser21(N\text{-}C\alpha\text{-}C\beta\text{-}O\gamma)}$	---	---	64.0	68.7	-56.8	-48.1	-42.9	-43.2	-60.7	-73.5	-70.1	-64.8	74.0	---
$d._{Asp166(C\beta\text{-}C\gamma\text{-}O\delta 2)\text{-}O2\gamma ATP}$	158.6	162.1	160.0	167.2	119.6	118.4	118.7	124.5	145.8	172.4	175.0	117.8*	-119.2*	129.34
$d._{Asp166(C\beta\text{-}C\gamma\text{-}O\delta 2)\text{-}O3\gamma ATP}$	-117.2	-107.6	-105.5	-96.1	49.4	69.4	85.8	110.2	-122.7	-111.9	-98.5	-88.4*	-152.5* -104.8*	-140.6
$d._{phiAsp166}$	-141.3	-148.0	-149.2	-128.2	-97.4	-98.1	-94.8	-99.2	-99.6	-100.6	-101.4	-148.5	-148.2	-142.4

$d._{psiAsp166}$	48.6	47.6	43.5	68.2	70.9	67.1	65.9	63.9	63.2	64.9	66.4	44.2	39.9	40.7
	4.05*$^{i=1}$	3.98*$^{i=1}$	3.29$^{i=1}$	4.00$^{i=1}$	3.60$^{i=1}$	2.83$^{i=1}$	2.61$^{i=1}$	2.57$^{i=1}$	2.55$^{i=1}$	2.56$^{i=1}$	2.46$^{i=1}$	3.08*$^{i=F3}$	2.63*	2.75*$^{i=1}$
OγSer21-OiγATP	3.69*$^{i=2}$	4.03*$^{i=2}$	4.07$^{i=2}$	4.36$^{i=2}$	3.29$^{i=2}$	2.72$^{i=2}$	2.54$^{i=2}$	2.51$^{i=2}$	2.50$^{i=2}$	2.46$^{i=2}$	2.59$^{i=2}$	2.81*$^{i=F1}$	2.53*	2.72*$^{i=2}$
	3.17*$^{i=3}$	3.53*$^{i=3}$	2.67$^{i=3}$	2.73$^{i=3}$	3.31$^{i=3}$	2.80$^{i=3}$	2.61$^{i=3}$	2.57$^{i=3}$	2.57$^{i=3}$	2.59$^{i=3}$	2.56$^{i=3}$	2.78*$^{i=F2}$	2.66*	2.59*$^{i=3}$
Catalytic core interaction distances	4DH3	4DH8	4IAC^{76}	$i_{model}S_{Mg}$	Rd_S	$TSd1P_S$	$Id1_S$	$Pd1_S$	$TSd2T_S$	$TSd2H_S$	$Pd2_S$	1L3R	4IAF	4DH5
Oγ1Thr201-Oδ1Asp166	2.91	2.85	2.62	2.68	2.75	2.71	2.72	2.76	2.80	2.83	2.76	2.76	3.13	3.28
Oγ1Thr201-NζLys168	3.16	2.78	2.99	2.79	2.81	2.77	2.79	2.82	2.80	2.76	2.74	2.86	2.80	2.92
Oγ1Thr201-OγSer21	4.26*	4.06*	5.27	4.63	3.04	3.20	3.19	3.22	3.50	3.85	3.87	3.56	5.59	3.70*
Oδ2Asp166-PγATP	4.39	4.47	4.66	4.83	4.33	3.85	3.44	3.45	3.52	3.39	3.63	3.60*	4.63	3.22
Oδ2Asp166-OH2XWAT1003	2.85	2.74	2.53	2.69	2.68	2.73	2.81	2.89	2.90	2.84	2.76	2.47	2.82	2.81
Oδ2Asp166-Nδ2Asn171	3.15	2.97	3.05	2.91	3.50	3.54	3.66	3.60	3.11	3.03	2.95	3.29	3.06	3.07
Oδ2Asp166-NζLys168	4.03	3.62	3.46	3.63	4.06	4.20	4.32	4.43	4.26	4.22	4.12	4.26	4.12	4.46
Oδ1Asp166-NζLys168	4.17	3.84	4.86	4.34	4.33	4.31	4.25	4.27	4.18	4.03	4.13	4.04	4.02	4.26
NζLys168-OγSer21	4.53*	4.23*	4.81	4.70	2.78	2.96	3.12	3.10	3.26	3.79	3.78	3.12	5.20	2.90*
NζLys168-PγATP	4.24	4.09	3.98	3.82	3.94	3.72	3.56	3.52	3.58	3.67	3.81	3.82*	5.20	3.32
NζLys168-O2γATP	2.87	2.78	2.77	2.83	2.92	2.85	2.79	2.75	2.74	2.67	2.74	2.92*$^{i=F1}$	4.73*	3.32
NζLys168-O1γATP	4.55	4.24	4.08	3.88	4.10	3.96	3.87	3.92	3.98	3.86	3.99	4.12*$^{i=F3}$	4.82* 6.78*	3.38
Nδ2Asn171-O2γATP	4.37	4.23	4.53	4.37	4.03	3.79	3.69	3.73	3.83	3.94	4.08	3.11*$^{i=F1}$	> 5	3.05
NζLys72-O1αATP	2.64	2.84	2.87	2.72	2.72	2.72	2.73	2.73	2.74	2.74	2.74	2.76	2.88	2.83
NζLys72-O1βATP	2.80	2.95	3.13	2.84	2.78	2.80	2.80	2.79	2.78	2.80	2.81	2.78	2.85	3.11
NζLys72-Oε2Glu91	2.72	2.71	2.72	2.66	2.65	2.66	2.66	2.66	2.67	2.67	2.67	2.79	2.67	2.55
OγSer53-O1γATP	3.46	3.68	5.42	5.69	5.12	5.00	4.97	4.93	4.88	4.94	4.91	3.47*$^{i=F3}$	2.77*	4.01
OγSer53-OγSer21	4.51*	4.51*	5.55	5.70	6.87	6.63	6.71	6.69	6.29	5.94	5.90	5.20	3.02	5.23*

OγSer53-OSer21	2.87*	2.72*	5.14	4.29	4.21	4.17	4.21	4.20	4.15	4.17	4.20	2.62	2.92	3.99~
OγSer53-NSer21	3.51*	3.41*	6.35	5.73	5.48	5.47	5.63	5.60	5.33	5.13	5.16	3.23	3.67	3.35~
NSer53-O2βATP	3.24	3.48	4.16	4.23	4.25	4.17	4.14	4.15	4.17	4.17	4.21	3.31	3.98	3.95
NSer53-O1γATP	2.55	2.83	5.63	5.41	5.08	5.23	5.32	5.31	5.19	5.33	5.26	2.67*$^{i=F3}$	2.94*	4.43
NPhe54-O2βATP	3.02	3.16	5.35	5.45	5.41	5.39	5.36	5.35	5.38	5.48	5.52	2.94	4.50	3.82
NGly55-O2βATP	3.08	3.04	5.82	5.95	5.91	5.96	5.91	5.88	5.90	6.04	6.06	3.06	5.30	3.68
Oδ1Asp24^{SP20}-Cε1His87	7.67	7.49	6.24	5.28	5.24	5.24	5.24	5.23	5.24	5.25	5.25	6.68	> 11	3.08
Oδ1Asp24^{SP20}-Nε2Gly84	4.79	4.66	3.58	2.80	2.82	2.82	2.82	2.82	2.81	2.82	2.82	6.56	> 10	3.17
Oε1Gly84-Nδ1His87	2.80	2.83	2.67	2.70	2.71	2.71	2.71	2.71	2.71	2.71	2.71	2.85	2.78	2.72
O2pThr197-Nε2His87	2.63	2.71	2.64	2.66	2.64	2.64	2.64	2.64	2.64	2.64	2.64	2.72	2.75	2.71
Mg^{2+} ions coordination sphere	4DH3	4DH8	4IAC^{76}	$i_{model}S_{Mg}$	Rd_S	$TSd1P_S$	$Id1_S$	$Pd1_S$	$TSd2T_S$	$TSd2H_S$	$Pd2_S$	1L3R	4IAF	4DH5
Mg1-O1βATP	2.39	2.14	2.20	2.08	2.10	2.05	2.03	2.01	2.01	2.02	2.03	2.13	2.27	2.23
Mg1-O3γATP	2.25	2.17	2.25	2.16	2.03	2.06	2.05	2.03	2.03	2.03	2.06	1.97*$^{i=F2}$	2.29*	2.14
Mg1-Oδ1Asp184	2.60	2.45	2.40	2.21	2.17	2.14	2.15	2.17	2.19	2.19	2.18	2.22	2.44	2.67
Mg1-Oδ2Asp184	2.35	2.31	2.29	2.20	2.28	2.27	2.27	2.28	2.30	2.37	2.32	2.32	2.27	2.40
Mg1-OH2XWAT1003	2.08	2.10	2.17	2.07	2.11	2.14	2.20	2.23	2.23	2.20	2.16	2.36	2.39	2.27
Mg1-OH2XWAT1001	2.10	2.11	2.16	2.02	2.11	2.11	2.12	2.13	2.13	2.13	2.12	2.12	2.36	2.13
Mg2-O2αATP	2.43	2.09	2.18	1.99	2.00	2.01	2.04	2.05	2.08	1.99	1.98	1.88	2.35	2.40
Mg2-O3βATP	2.67	2.48*	3.26*	2.96	2.40	2.16	2.05	2.04	2.03	2.01	2.02	2.06	2.27	2.32
Mg2-O2γATP	2.52	2.42	2.19	2.00	2.04	2.12	2.17	2.15	2.24	3.33	3.25	1.97*$^{i=F1}$	2.27*^{OH2}	1.99
Mg2-Oδ2Asp184	2.48	2.27	2.22	2.10	2.16	2.16	2.17	2.19	2.16	2.12	2.11	2.00	2.30	2.26
Mg2-Oδ1Asn171	2.39	2.22	2.19	2.01	2.04	2.10	2.16	2.20	2.22	2.08	2.07	2.11	2.32	2.37
Mg2-OH2XWAT002	2.06	2.04	2.27	2.12	2.11	2.14	2.18	2.18	2.16	2.13	2.12	2.18	2.24	2.13

Table A4. For the PKAc-Mg_2ATP-SP20 model, selected QM(B3LYP/6-31+G(d))/CHARMM bond distances (Å), bond angles (deg), and dihedrals (deg) in the optimized reactants (Rd_S), phosphoryl-transfer transition state ($TSd1P_S$), proton shift intermediate ($Id1_S$), phosphoryl-transfer products ($Pd1_S$), proton-transfer transition state ($TSd3H_S$), and proton-transfer products ($Pd3_S$) for the dissociative mechanism with the O3γATP as the final proton acceptor (O3γATP-dissociative path). Comparison with values from X-ray crystallographic structures characterizing different stages of the phosphoryl-transfer mechanism catalyzed by the PKAc with SP20 as substrate and Mg^{2+} ions.

Active core geometric features	4DH3[164]	4DH8[164]	4IAC[76]	$i_{model}S_{Mg}$	Rd_S	$TSd1P_S$	$Id1_S$	$Pd1_S$	$TSd3H_S$	$Pd3_S$	1L3R[79]	4IAF[76]	4DH5[164]
O3βATP-PγATP	1.68	1.74*	1.83*	1.70	1.76	2.31	2.89	3.05	3.21	3.15	2.31*	4.06	3.55
PγATP-OγSer21	3.80*	4.09*	3.49	3.76	3.36	2.36	1.87	1.74	1.66	1.64	2.27*	1.63	1.67*
OγSer21-HγSer21	---	---	---	0.98	0.99	1.00	1.12	1.67	2.69	2.56	---	---	---
Oδ2Asp166-HγSer21	---	---	---	4.23	1.81	1.71	1.35	1.02	1.14	1.71	---	---	---
O1γATP-HγSer21	---	---	---	3.12	4.10	3.62	3.57	4.02	3.72	3.39	---	---	---
O2γATP-HγSer21	---	---	---	3.52	3.26	2.82	2.76	2.93	2.86	2.72	---	---	---
O3γATP-HγSer21	---	---	4.40	1.81	3.20	2.92	2.83	2.95	1.33	1.00	---	---	---
OγSer21-Oδ2Asp166	4.00*	3.94*	3.81	4.28	2.80	2.71	2.46	2.66	3.56	3.46	2.48	4.67	2.70*
Oδ2Asp166-O2γATP	3.40	3.47	4.31	3.93	3.82	3.59	3.47	3.52	3.68	3.64	3.31*	3.34*	3.09
Oδ2Asp166-O3γATP	4.21	4.16	148.2*	4.49	3.81	3.61	3.39	3.33	2.43	2.71	3.36*	5.38* 5.78*	3.53
$angle_{O3\beta ATP\text{-}P\gamma ATP\text{-}O\gamma Ser21}$	160.8*	170.7*	---	141.3	167.7	168.4	166.2	166.3	161.9	167.4	162.6*	159.8	168.0*
$angle_{O\gamma Ser21\text{-}H\gamma Ser21\text{-}O\delta 2Asp166}$	---	---	---	86.4	173.3	172.0	169.3	162.2	131.7	106.5	---	---	---
$angle_{O\delta 2Asp166\text{-}H\gamma Ser21\text{-}O2\gamma ATP}$	---	---	---	60.2	93.6	101.6	110.8	117.8	128.4	108.5	---	---	---
$angle_{O\delta 2Asp166\text{-}H\gamma Ser21\text{-}O3\gamma ATP}$	---	---	---	86.2	94.9	99.0	102.4	102.9	159.0	175.0	---	---	---
$d._{Ser21(N\text{-}C\alpha\text{-}C\beta\text{-}O\gamma)}$	---	---	64.0	68.7	-56.8	-48.1	-42.9	-43.2	-45.7	-45.3	-64.8	74.0	---
$d._{Asp166(C\beta\text{-}C\gamma\text{-}O\delta 2)\text{-}O2\gamma ATP}$	158.6	162.1	160.0	167.2	119.6	118.4	118.7	124.5	145.7	141.3	117.8*	-119.2*	129.34
$d._{Asp166(C\beta\text{-}C\gamma\text{-}O\delta 2)\text{-}O3\gamma ATP}$	-117.2	-107.6	-105.5	-96.1	49.4	69.4	85.8	110.2	-176.6	-171.6	-88.4*	-152.5* -104.8*	-140.6
$d._{phiAsp166}$	-141.3	-148.0	-149.2	-128.2	-97.4	-98.1	-94.8	-99.2	-101.4	-102.3	-148.5	-148.2	-142.4

$d._{psiAsp166}$	48.6	47.6	43.5	68.2	70.9	67.1	65.9	63.9	59.3	61.5	44.2	39.9	40.7
	4.05*$^{i=1}$	3.98*$^{i=1}$	3.29$^{i=1}$	4.00$^{i=1}$	3.60$^{i=1}$	2.83$^{i=1}$	2.61$^{i=1}$	2.57$^{i=1}$	2.54$^{i=1}$	2.54$^{i=1}$	3.08*$^{i=F3}$	2.63*	2.75*$^{i=1}$
OγSer21-OiγATP	3.69*$^{i=2}$	4.03*$^{i=2}$	4.07$^{i=2}$	4.36$^{i=2}$	3.29$^{i=2}$	2.72$^{i=2}$	2.54$^{i=2}$	2.51$^{i=2}$	2.54$^{i=2}$	2.53$^{i=2}$	2.81*$^{i=F1}$	2.53*	2.72*$^{i=2}$
	3.17*$^{i=3}$	3.53*$^{i=3}$	2.67$^{i=3}$	2.73$^{i=3}$	3.31$^{i=3}$	2.80$^{i=3}$	2.61$^{i=3}$	2.57$^{i=3}$	2.54$^{i=3}$	2.54$^{i=3}$	2.78*$^{i=F2}$	2.66*	2.59*$^{i=3}$
Catalytic core interaction distances	4DH3^{164}	4DH8^{164}	4IAC^{76}	$i_{model}S_{Mg}$	Rd_S	$TSd1P_S$	$Id1_S$	$Pd1_S$	$TSd3H_S$	$Pd3_S$	1L3R^{79}	4IAF^{76}	4DH5^{164}
Oγ1Thr201-Oδ1Asp166	2.91	2.85	2.62	2.68	2.75	2.71	2.72	2.76	2.94	2.83	2.76	3.13	3.28
Oγ1Thr201-NζLys168	3.16	2.78	2.99	2.79	2.81	2.77	2.79	2.82	2.80	2.77	2.86	2.80	2.92
Oγ1Thr201-OγSer21	4.26*	4.06*	5.27	4.63	3.04	3.20	3.19	3.22	3.12	3.18	3.56	5.59	3.70*
Oδ2Asp166-PγATP	4.39	4.47	4.66	4.83	4.33	3.85	3.44	3.45	3.46	3.55	3.60*	4.63	3.22
Oδ2Asp166-OH2XWAT1003	2.85	2.74	2.53	2.69	2.68	2.73	2.81	2.89	2.69	2.70	2.47	2.82	2.81
Oδ2Asp166-Nδ2Asn171	3.15	2.97	3.05	2.91	3.50	3.54	3.66	3.60	3.34	3.27	3.29	3.06	3.07
Oδ2Asp166-NζLys168	4.03	3.62	3.46	3.63	4.06	4.20	4.32	4.43	4.95	4.69	4.26	4.12	4.46
Oδ1Asp166-NζLys168	4.17	3.84	4.86	4.34	4.33	4.31	4.25	4.27	4.26	4.31	4.04	4.02	4.26
NζLys168-OγSer21	4.53*	4.23*	4.81	4.70	2.78	2.96	3.12	3.10	2.97	2.99	3.12	5.20	2.90*
NζLys168-PγATP	4.24	4.09	3.98	3.82	3.94	3.72	3.56	3.52	3.51	3.50	3.82*	5.20	3.32
NζLys168-O2γATP	2.87	2.78	2.77	2.83	2.92	2.85	2.79	2.75	2.74	2.78	2.92*$^{i=F1}$	4.73*	3.32
NζLys168-O1γATP	4.55	4.24	4.08	3.88	4.10	3.96	3.87	3.92	4.38	4.42	4.12*$^{i=F3}$	4.82* 6.78*	3.38
Nδ2Asn171-O2γATP	4.37	4.23	4.53	4.37	4.03	3.79	3.69	3.73	3.81	3.89	3.11*$^{i=F1}$	> 5	3.05
NζLys72-O1αATP	2.64	2.84	2.87	2.72	2.72	2.72	2.73	2.73	2.75	2.74	2.76	2.88	2.83
NζLys72-O1βATP	2.80	2.95	3.13	2.84	2.78	2.80	2.80	2.79	2.88	2.86	2.78	2.85	3.11
NζLys72-Oε2Glu91	2.72	2.71	2.72	2.66	2.65	2.66	2.66	2.66	2.66	2.66	2.79	2.67	2.55
OγSer53-O1γATP	3.46	3.68	5.42	5.69	5.12	5.00	4.97	4.93	4.82	4.77	3.47*$^{i=F3}$	2.77*	4.01
OγSer53-OγSer21	4.51*	4.51*	5.55	5.70	6.87	6.63	6.71	6.69	6.55	6.49	5.20	3.02	5.23*

OγSer53-OSer21	2.87*	2.72*	5.14	4.29	4.21	4.17	4.21	4.20	4.21	4.21	2.62	2.92	3.99~
OγSer53-NSer21	3.51*	3.41*	6.35	5.73	5.48	5.47	5.63	5.60	5.45	5.44	3.23	3.67	3.35~
NSer53-O2βATP	3.24	3.48	4.16	4.23	4.25	4.17	4.14	4.15	4.20	4.21	3.31	3.98	3.95
NSer53-O1γATP	2.55	2.83	5.63	5.41	5.08	5.23	5.32	5.31	5.22	5.14	2.67*$^{i=F3}$	2.94*	4.43
NPhe54-O2βATP	3.02	3.16	5.35	5.45	5.41	5.39	5.36	5.35	5.42	5.42	2.94	4.50	3.82
NGly55-O2βATP	3.08	3.04	5.82	5.95	5.91	5.96	5.91	5.88	5.93	5.92	3.06	5.30	3.68
Oδ1Asp24^{SP20}-Cε1His87	7.67	7.49	6.24	5.28	5.24	5.24	5.24	5.23	5.24	5.25	6.68	> 11	3.08
Oδ1Asp24^{SP20}-Nε2Gly84	4.79	4.66	3.58	2.80	2.82	2.82	2.82	2.82	2.81	2.81	6.56	> 10	3.17
Oε1Gly84-Nδ1His87	2.80	2.83	2.67	2.70	2.71	2.71	2.71	2.71	2.71	2.71	2.85	2.78	2.72
O2pThr197-Nε2His87	2.63	2.71	2.64	2.66	2.64	2.64	2.64	2.64	2.64	2.64	2.72	2.75	2.71
Mg^{2+} ions coordination sphere	4DH3^{164}	4DH8^{164}	4IAC^{76}	$i_{model}S_{Mg}$	Rd_S	$TSd1P_S$	$Id1_S$	$Pd1_S$	$TSd3H_S$	$Pd3_S$	1L3R^{79}	4IAF^{76}	4DH5^{164}
Mg1-O1βATP	2.39	2.14	2.20	2.08	2.10	2.05	2.03	2.01	2.02	2.00	2.13	2.27	2.23
Mg1-O3γATP	2.25	2.17	2.25	2.16	2.03	2.06	2.05	2.03	2.20	2.32	1.97*$^{i=F2}$	2.29*	2.14
Mg1-Oδ1Asp184	2.60	2.45	2.40	2.21	2.17	2.14	2.15	2.17	2.14	2.11	2.22	2.44	2.67
Mg1-Oδ2Asp184	2.35	2.31	2.29	2.20	2.28	2.27	2.27	2.28	2.28	2.25	2.32	2.27	2.40
Mg1-OH2XWAT1003	2.08	2.10	2.17	2.07	2.11	2.14	2.20	2.23	2.19	2.17	2.36	2.39	2.27
Mg1-OH2XWAT1001	2.10	2.11	2.16	2.02	2.11	2.11	2.12	2.13	2.11	2.09	2.12	2.36	2.13
Mg2-O2αATP	2.43	2.09	2.18	1.99	2.00	2.01	2.04	2.05	2.07	2.05	1.88	2.35	2.40
Mg2-O3βATP	2.67	2.48*	3.26*	2.96	2.40	2.16	2.05	2.04	2.03	2.04	2.06	2.27	2.32
Mg2-O2γATP	2.52	2.42	2.19	2.00	2.04	2.12	2.17	2.15	2.22	2.24	1.97*$^{i=F1}$	2.27*^{OH2}	1.99
Mg2-Oδ2Asp184	2.48	2.27	2.22	2.10	2.16	2.16	2.17	2.19	2.19	2.20	2.00	2.30	2.26
Mg2-Oδ1Asn171	2.39	2.22	2.19	2.01	2.04	2.10	2.16	2.20	2.18	2.16	2.11	2.32	2.37
Mg2-OH2XWAT002	2.06	2.04	2.27	2.12	2.11	2.14	2.18	2.18	2.17	2.17	2.18	2.24	2.13

Table A5. For the PKAc(4IAC)-Mg_2ATP-Kemptide model, selected QM(B3LYP/6-31+G(d))/CHARMM bond distances (Å), bond angles (deg), and dihedrals (deg) in the optimized reactants ($Ra1_K$), transition state ($TSa1_K$), and products ($Pa1_K$) for the associative mechanism with the O1γATP as the proton acceptor (O1γATP-associative path).

Active core geometric features	$i_{model}K_{Mg}$	$Ra1_K$	$TSa1_K$	$Pa1_K$
O3βATP-PγATP	1.68	1.76	1.78	2.92
PγATP-OγSer21	3.62	2.85	2.28	1.65
OγSer21-HγSer21	0.99	1.00	1.64	2.86
O1γATP-HγSer21	3.03	1.77	1.02	0.99
$angle_{O3\beta ATP\text{-}P\gamma ATP\text{-}O\gamma Ser21}$	137.5	177.1	169.1	169.2
$angle_{O\gamma Ser21\text{-}H\gamma Ser21\text{-}O1\gamma ATP}$	112.4	147.4	128.9	62.6
$dihedral_{O\gamma Ser21\text{-}P\gamma ATP\text{-}O1\gamma ATP\text{-}H\gamma Ser21}$	4.0	6.32	4.13	72.0
Catalytic core interaction distances	$i_{model}K_{Mg}$	$Ra1_K$	$TSa1_K$	$Pa1_K$
Oγ1Thr201-Oδ1Asp166	2.70	2.73	2.74	2.73
Oγ1Thr201-NζLys168	2.82	2.73	2.73	2.72
Oγ1Thr201-OγSer21	5.10	3.93	4.16	3.87
Oδ2Asp166-OγSer21	4.48	3.87	4.05	3.35
Oδ2Asp166-PγATP	4.60	4.74	4.51	3.97
Oδ2Asp166-OH2XWAT1003	2.67	2.69	2.67	2.68
Oδ2Asp166-Nδ2Asn171	3.01	2.93	2.94	3.01
Oδ2Asp166-NζLys168	3.84	3.90	3.98	4.01
Oδ1Asp166-NζLys168	4.41	4.34	4.40	4.42
NζLys168-OγSer21	4.91	2.82	2.66	2.89
NζLys168-PγATP	3.74	4.02	3.93	3.55
NζLys168-O2γATP	2.80	3.17	3.14	3.03
NζLys168-O1γATP	3.74	3.94	4.08	3.91
Nδ2Asn171-O2γATP	4.45	4.35	3.24	4.04
NζLys72-O1αATP	2.75	2.75	2.74	2.76
NζLys72-O1βATP	2.86	2.83	2.82	2.82
NζLys72-Oε2Glu91	2.70	2.71	2.70	2.72
OγSer53-O1γATP	5.98	6.26	6.36	6.24
NSer53-O2βATP	4.37	4.81	4.84	4.89
NPhe54-O2βATP	5.42	5.82	5.90	5.99
NGly55-O2βATP	5.64	5.77	5.92	5.98
Mg^{2+} ions coordination sphere	$i_{model}K_{Mg}$	$Ra1_K$	$TSa1_K$	$Pa1_K$
Mg1-O1βATP	2.06	2.09	2.09	2.03
Mg1-O3γATP	2.06	2.02	2.07	2.12
Mg1-Oδ1Asp184	2.21	2.21	2.20	2.24
Mg1-Oδ2Asp184	2.18	2.16	2.17	2.13
Mg1-OH2XWAT1003	2.04	2.07	2.06	2.10
Mg1-OH2XWAT1001	2.05	2.10	2.09	2.10
Mg2-O2αATP	1.99	2.01	2.02	2.08
Mg2-O3βATP	3.09	2.79	2.50	2.05
Mg2-O2γATP	2.01	2.00	2.01	2.14
Mg2-Oδ2Asp184	2.11	2.12	2.13	2.14
Mg2-Oδ1Asn171	2.01	2.02	2.02	2.17
Mg2-OH2XWAT1002	2.10	2.10	2.10	2.11

Table A6. For the PKAc(4IAC)-Mg_2ATP-Kemptide model, selected QM(B3LYP/6-31+G(d))/CHARMM bond distances (Å), bond angles (deg), and dihedrals (deg) in the optimized reactants ($Ra3_K$), transition state ($TSa3_K$), and products ($Pa3_K$) for the associative mechanism with the O3γATP as the proton acceptor (O3γATP-associative path).

Active core geometric features	$i_{model}K_{Mg}$	$Ra3_K$	$TSa3_K$	$Pa3_K$
O3βATP-PγATP	1.68	1.70	1.82	3.02
PγATP-OγSer21	3.62	3.43	2.25	1.65
OγSer21-HγSer21	0.99	0.99	1.72	2.31
O3γATP-HγSer21	1.73	1.78	1.01	1.00
$angle_{O3\beta ATP\text{-}P\gamma ATP\text{-}O\gamma Ser21}$	137.5	147.1	161.9	161.6
$angle_{O\gamma Ser21\text{-}H\gamma Ser21\text{-}O3\gamma ATP}$	170.5	169.0	119.5	84
$dihedral_{O\gamma Ser21\text{-}P\gamma ATP\text{-}O3\gamma ATP\text{-}H\gamma Ser21}$	0.2	1.3	-4.1	-28.6
Catalytic core interaction distances	$i_{model}K_{Mg}$	$Ra3_K$	$TSa3_K$	$Pa3_K$
Oγ1Thr201-Oδ1Asp166	2.70	2.70	2.73	2.74
Oγ1Thr201-NζLys168	2.82	2.83	2.79	2.82
Oγ1Thr201-OγSer21	5.10	5.00	4.75	4.52
Oδ2Asp166-OγSer21	4.48	4.49	4.24	3.60
Oδ2Asp166-PγATP	4.60	4.56	4.53	3.91
Oδ2Asp166-OH2XWAT1003	2.67	2.71	2.66	2.67
Oδ2Asp166-Nδ2Asn171	3.01	3.08	2.95	3.04
Oδ2Asp166-NζLys168	3.84	3.87	3.94	4.03
Oδ1Asp166-NζLys168	4.41	4.40	4.39	4.42
NζLys168-OγSer21	4.91	4.68	3.85	4.05
NζLys168-PγATP	3.74	3.86	3.92	3.72
NζLys168-O2γATP	2.80	2.76	2.76	2.77
NζLys168-O1γATP	3.74	4.13	4.45	4.17
Nδ2Asn171-O2γATP	4.45	4.44	4.37	4.26
NζLys72-O1αATP	2.75	2.72	2.72	2.73
NζLys72-O1βATP	2.86	2.82	2.76	2.77
NζLys72-Oε2Glu91	2.70	2.67	2.67	2.69
OγSer53-O1γATP	5.98	5.46	5.39	5.30
NSer53-O2βATP	4.37	4.42	4.53	4.49
NPhe54-O2βATP	5.42	5.36	5.48	5.49
NGly55-O2βATP	5.64	5.72	5.82	5.79
Mg^{2+} ions coordination sphere	$i_{model}K_{Mg}$	$Ra3_K$	$TSa3_K$	$Pa3_K$
Mg1-O1βATP	2.06	2.09	2.07	2.03
Mg1-O3γATP	2.06	2.07	2.14	2.19
Mg1-Oδ1Asp184	2.21	2.18	2.14	2.17
Mg1-Oδ2Asp184	2.18	2.23	2.20	2.15
Mg1-OH2XWAT1003	2.04	2.06	2.06	2.09
Mg1-OH2XWAT1001	2.05	2.05	2.05	2.09
Mg2-O2αATP	1.99	2.00	2.03	2.05
Mg2-O3βATP	3.09	2.73	2.30	2.03
Mg2-O2γATP	2.01	2.04	2.15	2.50
Mg2-Oδ2Asp184	2.11	2.12	2.12	2.10
Mg2-Oδ1Asn171	2.01	2.04	2.11	2.23
Mg2-OH2XWAT1002	2.10	2.10	2.10	2.10

Table A7. For the PKAc(4IAC)-Mg_2ATP-Kemptide model and blue potential energy profile, selected QM(B3LYP/6-31+G(d))/CHARMM bond distances (Å), bond angles (deg), and dihedrals (deg) in the optimized reactants (Rd'_K), phosphoryl-transfer transition state ($TSd1P'_K$), and phosphoryl-transfer products ($Pd1'_K$) for the O2γATP-dissociative path.

Active core geometric features	$i_{model}K_{Mg}$	Rd'_K	$TSd1P'_K$	$Pd1'_K$
O3βATP-PγATP	1.68	1.72	2.44	2.97
PγATP-OγSer21	3.62	3.60	2.21	1.76
OγSer21-HγSer21	0.99	0.99	1.02	1.57
Oδ2Asp166-HγSer21	4.11	1.76	1.60	1.03
O2γATP-HγSer21	3.74	3.45	2.75	2.90
$angle_{O3\beta ATP\text{-}P\gamma ATP\text{-}O\gamma Ser21}$	137.5	162.9	164.2	165.0
$angle_{O\gamma Ser21\text{-}H\gamma Ser21\text{-}O\delta 2Asp166}$	105.4	171.9	173.3	164.7
$angle_{O\delta 2Asp166\text{-}H\gamma Ser21\text{-}O2\gamma ATP}$	60.2	96.0	106.9	119.6
$dihedral_{Asp166(C\beta\text{-}C\gamma\text{-}O\delta 2)\text{-}O2\gamma ATP}$	173.4	136.8	128.1	130.5
Catalytic core interaction distances	$i_{model}K_{Mg}$	Rd'_K	$TSd1P'_K$	$Pd1'_K$
Oγ1Thr201-Oδ1Asp166	2.70	2.78	2.75	2.81
Oγ1Thr201-NζLys168	2.82	2.84	2.78	2.84
Oγ1Thr201-OγSer21	5.10	3.15	3.50	3.53
Oδ2Asp166-OγSer21	4.48	2.74	2.61	2.58
Oδ2Asp166-PγATP	4.60	4.59	3.79	3.51
Oδ2Asp166-OH2XWAT1003	2.67	2.67	2.71	2.81
Oδ2Asp166-NζLys168	3.84	4.06	4.30	4.54
Oδ1Asp166-NζLys168	4.41	4.36	4.33	4.35
NζLys168-OγSer21	4.91	2.76	3.01	3.17
NζLys168-PγATP	3.74	4.04	3.68	3.50
NζLys168-O2γATP	2.80	2.97	2.87	2.78
NζLys168-O1γATP	3.74	4.30	3.90	3.75
Nδ2Asn171-O2γATP	4.45	4.34	3.85	3.79
Nδ2Asn171- Oδ2Asp166	3.01	3.44	3.63	3.77
NζLys72-O1αATP	2.75	2.74	2.73	2.73
NζLys72-O1βATP	2.86	2.76	2.75	2.75
NζLys72-Oε2Glu91	2.70	2.68	2.69	2.70
OγSer53-O1γATP	5.98	5.29	5.42	5.43
NSer53-O2βATP	4.37	4.52	4.45	4.41
NPhe54-O2βATP	5.42	5.52	5.57	5.54
NGly55-O2βATP	5.64	5.99	6.11	6.09
Mg^{2+} ions coordination sphere	$i_{model}K_{Mg}$	Rd'_K	$TSd1P'_K$	$Pd1'_K$
Mg1-O1βATP	2.06	2.10	2.05	2.03
Mg1-O3γATP	2.06	2.04	2.08	2.04
Mg1-Oδ1Asp184	2.21	2.16	2.15	2.18
Mg1-Oδ2Asp184	2.18	2.21	2.19	2.20
Mg1-OH2XWAT1003	2.04	2.06	2.09	2.15
Mg1-OH2XWAT1001	2.05	2.05	2.05	2.06
Mg2-O2αATP	1.99	2.01	2.03	2.07
Mg2-O3βATP	3.09	2.63	2.11	2.04
Mg2-O2γATP	2.01	2.04	2.13	2.13
Mg2-Oδ2Asp184	2.11	2.14	2.17	2.20
Mg2-Oδ1Asn171	2.01	2.05	2.15	2.23
Mg2-OH2XWAT1002	2.10	2.09	2.11	2.13

Table A8. For the PKAc(4IAC)-Mg_2ATP-Kemptide model and black potential energy profile, selected QM(B3LYP/6-31+G(d))/CHARMM bond distances (Å), bond angles (deg), and dihedrals (deg) in the optimized reactants (Rd''_K), phosphoryl-transfer transition state ($TSd1P''_K$), phosphoryl-transfer products ($Pd1''_K$), protonated Asp166 side chain-rotation transition state ($TSd2T''_K$), proton-transfer transition state ($TSd2H''_K$), and proton-transfer products ($Pd2''_K$) for the dissociative mechanism with the O2γATP as the final proton acceptor (O2γATP-dissociative path).

Active core geometric features	$i_{model}K_{Mg}$	Rd''_K	$TSd1P''_K$	$Pd1''_K$	$TSd2T''_K$	$Id2''_K$	$TSd2H''_K$	$Pd2''_K$
O3βATP-PγATP	1.68	1.79	2.33	3.03	3.06	3.10	3.16	3.23
PγATP-OγSer21	3.62	3.25	2.37	1.75	1.69	1.67	1.66	1.64
OγSer21-HγSer21	0.99	0.99	1.01	1.55	2.12	2.38	2.47	2.43
Oδ2Asp166-HγSer21	4.11	1.73	1.61	1.03	1.00	1.03	1.13	1.56
O2γATP-HγSer21	3.74	3.17	2.82	2.84	1.99	1.64	1.34	1.02
$angle_{O3\beta ATP\text{-}P\gamma ATP\text{-}O\gamma Ser21}$	137.5	170.2	169.9	168.5	169.8	171.3	172.4	169.8
$angle_{O\gamma Ser21\text{-}H\gamma Ser21\text{-}O\delta 2Asp166}$	105.4	173.1	172.1	164.0	132.2	118.0	112.5	105.6
$angle_{O\delta 2Asp166\text{-}H\gamma Ser21\text{-}O2\gamma ATP}$	60.2	92.5	99.5	115.6	138.1	155.6	164.6	170.7
$dihedral_{Asp166(C\beta\text{-}C\gamma\text{-}O\delta 2)\text{-}O2\gamma ATP}$	173.4	130.1	123.5	128.6	168.3	177.3	-178.5	-172.8
Catalytic core interaction distances	$i_{model}K_{Mg}$	Rd''_K	$TSd1P''_K$	$Pd1''_K$	$TSd2T''_K$	$Id2''_K$	$TSd2H''_K$	$Pd2''_K$
Oγ1Thr201-Oδ1Asp166	2.70	2.80	2.77	2.83	2.86	2.88	2.87	2.80
Oγ1Thr201-NζLys168	2.82	2.78	2.76	2.86	2.84	2.83	2.81	2.79
Oγ1Thr201-OγSer21	5.10	3.19	3.50	3.51	3.56	3.59	3.62	3.68
Oδ2Asp166-OγSer21	4.48	2.71	2.61	2.56	2.89	3.01	3.08	3.22
Oδ2Asp166-PγATP	4.60	4.30	3.85	3.52	3.45	3.38	3.34	3.54
Oδ2Asp166-OH2XWAT1003	2.67	2.66	2.68	2.77	2.81	2.79	2.75	2.71
Oδ2Asp166-NζLys168	3.84	4.15	4.26	4.64	4.50	4.53	4.50	4.39
Oδ1Asp166-NζLys168	4.41	4.36	4.35	4.50	4.39	4.23	4.19	4.33
NζLys168-OγSer21	4.91	2.75	2.90	3.19	3.31	3.41	3.49	3.49
NζLys168-PγATP	3.74	3.87	3.65	3.38	3.37	3.38	3.40	3.44

NζLys168-O2γATP	2.80	3.06	3.06	2.97	3.01	3.20	3.02	2.98
NζLys168-O1γATP	3.74	3.73	3.55	3.21	3.05	3.00	2.96	3.03
Nδ2Asn171-O2γATP	4.45	3.89	3.60	3.49	3.57	3.61	3.63	3.72
Nδ2Asn171- Oδ2Asp166	3.01	3.50	3.65	3.73	3.07	2.98	2.96	2.94
NζLys72-O1αATP	2.75	2.71	2.72	2.74	2.74	2.74	2.74	2.74
NζLys72-O1βATP	2.86	2.78	2.76	2.76	2.75	2.75	2.76	2.77
NζLys72-Oε2Glu91	2.70	2.68	2.69	2.69	2.70	2.70	2.70	2.70
OγSer53-O1γATP	5.98	5.43	5.54	5.67	5.73	5.78	5.81	5.72
NSer53-O2βATP	4.37	4.31	4.34	4.37	4.32	4.33	4.33	4.34
NPhe54-O2βATP	5.42	5.47	5.55	5.54	5.56	5.57	5.60	5.63
NGly55-O2βATP	5.64	6.12	6.19	6.13	6.16	6.19	6.21	6.23
Mg^{2+} ions coordination sphere	$i_{model}K_{Mg}$	Rd''_K	$TSd1P''_K$	$Pd1''_K$	$TSd2T''_K$	$Id2''_K$	$TSd2H''_K$	$Pd2''_K$
Mg1-O1βATP	2.06	2.09	2.05	2.03	2.02	2.02	2.02	2.02
Mg1-O3γATP	2.06	2.07	2.12	2.09	2.11	2.11	2.12	2.16
Mg1-Oδ1Asp184	2.21	2.18	2.17	2.24	2.28	2.28	2.27	2.24
Mg1-Oδ2Asp184	2.18	2.21	2.18	2.16	2.16	2.17	2.18	2.18
Mg1-OH2XWAT1003	2.04	2.05	2.07	2.12	2.12	2.11	2.10	2.08
Mg1-OH2XWAT1001	2.05	2.06	2.05	2.07	2.06	2.06	2.06	2.06
Mg2-O2αATP	1.99	2.00	2.01	2.07	2.09	2.08	2.06	2.02
Mg2-O3βATP	3.09	2.53	2.17	2.06	2.05	2.05	2.04	2.03
Mg2-O2γATP	2.01	2.00	2.08	2.11	2.19	2.29	2.51	2.76
Mg2-Oδ2Asp184	2.11	2.16	2.17	2.18	2.14	2.12	2.10	2.10
Mg2-Oδ1Asn171	2.01	2.02	2.09	2.16	2.16	2.16	2.13	2.09
Mg2-OH2XWAT1002	2.10	2.12	2.13	2.14	2.14	2.14	2.14	2.03

For 4XW4[80] * is O3βATP=NβAMPPNP; for 4XW5[80] * is OγSer21=SγCys21 from CP20 (or XSer21=XCys21; in CP20, Ser21 of SP20 has been substituted with Cys); for 4IAI[76] * means that is not possible to establish the chemical correspondence of the O*i*γATP atoms in relation to the 4IAC[76] nomenclature; for 4XW6[80] * is OγSer21=SγCys21 (or XSer21=XCys21): first value corresponds to conformation A (64% occupancy) with the side chain of Cys21 is rotated toward the bulk solvent and away from Asp166; second value correspond to conformation B (36% occupancy) with the SH group pointing toward Asp166.

Table A9. For the PKAc-Ca_2ATP-SP20 model, selected QM(B3LYP/6-31+G(d))/CHARMM bond distances (Å), bond angles (deg), and dihedrals (deg) in the optimized reactants ($Rd_{Ca/S}$), phosphoryl-transfer transition state ($TSd1P_{Ca/S}$), proton shift intermediate ($Id1_{Ca/S}$), proton shift transition state ($TSd1H_{Ca/S}$), phosphoryl-transfer products ($Pd1_{Ca/S}$), protonated Asp166 side chain-rotation transition state ($TSd2T_{Ca/S}$), and proton-transfer products ($Pd2_{Ca/S}$) for the dissociative mechanism with the O2γATP as the final proton acceptor (O2γATP-dissociative path). Comparison with values from X-ray crystallographic structures characterizing different stages of the phosphoryl-transfer mechanism catalyzed by the PKAc with SP20 or CP20 as substrates and Ca^{2+} ions.

Active core geometric features	4XW4	4XW5	$i_{model}S_{Ca}$	$Rd_{Ca/S}$	$TSd1P_{Ca/S}$	$Id1_{Ca/S}$	$TSd1H_{Ca/S}$	$Pd1_{Ca/S}$	$TSd2T_{Ca/S}$	$Pd2_{Ca/S}$	4IAI	4XW6
O3βATP-PγATP	1.74*	1.68	1.72	1.77	2.40	3.04	3.21	3.37	3.35	3.35	4.01	3.33
PγATP-OγSer21	4.70	5.55*	3.59	3.47	2.45	1.94	1.84	1.73	1.69	1.63	1.63	4.44/2.37*
OγSer21-HγSer21	---	---	0.99	0.98	0.99	1.04	1.20	1.56	2.01	2.62	---	---
Oδ2Asp166-HγSer21	---	---	4.69	1.87	1.78	1.57	1.25	1.03	1.00	1.53	---	---
O2γATP-HγSer21	---	---	3.47	3.26	2.86	2.74	2.78	2.72	2.06	1.03	---	---
OγSer21-Oδ2Asp166	4.55	3.36/3.17*	4.93	2.84	2.77	2.60	2.44	2.58	2.91	3.55	5.01	5.80/3.06*
$angle_{O3\beta ATP\text{-}P\gamma ATP\text{-}O\gamma Ser21}$	136.8*	161.1	143.2	155.4	164.6	166.1	169.1	175.4	173.6	174.1	155.4	115.1/152.0*
$angle_{O\gamma Ser21\text{-}H\gamma Ser21\text{-}O\delta 2Asp166}$	---	---	98.0	170.7	176.4	172.0	171.0	169.5	148.8	114.7	---	---
$angle_{O\delta 2Asp166\text{-}H\gamma Ser21\text{-}O2\gamma ATP}$	---	---	57.1	103.0	107.1	111.5	114.5	112.1	129.7	172.6	---	---
$d._{Ser21(N\text{-}C\alpha\text{-}C\beta\text{-}O\gamma)}$	64.3	-76.6	61.2	-54.9	-56.1	-46.1	-46.1	-52.9	-56.3	-55.7	63.9	56.9/-66.7*
$d._{Asp166(C\beta\text{-}C\gamma\text{-}O\delta 2)\text{-}O2\gamma ATP}$	135.9	159.1	-179.7	144.2	130.5	125.8	124.6	120.3	137.8	170.8	~130	129.5
$d._{phiAsp166}$	-147.2	-142.3	-92.6	-95.4	-90.7	-88.1	-87.2	-94.9	-96.1	-95.7	-150.9	-144.9
$d._{psiAsp166}$	40.5	34.4	88.0	85.6	82.5	80.4	79.2	77.3	78.8	83.9	43.0	36.7
$d._{O\gamma Ser21\text{-}P\gamma ATP\text{-}O2\gamma ATP\text{-}O\delta 2Asp166}$	-36.6	-32.2	-37.4	-40.8	-39.2	-37.9	-37.5	-35.3	-39.3	-51.0	25.3*	-3.2/-29.2*
$O\delta 1Asp24^{SP20}$-Cε1His87	6.00	5.04	5.7	5.4	5.4	5.4	5.4	5.4	5.4	5.4	5.56	12.33
$O\delta 1Asp24^{SP20}$-Nε2Gly84	3.67	3.39	3.0	2.9	2.9	2.9	2.9	2.9	2.9	2.9	5.26	11.36

Oε1Gly84-Nδ1His87	2.74	3.20	2.7	2.70	2.70	2.70	2.70	2.70	2.70	2.70	2.72	2.86
O2pThr197-Nε2His87	2.67	2.59	2.7	2.65	2.65	2.65	2.65	2.65	2.65	2.65	2.72	2.63
OγSer21-O/γATP	5.54*$^{i=2}$ 3.97*$^{i=3}$	5.62*$^{i=2}$ 4.80*$^{i=3}$	4.3$^{i=2}$ 2.6$^{i=3}$	3.20$^{i=2}$ 3.30$^{i=3}$	2.73$^{i=2}$ 2.83$^{i=3}$	2.57$^{i=2}$ 2.64$^{i=3}$	2.53$^{i=2}$ 2.60$^{i=3}$	2.54$^{i=2}$ 2.58$^{i=3}$	2.49$^{i=2}$ 2.58$^{i=3}$	2.50$^{i=2}$ 2.58$^{i=3}$	2.66 2.55 2.57	5.84$^{i=2}$/3.36$^{i=2}$ 4.22$^{i=3}$/3.01$^{i=3}$
Catalytic core interaction distances	4XW4	4XW5	$i_{model}S_{Ca}$	$Rd_{Ca/S}$	$TSd1P_{Ca/S}$	$Id1_{Ca/S}$	$TSd1H_{Ca/S}$	$Pd1_{Ca/S}$	$TSd2T_{Ca/S}$	$Pd2_{Ca/S}$	4IAI	4XW6
Oγ1Thr201-Oδ1Asp166	2.98	3.47	2.76	2.80	2.74	2.73	2.75	2.89	2.99	2.94	2.88	3.04
Oγ1Thr201-NζLys168	2.78	2.79	2.75	2.74	2.71	2.72	2.73	2.75	2.75	2.73	2.84	2.66
Oγ1Thr201-OγSer21	5.54	3.39	5.21	2.96	3.06	3.04	3.08	3.02	3.07	3.05	5.55	5.99/3.51*
Oδ2Asp166-OγSer21	4.55	3.36/3.17*	4.93	2.84	2.77	2.60	2.44	2.58	2.91	3.55	5.01	5.80/3.06*
Oδ2Asp166-PγATP	6.18	6.02	4.94	4.70	4.11	3.69	3.48	3.43	3.40	3.59	5.09	3.27
Oδ2Asp166-OH2XWAT1003	OH589 2.74	OH595 2.63 OH598 3.02	2.70	2.71	2.74	2.79	2.86	2.92	2.90	2.78	OH1001 2.65 OH1003 2.79	OH714 2.88
Oδ2Asp166-NζLys168	4.35	4.36	3.98	4.31	4.45	4.60	4.62	5.05	4.95	4.88	4.41	3.98
Oδ1Asp166-NζLys168	4.06	3.86	4.32	4.41	4.42	4.43	4.39	4.63	4.67	4.62	4.15	3.77
NζLys168-OγSer21	5.16	3.26	5.15	2.86	3.05	3.27	3.31	3.37	3.37	3.35	5.36	5.94/3.22*
NζLys168-PγATP	5.84	5.97	3.95	3.88	3.64	3.51	3.46	3.31	3.31	3.34	5.33	3.06
NζLys168-O2γATP	5.23	5.22	2.71	2.71	2.72	2.69	2.69	3.11	3.15	3.08	5.03	2.98
NζLys168-O1γATP	5.77	6.14	4.26	4.18	3.84	3.72	3.63	2.81	2.77	2.80	4.76	3.10
Nδ2Asn171-O2γATP	6.08	5.97	4.85	4.64	4.26	4.10	3.92	3.31	3.38	3.70	5.57	3.19
Nδ2Asn171-Oδ2Asp166	2.99	2.85	3.01	3.58	3.84	4.06	4.11	4.23	3.66	3.11	3.00	4.81
NζLys72-O1αATP	3.02	2.75	2.75	2.72	2.71	2.72	2.72	2.73	2.73	2.73	3.84	3.17
NζLys72-O1βATP	3.37	2.91	2.78	2.78	2.75	2.73	2.73	2.73	2.73	2.74	2.82	2.87
NζLys72-Oε2Glu91	2.86	2.67	2.72	2.72	2.75	2.75	2.75	2.75	2.75	2.74	2.71	2.73

OγSer53-O1γATP	6.01	2.57	5.63	5.64	5.63	5.67	5.78	6.55	6.62	6.72	2.39	2.97
NSer53-O2βATP	4.54	4.34	4.24	4.47	4.17	4.48	4.46	4.45	4.47	4.49	4.13	3.26
NPhe54-O2βATP	5.45	4.94	5.38	5.85	5.39	5.79	5.77	5.77	5.79	5.83	4.58	3.49
NGly55-O2βATP	5.59	5.09	5.57	5.83	5.96	5.68	5.66	5.68	5.71	5.77	3.53	5.11
OγSer53-OSer21	6.45	7.25	4.8	4.70	4.64	4.70	4.72	4.67	4.61	4.53	4.46	4.80
Ca^{2+} ions coordination sphere	4XW4	4XW5	$i_{model}S_{Ca}$	$Rd_{Ca/S}$	$TSd1P_{Ca/S}$	$Id1_{Ca/S}$	$TSd1H_{Ca/S}$	$Pd1_{Ca/S}$	$TSd2T_{Ca/S}$	$Pd2_{Ca/S}$	4IAI	4XW6
Ca1-O1βATP	2.42	2.26	2.38	2.41	2.38	2.36	2.35	2.36	2.36	2.36	2.26	2.37
Ca1-O3γATP	2.63	2.37	2.47	2.40	2.41	2.41	2.40	2.44	2.46	2.53	2.29*	2.13
Ca1-Oδ1Asp184	2.59	2.37	2.47	2.47	2.46	2.47	2.46	2.52	2.54	2.52	2.41	2.73
Ca1-Oδ2Asp184	2.54	2.42	2.58	2.60	2.61	2.59	2.59	2.53	2.53	2.55	2.45	2.25
Ca1-OH2XWAT1003	OH589 2.42	OH598 2.69	2.44	2.46	2.48	2.50	2.53	2.54	2.53	2.48	OH1003 2.41	OH714 2.19
Ca1-OH2XWAT1001	OH592 2.42	OH802 2.39	2.43	2.44	2.45	2.47	2.48	2.48	2.47	2.43	OH702 2.43	OH713 2.34
Ca1-OH2XWAT1029	OH711 2.61 OH813 2.69	OH594 2.64	2.51	2.53	2.50	2.50	2.50	2.51	2.52	2.51	OH1004 2.47	
Ca2-O2αATP	2.34	2.32	2.32	2.31	2.31	2.33	2.34	2.36	2.37	2.36	2.27	1.92
Ca2-O3βATP	4.21*	4.23	2.65	2.52	2.40	2.32	2.31	2.31	2.30	2.30	2.25	2.07
Ca2-O2γATP	2.68 O3γATP 2.78	2.42	2.35	2.33	2.34	2.38	2.39	2.45	2.49	2.63	OH701 2.57	2.47
Ca2-Oδ2Asp184	2.29	2.40	2.37	2.40	2.41	2.42	2.43	2.40	2.39	2.38	2.39	2.29
Ca2-Oδ1Asn171	2.40	2.38	2.30	2.29	2.32	2.35	2.36	2.34	2.35	2.35	2.43	2.20
Ca2-OH2XWAT1002	OH587 2.46 OH590 2.66	OH596 2.57 OH595 2.63	2.41	2.42	2.44	2.46	2.46	2.47	2.47	2.45	OH1002 2.42 OH1001 2.46	2.35

For 4IAK[76] and 4IAY[76] * means that is not possible to establish the chemical correspondence of the O*i*γATP atoms in relation to the 4IAC[76] nomenclature

Table A10. For the PKAc-Sr_2ATP-SP20 model, selected QM(B3LYP/def2-TZVP)/CHARMM bond distances (Å), bond angles (deg), and dihedrals (deg) in the optimized reactants ($Rd_{Sr/S}$), phosphoryl-transfer transition state ($TSd1P_{Sr/S}$), phosphoryl-transfer products ($Pd1_{Sr/S}$), protonated Asp166 side chain-rotation transition state ($TSd2T_{Sr/S}$), and proton-transfer products ($Pd2_{Sr/S}$) for the dissociative mechanism with the O2γATP as the final proton acceptor (O2γATP-dissociative path). Comparison with values from X-ray crystallographic structures characterizing the product complex stage of the phosphoryl-transfer mechanism catalyzed by the PKAc with SP20 as substrate and with Sr^{2+} ions.

Active core geometric features	$i_{model}S_{Sr}$	$Rd_{Sr/S}$	$TSd1P_{Sr/S}$	$Pd1_{Sr/S}$	$TSd2T_{Sr/S}$	$Pd2_{Sr/S}$	4IAK	4IAY
O3βATP-PγATP	1.70	1.77	2.60	4.05	4.21	4.34	4.72	4.49
PγATP-OγSer21	3.70	3.59	2.73	1.72	1.67	1.61	1.62	1.63
OγSer21-HγSer21	0.99	0.98	0.99	1.67	2.03	2.64	---	---
Oδ2Asp166-HγSer21	4.23	1.77	1.72	1.01	0.99	1.41	---	---
O2γATP-HγSer21	3.23	3.27	2.98	2.89	2.11	1.05	---	---
OγSer21-Oδ2Asp166	4.24	2.74	2.71	2.66	2.93	3.47	5.21	5.09
$angle_{O3\beta ATP\text{-}P\gamma ATP\text{-}O\gamma Ser21}$	142.2	154.1	158.5	161.5	164.3	152.9	159.0	159.2
$angle_{O\gamma Ser21\text{-}H\gamma Ser21\text{-}O\delta 2Asp166}$	83.8	170.2	178.4	166.6	149.7	114.5	---	---
$angle_{O\delta 2Asp166\text{-}H\gamma Ser21\text{-}O2\gamma ATP}$	67.0	105.7	110.2	124.6	131.4	174.3	---	---
$d._{Ser21(N\text{-}C\alpha\text{-}C\beta\text{-}O\gamma)}$	68.7	-53.3	-42.2	-39.4	-49.9	-51.3	72.1	72.1
$d._{Asp166(C\beta\text{-}C\gamma\text{-}O\delta 2)\text{-}O2\gamma ATP}$	-177.8	160.5	140.0	130.8	133.9	155.9	-163.1	-132.5
$d._{phiAsp166}$	-121.6	-119.6	-119.7	-119.5	-125.8	-128.1	-151.4	-142.8
$d._{psiAsp166}$	75.6	80.5	76.6	70.4	65.4	66.1	45.2	41.2
$d._{O\gamma Ser21\text{-}P\gamma ATP\text{-}O2\gamma ATP\text{-}O\delta 2Asp166}$	-27.8	-39.3	-36.5	-42.6	-39.2	-56.3	-85.7	31.4
$O\delta 1Asp24^{SP20}$-Cε1His87	5.5	5.5	5.5	5.5	5.5	5.5	10.23	10.99
$O\delta 1Asp24^{SP20}$-Nε2Gly84	3.0	2.9	2.9	3.0	2.9	2.9	7.14	9.32
Oε1Gly84-Nδ1His87	2.8	2.8	2.8	2.8	2.8	2.8	2.76	2.78
O2pThr197-Nε2His87	2.7	2.6	2.6	2.6	2.6	2.6	2.69	2.84

OγSer21-O/γATP	$4.1^{i=2}$ $2.7^{i=3}$	$3.15^{i=2}$ $3.49^{i=3}$	$2.83^{i=2}$ $3.01^{i=3}$	$2.46^{i=2}$ $2.59^{i=3}$	$2.46^{i=2}$ $2.54^{i=3}$	$2.47^{i=2}$ $2.54^{i=3}$	$2.58^{*i=1}$ $2.58^{*i=2}$ $2.71^{*i=3}$	$2.57^{*i=1}$ $2.66^{*i=2}$ $2.66^{*i=3}$
Catalytic core interaction distances	$i_{model}S_{Sr}$	$Rd_{Sr/S}$	$TSd1P_{Sr/S}$	$Pd1_{Sr/S}$	$TSd2T_{Sr/S}$	$Pd2_{Sr/S}$	4IAK	4IAY
Oγ1Thr201-Oδ1Asp166	2.68	2.79	2.73	2.77	2.93	2.93	2.93	2.88
Oγ1Thr201-NζLys168	2.74	2.80	2.74	2.79	2.79	2.77	2.74	2.84
Oγ1Thr201-OγSer21	4.86	2.96	3.18	3.31	3.28	3.28	5.41	5.55
Oδ2Asp166-OγSer21	4.24	2.74	2.71	2.66	2.93	3.47	5.09	5.01
Oδ2Asp166-PγATP	5.17	4.87	4.33	3.53	3.43	3.42	5.19	5.09
Oδ2Asp166-OH2XWAT1003	2.72	2.70	2.74	3.04	2.94	2.74	OH1002 2.80 OH1003 2.67	OH1001 2.65 OH1003 2.79
Oδ2Asp166-NζLys168	3.99	4.18	4.30	4.53	4.81	4.82	4.06	4.41
Oδ1Asp166-NζLys168	4.38	4.27	4.17	4.06	4.32	4.36	4.04	4.15
NζLys168-OγSer21	4.90	2.80	2.96	3.21	3.25	3.22	5.28	5.36
NζLys168-PγATP	3.99	3.99	3.76	3.51	3.35	3.40	5.21	5.33
NζLys168-O2γATP	2.72	2.79	2.81	2.70	3.17	3.15	4.89*	5.03*
NζLys168-O1γATP	4.28	4.22	4.01	3.86	2.92	2.98	4.56*	4.76*
Nδ2Asn171-O2γATP	5.08	4.88	4.54	4.20	3.51	3.52	5.79*	5.57*
Nδ2Asn171-Oδ2Asp166	2.95	3.26	3.66	4.11	3.83	3.39	3.13	3.00
NζLys72-O1αATP	2.73	2.73	2.72	2.71	2.70	2.70	2.77	3.84
NζLys72-O1βATP	2.83 XW1029 2.83	2.81 XW1029 2.83	2.72 XW1029 2.92	3.23 XW1029 2.81	3.45 XW1029 2.80	3.62 XW1029 2.79	2.85 XW1003 2.97	2.82
NζLys72-Oε2Glu91	2.71	2.73	2.75	2.72	2.70	2.69	2.94	2.71
OγSer53-O1γATP	5.44	5.39	5.21	5.18	6.05	6.20	2.34	2.39
NSer53-O2βATP	4.21	4.14	4.16	4.27	4.15	4.09	3.75	4.13

NPhe54-O2βATP	5.33	5.40	5.39	5.43	5.43	5.41	4.85	4.58
NGly55-O2βATP	5.74	5.84	5.82	5.82	5.88	5.89	5.67	3.53
OγSer53-OSer21	4.55	4.66	4.63	4.64	4.52	4.45	5.32	4.46
Sr^{2+} ions coordination sphere	$i_{model}S_{Sr}$	$Rd_{Sr/S}$	$TSd1P_{Sr/S}$	$Pd1_{Sr/S}$	$TSd2T_{Sr/S}$	$Pd2_{Sr/S}$	4IAK	4IAY
Sr1-O1βATP	2.54	2.53	2.50	2.54	2.50	2.52	2.33	2.27
Sr1-O3γATP	2.74	2.57	2.63	2.49	2.59	2.62	2.44*	2.44*
Sr1-Oδ1Asp184	2.63	2.64	2.59	2.60	2.66	2.61	2.64	2.61
Sr1-Oδ2Asp184	2.77	2.79	2.79	2.78	2.72	2.73	2.64	2.55
Sr1-OH2XWAT1003	2.64	2.68	2.70	2.88	2.93	2.84	OH1001 2.52	OH1002 2.88
Sr1-OH2XWAT1001	2.63	2.56	2.57	2.62	2.61	2.58	OH1003 2.49	OH1006 2.86
Sr1-OH2XWAT1029	2.66	2.68	2.62	2.64	2.68	2.67	OH701 2.49	OH701 2.79
Sr1-OH2XWAT1057	2.59	2.69	2.68	2.65	2.66	2.68	OH702 2.56	OH1001 2.87
Sr2-O2αATP	2.41	2.42	2.40	2.47	2.48	2.46	2.35	2.37
Sr2-O3βATP	2.89	2.83	2.57	2.56	2.60	2.61	2.59	2.42
Sr2-O2γATP	2.42	2.39	2.46	2.51	2.63	2.87	3.90*	3.82*
Sr2-Oδ2Asp184	2.47	2.49	2.52	2.63	2.61	2.59	2.46	2.50
Sr2-Oδ1Asn171	2.39	2.40	2.46	2.55	2.52	2.54	2.62	2.70
Sr2-OH2XWAT1002	2.53	2.52	2.53	2.56	2.59	2.56	2.61	OH703 2.88
Sr2-O1βATP	3.48	3.71	3.60	2.75	2.68	2.65	3.22	3.70
Sr2-	O1γATP 4.53[not directed]	O1γATP 4.48[not directed]	O1γATP 4.50[not directed]	O1γATP 4.37[not directed]	O1γATP 3.57[not directed]	O1γATP 3.13	OH703 2.66	OH702 3.06
Sr2-							OH1004 2.47	OH1003 2.77

Table A11. For the PKAc-Ca_2ATP-Kemptide model, selected QM(B3LYP/6-31+G(d))/CHARMM bond distances (Å), bond angles (deg), and dihedrals (deg) in the optimized reactants ($Rd_{Ca/K}$), phosphoryl-transfer transition state ($TSd1P_{Ca/K}$), proton shift intermediate ($Id1_{Ca/K}$), proton shift transition state ($TSd1H_{Ca/K}$), phosphoryl-transfer products ($Pd1_{Ca/K}$), protonated Asp166 side chain-rotation transition state ($TSd2T_{Ca/K}$), and proton-transfer products ($Pd2_{Ca/K}$) for the dissociative mechanism with the O2γATP as the final proton acceptor (O2γATP-dissociative path).

Active core geometric features	$i_{model}K_{Ca}$	$Rd_{Ca/K}$	$TSd1P_{Ca/K}$	$Id1_{Ca/K}$	$TSd1H_{Ca/K}$	$Pd1_{Ca/K}$	$TSd2T_{Ca/K}$	$Pd2_{Ca/K}$
O3βATP-PγATP	1.74	1.79	2.62	3.26	3.39	3.56	3.65	3.66
PγATP-OγSer21	3.68	3.69	2.53	1.97	1.89	1.76	1.71	1.65
OγSer21-HγSer21	1.00	0.99	1.00	1.05	1.18	1.70	2.05	2.50
Oδ2Asp166-HγSer21	4.24	1.80	1.74	1.52	1.28	1.02	1.00	1.57
O2γATP- HγSer21	3.31	3.27	2.83	2.68	2.75	2.92	2.00	1.03
OγSer21-Oδ2Asp166	4.30	2.79	2.74	2.56	2.46	2.71	2.91	3.28
$angle_{O3\beta ATP\text{-}P\gamma ATP\text{-}O\gamma Ser21}$	141.7	148.7	157.4	161.2	161.7	161.2	171.6	170.2
$angle_{O\gamma Ser21\text{-}H\gamma Ser21\text{-}O\delta 2Asp166}$	86.6	174.3	173.5	170.3	171.1	167.0	142.1	105.0
$angle_{O\delta 2Asp166\text{-}H\gamma Ser21\text{-}O2\gamma ATP}$	64.8	108.7	112.8	115.4	117.6	126.4	139.1	175.4
$d._{Ser21(N\text{-}C\alpha\text{-}C\beta\text{-}O\gamma)}$	70.8	-48.1	-33.1	-33.8	-34.7	-33.7	-36.2	-36.5
$d._{Asp166(C\beta\text{-}C\gamma\text{-}O\delta 2)\text{-}O2\gamma ATP}$	178.2	152.9	141.1	132.6	131.1	136.9	154.6	171.8
$d._{phiAsp166}$	-128.1	-124.7	-122.9	-120.7	-119.4	-120.1	-123.4	-121.8
$d._{psiAsp166}$	80.8	76.0	73.2	71.7	71.4	71.1	73.0	76.0
$d._{O\gamma Ser21\text{-}P\gamma ATP\text{-}O2\gamma ATP\text{-}O\delta 2Asp166}$	-31.1	-41.7	-40.2	-38.7	-38.1	-43.2	-43.0	-50.3
OγSer21-O/γATP	$4.1^{i=2}$	$3.18^{i=2}$	$2.71^{i=2}$	$2.52^{i=2}$	$2.50^{i=2}$	$2.45^{i=2}$	$2.44^{i=2}$	$2.46^{i=2}$
	$2.7^{i=3}$	$3.65^{i=3}$	$2.96^{i=3}$	$2.70^{i=3}$	$2.65^{i=3}$	$2.60^{i=3}$	$2.62^{i=3}$	$2.63^{i=3}$
Catalytic core interaction distances	$i_{model}K_{Ca}$	$Rd_{Ca/K}$	$TSd1P_{Ca/K}$	$Id1_{Ca/K}$	$TSd1H_{Ca/K}$	$Pd1_{Ca/K}$	$TSd2T_{Ca/K}$	$Pd2_{Ca/K}$
Oγ1Thr201-Oδ1Asp166	2.74	3.00	2.84	2.81	2.81	2.91	3.17	3.23
Oγ1Thr201-NζLys168	2.82	2.88	2.78	2.81	2.82	2.84	2.82	2.79
Oγ1Thr201-OγSer21	5.21	2.93	3.24	3.33	3.35	3.39	3.27	3.24

Oδ2Asp166-OγSer21	4.30	2.79	2.74	2.56	2.46	2.71	2.91	3.28
Oδ2Asp166-PγATP	5.05	4.80	4.14	3.68	3.54	3.60	3.41	3.48
Oδ2Asp166-OH2XWAT1003	2.69	2.74	2.78	2.84	2.88	2.97	2.95	2.77
Oδ2Asp166-NζLys168	3.96	4.37	4.38	4.44	4.42	4.56	4.82	4.87
Oδ1Asp166-NζLys168	4.45	4.46	4.36	4.34	4.30	4.32	4.53	4.43
NζLys168-OγSer21	5.00	2.74	2.94	3.13	3.15	3.11	3.15	3.17
NζLys168-PγATP	4.11	4.16	3.81	3.61	3.56	3.52	3.36	3.41
NζLys168-O2γATP	2.82	2.87	2.83	2.79	2.77	2.74	3.16	3.21
NζLys168-O1γATP	4.52	4.62	4.15	2.87	3.82	3.87	2.94	2.93
Nδ2Asn171-O2γATP	4.79	4.77	4.34	4.09	4.03	4.08	3.47	3.66
Nδ2Asn171-Oδ2Asp166	3.01	3.26	3.42	3.62	3.67	3.64	3.19	2.98
NζLys72-O1αATP	2.74	2.72	2.71	2.72	2.72	2.72	2.72	2.72
NζLys72-O1βATP	2.76	2.76	2.73	2.74	2.74	2.75	2.76	2.76
NζLys72-Oε2Glu91	2.70	2.69	2.71	2.72	2.72	2.73	2.73	2.72
OγSer53-O1γATP	5.49	5.17	5.35	5.47	5.49	5.44	6.25	6.39
NSer53-O2βATP	4.21	4.29	4.28	4.28	4.27	4.28	4.24	4.23
NPhe54-O2βATP	5.46	5.46	5.47	5.45	5.44	5.44	5.44	5.47
NGly55-O2βATP	5.77	5.70	5.70	5.65	5.64	5.62	5.64	5.70
OγSer53-OSer21	4.75	4.96	4.94	4.97	4.98	4.95	5.07	5.05
Ca^{2+} ions coordination sphere	$i_{model}K_{Ca}$	$Rd_{Ca/K}$	$TSd1P_{Ca/K}$	$Id1_{Ca/K}$	$TSd1H_{Ca/K}$	$Pd1_{Ca/K}$	$TSd2T_{Ca/K}$	$Pd2_{Ca/K}$
Ca1-O1βATP	2.38	2.37	2.33	2.32	2.32	2.32	2.32	2.32
Ca1-O3γATP	2.47	2.41	2.47	2.47	2.45	2.43	2.56	2.66
Ca1-Oδ1Asp184	2.49	2.45	2.44	2.45	2.46	2.47	2.55	2.52
Ca1-Oδ2Asp184	2.53	2.60	2.58	2.58	2.58	2.61	2.53	2.54

Ca1-OH2XWAT1003	2.43	2.45	2.47	2.48	2.50	2.51	2.49	2.46
Ca1-OH2XWAT1001	2.45	2.40	2.41	2.42	2.42	2.41	2.41	2.40
Ca1-OH2XWAT1029	2.42	2.63	2.57	2.59	2.59	2.60	2.61	2.59
Ca2-O2αATP	2.32	2.31	2.30	2.31	2.32	2.34	2.36	2.35
Ca2-O3βATP	2.55	2.57	2.39	2.35	2.34	2.34	2.35	2.35
Ca2-O2γATP	2.39	2.36	2.38	2.39	2.38	2.37	2.41	2.55
Ca2-Oδ2Asp184	2.38	2.42	2.44	2.46	2.46	2.48	2.43	2.40
Ca2-Oδ1Asn171	2.30	2.31	2.34	2.36	2.37	2.39	2.36	2.36
Ca2-OH2XWAT1002	2.40	2.40	2.41	2.42	2.43	2.43	2.42	2.40

References

(1) Krebs, E. G.; Fischer, E. H. *Biochim. Biophys. Acta* **1956**, *20*, 150-157.
(2) Krebs, E. G.; Graves, D. J.; Fischer, E. H. *J. Biol. Chem.* **1959**, *234*, 2867-2873.
(3) Plowman, G. D.; Sudarsanam, S.; Bingham, J.; Whyte, D.; Hunter, T. *Proc. Natl. Acad. Sci. USA* **1999**, *96*, 13603-13610.
(4) Bowler, M. W.; Cliff, M. J.; Waltho, J. P.; Blackburn, G. M. *New Journal of Chemistry* **2010**, *34*, 784-794.
(5) Kamerlin, S. C. L.; Sharma, P. K.; Prasad, R. B.; Warshel, A. *Q. Rev. Biophys.* **2013**, *46*, 1-132.
(6) Manning, G.; Whyte, D. B.; Martinez, R.; Hunter, T.; Sudarsanam, S. *Science* **2002**, *298*, 1912-1934.
(7) Cohen, P. *Eur. J. Biochem.* **2001**, *268*, 5001-5010.
(8) Graves, J. D.; Krebs, E. G. *Pharmacol. Ther.* **1999**, *82*, 111-121.
(9) Cheetham, G. M. T. *Curr. Opin. Struct. Biol.* **2004**, *14*, 700-705.
(10) Eswaran, J.; Knapp, S. *Biochimica et Biophysica Acta (BBA) - Proteins and Proteomics* **2010**, *1804*, 429-432.
(11) Lassila, J. K.; Zalatan, J. G.; Herschlag, D. *Annu. Rev. Biochem.* **2011**, *80*, 669-702.
(12) Taylor, S. S.; Keshwani, M. M.; Steichen, J. M.; Kornev, A. P. *Philos. Trans. R. Soc. Lond. B Biol. Sci.* **2012**, *367*, 2517-2528.
(13) Ryšlavá, H.; Doubnerová, V.; Kavan, D.; Vaněk, O. *J. Proteomics* **2013**, *92*, 80-109.
(14) Pawson, T.; Scott, J. D. *Trends Biochem. Sci.* **2005**, *30*, 286-290.
(15) Bossemeyer, D. *FEBS Lett.* **1995**, *369*, 57-61.
(16) Taylor, S. S.; Kornev, A. P. *Trends Biochem. Sci.* **2011**, *36*, 65-77.
(17) Endicott, J. A.; Noble, M. E. M.; Johnson, L. N. *Annu. Rev. Biochem.* **2012**, *81*, 587-613.
(18) Shaw, A. S.; Kornev, A. P.; Hu, J.; Ahuja, L. G.; Taylor, S. S. *Mol. Cell. Biol.* **2014**, *34*, 1538-1546.
(19) Chen, C.-A.; Yeh, R.-H.; Yan, X.; Lawrence, D. S. *Biochimica et Biophysica Acta (BBA) - Proteins and Proteomics* **2004**, *1697*, 39-51.
(20) Riel-Mehan, M. M.; Shokat, K. M. *Chem. Biol.* **2014**, *21*, 585-590.
(21) Adams, J. A. *Chem. Rev.* **2001**, *101*, 2271-2290.
(22) Besant, P. G.; Tan, E.; Attwood, P. V. *The International Journal of Biochemistry & Cell Biology* **2003**, *35*, 297-309.
(23) Taylor, S. S.; Ilouz, R.; Zhang, P.; Kornev, A. P. *Nat. Rev. Mol. Cell Biol.* **2012**, *13*, 646-658.
(24) Duong-Ly, K. C.; Peterson, J. R. In *Curr. Protoc. Pharmacol.*; John Wiley & Sons, Inc., 2013.
(25) Johnson, S. A.; Hunter, T. *Nat Meth* **2005**, *2*, 17-25.
(26) Johnson, D. A.; Akamine, P.; Radzio-Andzelm, E.; Madhusudan; Taylor, S. S. *Chem. Rev.* **2001**, *101*, 2243-2270.
(27) Johnson, L. N.; Noble, M. E. M.; Owen, D. J. *Cell* **1996**, *85*, 149-158.
(28) Cohen, P.; Alessi, D. R. *ACS Chem. Biol.* **2013**, *8*, 96-104.
(29) Cohen, P. *Nat Rev Drug Discov* **2002**, *1*, 309-315.
(30) Harr, M. W.; Distelhorst, C. W. *Cold Spring Harb. Perspect. Biol.* **2010**, *2*, a005579.
(31) Birchmeier, C.; Birchmeier, W.; Gherardi, E.; Vande Woude, G. F. *Nat. Rev. Mol. Cell Biol.* **2003**, *4*, 915-925.
(32) Dhanasekaran, D. N.; Reddy, E. P. *Oncogene* **2008**, *27*, 6245-6251.
(33) Zhang, J.; Yang, P. L.; Gray, N. S. *Nat. Rev. Cancer* **2009**, *9*, 28-39.
(34) Parang, K.; Cole, P. A. *Pharmacol. Ther.* **2002**, *93*, 145-157.
(35) Bogoyevitch, M. A.; Barr, R. K.; Ketterman, A. J. *Biochimica et Biophysica Acta (BBA) - Proteins and Proteomics* **2005**, *1754*, 79-99.
(36) Bogoyevitch, M. A.; Fairlie, D. P. *Drug Discov. Today* **2007**, *12*, 622-633.

(37) Taylor, S. S.; Kim, C.; Cheng, C. Y.; Brown, S. H. J.; Wu, J.; Kannan, N. *Biochimica et Biophysica Acta (BBA) - Proteins and Proteomics* **2008**, *1784*, 16-26.
(38) Shugar, D. *Biochim. Biophys. Acta* **2010**, *1804*, 427-428.
(39) Bhalla, N.; Di Lorenzo, M.; Pula, G.; Estrela, P. *Biosens. Bioelectron.* **2014**, *54*, 109-114.
(40) Blume-Jensen, P.; Hunter, T. *Nature* **2001**, *411*, 355-365.
(41) Evans, J. L.; Goldfine, I. D.; Maddux, B. A.; Grodsky, G. M. *Endocr. Rev.* **2002**, *23*, 599-622.
(42) Kumar, S.; Boehm, J.; Lee, J. C. *Nat Rev Drug Discov* **2003**, *2*, 717-726.
(43) Masterson, L. R.; Cembran, A.; Shi, L.; Veglia, G. *Adv. Protein Chem. Struct. Biol.* **2012**, *87*, 363-389.
(44) Masterson, L. R.; Shi, L.; Metcalfe, E.; Gao, J.; Taylor, S. S.; Veglia, G. *Proc. Natl. Acad. Sci. USA* **2011**, *108*, 6969-6974.
(45) Masterson, L. R.; Cheng, C.; Yu, T.; Tonelli, M.; Kornev, A.; Taylor, S. S.; Veglia, G. *Nat. Chem. Biol.* **2010**, *6*, 821-828.
(46) Antoniou, D.; Basner, J.; Núñez, S.; Schwartz, S. D. *Chem. Rev.* **2006**, *106*, 3170-3187.
(47) Świderek, K.; Javier Ruiz-Pernía, J.; Moliner, V.; Tuñón, I. *Curr. Opin. Chem. Biol.* **2014**, *21*, 11-18.
(48) Orozco, M. *Chem. Soc. Rev.* **2014**, *43*, 5051-5066.
(49) Bruice, T. C. *Chem. Rev.* **2006**, *106*, 3119-3139.
(50) Gao, J.; Ma, S.; Major, D. T.; Nam, K.; Pu, J.; Truhlar, D. G. *Chem. Rev.* **2006**, *106*, 3188-3209.
(51) Garcia-Viloca, M.; Gao, J.; Karplus, M.; Truhlar, D. G. *Science* **2004**, *303*, 186-195.
(52) Nashine, V. C.; Hammes-Schiffer, S.; Benkovic, S. J. *Curr. Opin. Chem. Biol.* **2010**, *14*, 644-651.
(53) Doshi, U.; McGowan, L. C.; Ladani, S. T.; Hamelberg, D. *Proceedings of the National Academy of Sciences* **2012**, *109*, 5699-5704.
(54) Callender, R.; Dyer, R. B. *Chem. Rev.* **2006**, *106*, 3031-3042.
(55) Kiani, F. A.; Fischer, S. *J. Biol. Chem.* **2013**, *288*, 35569-35580.
(56) Saunders, M. G.; Voth, G. A. *Annu. Rev. Biophys.* **2013**, *42*, 73-93.
(57) Klinman, J. P.; Kohen, A. *Annu. Rev. Biochem.* **2013**, *82*, 471-496.
(58) He, X.; Zhu, T.; Wang, X.; Liu, J.; Zhang, J. Z. *Acc. Chem. Res.* **2014**.
(59) Kiani, F. A.; Fischer, S. *Proc. Natl. Acad. Sci. USA* **2014**.
(60) Goh, G. B.; Hulbert, B. S.; Zhou, H.; Brooks, C. L., 3rd *Proteins* **2014**, *82*, 1319-1331.
(61) Taylor, S. S.; Shaw, A. S.; Kannan, N.; Kornev, A. P. *Biochimica et Biophysica Acta (BBA) - Proteins and Proteomics*.
(62) Smith, C. M.; Radzio-Andzelm, E.; Madhusudan; Akamine, P.; Taylor, S. S. *Prog. Biophys. Mol. Biol.* **1999**, *71*, 313-341.
(63) Hanks, S. K.; Quinn, A. M.; Hunter, T. *Science* **1988**, *241*, 42-52.
(64) Gosal, G.; Kochut, K. J.; Kannan, N. *PLoS One* **2011**, *6*, e28782.
(65) McSkimming, D. I.; Dastgheib, S.; Talevich, E.; Narayanan, A.; Katiyar, S.; Taylor, S. S.; Kochut, K.; Kannan, N. *Hum. Mutat.* **2015**, *36*, 175-186.
(66) Yonemoto, W.; Garrod, S. M.; Bell, S. M.; Taylor, S. S. *J. Biol. Chem.* **1993**, *268*, 18626-18632.
(67) Krupa, A.; Preethi, G.; Srinivasan, N. *J. Mol. Biol.* **2004**, *339*, 1025-1039.
(68) Lopez-Garcia, Laura A.; Schulze, Jörg O.; Fröhner, W.; Zhang, H.; Süß, E.; Weber, N.; Navratil, J.; Amon, S.; Hindie, V.; Zeuzem, S.; Jørgensen, Thomas J. D.; Alzari, Pedro M.; Neimanis, S.; Engel, M.; Biondi, Ricardo M. *Chem. Biol.* **2011**, *18*, 1463-1473.
(69) Cheng, X.; Ma, Y.; Moore, M.; Hemmings, B. A.; Taylor, S. S. *Proceedings of the National Academy of Sciences* **1998**, *95*, 9849-9854.
(70) Kornev, A. P.; Taylor, S. S. *Biochimica et Biophysica Acta (BBA) - Proteins and Proteomics* **2010**, *1804*, 440-444.

(71) McClendon, C. L.; Kornev, A. P.; Gilson, M. K.; Taylor, S. S. *Proceedings of the National Academy of Sciences* **2014**, *111*, E4623-E4631.
(72) Huse, M.; Kuriyan, J. *Cell* **2002**, *109*, 275-282.
(73) Madhusudan; Trafny, E. A.; Xuong, N.-H.; Adams, J. A.; Eyck, L. F. T.; Taylor, S. S.; Sowadski, J. M. *Protein Sci.* **1994**, *3*, 176-187.
(74) Taylor, S. S.; Radzio-Andzelm, E. *Structure* **1994**, *2*, 345-355.
(75) Hanks, S. K.; Hunter, T. *FASEB J.* **1995**, *9*, 576-596.
(76) Gerlits, O.; Waltman, M. J.; Taylor, S.; Langan, P.; Kovalevsky, A. *Biochemistry* **2013**, *52*, 3721-3727.
(77) Narayana, N.; Cox, S.; Xuong, N.-h.; Eyck, L. F. T.; Taylor, S. S. *Structure* **1997**, *5*, 921-935.
(78) Bossemeyer, D. *Trends Biochem. Sci.* **1994**, *19*, 201-205.
(79) Madhusudan; Akamine, P.; Xuong, N.-H.; Taylor, S. S. *Nat. Struct. Mol. Biol.* **2002**, *9*, 273-277.
(80) Gerlits, O.; Tian, J.; Das, A.; Langan, P.; Heller, W. T.; Kovalevsky, A. *J. Biol. Chem.* **2015**, *290*, 15538-15548.
(81) Taylor, S. S.; Radzio-Andzelm, E.; Madhusudan; Cheng, X.; Ten Eyck, L.; Narayana, N. *Pharmacol. Ther.* **1999**, *82*, 133-141.
(82) Thoden, J. B.; Holden, H. M. *J. Biol. Chem.* **2005**, *280*, 32784-32791.
(83) Meharena, H. S.; Chang, P.; Keshwani, M. M.; Oruganty, K.; Nene, A. K.; Kannan, N.; Taylor, S. S.; Kornev, A. P. *PLoS Biol.* **2013**, *11*, e1001680.
(84) Yang, J.; Garrod, S. M.; Deal, M. S.; Anand, G. S.; Woods, V. L., Jr.; Taylor, S. *J. Mol. Biol.* **2005**, *346*, 191-201.
(85) Skamnaki, V. T.; Owen, D. J.; Noble, M. E. M.; Lowe, E. D.; Lowe, G.; Oikonomakos, N. G.; Johnson, L. N. *Biochemistry* **1999**, *38*, 14718-14730.
(86) Kobe, B.; Kampmann, T.; Forwood, J. K.; Listwan, P.; Brinkworth, R. I. *Biochimica et Biophysica Acta (BBA) - Proteins and Proteomics* **2005**, *1754*, 200-209.
(87) Pearson, R. B.; Kemp, B. E. In *Methods Enzymol.*; Tony Hunter, B. M. S., Ed.; Academic Press, 1991; Vol. Volume 200.
(88) Kemp, B. E.; Pearson, R. B. In *Methods Enzymol.*; Tony Hunter, B. M. S., Ed.; Academic Press, 1991; Vol. Volume 200.
(89) Kemp, B. E.; Pearson, R. B. *Trends Biochem. Sci.* **1990**, *15*, 342-346.
(90) Songyang, Z.; Carraway, K. L.; Eck, M. J.; Harrison, S. C.; Feldman, R. A.; Mohammadi, M.; Schlessinger, J.; Hubbard, S. R.; Smith, D. P.; Eng, C.; Lorenzo, M. J.; Ponder, B. A. J.; Mayer, B. J.; Cantley, L. C. *Nature* **1995**, *373*, 536-539.
(91) Luo, K.; Zhou, P.; Lodish, H. F. *Proc. Natl. Acad. Sci. U. S. A.* **1995**, *92*, 11761-11765.
(92) Nishikawa, K.; Toker, A.; Johannes, F.-J.; Songyang, Z.; Cantley, L. C. *J. Biol. Chem.* **1997**, *272*, 952-960.
(93) Knighton, D.; Zheng, J.; Ten Eyck, L.; Xuong, N.; Taylor, S.; Sowadski, J. *Science* **1991**, *253*, 414-420.
(94) Kornev, A. P.; Haste, N. M.; Taylor, S. S.; Ten Eyck, L. F. *Proceedings of the National Academy of Sciences* **2006**, *103*, 17783-17788.
(95) Taylor, S. S.; Zhang, P.; Steichen, J. M.; Keshwani, M. M.; Kornev, A. P. *Biochim. Biophys. Acta* **2013**, *1834*, 1271-1278.
(96) Adams, J. A.; Taylor, S. S. *Protein Sci.* **1993**, *2*, 2177-2186.
(97) Bhatnagar, D.; Roskoski, R.; Rosendahl, M. S.; Leonard, N. J. *Biochemistry* **1983**, *22*, 6310-6317.
(98) Storer, A. C.; Cornish-Bowden, A. *Biochem. J.* **1976**, *159*, 1-5.
(99) Armstrong, R. N.; Kondo, H.; Granot, J.; Kaiser, E. T.; Mildvan, A. S. *Biochemistry* **1979**, *18*, 1230-1238.
(100) Zheng, J.; Trafny, E. A.; Knighton, D. R.; Xuong, N.; Taylor, S. S.; Ten Eyck, L. F.; Sowadski, J. M. *Acta Crystallographica Section D* **1993**, *49*, 362-365.

(101) Gerlits, O.; Das, A.; Keshwani, M. M.; Taylor, S.; Waltman, M. J.; Langan, P.; Heller, W. T.; Kovalevsky, A. *Biochemistry* **2014**, *53*, 3179-3186.
(102) Bastidas, A. C.; Deal, M. S.; Steichen, J. M.; Guo, Y.; Wu, J.; Taylor, S. S. *J. Am. Chem. Soc.* **2013**, *135*, 4788-4798.
(103) Jacobsen, D. M.; Bao, Z.-Q.; O'Brien, P.; Brooks, C. L.; Young, M. A. *J. Am. Chem. Soc.* **2012**, *134*, 15357-15370.
(104) Bao, Zhao Q.; Jacobsen, Douglas M.; Young, Matthew A. *Structure* **2011**, *19*, 675-690.
(105) Mukherjee, K.; Sharma, M.; Urlaub, H.; Bourenkov, G. P.; Jahn, R.; Sudhof, T. C.; Wahl, M. C. *Cell* **2008**, *133*, 328-339.
(106) Walsh, D. A.; Perkins, J. P.; Krebs, E. G. *J. Biol. Chem.* **1968**, *243*, 3763-3765.
(107) Knighton, D.; Zheng, J.; Ten Eyck, L.; Ashford, V.; Xuong, N.; Taylor, S.; Sowadski, J. *Science* **1991**, *253*, 407-414.
(108) Taylor, S. S.; Buechler, J. A.; Yonemoto, W. *Annu. Rev. Biochem.* **1990**, *59*, 971-1005.
(109) Francis, S.; Corbin, J. *Annu. Rev. Physiol.* **1994**, *56*, 237-272.
(110) Taylor, S. S.; Yang, J.; Wu, J.; Haste, N. M.; Radzio-Andzelm, E.; Anand, G. *Biochim. Biophys. Acta* **2004**, *1697*, 259-269.
(111) Taylor, S. S.; Kornev, A. P. In *Quatitative Biology: From Molecular to Cellular Systems*; Wall, M. E., Ed.; CRC Press: Boca Raton, London, New York, 2012.
(112) Taylor, S. S.; Bubis, J.; Toner-Webb, J.; Saraswat, L. D.; First, E. A.; Buechler, J. A.; Knighton, D. R.; Sowadski, J. *FASEB J.* **1988**, *2*, 2677-2685.
(113) Rall, T. W.; Sutherland, E. W. *J. Biol. Chem.* **1958**, *232*, 1065-1076.
(114) Northup, J. K.; Sternweis, P. C.; Smigel, M. D.; Schleifer, L. S.; Ross, E. M.; Gilman, A. G. *Proc. Natl. Acad. Sci. U. S. A.* **1980**, *77*, 6516-6520.
(115) Tao, M.; Salas, M. L.; Lipmann, F. *Proc. Natl. Acad. Sci. U. S. A.* **1970**, *67*, 408-414.
(116) Gill, G. N.; Garren, L. D. *Biochem. Biophys. Res. Commun.* **1970**, *39*, 335-343.
(117) Brostrom, C. O.; Corbin, J. D.; King, C. A.; Krebs, E. G. *Proc. Natl. Acad. Sci. U. S. A.* **1971**, *68*, 2444-2447.
(118) Wong, W.; Scott, J. D. *Nat. Rev. Mol. Cell Biol.* **2004**, *5*, 959-970.
(119) Ross, E. M.; Maguire, M. E.; Sturgill, T. W.; Biltonen, R. L.; Gilman, A. G. *J. Biol. Chem.* **1977**, *252*, 5761-5775.
(120) Sarma, G. N.; Kinderman, F. S.; Kim, C.; von Daake, S.; Chen, L.; Wang, B.-C.; Taylor, S. S. *Structure*, *18*, 155-166.
(121) Granot, J.; Mildvan, A. S.; Hiyama, K.; Kondo, H.; Kaiser, E. T. *J. Biol. Chem.* **1980**, *255*, 4569-4573.
(122) Boras, B. W.; Kornev, A.; Taylor, S. S.; McCulloch, A. D. *J. Biol. Chem.* **2014**, *289*, 30040-30051.
(123) Kim, C.; Cheng, C.; Saldanha, S.; Taylor, S. S. *Cell* **2007**, *130*, 1032-1043.
(124) Zhang, P.; Smith-Nguyen, E. V.; Keshwani, M. M.; Deal, M. S.; Kornev, A. P.; Taylor, S. S. *Science* **2012**, *335*, 712-716.
(125) Taylor, S. S.; Knighton, D. R.; Zheng, J.; Ten Eyck, L. F.; Sowadski, J. M. *Annu. Rev. Cell Biol.* **1992**, *8*, 429-462.
(126) Herberg, F. W.; Taylor, S. S.; Dostmann, W. R. G. *Biochemistry* **1996**, *35*, 2934-2942.
(127) Kemp, B. E.; Graves, D. J.; Benjamini, E.; Krebs, E. G. *J. Biol. Chem.* **1977**, *252*, 4888-4894.
(128) Qamar, R.; Yoon, M. Y.; Cook, P. F. *Biochemistry* **1992**, *31*, 9986-9992.
(129) Adams, J. A.; Taylor, S. S. *Biochemistry* **1992**, *31*, 8516-8522.
(130) Grant, B. D.; Adams, J. A. *Biochemistry* **1996**, *35*, 2022-2029.
(131) Li, C.; Ma, N.; Wang, Y.; Wang, Y.; Chen, G. *J. Phys. Chem. B* **2014**, *118*, 1273-1287.
(132) Sims, P. C.; Moody, I. S.; Choi, Y.; Dong, C.; Iftikhar, M.; Corso, B. L.; Gul, O. T.; Collins, P. G.; Weiss, G. A. *J. Am. Chem. Soc.* **2013**, *135*, 7861-7868.
(133) Cheng, H. C.; Kemp, B. E.; Pearson, R. B.; Smith, A. J.; Misconi, L.; Van Patten, S. M.; Walsh, D. A. *J. Biol. Chem.* **1986**, *261*, 989-992.
(134) Wen, W.; Meinkotht, J. L.; Tsien, R. Y.; Taylor, S. S. *Cell* **1995**, *82*, 463-473.

(135) Belyamani, M.; Gangolli, E. A.; Idzerda, R. L. *Mol. Cell. Biol.* **2001**, *21*, 3959-3963.
(136) Gangolli, E. A.; Belyamani, M.; Muchinsky, S.; Narula, A.; Burton, K. A.; McKnight, G. S.; Uhler, M. D.; Idzerda, R. L. *Mol. Cell. Biol.* **2000**, *20*, 3442-3448.
(137) Gibbs, C. S.; Zoller, M. J. *J. Biol. Chem.* **1991**, *266*, 8923-8931.
(138) Kivi, R.; Loog, M.; Jemth, P.; Järv, J. *The protein journal* **2013**, *32*, 519-525.
(139) Kivi, R.; Jemth, P.; Jarv, J. *The protein journal* **2014**, *33*, 386-393.
(140) Lew, J.; Taylor, S. S.; Adams, J. A. *Biochemistry* **1997**, *36*, 6717-6724.
(141) Kim, C.; Xuong, N. H.; Taylor, S. S. *Science* **2005**, *307*, 690-696.
(142) Zheng, J.; Knighton, D. R.; ten Eyck, L. F.; Karlsson, R.; Xuong, N.; Taylor, S. S.; Sowadski, J. M. *Biochemistry* **1993**, *32*, 2154-2161.
(143) Zheng, J.; Knighton, D. R.; Xuong, N. H.; Taylor, S. S.; Sowadski, J. M.; Ten Eyck, L. F. *Protein Sci.* **1993**, *2*, 1559-1573.
(144) Akamine, P.; Madhusudan; Wu, J.; Xuong, N.-H.; Eyck, L. F. T.; Taylor, S. S. *J. Mol. Biol.* **2003**, *327*, 159-171.
(145) Kong, C. T.; Cook, P. F. *Biochemistry* **1988**, *27*, 4795-4799.
(146) Bastidas, A. C.; Wu, J.; Taylor, S. S. *Biochemistry* **2015**, *54*, 2-10.
(147) Yang, J.; Ten Eyck, L. F.; Xuong, N.-H.; Taylor, S. S. *J. Mol. Biol.* **2004**, *336*, 473-487.
(148) Montenegro, M.; Garcia-Viloca, M.; Lluch, J. M.; Gonzalez-Lafont, A. *Phys. Chem. Chem. Phys.* **2011**, *13*, 530-539.
(149) Cembran, A.; Masterson, L. R.; McClendon, C. L.; Taylor, S. S.; Gao, J.; Veglia, G. *Biochemistry* **2012**, *51*, 10186-10196.
(150) Shaltiel, S.; Cox, S.; Taylor, S. S. *Proc. Natl. Acad. Sci. U. S. A.* **1998**, *95*, 484-491.
(151) Bjarnadottir, U.; Nielsen, J. E. *Biopolymers* **2012**, *97*, 65-72.
(152) Srivastava, Atul K.; McDonald, Leanna R.; Cembran, A.; Kim, J.; Masterson, Larry R.; McClendon, Christopher L.; Taylor, Susan S.; Veglia, G. *Structure* **2014**, *22*, 1735-1743.
(153) Aimes, R. T.; Hemmer, W.; Taylor, S. S. *Biochemistry* **2000**, *39*, 8325-8332.
(154) Iyer, G. H.; Garrod, S.; Woods, V. L., Jr.; Taylor, S. S. *J. Mol. Biol.* **2005**, *351*, 1110-1122.
(155) Iyer, G. H.; Moore, M. J.; Taylor, S. S. *J. Biol. Chem.* **2005**, *280*, 8800-8807.
(156) Herberg, F. W.; Doyle, M. L.; Cox, S.; Taylor, S. S. *Biochemistry* **1999**, *38*, 6352-6360.
(157) Tereshko, V.; Teplova, M.; Brunzelle, J.; Watterson, D. M.; Egli, M. *Nat. Struct. Mol. Biol.* **2001**, *8*, 899-907.
(158) Waas, W. F.; Dalby, K. N. *Biochemistry* **2003**, *42*, 2960-2970.
(159) Liu, M.; Girma, E.; Glicksman, M. A.; Stein, R. L. *Biochemistry* **2010**, *49*, 4921-4929.
(160) Zhou, J.; Adams, J. A. *Biochemistry* **1997**, *36*, 15733-15738.
(161) Shaffer, J.; Adams, J. A. *Biochemistry* **1999**, *38*, 5572-5581.
(162) Shaffer, J.; Adams, J. A. *Biochemistry* **1999**, *38*, 12072-12079.
(163) Khavrutskii, I. V.; Grant, B.; Taylor, S. S.; McCammon, J. A. *Biochemistry* **2009**, *48*, 11532-11545.
(164) Kovalevsky, A. Y.; Johnson, H.; Hanson, B. L.; Waltman, M. J.; Fisher, S. Z.; Taylor, S.; Langan, P. *Acta Crystallogr. D Biol. Crystallogr.* **2012**, *68*, 854-860.
(165) Szarek, P.; Dyguda-Kazimierowicz, E.; Tachibana, A.; Sokalski, W. A. *The Journal of Physical Chemistry B* **2008**, *112*, 11819-11826.
(166) Cheng, Y.; Zhang, Y.; McCammon, J. A. *J. Am. Chem. Soc.* **2005**, *127*, 1553-1562.
(167) Valiev, M.; Yang, J.; Adams, J. A.; Taylor, S. S.; Weare, J. H. *J. Phys. Chem. B* **2007**, *111*, 13455-13464.
(168) Yount, R. G.; Babcock, D.; Ballantyne, W.; Ojala, D. *Biochemistry* **1971**, *10*, 2484-2489.
(169) Olsen, S. R.; Uhler, M. D. *Mol. Endocrinol.* **1991**, *5*, 1246-1256.
(170) Mitchell, R. D.; Glass, D. B.; Wong, C.-W.; Angelos, K. L.; Walsh, D. A. *Biochemistry* **1995**, *34*, 528-534.
(171) Knighton, D. R.; Bell, S. M.; Zheng, J.; Ten Eyck, L. F.; Xuong, N.; Taylor, S. S.; Sowadski, J. M. *Acta Crystallographica Section D* **1993**, *49*, 357-361.

(172) Narayana, N.; Cox, S.; Shaltiel, S.; Taylor, S. S.; Xuong, N.-h. *Biochemistry* **1997**, *36*, 4438-4448.
(173) Herberg, F. W.; Zimmermann, B.; McGlone, M.; Taylor, S. S. *Protein Sci.* **1997**, *6*, 569-579.
(174) Taylor, S. S.; Knighton, D. R.; Zheng, J.; Sowadski, J. M.; Gibbs, C. S.; Zoller, M. J. *Trends Biochem. Sci.* **1993**, *18*, 84-89.
(175) Bossemeyer, D.; Engh, R. A.; Kinzel, V.; Ponstingl, H.; Huber, R. *The EMBO Journal* **1993**, *12*, 849-859.
(176) Lee, J. H.; Maeda, S.; Angelos, K. L.; Kamita, S. G.; Ramachandran, C.; Walsh, D. A. *Biochemistry* **1992**, *31*, 10616-10625.
(177) Grant, B. D.; Hemmer, W.; Tsigelny, I.; Adams, J. A.; Taylor, S. S. *Biochemistry* **1998**, *37*, 7708-7715.
(178) Hemmer, W.; McGlone, M.; Tsigelny, I.; Taylor, S. S. *J. Biol. Chem.* **1997**, *272*, 16946-16954.
(179) Bastidas, A. C.; Deal, M. S.; Steichen, J. M.; Keshwani, M. M.; Guo, Y.; Taylor, S. S. *J. Mol. Biol.* **2012**, *422*, 215-229.
(180) Li, F.; Gangal, M.; Juliano, C.; Gorfain, E.; Taylor, S. S.; Johnson, D. A. *J. Mol. Biol.* **2002**, *315*, 459-469.
(181) De Bondt, H. L.; Rosenblatt, J.; Jancarik, J.; Jones, H. D.; Morgant, D. O.; Kim, S.-H. *Nature* **1993**, *363*, 595-602.
(182) Sicheri, F.; Moarefi, I.; Kuriyan, J. *Nature* **1997**, *385*, 602-609.
(183) Xu, W.; Doshi, A.; Lei, M.; Eck, M. J.; Harrison, S. C. *Mol. Cell* **1999**, *3*, 629-638.
(184) Tsigelny, I.; Greenberg, J. P.; Cox, S.; Nichols, W. L.; Taylor, S. S.; Ten Eyck, L. F. *Biopolymers* **1999**, *50*, 513-524.
(185) Yoon, M. Y.; Cook, P. F. *Biochemistry* **1987**, *26*, 4118-4125.
(186) Zhou, J.; Adams, J. A. *Biochemistry* **1997**, *36*, 2977-2984.
(187) Valiev, M.; Kawai, R.; Adams, J. A.; Weare, J. H. *J. Am. Chem. Soc.* **2003**, *125*, 9926-9927.
(188) Montenegro, M.; Masgrau, L.; González-Lafont, À.; Lluch, J. M.; Garcia-Viloca, M. *Biophys. Chem.* **2012**, *161*, 17-28.
(189) González, B.; Schell, M. J.; Letcher, A. J.; Veprintsev, D. B.; Irvine, R. F.; Williams, R. L. *Mol. Cell* **2004**, *15*, 689-701.
(190) Díaz, N.; Field, M. J. *J. Am. Chem. Soc.* **2004**, *126*, 529-542.
(191) Moore, M. J.; Adams, J. A.; Taylor, S. S. *J. Biol. Chem.* **2003**, *278*, 10613-10618.
(192) Moore, M. J.; Kanter, J. R.; Jones, K. C.; Taylor, S. S. *J. Biol. Chem.* **2002**, *277*, 47878-47884.
(193) Adams, J. A. *Biochemistry* **2003**, *42*, 601-607.
(194) Adams, J. A.; McGlone, M. L.; Gibson, R.; Taylor, S. S. *Biochemistry* **1995**, *34*, 2447-2454.
(195) Cheng, Y.; Zhang, Y.; McCammon, J. A. *Protein Sci.* **2006**, *15*, 672-683.
(196) Shoji, S.; Ericsson, L. H.; Walsh, K. A.; Fischer, E. H.; Titani, K. *Biochemistry* **1983**, *22*, 3702-3709.
(197) Mildvan, A. S. *Proteins* **1997**, *29*, 401-416.
(198) Prasad, B. R.; Plotnikov, N. V.; Warshel, A. *J. Phys. Chem. B* **2013**, *117*, 153-163.
(199) Plotnikov, N. V.; Prasad, B. R.; Chakrabarty, S.; Chu, Z. T.; Warshel, A. *J. Phys. Chem. B* **2013**, *117*, 12807-12819.
(200) Ho, M.; Bramson, H. N.; Hansen, D. E.; Knowles, J. R.; Kaiser, E. T. *J. Am. Chem. Soc.* **1988**, *110*, 2680-2681.
(201) Granot, J.; Mildvan, A. S.; Bramson, H. N.; Kaiser, E. T. *Biochemistry* **1980**, *19*, 3537-3543.
(202) Adams, J. A.; Taylor, S. S. *J. Biol. Chem.* **1993**, *268*, 7747-7752.
(203) Błachut-Okrasińska, E.; Lesyng, B.; Briggs, J. M.; McCammon, J. A.; Antosiewicz, J. M. *Eur. Biophys. J.* **1999**, *28*, 457-467.
(204) C. Hart, J.; W. Sheppard, D.; H. Hillier, I.; A. Burton, N. *Chem. Commun.* **1999**, 79-80.
(205) Hutter, M. C.; Helms, V. *Int. J. Quantum Chem.* **2003**, *95*, 479-486.

(206) Smith, G. K.; Ke, Z.; Guo, H.; Hengge, A. C. *J. Phys. Chem. B* **2011**, *115*, 13713-13722.
(207) Sheppard, D. W.; Burton, N. A.; Hillier, I. H. *J. Mol. Struct. (THEOCHEM)* **2000**, *506*, 35-44.
(208) Montenegro, M.; Garcia-Viloca, M.; González-Lafont, À.; Lluch, J. *J. Comput. Aided Mol. Des.* **2007**, *21*, 603-615.
(209) Krishna, S. S.; Zhou, T.; Daugherty, M.; Osterman, A.; Zhang, H. *Biochemistry* **2001**, *40*, 10810-10818.
(210) Grigorenko, B. L.; Nemukhin, A. V.; Shadrina, M. S.; Topol, I. A.; Burt, S. K. *Proteins: Structure, Function, and Bioinformatics* **2007**, *66*, 456-466.
(211) De Vivo, M.; Cavalli, A.; Carloni, P.; Recanatini, M. *Chemistry – A European Journal* **2007**, *13*, 8437-8444.
(212) Lin, P.; Pedersen, L. C.; Batra, V. K.; Beard, W. A.; Wilson, S. H.; Pedersen, L. G. *Proceedings of the National Academy of Sciences* **2006**, *103*, 13294-13299.
(213) Alberts, I. L.; Wang, Y.; Schlick, T. *J. Am. Chem. Soc.* **2007**, *129*, 11100-11110.
(214) Wang, L.; Yu, X.; Hu, P.; Broyde, S.; Zhang, Y. *J. Am. Chem. Soc.* **2007**, *129*, 4731-4737.
(215) Glennon, T. M.; Villà, J.; Warshel, A. *Biochemistry* **2000**, *39*, 9641-9651.
(216) Shurki, A.; Warshel, A. *Proteins: Structure, Function, and Bioinformatics* **2004**, *55*, 1-10.
(217) Jin, Y.; Cliff, M. J.; Baxter, N. J.; Dannatt, H. R. W.; Hounslow, A. M.; Bowler, M. W.; Blackburn, G. M.; Waltho, J. P. *Angew. Chem. Int. Ed.* **2012**, *51*, 12242-12245.
(218) Smith, A. J. T.; Li, Y.; Houk, K. N. *Org. Biomol. Chem.* **2009**, *7*, 2716-2724.
(219) Li, C.; Ma, N.; Wang, Y.; Wang, Y.; Chen, G. *The Journal of Physical Chemistry B* **2014**, *118*, 1273-1287.
(220) Leigh, K. N.; Webster, C. E. *Dalton Trans.* **2014**, *43*, 3039-3043.
(221) Brunk, E.; Rothlisberger, U. *Chem. Rev.* **2015**, *115*, 6217-6263.
(222) Thiel, W. *Angew. Chem. Int. Ed.* **2014**.
(223) Senn, H. M.; Thiel, W. *Angew. Chem. Int. Ed.* **2009**, *48*, 1198-1229.
(224) Warshel, A.; Levitt, M. *J. Mol. Biol.* **1976**, *103*, 227-249.
(225) Field, M. J. *J. Comput. Chem.* **2002**, *23*, 48-58.
(226) Friesner, R. A.; Guallar, V. *Annu. Rev. Phys. Chem.* **2005**, *56*, 389-427.
(227) Senn, H.; Thiel, W. In *Atomistic Approaches in Modern Biology*; Reiher, M., Ed.; Springer Berlin Heidelberg, 2007; Vol. 268.
(228) Sherwood, P.; de Vries, A. H.; Guest, M. F.; Schreckenbach, G.; Catlow, C. R. A.; French, S. A.; Sokol, A. A.; Bromley, S. T.; Thiel, W.; Turner, A. J.; Billeter, S.; Terstegen, F.; Thiel, S.; Kendrick, J.; Rogers, S. C.; Casci, J.; Watson, M.; King, F.; Karlsen, E.; Sjøvoll, M.; Fahmi, A.; Schäfer, A.; Lennartz, C. *J. Mol. Struct. (THEOCHEM)* **2003**, *632*, 1-28.
(229) Billeter, S. R.; Turner, A. J.; Thiel, W. *Phys. Chem. Chem. Phys.* **2000**, *2*, 2177-2186.
(230) Ochsenfeld, C.; Kussmann, J.; Lambrecht, D. S. In *Reviews in Computational Chemistry*; John Wiley & Sons, Inc., 2007.
(231) *Linear-Scaling Techniques in Computational Chemistry and Physics. Methods and Applications.*; Springer Netherlands, 2011.
(232) Lin, H.; Truhlar, D. G. *Theor. Chem. Acc.* **2006**, *117*, 185-199.
(233) van der Kamp, M. W.; Mulholland, A. J. *Biochemistry* **2013**, *52*, 2708-2728.
(234) Schlegel, H. B. In *Modern Electronic Structure Theory*; World Scientific Publishing Company, 2012.
(235) von Arnim, M.; Ahlrichs, R. *The Journal of Chemical Physics* **1999**, *111*, 9183-9190.
(236) Fogarasi, G.; Zhou, X.; Taylor, P. W.; Pulay, P. *J. Am. Chem. Soc.* **1992**, *114*, 8191-8201.
(237) Baker, J.; Kinghorn, D.; Pulay, P. *The Journal of Chemical Physics* **1999**, *110*, 4986-4991.
(238) Paizs, B.; Baker, J.; Suhai, S.; Pulay, P. *The Journal of Chemical Physics* **2000**, *113*, 6566-6572.
(239) Paizs, B.; Fogarasi, G.; Pulay, P. *The Journal of Chemical Physics* **1998**, *109*, 6571-6576.
(240) Liu, D.; Nocedal, J. *Math. Prog.* **1989**, *45*, 503-528.
(241) Banerjee, A.; Adams, N.; Simons, J.; Shepard, R. *J. Phys. Chem.* **1985**, *89*, 52-57.

(242) Baker, J. *J. Comput. Chem.* **1986**, *7*, 385-395.
(243) Turner, A. J.; Moliner, V.; Williams, I. H. *Phys. Chem. Chem. Phys.* **1999**, *1*, 1323-1331.
(244) Brünger, A. T.; Karplus, M. *Proteins: Structure, Function, and Bioinformatics* **1988**, *4*, 148-156.
(245) Brooks, B. R.; Bruccoleri, R. E.; Olafson, B. D.; States, D. J.; Swaminathan, S.; Karplus, M. *J. Comput. Chem.* **1983**, *4*, 187-217.
(246) Brooks, B. R.; Brooks, C. L.; Mackerell, A. D.; Nilsson, L.; Petrella, R. J.; Roux, B.; Won, Y.; Archontis, G.; Bartels, C.; Boresch, S.; Caflisch, A.; Caves, L.; Cui, Q.; Dinner, A. R.; Feig, M.; Fischer, S.; Gao, J.; Hodoscek, M.; Im, W.; Kuczera, K.; Lazaridis, T.; Ma, J.; Ovchinnikov, V.; Paci, E.; Pastor, R. W.; Post, C. B.; Pu, J. Z.; Schaefer, M.; Tidor, B.; Venable, R. M.; Woodcock, H. L.; Wu, X.; Yang, W.; York, D. M.; Karplus, M. *J. Comput. Chem.* **2009**, *30*, 1545-1614.
(247) MacKerell, A. D.; Bashford, D.; Bellott, M.; Dunbrack, R. L.; Evanseck, J. D.; Field, M. J.; Fischer, S.; Gao, J.; Guo, H.; Ha, S.; Joseph-McCarthy, D.; Kuchnir, L.; Kuczera, K.; Lau, F. T. K.; Mattos, C.; Michnick, S.; Ngo, T.; Nguyen, D. T.; Prodhom, B.; Reiher, W. E.; Roux, B.; Schlenkrich, M.; Smith, J. C.; Stote, R.; Straub, J.; Watanabe, M.; Wiórkiewicz-Kuczera, J.; Yin, D.; Karplus, M. *J. Phys. Chem. B* **1998**, *102*, 3586-3616.
(248) MacKerell, A. D.; Feig, M.; Brooks, C. L. *J. Am. Chem. Soc.* **2003**, *126*, 698-699.
(249) Ahlrichs, R.; Bär, M.; Häser, M.; Horn, H.; Kölmel, C. *Chem. Phys. Lett.* **1989**, *162*, 165-169.
(250) Slater, J. C. *Phys. Rev.* **1951**, *81*, 385-390.
(251) Vosko, S. H.; Wilk, L.; Nusair, M. *Canadian Journal of Physics* **1980**, *58*, 1200-1211.
(252) Becke, A. D. *Phys. Rev. A* **1988**, *38*, 3098-3100.
(253) Becke, A. D. *J. Chem. Phys.* **1993**, *98*, 5648-5652.
(254) Stephens, P. J.; Devlin, F. J.; Chabalowski, C. F.; Frisch, M. J. *J. Phys. Chem.* **1994**, *98*, 11623-11627.
(255) Lee, C.; Yang, W.; Parr, R. G. *Phys. Rev. B* **1988**, *37*, 785-789.
(256) Hehre, W. J.; Ditchfield, R.; Pople, J. A. *J. Chem. Phys.* **1972**, *56*, 2257-2261.
(257) Hariharan, P. C.; Pople, J. A. *Theoret. Chim. Acta* **1973**, *28*, 213-222.
(258) Francl, M. M.; Pietro, W. J.; Hehre, W. J.; Binkley, J. S.; Gordon, M. S.; DeFrees, D. J.; Pople, J. A. *J. Chem. Phys.* **1982**, *77*, 3654-3665.
(259) Clark, T.; Chandrasekhar, J.; Spitznagel, G. W.; Schleyer, P. V. R. *J. Comput. Chem.* **1983**, *4*, 294-301.
(260) Weigend, F.; Ahlrichs, R. *Phys. Chem. Chem. Phys.* **2005**, *7*, 3297-3305.
(261) Smith, W.; Forester, T. R. *J. Mol. Graph.* **1996**, *14*, 136-141.
(262) Babu, C. S.; Lim, C. *The Journal of Physical Chemistry A* **2006**, *110*, 691-699.
(263) Bakowies, D.; Thiel, W. *J. Phys. Chem.* **1996**, *100*, 10580-10594.
(264) de Vries, A. H.; Sherwood, P.; Collins, S. J.; Rigby, A. M.; Rigutto, M.; Kramer, G. J. *J. Phys. Chem. B* **1999**, *103*, 6133-6141.
(265) Sherwood, P.; H. de Vries, A.; J. Collins, S.; P. Greatbanks, S.; A. Burton, N.; A. Vincent, M.; H. Hillier, I. *Faraday Discuss.* **1997**, *106*, 79-92.
(266) Nocedal, J. *Math. Comp.* **1980**, *35*, 773-782.
(267) Pople, J. A.; Binkley, J. S.; Seeger, R. *Int. J. Quantum Chem.* **1976**, *10*, 1-19.
(268) Head-Gordon, M.; Pople, J. A.; Frisch, M. J. *Chem. Phys. Lett.* **1988**, *153*, 503-506.
(269) Dunning, T. H. *J. Chem. Phys.* **1989**, *90*, 1007-1023.
(270) Woon, D. E.; Dunning, T. H. *J. Chem. Phys.* **1993**, *98*, 1358-1371.
(271) Humphrey, W.; Dalke, A.; Schulten, K. *J. Mol. Graph.* **1996**, *14*, 33-38.
(272) Pettersen, E. F.; Goddard, T. D.; Huang, C. C.; Couch, G. S.; Greenblatt, D. M.; Meng, E. C.; Ferrin, T. E. *J. Comput. Chem.* **2004**, *25*, 1605-1612.
(273) Lee, J. Y.; Yang, W. *Cell* **2006**, *127*, 1349-1360.
(274) Reed, A. E.; Weinstock, R. B.; Weinhold, F. *J. Chem. Phys.* **1985**, *83*, 735-746.
(275) Garcia-Viloca, M.; Truhlar, D. G.; Gao, J. *Biochemistry* **2003**, *42*, 13558-13575.

(276) Blackburn, G. M.; Bowler, M. W.; Jin, Y.; Waltho, J. P. *Biochemistry (Mosc.)* **2012**, *77*, 1083-1096.
(277) Pérez-Gallegos, A.; Garcia-Viloca, M.; González-Lafont, À.; Lluch, J. *J. Comput. Aided Mol. Des.* **2014**, *28*, 1077-1091.
(278) Perez-Gallegos, A.; Garcia-Viloca, M.; Gonzalez-Lafont, A.; Lluch, J. M. *Phys. Chem. Chem. Phys.* **2015**, *17*, 3497-3511.
(279) Pérez-Gallegos, A.; Garcia-Viloca, M.; González-Lafont, À.; Lluch, J. M. *ACS Catalysis* **2015**, 4897-4912.
(280) Schutz, C. N., Warshel, A. *Proteins* **2004**, *55*, 711-723